Study of the effect of gaseous additives on the growth of Ag films during magnetron sputtering deposition, using in situ and real-time measurements

Ramiro Zapata

THÈSE DE DOCTORAT
SORBONNE UNIVERSITÉ

Spécialité

Physique et Chimie des Matériaux

École doctorale 397 "Physique et Chimie des Matériaux"

réalisée aux laboratoires

Surface du Verre et Interfaces, UMR 125 CNRS – Saint-Gobain
Institut des Nanosciences de Paris, UMR 7588 CNRS – Sorbonne Université

présentée par

Ramiro ZAPATA

pour obtenir le grade de

DOCTEUR DE SORBONNE UNIVERSITÉ

Sujet de la thèse

Study of the effect of gaseous additives on the growth of Ag films during magnetron sputtering deposition, using in situ and real-time measurements

soutenue publiquement le 24 octobre 2023

devant le jury composé de :

M. Abhay Shukla	Professeur, Sorbonne Université	Président du jury
Mme Christine Robert-Goumet	MCF-HDR, Univ. Clermont-Auvergne	Rapporteuse
M. Grégory Abadias	Professeur, Université de Poitiers	Rapporteur
M. Pascal Andreazza	Professeur, Université d'Orléans	Examinateur
M. Rémi Lazzari	Directeur de Recherche, INSP	Directeur
M. Hervé Montigaud	Ingénieur de Recherche, SGRP-SVI	Encadrant, invité

Remerciements

Je voudrais dans un premier temps remercier chaleureusement mon directeur de thèse Rémi Lazzari, ainsi que Hervé Montigaud, Matteo Balestrieri, et Iryna Gozhyk pour leur encadrement, leur disponibilité, et pour toutes les conversations pendant ces trois années de thèse. Je repars avec de très beaux souvenirs des discussions du lundi après-midi, des points de thèse et des conférences, ainsi qu'avec un fichier Powerpoint avec 436+ slides que je garderai comme souvenir. Un grand merci à Jean-François *"Jeff"* Crépet, car ce n'est pas une exagération que de dire que le bon déroulement de cette thèse n'aurait pas été possible sans son travail et sa passion. Un grand merci à Johann Skolski pour ses conseils tout au long de cette aventure, et pour les conversations autour d'un café en travée 6.

Merci également aux membres du jury pour la relecture de ce manuscrit de thèse et ses précieux conseils et commentaires, qui ont contribué à sa version finale.

Je voudrais remercier ma famille et mes amis pour leur soutien inconditionnel tout au long de mes études.

Un grand merci à tout le laboratoire SVI : non seulement pour l'ambiance de travail quotidienne, les pauses-thé, les voyages et les évènements, mais aussi pour m'avoir introduit aux perles du cinéma français et aux compétitions de haut niveau en pâtisserie. Merci à tous les membres permanents, doctorants, post-doctorants et stagiaires que j'ai eu le plaisir et la chance de rencontrer pendant ces trois années de travail.

Résumé en français

Dans le cadre de la production de vitrages dits bas-émissifs (Low-E) aux propriétés d'isolation thermique renforcée, des empilements complexes de couches contenant un ou des films minces d'Ag d'une épaisseur d'environ 12 nm sont déposés à la surface du verre plat (Figure 1). La pulvérisation cathodique magnétron est la technique utilisée par l'industrie verrière pour leur synthèse. La réflexion de ces films d'Ag dans l'infrarouge thermique étant liée à leur conductivité électrique, les recherches actuelles visent à trouver des stratégies pour contrôler la croissance et la microstructure de ces films métalliques. En effet, une bonne cristallinité, un faible taux d'impuretés, une faible rugosité et une faible densité de joints de grains sont des caractéristiques qui favorisent une plus faible résistance électrique. L'objectif final est d'améliorer l'efficacité d'isolation thermique de ces vitrages tout en gardant une faible épaisseur de la couche métallique, afin de garantir une bonne transmission lumineuse dans le visible.

Le dépôt de couches minces par pulvérisation cathodique magnétron est un procédé de dépôt en phase vapeur dans lequel le dépôt d'une couche mince se fait par la condensation d'un gaz d'atomes sur un substrat dans une enceinte fermée. Le gaz d'atomes est créé par la pulvérisation d'une surface dite cible sous l'impact de particules ionisées d'un plasma. L'Ag étant un métal noble, sa faible énergie d'interaction avec de surfaces telles que les oxides induit un mode de croissance 3D ou Volmer-Weber . Celui-ci peut être décrit par une succession d'étapes comportant : (i) la nucléation d'îlots sur la surface, (ii) la croissance de ces îlots par incorporation d'atomes adsorbés, (iii) leur coalescence, (iv) la formation d'un réseau conducteur (dit percolé), puis (v) d'une couche continue (avec un recouvrement total du substrat) et finalement (vi) la formation d'une couche uniforme (en épaisseur) par remplissage des joints de grains et diminution de la rugosité. Du fait du caractère hors-équilibre de la croissance d'une couche d'Ag déposée par pulvérisation cathodique magnétron, une approche cinétique du mécanisme de croissance est nécessaire pour comprendre et modéliser la croissance au travers des différents processus atomiques élémentaires impliqués à chaque étape et des barrières énergétiques associées.

Parmi les approches mises en œuvre pour contrôler la croissance des couches minces d'Ag, l'utilisation d'additifs gazeux dits surfactants pendant le dépôt magnétron a suscité beaucoup d'intérêt ces dernières années auprès de la communauté scientifique et de l'industrie verrière. Ces gaz contrebalancent la tendance naturelle de l'Ag à une croissance de type 3D en favorisant l' étalement du métal, et donc une croissance plus 2D. Idéalement, un surfactant devrait permettre le dépôt de films conducteurs avec une plus faible épaisseur, sans pour autant s'incorporer dans le film et sans effet délétère sur sa conductivité. Parmi ces gaz surfactants on retrouve notamment l'azote (N_2) et l'oxygène (O_2), qui ont déjà été étudiés dans la littérature dans le cas de couches minces métalliques (Ag, Cu, Ni ...) élaborées par pulvérisation cathodique magnétron. Au-delà de cette image idéale, cependant, le rôle de ces additifs ainsi que les mécanismes impliqués ne sont pas encore bien compris. Même si ces travaux précédents ont montré que l'ajout de ces gaz conduit à une percolation plus précoce et une inhibition de la coalescence

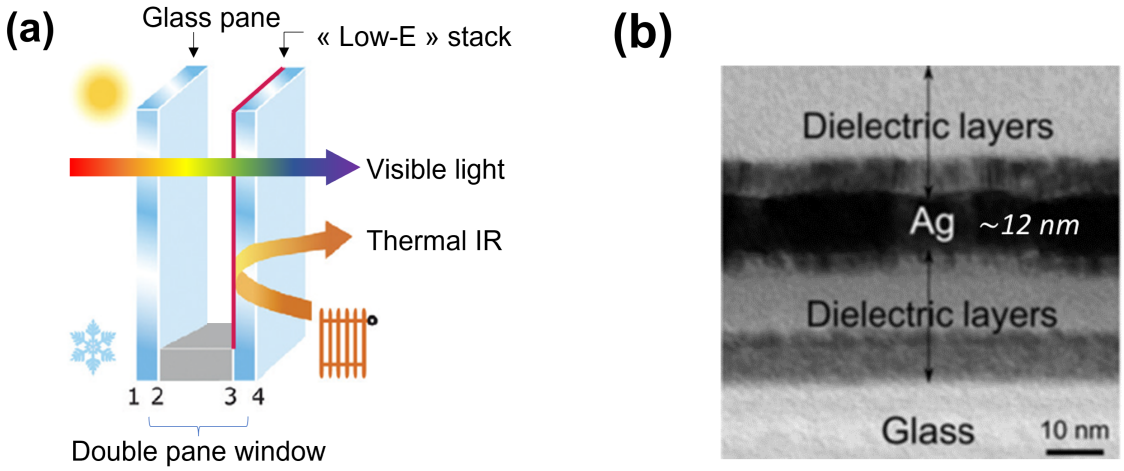

Figure 1 (a) Illustration d'un double vitrage bas-émissif , avec un empilement de couches minces sur une des faces internes, qui augmente la réflexion dans l'infrarouge lointain. (b) Image de microscopie en transmission (Bright field TEM) d'un tel empilement avec une couche d'Ag d'une épaisseur de $\sim$ 12 nm.

entre particules, beaucoup d'entre eux souffrent de limitations inhérentes à l'utilisation de techniques de caractérisation *ex situ* (manque de contrôle sur l'évolution morphologique et chimique post-dépôt, exposition à l'atmosphère et vieillissement . . .). Dans ce contexte, les techniques de caractérisation *in situ* (après dépôt et sans contact avec l'atmosphère) et en temps réel (pendant le dépôt de la couche) apparaissent plus pertinentes pour mieux appréhender cet effet surfactant .

Dans ce travail de thèse, les effets de l'ajout de deux gaz N_2 et O_2 ont été étudiés à l'aide d'une combinaison de techniques. Des mesures en temps réel de résistance électrique ont permis de détecter le seuil de formation d'une couche conductrice (la percolation) et de caractériser la résistivité finale du film, tandis que la spectroscopie de réflectivité différentielle UV-visible a fourni des informations sur le mouillage des nanoparticules d'Ag dans les étapes initiales de croissance (nucléation, croissance, coalescence). En parallèle, la composition chimique du film a été caractérisée par spectroscopie photoélectronique *in situ*. En complément, des mesures *ex situ* de microscopie électronique de transmission et diffraction de rayons-x ont été faites.

Une étude systématique a été réalisée en fonction de la fraction de N_2 ou O_2 dans le flux total de gaz plasmagène (Ar). L'ajout de chacun des deux gaz favorise la formation d'une couche conductrice à une épaisseur plus faible que lors d'un dépôt sous Ar pur en agissant sur les premières étapes de croissance et sur la texture du film. Une oxydation complexe de l'Ag dépendante du flux d'O_2 a été observée, mais aucune formation de nitrure ni d'adsorbat azoté n'a été détectée avec N_2 par photoémission. La modification de l'énergie de surface du métal par adsorption irréversible (oxyde) ou dynamique (N) augmente l'étalement des nanoparticules d'Ag, mais n'est pas la même en fonction des facettes exposées, ce qui génère une compétition entre différentes orientations cristallines. Par conséquent, la coalescence des particules est en partie inhibée par cette compétition et par la présence de différentes espèces à leur surface. Cette coalescence in-

hibée produit des formes d'îlots allongées et irrégulières, contribuant ainsi à une percolation plus rapide du film. CCes effets, ainsi que l'oxydation du film dans le cas du O_2, induisent cependant une perte de conductivité du film continu. Les mesures ont démontré l'existence d'un gradient d'oxydation en profondeur avec un film plus métallique près de l'interface. La compétition entre l'agrégation métal-métal et l'oxydation de l'Ag et du substrat a été mis en avant pour l'expliquer.

Finalement, afin d'étudier l'impact du substrat sur l'effet des gaz surfactants , des dépôts d'Ag sur une sous-couche de SiO_2 et de ZnO dopé aluminium (AZO) ont été comparés. La plus faible énergie de l'interface métal-substrat ainsi que la plus forte texturation du film de Ag déposé sur AZO ont eu comme conséquence l'augmentation du mouillage des nanoparticules d'Ag, et la formation de couches plus conductrices et à des épaisseurs plus faibles. Cela conduit également à une différence nette sur le profil d'oxydation.

General introduction

In a context of global climate change and energy transition, housing thermal insulation is a relevant way of reducing our total energy consumption. For instance, the residential and tertiary sectors represent one of the main source of greenhouse gas emissions in France, with ~ 63 Mt CO_2 eq in 2019 [1], mostly in the form of CO_2 produced by the burning of fossil fuels for heating. 64% of the energy consumption in this sector in 2017 was used for heating [2]. A non-negligible fraction of thermal losses in buildings comes from windows, making them a prime target for building thermal insulation. To tackle the issue, low-emissivity ("Low-E") glazings have been continuously developed since the late 20^{th} century as window products with enhanced thermal insulation properties. They typically consist of double glass panes separated by a cavity, with a complex stack of thin films deposited on one of the inside glass surfaces (Figure 2-a). While heat transport via conduction and convection between the two panes is strongly reduced by the presence of a low thermal conductivity gas in the cavity, thermal radiations losses are reduced by a metallic Ag film included in the layer stack that reflects far-infrared (far-IR $\lambda \geq 3$ μm). Its thickness, in the range of 10-15 nm, allows for a high transmission of visible light, but is still enough to reduce radiative heat transport across the window (Figure 2-b). Figure 3 shows an example of a cross section image of a typical low-E stack containing a thin Ag film.

The main challenge when engineering Low-E products lies in finding the right balance between transparency in the visible region and increased thermal-IR reflection. For a material, the Hagen-Rubens relation [3] links the reflection in the far-IR region R and the electrical conductivity σ via $R \simeq 1 - \sqrt{2\varepsilon_0\omega/\sigma}$; ε_0 corresponds to the vacuum permittivity, ω to the light frequency ($\lambda = \frac{2\pi c}{\omega}$), and c to speed of light in vacuum. This relation shows that increasing the reflectivity of a coating in the IR region involves decreasing its electrical resistivity $\rho = 1/\sigma$. This must be performed, however, without impacting its transparency in the visible range, which effectively rules out the strategy of increasing the film thickness. In this context, thin metallic films are generally preferred over transparent conducting semiconductors due to their better conductivity [4–6]. Regarding the choice of the metal, noble metals such as copper, gold and silver are all suitable candidates in terms of resistivity and chemical resistance. But silver is the only one that does not have a distinct colour due to interband transitions and presents the highest conductivity among all the elements (1.59 $\mu\Omega$.cm [7]).

Industrially, Ag films are deposited on large (3.2×6.0 m^2) glass pane surfaces as part of complex dielectric stacks that are designed to tune the overall optics of the system, its mechanics, and its chemical stability, in particular during thermal treatments such as glass tempering or bending that are performed above the glass transition. In the glass industry, magnetron sputtering deposition is the technique of choice for the deposition of film stacks. Its relevance lies in its versatility in terms of materials (from dielectric, such as oxides or nitrides, to metals), its fast deposition rate (up to tens of nm per second), its reproducibility and its scalability. Current research efforts aim at better understanding the growth mechanism of the Ag thin film and

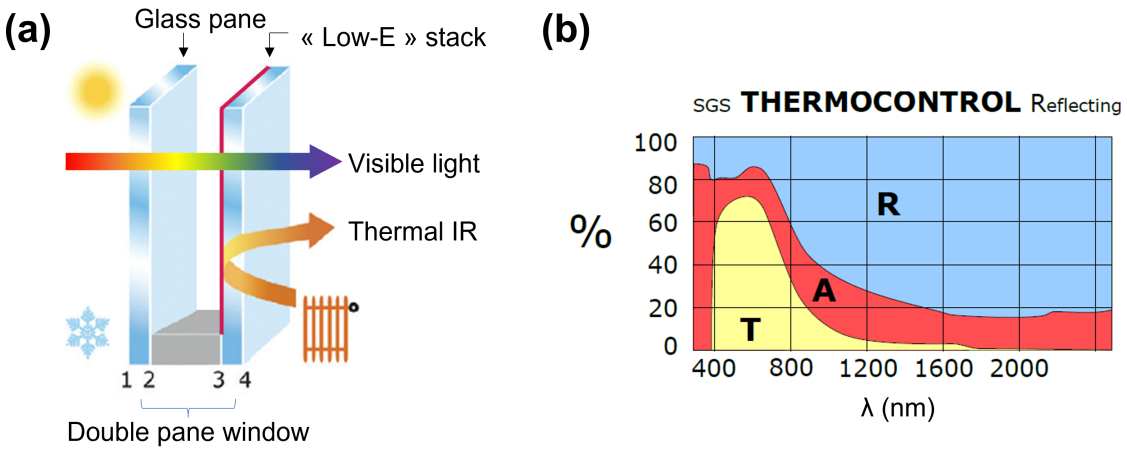

Figure 2 (a) Illustration of a Low-E double glazing with a stack containing the Ag thin film in one of the inside faces of the double pane window. The thin Ag film increases the reflection of thermal infrared radiation from the inside while still remaining transparent towards visible light due to its low thickness. (b) Percentage of transmitted (T), absorbed (A), and reflected (R) light as a function of the wavelength (λ) for a Saint-Gobain Thermocontrol R product containing a Ag thin film deposited on glass.

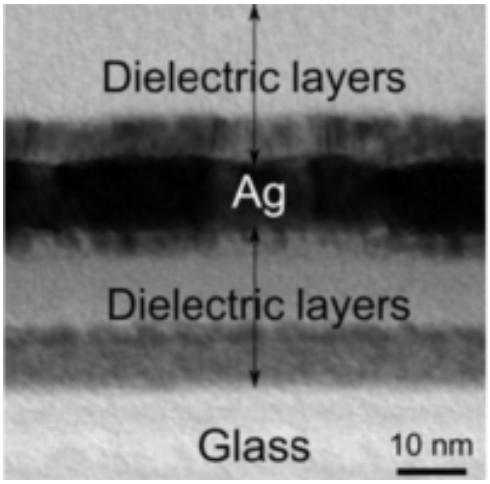

Figure 3 Transverse bright field transmission electron microscopy image of a Low-E stack containing a 10-12 nm-thick Ag thin film.

developing new methods and strategies for controlling it to tailor the final properties of the products. In this context, the use of so-called "surfactant" gas additives during sputtering deposition has garnered much attention over the last years. These gases act upon the growing Ag film to counterbalance the 3D Volmer-Weber growth mode and to favour a more 2D-like growth. Ideally, they should allow for the deposition of thinner conductive films without incorporating in it and without compromising the final properties. However, beyond this ideal picture, the exact role of these additives and the complex mechanisms involved are not yet fully understood.

In this work, the effect of two "surfactant" gases, namely N_2 and O_2, on the growth of Ag films during magnetron sputtering deposition was studied using a combination of real-time (performed during film deposition) and *in situ* measurements (performed after deposition, with no contact with the atmosphere during sample transfer). Real-time electrical film resistance was used to probe the percolation threshold thickness and film resistivity, while Surface Differential Reflectivity Spectroscopy (SDRS) provided information on the wetting behaviour of the Ag nanoparticles in the initial growth stages. In parallel, film chemistry was characterized using *in situ* X-Ray Photoelectron Spectroscopy (XPS). These analyses were further supplemented by *ex situ* Transmission Electron Microscopy (TEM) and X-Ray Diffraction measurements (XRD). After a first study on the effects of these gases on Ag growth on model glass surfaces, deposition on Al-doped Zinc Oxide (AZO) wetting underlayers was explored to unravel the interplay between the substrate and the gas additive on film growth.

Structure of the manuscript

This manuscript will be structured as follows. In the first chapter, a literature review is made covering the fundamentals on magnetron sputtering deposition and the different stages of metallic film growth on weakly-interacting surfaces, especially in the case of Ag films on oxide surfaces. Different strategies for controlling Ag film growth are then discussed, focusing especially on the main subjects of this work, the gaseous "surfactants" and the use of a ZnO underlayer, an epitaxial template for Ag growth. The chapter ends with a comment on the importance of real-time and *in situ* measurements for the study of thin film growth.

The second chapter describes the specificities of the "MISSTIC" experimental set-up used along this thesis work, both for film deposition and for film characterization (real-time, *in situ* and *ex situ* techniques). Care is taken to explain the details of data treatment, especially for the results of real-time techniques (film electrical resistance and SDRS measurements) that are used for detecting different stages of film growth (from nucleation to uniform film formation).

The third and fourth chapters deal with N_2 and O_2 gas addition, respectively, during Ag deposition on oxidized silicon surfaces ("SiO_x"). First, the results from each of the techniques are systematically reviewed. They are then combined in the discussion to comment on the effect of the gas on film morphology, chemistry and microstructure. While all other growth parameters are kept constant, the main explored lever is the flow of reactive gas.

The final chapter focuses once again on the effect of the same gases, but for Ag deposition on an AZO underlayer. The followed approach is the same as in the previous chapters, allowing a systematic comparison to be made between deposition on AZO and on amorphous silica.

Table of contents

Chapter 1

An introduction to Ag thin film sputter deposition, growth and control

In this chapter, a general introduction to the magnetron sputtering deposition process will be given, followed by a description of the growth mechanisms for metallic films from a thermodynamic and kinetic perspective, particularly in the case of weakly-interacting dielectric substrates such as oxides. After these general premises, the discussion will focus on Ag thin films deposited on oxide surfaces, which is a topic of interest both from a fundamental and an applicative point of view. A brief explanation on the kinds of film microstructural properties that lead to lower film resistivity will be given. This will be followed by the state-of-the-art regarding the different strategies for film growth control, with an emphasis on the use of gaseous "surfactant" additives and the effect of underlayers with epitaxial relationships with Ag, such as zinc oxide (ZnO). Although this thesis project deals exclusively with magnetron sputtering deposition, many of the concepts and techniques described in this chapter could also be adapted and/or applied to other kinds of physical vapour deposition (PVD) techniques.

Table of contents

1.1 Growth of metallic thin films on weakly-interacting substrates by magnetron sputtering

1.1.1 The magnetron sputtering deposition process

Magnetron sputtering deposition is a physical vapour deposition (PVD) technique suitable for metallic, semiconductor and dielectric thin films. Its main advantages include a relatively high deposition rate (up to several tens of nanometres per second), its versatility in terms of the choice of materials that can be deposited, its reproducibility, and its adaptability and scaling to industrial settings. In this section, we will give a brief description of this technique. Unlike other PVD processes which rely on thermal energy, laser pulses, or even cathodic arcs to transfer coating precursors (generally atoms) from a crucible or a target to the gas phase, magnetron sputtering deposition relies on the momentum transfer that occurs during collisions between accelerated ions created in a plasma and the surface of a material, called the "target" (Figure 1.1).

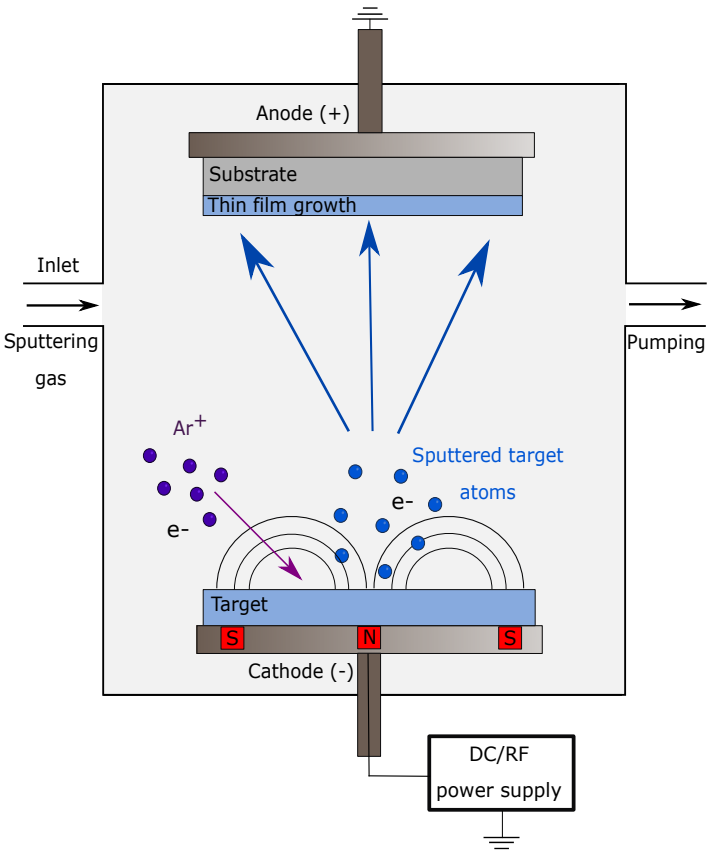

Figure 1.1 Illustration of the magnetron sputtering deposition process. Atoms are sputtered from the target surface to the gas phase during the collision of accelerated Ar^+ ions produced in a plasma, and then condense on the substrate surface to form a film.

The process occurs in a closed deposition vacuum chamber containing the target and the "substrate", on which the film will grow. At the start of the deposition process, a working gas (or "plasmagenic" gas) is inserted into the chamber (up to a working pressure of generally ≥ 1 μbar), and a voltage difference is applied between the target (which acts as the cathode) and the substrate (which acts as the anode). This polarisation is typically in the order of several hundreds of volts, and it brings about the ionisation of a number of gas atoms near the surface of the target. Most of the time, a noble gas (in general argon gas) is used. The ionised Ar^+ ions initially form due to energetic collisions between gas atoms and electrons emitted from the target surface by the high potential difference. Ionisation of an Ar atom liberates another electron, which can in turn collide with another Ar atom. As electrons are liberated in the ionisation process but also recaptured, the process will become stabilised and self-sustained under conditions determined by the system, the ionization energy of the gas and the pressure. At this point, the amount of ionised Ar^+ in the chamber increases and a plasma is formed near the target surface. The collision density between Ar atoms and electrons can be further increased using a magnetic field induced by permanent magnets (shown in Figure 1.1 as the North and South poles under the target). This magnetic field confines the electrons near the target surface, and allows the process to occur at lower gas pressures, lower applied voltage and higher deposition rate.
As previously mentioned, the newly-formed plasma contains a relatively large number of positively-charged, ionised Ar^+ ions. The electric field stemming from the applied potential between the cathode (target) and the anode accelerates these positively-charged ions towards the target surface, leading to an increase in their kinetic energy (acceleration), followed by collision with the target material. The phenomena occurring during this collision will ultimately depend on the kinetic energy of the ion before impact, its incidence angle, the target-to-ion atomic mass ratio, and the composition and topography of the target surface. As a guide, according to Kasi *et al.* [8,9] (Figure 1.2), it is for intermediate ion energies - between roughly 10^{-2} and 10^4 eV - that the "sticking probability" (*i.e* probability for the ion to remain "trapped" on the surface of the target) reaches its minimum, and other phenomena such as sputtering are most probable. Lower kinetic energies result in sticking of the ion to the surface by physisorption or chemisorption, while higher energies lead to implantation of the ions in the target.

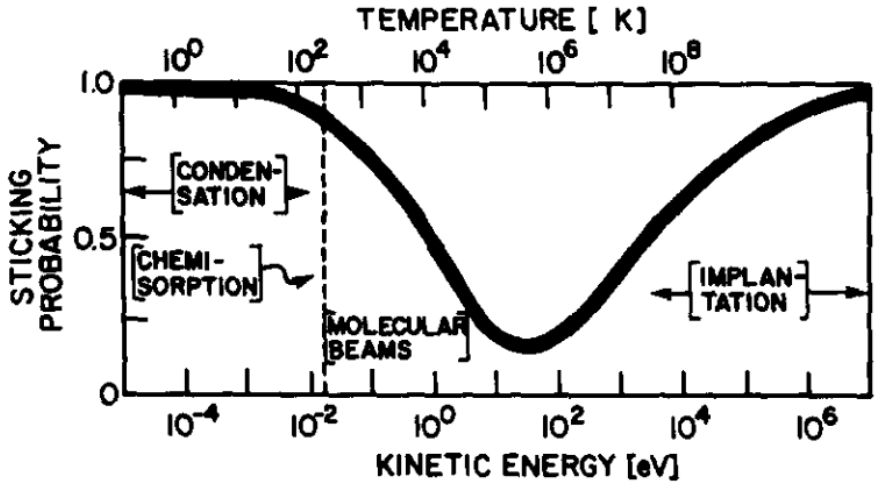

Figure 1.2 Sticking probability of an incoming ion or atom on a surface as a function of its kinetic energy. Reproduced from [8].

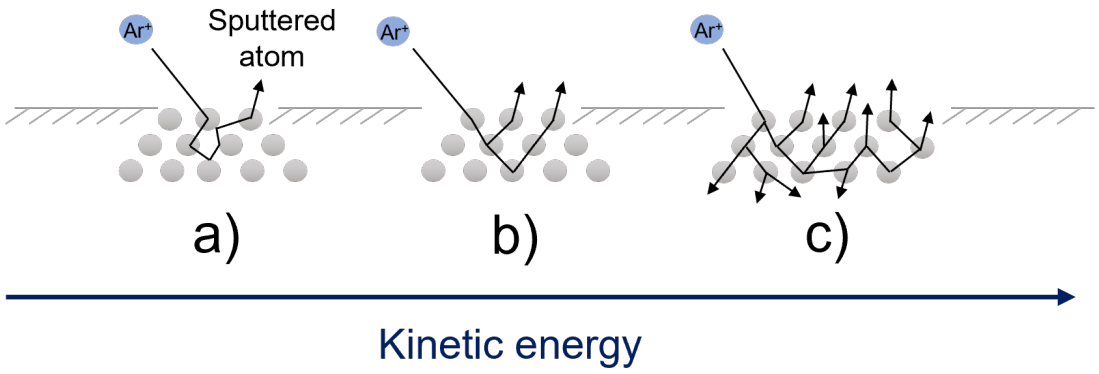

Figure 1.3 Illustration of the three sputtering regimes as a function of the kinetic energy of the colliding Ar^+ ion. (a) Single knock-on at low energy, leading to a series of sequential collisions and the sputtering of a surface atom ; (b) linear cascade regime at intermediate energy, leading to a series of simultaneous collisions between fixed and moving atoms ; and (c) thermal spike regime, with a large number of collisions between moving atoms, and a local rise in temperature.

Sputtering requires sufficient energy transfer to the surface atoms, to the point where they overcome their binding energies, escape the surface and move to the gas phase. According to the works by Sigmund [10], the sputtering interaction between the accelerated ion and the target surface can be divided into three regimes for increasing ion energy (as illustrated in Figure 1.3):

- **Single knock-on regime**: upon collision, an energy transfer occurs from accelerated Ar^+ ions to surface target atoms. If enough energy is transmitted, then the target atoms can overcome their binding energy in the material and escape from the surface to the gas phase. The threshold energy for sputtering in this regime ranges from 5 to 40 eV, approximately. We note that while it is commonly accepted that these threshold values for sputtering scale with the binding energy, the exact relation is still not clear-cut in the literature [11].
- **Linear cascade regime**: at higher kinetic energies, the collision between Ar^+ ions and the target surface generates a "cascade" effect. The density of collisions is low enough that most of the collisions involve a stationary atom and a moving one, and not two moving atoms. As a consequence, an atom is eventually sputtered from the surface into the gas phase. In the case of magnetron sputtering deposition of thin films, kinetic energies for Ar^+ ions arriving at the surface will be in the ballpark of $\sim$ 100 eV [9, 12], which puts us in the linear cascade regime.
- **Thermal spike regime**: this regime is observed for very energetic ions (keV to MeV) impinging on the surface of a dense material. Unlike the previous cascade regime, in which energy tended to be transferred from a moving atom to a stationary atom, the number of collisions in this regime is much higher and occurs indistinctly between all atoms in the collision area. Furthermore, the temperature locally rises in this area ("temperature spike").

After escaping the substrate surface, the sputtered target atoms will cross the deposition chamber and condense on the substrate surface. Their arrival kinetic energy (E_k) will be mainly determined by the energy gained during the sputtering process (E_{sputt}) and by energy lost due to collisions with gas atoms atoms in the chamber (E_{coll}), as shown in Equation 1.1 (with η the collision cross-section, μ a parameter related to the mass ratio of the gas to the particle, d the

substrate-target distance and λ the atom mean-free path).

$$\begin{aligned} E_k &= E_{sputt} - E_{coll} \\ E_k &= E_{sputt} \exp\left(-\frac{\mu d}{\lambda}\right) \\ E_k &= E_{sputt} \exp\left(-\frac{\mu \eta P d}{k_B T}\right) \end{aligned} \tag{1.1}$$

The number of collisions with gas atoms can be described by the mean-free path λ, which is the average distance travelled by a sputtered atom between two collisions. This value is inversely proportional to the gas pressure; an approximate relation between pressure and mean-free path is $\lambda \sim \frac{5}{P}$. Even if this is an approximation for the mean-free path of nitrogen molecules, we can still use it for a ballpark approximation of the value of λ in our system. For our working conditions (total pressure of 2 μbar), this value will be roughly 3.3 cm [13, 14]. With a target-substrate distance of 15 cm in our system, this results to an average number of collisions between the target and the substrate of 4 or 5 per sputtered atom.

At the end, the flux of sputtered atoms arriving at the substrate surface will be responsible for film growth. We will analyse this film growth process in the following section, both from a thermodynamic and a kinetic standpoint.

One important aspect of magnetron sputtering we will mention before moving on, is reactive sputtering deposition, which is of great relevance for the growth of compound thin films. In this process, materials such as oxides, nitrides, borides, carbides and sulfides are deposited using a metallic target (from the metal corresponding to the cation in the desired compound), and a gaseous mixture of a plasmagenic gas (like Ar) with a reactive gas like O_2, N_2, B_2H_6, CH_4 or H_2S, respectively for the above given examples. As the metal of the target is most of the time not inert towards the reactive, their interaction will greatly depend on the reactive gas flow. At very low flow value, there is no major change compared to pure Ar and the reactive gas is simply evacuated by the vacuum pump. Above a certain flow threshold, the gas starts reacting with the target surface, thus disturbing the sputtering dynamics with changes in voltage and sputtering rate. A hysteresis behaviour is observed since the behaviour of the target will depend on its history; that is to say, on whether the target surface was completely metallic at the start of the sputtering process ("metallic regime"), or whether it had previously been covered with compound ("poisoned regime") due to the adsorption of the reactive gas. Figure 1.4 shows an example taken from Reference [15] for the deposition of Al_2O_3 from an Al target under an Ar:O_2 mixture. When the O_2 flux increases from 0 to 2 sccm, the target is initially in the metallic regime and reacts with the incoming O_2 flux. The total pressure remains constant up until $\sim$ 1.7 sccm, when the target finally becomes poisoned and a sudden increase in pressure is observed. On the other hand, when the O_2 flux decreases from 2 sccm down to zero, the target is initially in its poisoned state. Reducing the O_2 flux simply leads to a linear decrease in pressure, no sudden change in the total gas pressure is observed in this case. A similar hysteresis loop is observed on the voltage.
Later in this work, we will deal with the sputtering of an Ag target with Ar:O_2 and Ar:N_2 gas mixtures. We will, however, not focus on the intricacies of the hysteresis behaviour and state of the target in the context of this thesis, and will instead focus on the Ag film growth dynamics. In addition to this, we note that no appreciable hysteresis was observed under all our operating conditions with O_2 or N_2.

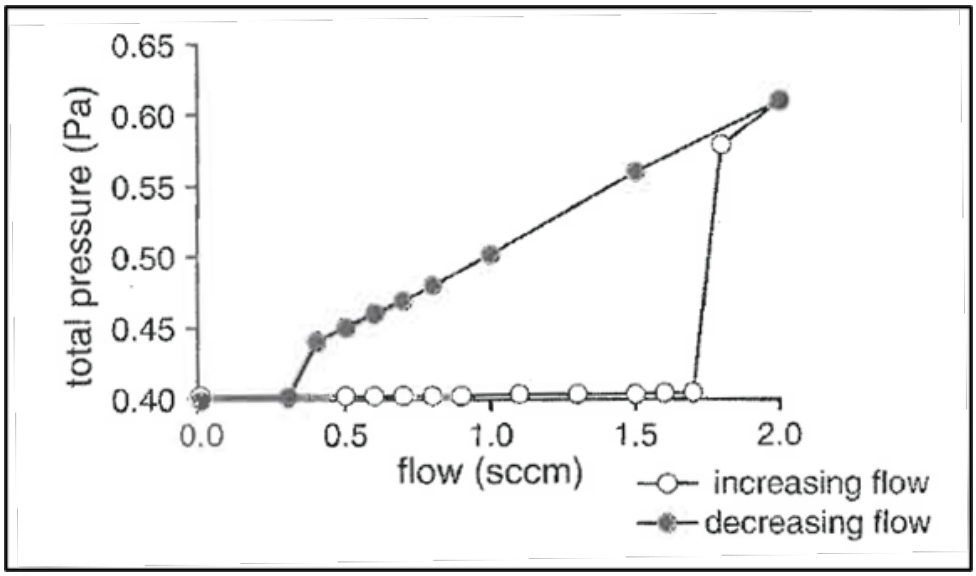

Figure 1.4 Example for the reactive sputtering of Al_2O_3 from an Al target sputtered under an Ar:O_2 mixture with increasing O_2 flow. The hysteresis loop is clearly seen in the total pressure vs O_2 flow. Reproduced from [15].

1.1.2 Thermodynamic and kinetic approaches of film growth

The growth of Ag films on weakly-interacting surfaces (such as oxides) during magnetron sputtering deposition will be the main topics of this thesis work. As such, it is important to start by exploring the existing mechanisms, models and literature reports, regarding the growth process of a thin film. This will lay the foundations for our study on the growth and microstructure control of Ag films on oxide substrates.

Thermodynamic description of film growth: Bauer's criterium and 2D/3D growth modes

The growth of a film on a substrate involves the formation and disappearance of different interfaces. Analysing the total surface energy changes due to film growth is the basis of the thermodynamic approach to film growth. If we take a system consisting of a film growing on a substrate surface, then a fraction of the substrate surface will disappear with time, while a new film surface and film-substrate interface will appear. Atoms on a surface are less bonded than atoms in the bulk of a material, and their potential energy is therefore higher. For interfaces, this will generally also be true, though the extent of the energy increase will depend on the nature of the two phases in contact and their bonding. Surface energies (given in $J.m^{-2}$) are a measure of the energetic cost for the creation of a surface or interface; a lower surface energy will be associated with a more stable surface, and systems will evolve towards equilibrium by minimizing the areas of the most energetic interfaces. In this work, we will be working mostly with "weakly-interacting surfaces", implying a poor interaction between film and substrate atoms at the interface, and a relatively high associated interface energy.

Going back to our system with a growing film on a substrate surface, Bauer [16, 17] defined a simple criterium based on the surface/interface energies of the different materials, that is used for predicting the growth mode of a film on a given substrate. This purely thermody-

namic consideration (so-called "Bauer's criterium") is useful for predicting general trends in film morphology during the initial growth stages, which can end up affecting the final film morphology. It is based on the relative surface energies of the film γ_f, of the substrate γ_s, and of the film/substrate interface γ_{fs}. For a system consisting of an "island" on a planar substrate as shown in Figure 1.5, Young's equations can be used to predict the contact angle θ_c between the island and the substrate surface at equilibrium.

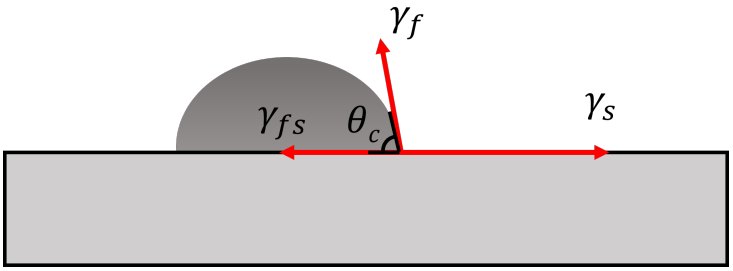

Figure 1.5 Equilibrium shape of a droplet in the initial stages of film growth as a function of surface/interface energies: f = film, s = substrate, fs = film/substrate interface.

It reads:

$$\gamma_s = \gamma_{fs} + \gamma_f \cdot \cos(\theta_c). \tag{1.2}$$

By definition, lower values for θ_c correspond to better wetting of the film. Based on Equation 1.2, three growth modes can be predicted (Figure 1.6):

- **2D "layer-by-layer growth" (or "Frank-van der Merwe"):** in this mode, $\gamma_s \geq \gamma_{fs} + \gamma_f$, and thus $\theta_c \simeq 0$. The film tends to spread on the substrate surface, and a 2D morphology is obtained. This mode is typical for metal-on-metal homoepitaxy.
- **3D "island growth" (or "Volmer-Weber"):** in this mode $\gamma_s \leq \gamma_{fs} + \gamma_f$ and thus $\theta_c > 0$. The film does not wet the substrate effectively, and instead tends to minimize its exposed surface by forming "islands" on the substrate surface. This growth mode is typical for noble metals on weakly-interacting surfaces. It is at the heart of this thesis work.
- **Intermediate 2D-3D growth (or "Stranski-Krastanov"):** this mode is similar to the 2D "Frank-van der Merwe" mode for the initial monolayers, but then changes to a 3D-like growth, with islands forming on top of the initial 2D monolayers. This switch from 2D to 3D originates from the accumulation of elastic stress in the film, usually due to lattice mismatch between the film and the substrate in hetero-epitaxial film growth. The strain from the mismatch adds an extra cost in the energy balance alongside surface/interface energies, and ends up compensating the initial preference for a layer-by-layer growth [18]. It is often encountered in the case of semiconductor heteroepitaxy.

Although based only on thermodynamics arguments at equilibrium, Bauer's criterium turns out to be very useful for predicting the general trends of film growth for a given film-substrate system; we will be referencing it throughout this thesis work. However, magnetron sputtering deposition occurs in far-from-equilibrium conditions, and as such, kinetics cannot be ignored.

Kinetic description of film growth

The principle behind the growth of a film by PVD lies in the transfer of atoms from the gas phase to the solid phase. A purely thermodynamic description of film growth would require the

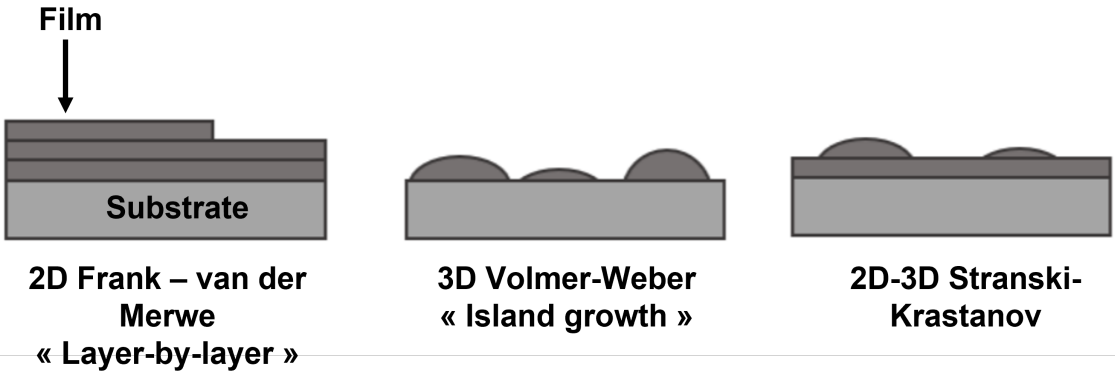

Figure 1.6 Three growth modes according to Bauer's criterium: (left) 2D Frank-van der Merwe or "layer-by-layer" mode; (center) 3D Volmer-Weber or "island growth" mode; (right) 2D-3D Stranski-Krastanov mode.

system to be at equilibrium, with the chemical potential of atoms in the gas phase μ_g and in the solid film phase μ_s being equal. In practice, PVD techniques increase the amount of film precursor atoms in the gas phase using different methods (target sputtering, molecular or ion beams, laser pulses ...) in such a way that the pressure of the gas in contact with the substrate (p) is higher than the equilibrium vapour pressure p_{eq} of the film material. This leads to an increase in chemical potential $\Delta\mu = k_B T \cdot ln(S)$, where $S = \dfrac{p}{p_{eq}}$ is the system supersaturation. Under PVD deposition, the system will not be in equilibrium. It will instead evolve through different metastable states and cross different activation energy barriers between these states. It is clear at this point, that in this far-from-equilibrium system, a kinetic description is required to go further.

We will begin our kinetic description by listing the main elemental atomic events (see Figure 1.7) that occur during film growth, before examining their dynamics and rates during different stages of the process.

Incoming atom flux: incoming atoms arrive at the substrate surface with a given flux F and an associated kinetic energy E_k given by Equation 1.1. Barring other energy sources such as impingement from accelerated ions or other energetic species in the plasma, this E_k value will be important since it will determine the energy available for other elemental processes after landing on the substrate.

Adsorption and accommodation: for E_k values in the range of $\sim 10^{-4} - 10^{-2}$ eV, the atom can be adsorbed at the substrate surface (becoming an "adatom") through weak Van der Waals interactions (also called "physisorption"), whose typical energies are $\leq$ 1.0 eV. At higher E_k values, the atom can incorporate to the substrate though stronger chemical bonds (the so-called "chemisorption"), or even implant into the bulk if E_k is too high (Figure 1.2).

Surface diffusion: the adsorption of an incoming atom (now an *adatom*) onto an adsorption site, which corresponds to a local minimum in the potential energy surface, will decrease its kinetic energy and leave it in an adsorbed state with an energy $E'_k < E_k$ that will be available for other elemental events. E'_k can help the "adatom" overcome diffusion barriers E_D (activation barriers for diffusion between neighbouring sites, usually in the order of a few tenths of eV) and

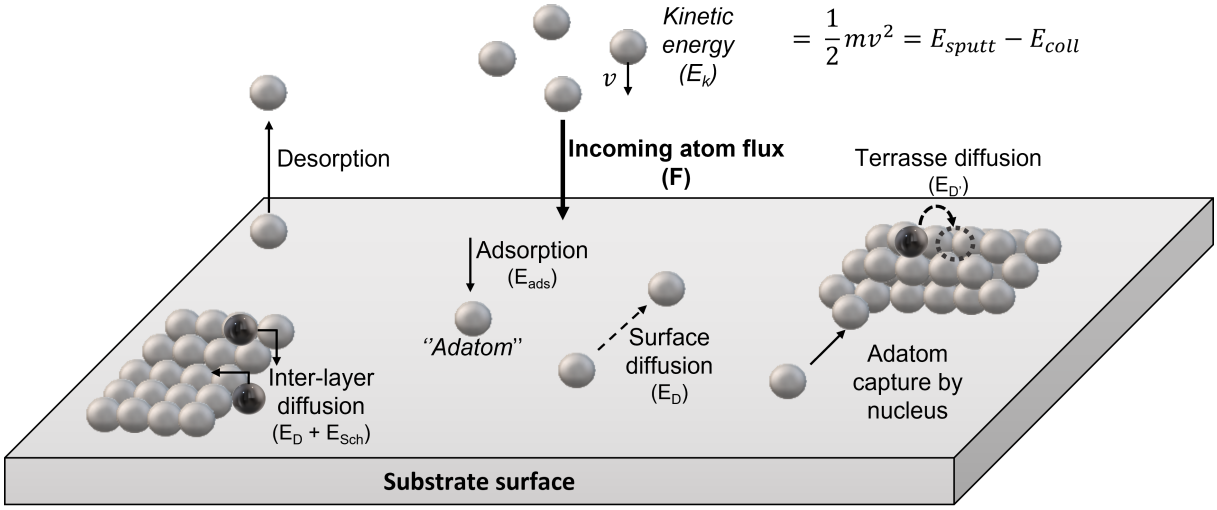

Figure 1.7 Illustration of the typical atomic processes occurring at the substrate surface during thin film growth.

"hop" or "jump" between different neighbouring sites of the surface (Figure 1.8, from sites A to B), giving rise to the so-called "transient adatom mobility" after adsorption. Aside from this leftover energy after adsorption, adatoms can also jump between sites in a stochastic process thanks to thermal energy. This classical, thermally-activated series of jumps along different neighbouring sites is a 2D-diffusion process characterized by a diffusion constant $D = \frac{1}{4}l^2\nu$, where l^2 denotes the mean square displacement per atomic jump, and ν the diffusion or jump rate. This jump rate is thermally activated and can be expressed as an Arrhenius-type law as $\nu = \nu_0 \exp\left(\frac{-E_D}{k_B T}\right)$, with ν_0 being the attempt frequency, k_B the Boltzmann constant and T the substrate temperature. Injecting this expression into the previous equation leads to $D = D_0 \exp\left(\frac{-E_D}{k_B T}\right)$. In short, diffusion on the surface will be more active given lower values of E_D, higher initial values of E'_k, and/or higher substrate temperatures.

Adatom capture: if an adatom diffuses towards a site neighbouring another adatom, then the two adatoms will bond and form a dimer after coming into contact. This dimer is an example of a cluster, which we will later refer to as "nucleus". If an adatom diffuses to a site near a pre-existing nucleus, then it will be captured by the nucleus, making it grow by adatom incorporation. The reverse process, detachment from a nucleus, is also possible, but the activation energy will be higher than for a normal diffusion between unoccupied sites because the atom in a nucleus is more bonded and therefore more stable. Bocchese et al [19] simulated the activation energies for free surface diffusion and atomic detachment from an nucleus, and found a 5 or 6-fold increase in the activation energy for atom detachment from an island compared to free surface diffusion. We note that this initial description of the adatom capture process applies to homogeneous nucleation process, but on real substrates, a diffusing adatom can also bind more strongly to a defective site of the substrate (impurities, kinks, edges ...) creating an initial nucleus. This is called "heterogeneous nucleation". According to a simple broken-bond picture, kink sites are more stable than edge sites towards adatom detachment, and edge sites are more stable than isolated adatoms. The more stable the site, the higher the activation energy an adatom will need to face in order to detach from a nucleus.

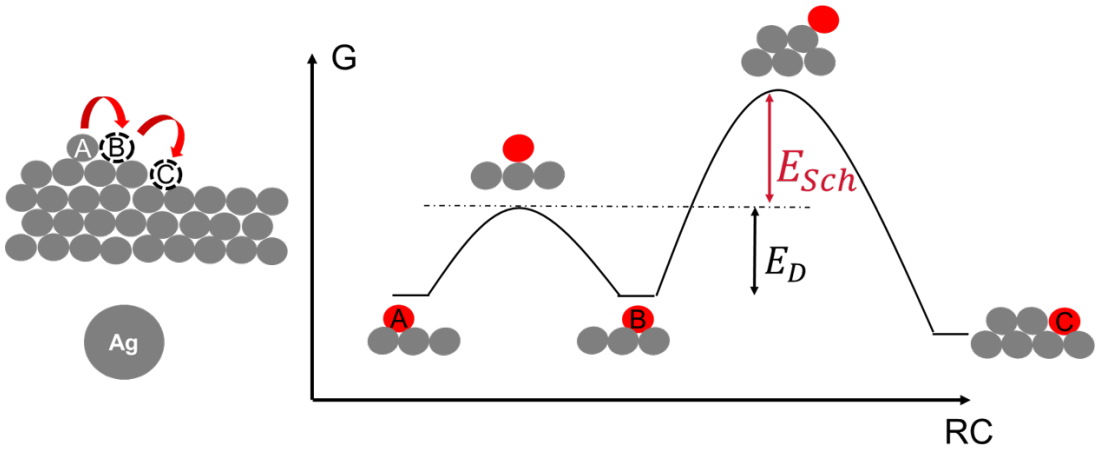

Figure 1.8 Atomic diffusion with the associated energy barriers: E_D for intra-layer diffusion (from sites A to B) and E_D + E_{sch} (Ehrlich-Schwöbel barrier) for inter-layer diffusion between different atomic planes (from sites B to C).

Inter-layer diffusion: given a layer of atoms on the substrate surface, an adatom can also diffuse across different atomic layers, either downwards or upwards. In addition to the diffusion barrier E_D between unoccupied sites on the same layer (intra-layer diffusion), inter-layer diffusion is also subject to an additional energy barrier, called the Ehrlich-Schwöbel barrier E_{sch} [20, 21]. As shown in Figure 1.8 for diffusion between sites B and C, the transition state for interlayer diffusion is less coordinated than in the case of intralayer transfer, and thus the energetic barrier is greater.

Desorption: given enough energy (remaining kinetic energy after adsorption, or from other sources such as thermal energy or collisions by energetic species from the plasma), adatoms can overcome their adsorption energy, desorb from the surface and escape, going back to the gas phase. In our work, this particular process will be neglected, given the energies [12] and deposition rates we will be working with, and knowing that deposition will always be made at room temperature.

1.1.3 The growth stages

Metals tend to have relatively high surface energies, and when deposited on weakly-interacting surfaces the interface energy γ_{fs} will also be - by definition - relatively large. For a metallic thin film on an oxide substrate, Bauer's criterium (Equation 1.2) predicts a 3D-like growth with disconnected islands forming on the surface of the substrate. This growing film will continue evolving under the flux of sputtered atoms arriving at the surface, and will go through a series of stages: (i) nucleation and growth of isolated islands, (ii) coalescence of these islands upon contact, (iii) formation of a percolated (and conductive) network, and finally (iv) the formation of a continuous and then a uniform film. Figure 1.9 illustrates these growth stages.
For each stage, we will describe the main elemental atomic processes involved, as well as the corresponding kinetic models that have been developped in the literature. These models will be useful in later sections when discussing methods for controlling the growth of metallic thin films.

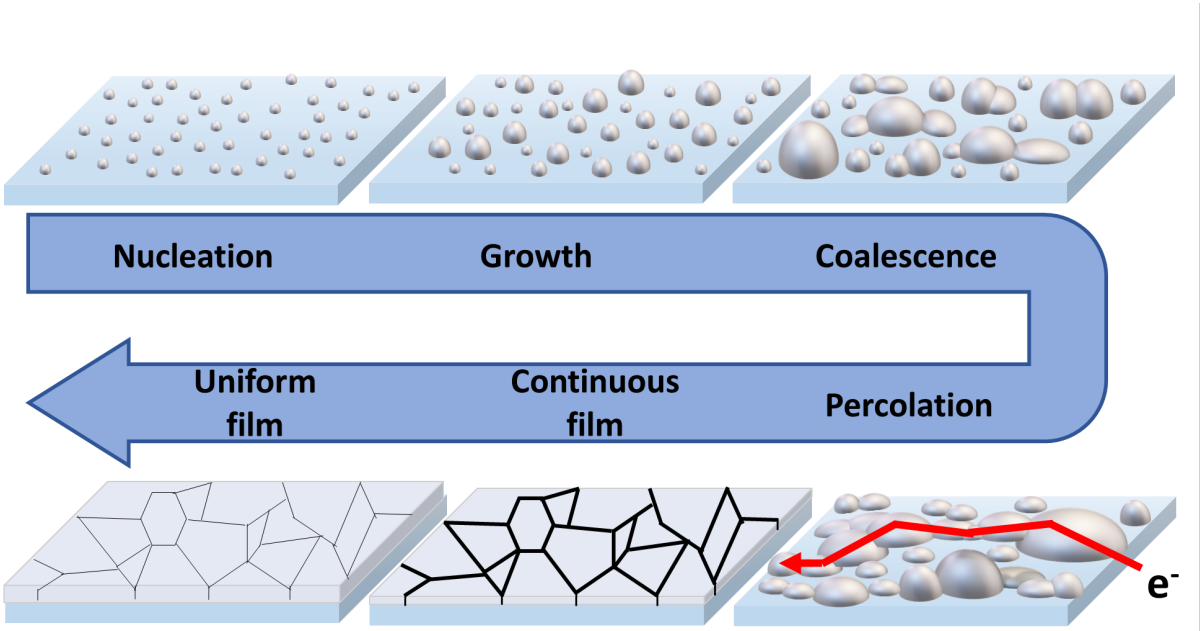

Figure 1.9 Illustration of the growth stages for a metallic film on a weakly-interacting substrate.

Nucleation and growth

With the increase of atom gas pressure near the substrate surface and the onset of adatom diffusion, it becomes inevitable that at some point some of those adatoms will end up coming into contact and start bonding, forming dimers, trimers, and so on. The question would be, for a given nucleus, whether it will be stable and keep on growing or whether it will instead be unstable and shrink by losing atoms via adatom detachment.
To answer this question, we will use one of the results from the "Classical Nucleation Theory" [9, 22] model. This is a thermodynamic model for homogeneous island nucleation of atoms in the gas phase on a flat substrate surface of the same material, where equilibrium between the two phases is assumed ($\mu_g = \mu_s$). Upon creation of a hemispherical island (with a radius R) on the surface, the total free energy of the system (ΔG_{Tot}) increases by vertue of the surface energy γ of the newly-created nuclei. At the same time, upon nucleation, atoms are transferred from the gas phase to the less-energetic solid state: the difference in free energy per unit volume associated to this process is $\Delta G_v = -\frac{k_B T}{\Omega} ln(1+S) < 0$, with Ω being the atomic volume. Overall, there is balance between the a positive energy contribution from the creation of an island surface ($\propto R^2$) and a negative contribution from the volume ($\propto R^3$). For very small islands, the positive contribution from the surface of the island will predominate, and the island will be unstable ($\Delta G_{Tot} > 0$). But for R values higher than a critical radius R^*, the negative term will predominate and the island will be stable. This critical radius is given by to $R^* = -\frac{2\gamma}{\Delta G_v}$.
In our system, however, the continuous sputtering of atoms from the target leads to a large adatom supersaturation value S and therefore to a large ΔG_v. This means that the critical radius $R^* \to 0$. Or in other words, under large supersaturation conditions, the system tends to a limit in which dimers ($i = 2$) are stable nuclei. We will therefore assume that dimers are stable nuclei, and that the detachment of adatoms from existing nuclei is suppressed. We will also assume that only adatoms (not nuclei) can diffuse on the surface, with a diffusion constant

D. These hypotheses correspond to the "irreversible nucleation regime".
Regarding the adatom concentration n_1, we must take into account the effect of:

- the incoming atom flux F ;
- the formation of a dimer after the diffusion and aggregation of two adatoms, described by $D\sigma_1 n_1^2$ with σ_1 being the "capture number" for adatoms;
- the capture of adatoms by nuclei with $i > i^* = 1$ atoms, given by $Dn_1 \sum_{i=2}^{\infty} \sigma_i n_i$ (with σ_i being the capture number of nuclei with i atoms);
- the rate of direct atom capture on top of islands, described using κ_1 for the direct capture by a monomer ($Fn_1\kappa_1$) and by κ_i for the direct capture by a nucleus with i atoms ($F\sum_{i=2}^{\infty} \kappa_i n_i$).

All these factors lead to a differential equation for the change in the density of adatoms n_1:

$$\frac{dn_1}{dt} = F - 2D\sigma_1 n_1^2 - Dn_1 \sum_{i=2}^{\infty} \sigma_i n_i - F\kappa_1 n_1 - F \sum_{i=2}^{\infty} \kappa_i n_i. \tag{1.3}$$

For nuclei growth, we will proceed in the same way and only take adatom capture and direct capture by nuclei with i and $i-1$ atoms into account. For $i > i^*$ ($i > 1$ in our case), this leads to a series of differential equations for nuclei growth:

$$\frac{dn_i}{dt} = D\sigma_{i-1} n_1 n_{i-1} - D\sigma_i n_1 n_i + F(\kappa_{i-1} n_{i-1} - \kappa_i n_i). \tag{1.4}$$

Note that developing a detailed model for nucleation would require defining "capture numbers" for adatoms and for existing nuclei. We will not go further into detail on this vast topic which exceeds the aim of this work, and we will instead look at the use of scaling laws to provide a useful description of the underlying physics.

Let us now define N as the total number of nuclei ($N \gg n_1$), and $\theta = F \cdot t$ the surface coverage, proportional to the atom flux and deposition time t. Neglecting direct impingement ($\kappa_i = 0 \forall i$), one gets Equation 1.5 for the total number of nuclei N and Equation 1.6 for the adatoms n_1.

$$\frac{dN}{d\theta} = \frac{D}{F} n_1^2 \sigma_1 \tag{1.5}$$

$$\frac{dn_1}{d\theta} = 1 - \frac{D}{F} n_1 N \sigma_{avg}. \tag{1.6}$$

In the latter, we used σ_{avg} as an average capture number for all nuclei with $i > 1$; we assume that this value is independent of $\frac{D}{F}$. From these equations, it can be shown that under irreversible nucleation conditions, the number of nuclei N will first increase (initial transition regime) and then approach a stable value N_{sat}. Once in this steady-state stage, the rate for adatom increase is compensated by their incorporation into existing nuclei. N_{sat} follows a scaling law [22, 23]:

$$N_{sat} \propto \left(\frac{F}{D}\right)^{\chi}, \tag{1.7}$$

where the scaling exponent χ depends on the shape (2D or 3D) of the islands and on the critical nucleus size i^*. We see from this scaling law (Equation 1.7) that increasing the atom flux F onto the surface leads to an increase in the number of nuclei at saturation. Increasing surface diffusion (for instance using substrate heating) makes it more likely for an adatom to encounter an existing nucleus and be captured by it, rather than to form a new nucleus; the number of nuclei at saturation decreases as a consequence.

Lastly, there is a final scenario that needs to be mentioned, the case of nucleation on a defective substrate ("heterogeneous nucleation"). Adatoms coming into contact with these defects can bond with them and be "captured", forming new nuclei. According to the formalism developed by Venables and Harding [24], defects act as "traps" with a given density n_t and trapping energy E_t. By introducing a Langmuir-like isotherm to treat the temperature dependence of the occupation of these traps, one find an exponential relation for the fraction of occupied traps N_{oc} and the trapping energy: $N_{oc} \propto \exp\left(\frac{-E_t}{k_B T}\right)$. In the limit of high surface diffusion and high trapping energy (sensible assumptions for our deposition conditions in this work), then the nucleation density becomes the sum of the homogeneous and heterogeneous nucleation densities as shown in Equation 1.8 (with σ_t a capture number for adatoms by the traps).

$$\frac{dn_1}{dt} = F - \sigma_1 D n_1^2 + \sigma_t D n_1 n_t. \tag{1.8}$$

For low temperature values, the adsorbed adatoms do not have enough thermal energy to escape the traps. If on top of this n_t is high enough, then the second term in Equation 1.8 will predominate and the saturation density will be uniquely determined by the trap density. Experimentally, a plateau for particle density at intermediate temperatures will be observed, just like in the work by Venables and Harding [24]. Another example is given by the work of Lazzari and Jupille [25] on Ag/Al_2O_3 growth by evaporation; using plasmonics to study Ag growth, they found a constant nucleation density for low-enough temperatures ($\sim$ 300 K or lower) where the adatoms did not have enough energy to escape the traps and the nucleation density is dictated by the density of surface defects acting as nucleation sites.

Island coalescence

After nucleation of the nuclei on the substrate surface, the nanoparticles keep growing by adatom incorporation, eventually reaching a point in which average particle size is large enough that a large number of particles will come into contact (impinge on each other). This marks to the beginning of the coalescence stage. As illustrated in Figure 1.10, during a complete coalescence process two "mother" islands merge together and form a single "daughter" particle.

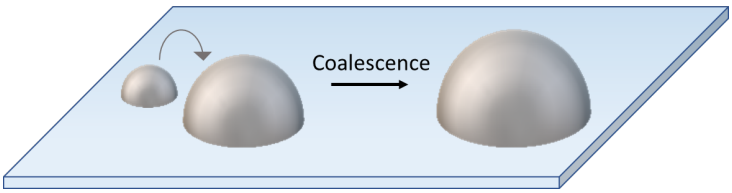

Figure 1.10 Illustration of island coalescence during film growth.

From a thermodynamic point of view, the driving force for coalescence is the reduction of the total surface energy of the system. Atoms on the surface of smaller islands, with higher curvature and therefore less average bonds per atoms, have higher chemical potential than atoms on the surface of larger islands. Upon contact, this chemical potential difference generates a diffusion from low-curvature zones towards high-curvature zones. Or in other words, atomic diffusion from small to large islands [26]. Under "complete coalescence" conditions, the two initial islands will end up coalescing into one and even adopt the equilibrium shape.

It is generally accepted that the two main limiting cases for coalescence are *static coalescence*, and *dynamic coalescence* (sometimes called "Smoluchowski coalescence"). The former case occurs between two islands at fixed positions via atom detachment, diffusion, and attachment on

the new particle. It is the preferred mechanism in cases with very strong bonding between the islands and the substrate. Dynamic coalescence, on the other hand, occurs in systems with relatively high nanoparticle mobility (low bonding). In this case, islands can move along the substrate, impinge on each other and coalesce by direct contact. Results from different studies on metallic film growth on weakly-interacting substrates such as oxides and graphite (for instance, Au [27] and Sb [28]) have generally favoured dynamic coalescence involving even the mobility of large islands, because of the incommensurability of metal/substrate interface and a weak interaction.

Historically, the mechanism for island coalescence upon direct contact was derived from sintering theory, with isotropic atomic surface diffusion of atoms from the smaller of the two islands towards the concave "neck" contact region between the coalescing particles [29, 30]. However, this mechanism requires the detachment of adatoms from edge and kink sites, which should not happen frequently for metallic film deposition at ambient temperatures. Instead, other mechanisms have been proposed. Grammatikopoulos *et al.* [31] gave a fairly detailed explanation of the coalescence mechanism for solid metallic nanoparticles, based on modelling and experimental results from the last two decades. In short, the mechanism involves an initial impingement between nanoparticles (via cluster surface diffusion or growth) leading to bonds between surface atoms from both nanoparticles. The initial contact region between the particles is usually very energetic because of crystalline mismatch. This crystalline mismatch forces torques on both nanoparticles, making them individually rotate until a more coherent, larger interface area is achieved [32]. Regarding this rotation of the coalescing nanoparticles, molecular dynamics simulations [26, 33] have also brought forward the effect of epitaxial relations between nanoparticles and the substrate on the rotation of these nanoparticles, since the higher interaction energy between the island and the substrate leads to a higher activation energy for rotation. Epitaxy should therefore inhibit adequate crystallographic alignment in the contact region and slow-down island coalescence compared to an amorphous substrate. Once contact is made between the particles, bond formation releases heat, which according to some simulation results should be enough to locally melt the nanoparticles and allow for recrystallization near the contact zone [34]. Indeed, simulation and experimental works have shown that the melting point of nanoparticles is lower than the melting point of bulk materials. For instance, Buesser and Pratsinis [35] simulated the transition temperatures, from solid to metastable (T_{meta}) and from metastable to liquid (T_{melt}), for Ag nanoparticles with different diameters. In accordance with other simulation works, they found lower values for T_{meta} and T_{melt} for smaller nanoparticles. For a diameter of 2 nm, in particular, they found values of $T_{meta} \sim 675$ K and $T_{melt} \sim 800$ K, which are both lower than the respective values for bulk Ag: 974 K and 1234 K. These results support the hypothesis of local melting in the contact region between nanoparticles, which leads to increased surface diffusion and a crystallographic reorganization. A larger, more defined "neck" is formed between the two nanoparticles, where atoms can migrate thanks to released energy from bond formation. Finally, when the neck is large enough, the initial surface energy gradient for surface diffusion (which was based on difference in size and therefore curvature) is lost, and the particles start behaving as a single elongated object. The final evolution stage is slower, with local heating playing only a minor role because the creation of new bonds is less frequent. Given enough time, the particle may slowly evolve towards its equilibrium shape, to minimize surface energy, or remain as an elongated particle.

Other works have focused on the case of island coalescence during film deposition, *i.e.* when a flux of incoming atoms is present. Gervilla *et al.* [30] ran kinetic Monte Carlo simulations of the

coalescence between two 3D faceted Ag islands with an initial neck formed between them on a weakly-interacting substrate, with and without a concurrent supply of atoms from a gas phase. Figure 1.11(from Reference [30]) shows the simulation results for the coalescence between two nanoparticles in contact, for both a "low" and "high" flux of incoming atoms (F).

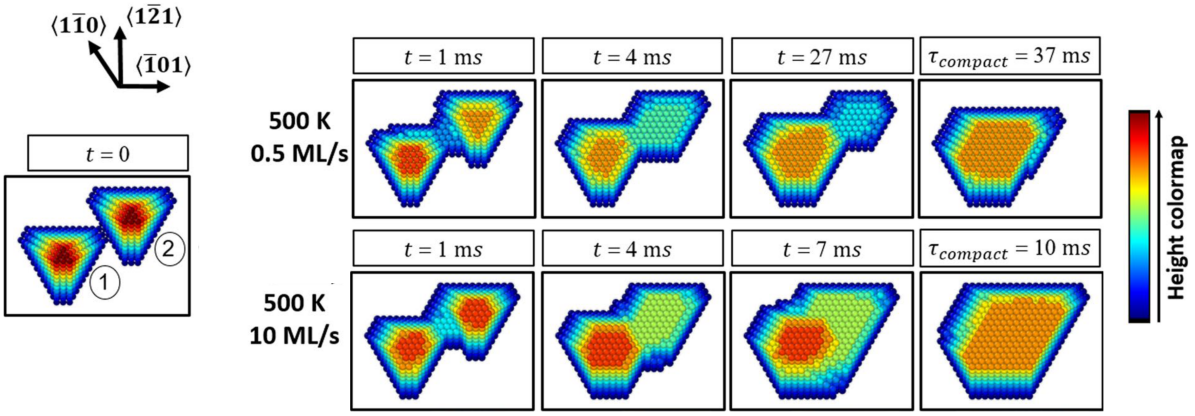

Figure 1.11 Simulation of the coalescence between two faceted Ag nanoparticles on a weakly-interacting substrate surface. Both simulations are performed at $T = 500$ K, which is lower than the roughening and melting temperature of the nanoparticles. In each case, the incoming flow of atoms from the gas phase is different (for reference, 1 ML$\simeq$ 0.2 nm). Adapted from Gervilla *et al.* [30].

Their simulations showed that the mechanism for Ag nanoparticle coalescence depends on the relative flux of incoming atoms. For a relatively low atom flux, coalescence occurs by atomic surface diffusion, with atoms from one of the particles migrating on its surface towards the intersection of atomic planes from each particle, in the neck area. Once at the intersection, those adatoms can nucleate and grow a new atomic plane on the other particle; this mechanism is called "facet migration coalescence", and leads to an atom transfer from the smaller to the larger island (shown in Figure 1.11 for 500K and 0.5 ML/s). The larger island incorporates the smaller one, and the resulting island after coalescence reaches a more stable 3D-shape. A low incoming atom flux speeds up this mechanism by providing extra adatoms and increasing the nucleation probability in the intersection between particles. In contrast, when a higher incoming atom flux F is provided, then particle coalescence occurs primarily via material deposition from this flux. Atoms adsorb on the substrate and on both particles regardless of their size, overpowering the surface diffusion mechanism. Simulation results showed that under these conditions, an elongated particle is formed from the two initial particles, in a process they called "agglomeration"(shown in Figure 1.11 for 500 K and 10 ML/s). This change in coalescence behaviour with increasing atom flux is in line with experimental results in the literature. In Q. Hérault's thesis work [12], for instance, he showed that for magnetron sputtering deposition of Ag on SiO_2 surfaces, increasing the deposition power led to a higher atom flux and a lower percolation threshold. A transition from coalescence by "facet migration" towards an agglomeration mechanism could explain this behaviour, since elongated particles should impinge on each other and form a percolated, conductive network faster than round, 3D-islands. He also showed that "intermittent sputtering deposition" of Ag on SiO_2 surfaces (meaning a series of intervals where the shutter was intermittently opened and closed) led to the formation of rounder, 3D islands and thus a higher percolation threshold. This is also in line with results by Gervilla *et al.*, if we assume that during the time when the shutter was closed the coalescence mechanism reverted

from an agglomeration mechanism to a facet migration mechanism, yielding rounder particles. Lastly, Grachev *et al.* [36] also compared particle aspect ratio during evaporation and sputtering deposition of Ag on Al_2O_3 surfaces, and evidenced an increased particle flattening (higher aspect ratio) during sputter deposition compared to evaporation. Again, this is in line with the modle of Gervilla *et al.* considering the much higher deposition rate of magnetron sputtering compared to evaporation (), according to their measurements. Using the faster magnetron sputtering deposition led to a higher flux of atoms and a transition towards an agglomeration mechanism.

Finally, as the particles get larger, the driving force for particle coalescence gets weaker. Moreover, the heat liberated during coalescence is distributed throughout a larger mass. Which means a lower temperature rise, less effective at enhancing surface adatom diffusion. Not to mention the increase in T_{meta} and T_{melt} with increasing particle size and the mass to transport. All in all, larger particles will coalesce and evolve in shape more slowly, forming elongated particles and grain boundaries [32].

These grain boundaries, in particular, form between large islands (called "grains" in the context of polycristalline films) when coalescence is inefficient. The crystalline mismatch in these regions makes these boundaries highly energetic and reflecting towards conduction electrons. As described in a forthcoming section, the density of grain boundaries and their misorientation is one of the main contributions to film electrical resistivity.

Film percolation

Looking at the growing film as a whole, the presence of isolated nanoparticles means that electrical conduction is not possible (we neglect any eventual thermal-activated tunnelling if the islands are close enough [37,38]). Thus in the initial stages of film growth, the film will not yet be conductive and a high and constant value of resistivity will be measured. A sharp drop in resistance is observed at a given threshold thickness when an electrical path is established across the film ; this stage is called the "percolation threshold". Note that percolated films do not need to be "continuous" as long an electrical path for the electrons exists, meaning that for a 3D-type growth, the percolation stage occurs before the complete coverage of the substrate surface. In addition, favouring a more 2D-like growth for the islands before percolation will lead to those islands coming into contact and forming an electrical path at a lower deposited thickness [12]. All in all, the percolation thickness t_p will strongly vary with the growth mechanism of the Ag film. Its determination using real-time measurements will play an important role all along this thesis work. Reducing this value of t_p ideally without impacting film resistivity would give us access to thinner and conductive metallic films [39–41].

Continuous and uniform film formation

After the percolation of the Ag film, the islands will keep on growing thanks to continued arrival of atoms from the incoming flux. The holes between the islands will be filled by these atoms. Once the continuous film stage is reached, the substrate is entirely covered by the film and no more holes are present. The film will not be flat and uniform, however. It will consist of a series of grains with varying height, separated by relatively deep grain boundary regions. The film roughness will therefore be high.
In the final stage of film growth, new adatoms will incorporate into the grain boundary regions and reduce roughness. Indeed, a large number of dangling bonds will be present in those grain boundary regions - because of the lack of contact between grains - and thus incoming

adatoms will tend to diffuse towards them [42, 43], reducing their depth and the film roughness in the process. Grain growth can also happen, but mostly in the direction perpendicular to the substrate surface, since the areas surrounding them are already occupied. This is the last stage of film growth, the uniform film formation stage. At this point, the film is composed mainly of grains with a height at their center that is close to the film thickness.

1.2 Ag thin films: properties and growth

The previous sections focused on the thermodynamic and kinetic descriptions of thin film growth during magnetron sputtering deposition and especially in the case of metallic thin films growing on weakly-interacting substrates. We will now tackle the specific case of Ag thin films grown on oxides, which is the main topic of this thesis work.

1.2.1 Properties of silver

Silver (Ag) is a noble metal ($A = 107.87; Z = 47$) that crystallizes in a cubic system, with a face centred cubic (fcc) unit cell and a lattice parameter $a = 0.408$ nm (Figure 1.12). The atomic planes with the lowest index and highest compacity (111), (001) and (101) are also shown in Figure 1.12. Their surface energies are 1.12 J.m^{-2}, 1.20 J.m^{-2} and 1.29 J.m^{-2}, respectively [44]; this makes the most compact Ag(111) plane, energetically favoured compared to the others although the anisotropy with (100) is not very large [45].

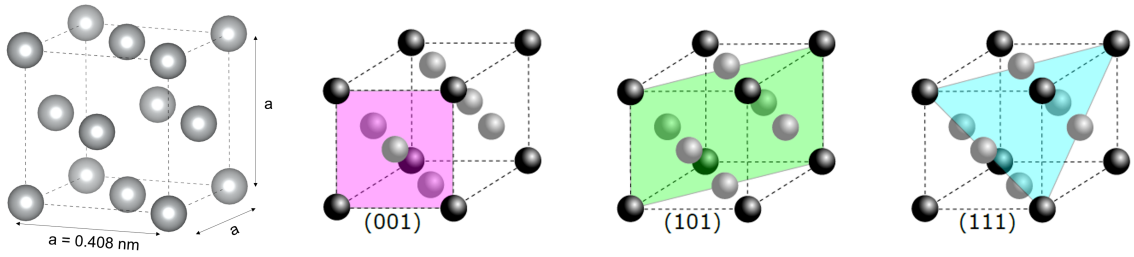

Figure 1.12 Unit cell for the fcc Ag lattice, and the corresponding (001), (101) and (111) planes. The most compact (111) plane has the lowest surface energy.

The Ag melting temperature is 961.8°C, which is the lowest among noble metals in the periodic table. Its bulk thermal and electrical conductivity are also the largest among all the elements, at 420 W.m^{-1}.K^{-1} and 1.59 $\mu\Omega$.cm [7]. The dielectric constant of Ag is dominated by a Drude metal behaviour below $\omega \sim 3.85$ eV and by interband transition above. The screening induced by d-electrons on $s-$electrons shifts the Drude intra-band plasmon frequency from ~ 9 eV down to $\omega_p = 3.85$ eV.

1.2.2 Ag thin film growth mechanism on glass surfaces

The growth of Ag thin films on glass (modelled herein as a SiO_2 surface) can be tackled from a thermodynamic point of view by comparing the surface energies involved in the process: $\gamma_s = 0.33$ J.m^{-2} for the SiO_2 substrate, $\gamma_f = 1.12$ J.m^{-2} [46] for the Ag film and $\gamma_{fs} = 0.21$ J.m^{-2} [47] for the film-substrate interface. Bauer's criterium (Equation 1.2) predicts a 3D Volmer-Weber or "island growth" mode for this system. The expected contact angle at equilibrium is in the range of $\theta_c = 130°$. As a noble metal, silver has very weak interactions

Table 1.1 Energy barriers (in eV) for free atomic diffusion, for a series of [deposited atom/surface] pairs from the literature. These values correspond to atomic diffusion between unoccupied surface sites.

[Atom/Surface]	Si/Si(001)	Ag/Ag(111)	Ag/MgO(001)	Ag/ZnO(0001)
E_D (eV)	0.94 [49]	0.1 [19]	0.05 [50]	0.3 [19]

with the substrate and will tend to aggregate into 3D islands instead of growing in a 2D "layer-by-layer" mode.

From a kinetic point of view, the same conclusion is reached. As the adsorption energy for Ag adatoms E_{ads} on an oxide is low in absolute value (a fraction of eV [19]), the flattened potential energy field leads to a lower energy barrier and fast diffusion on the oxide surface. Table 1.1 compares E_D values for free diffusion of different atoms on given surfaces. The much smaller value of E_D for Ag diffusion on Ag(111) compared to Si on Si(001) can simply be explained by the difference in bond nature between a highly-directed Si-Si covalent bond and the Ag-Ag metallic bond. The value for E_D decreases by half when Ag is deposited on MgO(001), illustrating the increased surface diffusion of Ag on weakly-interacting surfaces. Finally, we note the higher value of E_D on a ZnO(0001) surface, which will be the subject of a further section its role as an epitaxial template for Ag. Regarding inter-layer diffusion, the value of the E_{sch} barrier for interlayer diffusion between Ag(111) planes at 300 K has been estimated at a value of ~ 0.15 eV [18, 48].

Looking at the mechanism of island coalescence in the case of Ag, just like previously shown for other metals (Au and Sb), experiments and simulations have focused on the behaviour of Ag [25, 26, 51] and evidenced a predominantly dynamic coalescence mechanism. Once the islands are in contact, one can safely neglect generalized adatom detachment from kink and edge sites at ambient temperature, since room-temperature growth happens well below the estimated roughening temperature of Ag ($0.4 \cdot T_{melt} \sim 500$ K [30]). A sintering-like mechanism involving generalized detachment and surface diffusion is thus unlikely. Instead, the previously presented work of Gervilla *et al.* [30] on coalescence mechanism based of surface diffusion and facet migration between coalescing particles applies.

All these considerations on the mechanism of Ag film growth leads us to the next section of this chapter, which is the literature review on the strategies for film growth. However, we should first ask ourselves what kind of microstructural properties we should be aiming at, before studying the ways of controlling Ag film growth and achieving these properties. As a reminder, the use of silver films in Low-E glazing applications requires the deposition of thin, transparent, conductive Ag films inside complex dielectric stacks. The thermal-IR reflection properties of the Ag film is linked to the film conductivity. We already saw how the percolation threshold thickness defines the minimum necessary thickness for a film to become conductive. Thus we should therefore aim at reducing the percolation threshold as much as possible, so as to be able to deposit thinner, conductive Ag films which - ideally - will be more transparent in the visible range. Improving the conductivity of the Ag film, however, requires controlling the film microstructure, as explained in the next section.

1.2.3 Impact of film microstructure on electrical resistivity

The electrical resistivity ρ of a metal such as silver can be, in principle, described using the Sommerfeld model [52] which describes electron transport through collisions or scattering events. In this model, the bulk resistivity ρ_B (the inverse of the conductivity σ), is given by Equation 1.9:

$$\rho_B = \sigma^{-1} = \frac{m^*}{e^2 n \tau}, \tag{1.9}$$

where m^* is the effective electron mass, e the electron charge, n the charge carrier density, and τ the relaxation time for an electron between two scattering events. If we take these latter as independent, $\rho(T)$ at temperature T can be split into its different contributions. This is known as Matthiesen's rule:

$$\rho_B(T) = \rho_{phonon}(T) + \rho_{electrons}(T) + \rho_{defects}. \tag{1.10}$$

ρ_{phonon} involves scattering of electrons by collective oscillations of the atoms around their equilibrium position, namely phonons. This contribution is not really relevant for the present study since all experiments were performed at room-temperature, so that we should not expect any important variations in the contribution from the phonons between samples. Electron-electron collisions $\rho_{electrons}(T)$ are effective only at very low temperatures, and will therefore also be neglected. The last term $\rho_{defects}$, independent of temperature, involves the contribution of electron scattering on defects. These defects can be classified according to their dimensionality: 0D-point defects (impurities, vacancies...), 1D-defects (dislocations and other line defects), 2D-defects (such as interfaces and grain boundaries), and 3D-defects (such as voids, cracks, or precipitates in the material).

In the case of a thin silver film, the thickness t as well as the lateral grain size in the film D, which scales with t, can be of the order of the mean free path for a conducting electron ($l_B = v_F \tau \simeq 38$ nm with v_F the Fermi velocity). Thus, as the thickness is reduced, the contributions of electron scattering from the film surface and/or interface ρ_{surf} become increasingly important, as well as that of grain boundaries ρ_{GB}. For a metallic thin film, Equation 1.10 is thus modified as follows:

$$\rho = \rho_0 + \rho_f + \rho_{GB}, \tag{1.11}$$

where the term ρ_0 includes all other contributions from defects other than surface and grain boundaries scattering, as well as that of phonons. Models [53] have been developed by Fuchs and Sondheimer [54, 55] to describe the surface scattering contribution ρ_f and by Mayadas and Shatzkes [56] for that of grain boundaries ρ_{GB}.

The Fuchs-Sondheimer model assumes planar and identical interfaces for the metallic film, separated by a distance t corresponding to the film thickness and characterized by a parameter $0 \leq p \leq 1$ (Figure1.13-a). p corresponds to the fraction of electrons that are diffusively scattered upon collision at the interface. p is somehow related to interface roughness. p =1 corresponds to a specular reflection of electrons which keeps their momentum parallel to the layer and to the transport direction. p =0 corresponds to a completely diffusive interface that systematically increase the path length of electrons upon collision. In this model, for very thin films $t \ll l_B$, the resistivity contribution of film interfaces is given by:

$$\frac{\rho_f}{\rho_B} = \frac{4}{3}\frac{1-p}{1+p}\frac{l_B}{d \cdot \ln\left(\frac{l_B}{t}\right)}, \tag{1.12}$$

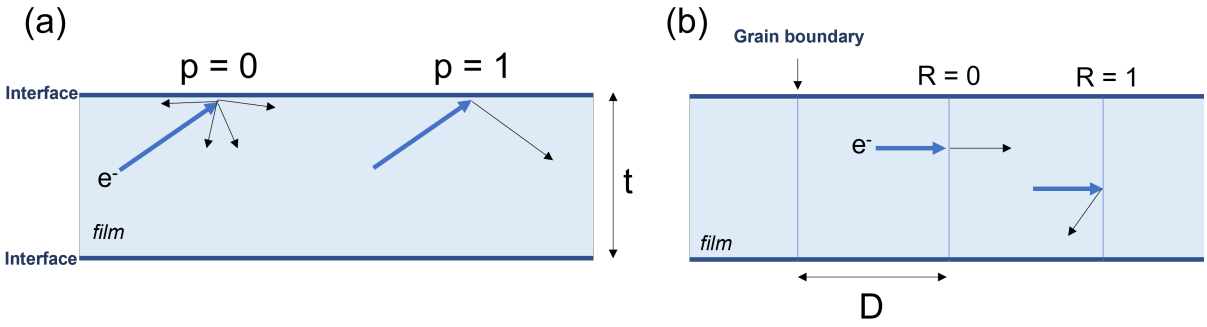

Figure 1.13 Schematic illustration of (a) electron scattering at the interfaces according to the Fuchs-Sondheimer model and (b) electron reflection at grain boundaries according to the Mayadas-Shatzkes model.

where ρ_B is the metal bulk resistivity and l_B the bulk electron mean free path according to the Sommerfeld model.

The Mayadas-Shatzkes model assumes an array of identical grain boundary planes, perpendicular to the film interfaces and separated by a distance that obeys a Gaussian distribution centred around the mean in-plane grain size D of the polycristalline film (Figure 1.13-b). The grain boundary is characterized by a reflection coefficient for electrons $0 \leq R \leq 1$; $R = 0$ corresponds to grain boundaries that are completely transparent towards conduction electrons while $R = 1$ is associated to perfectly reflecting boundaries (*i.e.* leading to a perfect insulator behaviour). In the limit $D \gg l_B$, ρ_{GB} in the Mayadas-Shatzkes model is given by:

$$\rho_{GB} = \rho_0 \left(1 - \frac{3}{2}\frac{R}{1-R} \cdot \frac{l_0}{D}\right). \tag{1.13}$$

In conclusion, both models show an increase of resistivity at small thickness t (Equation 1.12) or grain size D (Equation 1.13). Film microstructure has an impact on film resistivity. In order to obtain films with lower resistivity without increasing the thickness (which would negatively impact transparency in the visible region), the previous models show that we should aim at obtaining a film with:

- high purity and crystalline quality (low density of crystalline defects);
- low grain boundary density (D^{-1}), or in other words, with large in-plane grain sizes;
- poorly-reflecting grain boundaries (*i.e.* low value for R in the Mayadas-Shatzkes model) with the lowest possible crystalline mismatch;
- low surface/interface roughness (*i.e.* p close to 1 in the Fuchs-Sondheimer model).

In practice, meeting these criteria involves finding ways of overcoming the 3D thermodynamic tendency of Ag growth, and instead forcing it to grow in a more 2D-like mode. Ideally, we would try to achieve a situation in which the film grows via a low number of flattened islands, which will quickly percolate and form a continuous layer with low roughness and low grain boundary density. We will keep these objectives in mind for the following chapters. As a closing thought, provided that dewetting is avoided by encapsulation in a stack of films, we note that recrystallisation upon annealing as often done in the context of Low-E coatings is an effective way to improve film conductivity. But this is out of the scope of the present work that focuses mainly

on as-deposited films (grown at room temperature).

1.3 Strategies for controlling the Ag film growth mode

In the previous section, we listed the main available microstructural levers we can act upon in order to improve the conductivity of the Ag films. We will now study the different strategies that have been developed in the literature for controlling film growth and microstructure during magnetron sputtering deposition. Although this section will focus primarily on Ag thin-films, examples for other metals will also be given.

Many factors in the magnetron sputtering deposition process can impact the film growth mechanism and eventually favour a more 2D-like growth. These include, but are not limited to:

- the energy of the species involved in film growth processes ;
- the use of the so-called "surfactants";
- the control of the substrate: composition, crystallinity, presence of impurities, "wetting" layers and epitaxial relationships.

Let us analyze each of these factors and their impact on film growth.

1.3.1 Control of the energies of species during film growth

Most of instrumental parameters of the magnetron sputtering deposition process, such as deposition power and mode (DC, RF, HiPIMS), gas pressure, substrate-target distance, substrate polarisation and temperature, can have profound effects on the **the kinetic energy and flux** of the sputtered atoms arriving at the substrate and on the adatoms diffusing along the substrate.

The substrate temperature plays a major role in adatom surface diffusion. Higher substrate temperature enhances surface diffusion of adsorbed atoms (Figure 1.8), which in turn impacts the irreversible nucleation density (Equation 1.7 and 1.8) and the evolution of film morphology. While a higher substrate temperature reportedly increases film crystallinity and grain size [57], this comes at the cost of increased film roughness because of the strong tendency for the Ag nanoparticles to evolve in the out-of-plane direction towards their equilibrium shape [58]. This evolution requires atomic inter-layer diffusion, which is thermally activated. Favouring a more 3D-shape and increasing film roughness both result in different stages of film growth (percolation, continuous film, ...) being reached at higher thicknesses [12, 59].

Both working **gas pressure and deposition power** can also be modified. Their effects are less straightforward to analyze, however, because of the large number of elemental processes they can impact. Reducing the working gas pressure increases E_k of the sputtered target atoms arriving at the surface (Figure 1.7). Increasing deposition power also has a similar effect but it also increases the flux of sputtered atoms by enhancing the amount of sputtering events on the target (Figure 1.2). Separating flux and energy effects on film growth is not always simple, as shown in the thesis work by Q. Hérault *et al.* [12]. In their work, for the explored conditions, they found that the flux and the energy of incoming particles did not significantly impact the nucleation, growth, and coalescence stages, which seemed to be mostly determined by the substrate nature. They did observe, however, a reduction in the percolation and continuous film formation thresholds, which they linked to changes in the shapes of the particles (more elongated particles leading to earlier percolation). Other works have also reported beneficial effects of higher deposition power and lower pressure from a film resistivity point of view. In

general, higher E_k values for the arriving atoms leads to denser and better crystallized Ag films, because the new adatoms will be able to overcome more diffusion barriers after being adsorbed (higher E'_k after adsorption), and thus will be able diffuse further and reach more stable sites, increasing the crystallinity of the growing film [60–64]. This increase in crystallinity and density leads to a lower overall film resistivity. If the power is too high, however, then it can create a large amount of very energetic plasmagenic gas ions who are neutralized and backscattered at the target surface, and then reach the substrate surface where they can become implanted into the growing film [65,66]. This implantation of back-scattered gas atoms leads to defects, higher film stress and an increase in resistivity.

All in all, changing the kinetic energy of the species involved in film growth (incoming sputtered atoms and adatoms, especially) can impact many different elemental atomic processes, having complex and far-reaching effects on the film growth mechanism.

1.3.2 Structure zone models of sputtered-film microstructure

In the case of sputtering deposition, "structure zone models" (SZM) have been developed in the literature to illustrate the expected microstructure for a relatively thick film ($\sim$ 100 nm) deposited under given conditions. While they do not aim at explaining the effects of each parameter in detail, they are useful for illustrating trends induced by instrumental parameters.

The effects of substrate temperature and incoming atoms energies were illustrated by Thornton [67–69] in a SZM (Figure 1.14). He based his model on the initial work by Movchan and Demchisin [70] who linked the microstructure of evaporated films with the homologous temperature $T_h = \frac{T_s}{T_m}$, with T_s the substrate temperature and T_m the melting point of the material. In the case of sputtered thin films, Thornton added the working pressure as a new parameter to take the energy of the incoming sputtered target atoms into account.
Thornton's model divides the expected film microstructure in different "zones". High pressure and low substrate temperature lead to very low mobility of the adatoms on the surface and on the grain boundary regions, leading to the **Zone I** microstructure, characterized by a high density of tapered columns with voids between them. Increasing the substrate temperature during deposition increases adatom mobility and leads to a microstructure shown in **Zone II** with larger and denser column-like grains. Finally, at very high substrate temperatures, the grains in the film become denser and larger in size (**Zone III**) due to recrystallization. A transition zone exists between Zones I and II, **Zone T**, in which surface mobility of adatoms is suppressed on grain boundary regions, but collisions from energetic species in the plasma activate diffusion on the surface. Zone T is characterized by the formation of a dense series of columns with fixed grain boundary regions, and a V-shaped "overgrowth" initial region because of the competition in growth rate between the different orientations of the initial nuclei on the surface [71].

Sputtered atoms are not the only species impinging on the substrate surface during growth. Fast ions (from the plasmagenic gas or from the target), can also modify the surface upon impact by creating defects, nucleation sites, disrupting small clusters, implanting into the film, increasing effective atomic mobility and even increasing the local temperature [72]. Strategies for film growth control using fast ion collision with the substrate include the use of substrate bias [73], unbalanced magnetrons [74–77], and also the use of a dedicated ion source during film growth [78,79] (referred to as Ion-Beam Assisted Sputtering or "IBAS"). Reportedly, film texture can be modified by controlling the energy and flux of incident ions; a low flux of highly energetic particles will preferentially sputter dense planes and favour a texturation with more

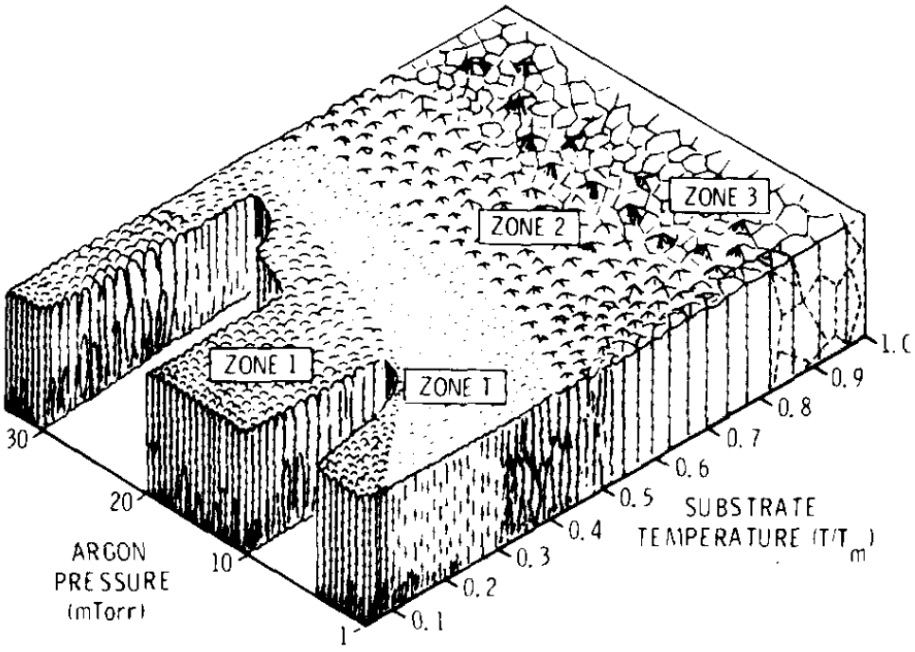

Figure 1.14 Structure zone model proposed by Thornton, summarizing the effect of Ar pressure during deposition and substrate temperature on film microstructure. Reproduced from [67].

open planes. On the contrary, a high flux of low-energy ions promotes coalescence, and this ends up favouring a textured film with the least-energetic atomic plane predominating [63]. Energetic particles colliding on existing porous structures can also make these structure collapse, favouring a denser film. Care must be taken, however, not to let the ion energy become too high so as to avoid excessive ion implantation and stress development in the film alongside densification. The SZM developped by Anders [80] (Figure 1.15) integrates the effect of ion energy to the basic SZM of Thornton by adding a third "net film thickness" axis (which can become negative in the case of ion etching). He also changed the homologous temperature T_h axis by a "generalized temperature", which adds to the homologous tempearature a temperature shift corresponding to the *potential* energy of the arriving atoms, and the pressure axis by a generalized energy axis E^*, which describes displacement and heating effects caused by the *kinetic* energy of bombarding atoms.

Neutral but energetic gas atoms can also impact the growing film and affect its growth. These atoms results from the neutralization of ions and their reflection upon the impact with the target, in a process called "backscattering". These energetic **backscattered neutrals** change not only the microstructure of the film, but also the film resistivity and stress state since some of them can penetrate the film and implant. Their kinetic energy E_k reportedly increases with the target-to-gas atomic mass ratio [81, 82]. Ag having an atomic mass of 107.87 au, Ar gas atoms (atomic mass 39.95 au) will be more energetically backscattered than heavier atoms such as Kr (atomic mass 83.80 u). As such, a handful of studies on the use of Kr instead of Ar as a plasmagenic gas for magnetron sputtering deposition of Ag films have been reported [64, 83–86]. In all cases, using Kr led to a decrease in Ag film resistivity, although the explanation is not clear-cut between the different authors. Experiments have shown that deposition under Kr is less sensitive to changes in deposition power [83] and working gas pressure [86] than Ar. Recently, Mizukoshi *et al.* reported no apparent effect of Kr on the texturation of 14 nm-thick Ag films

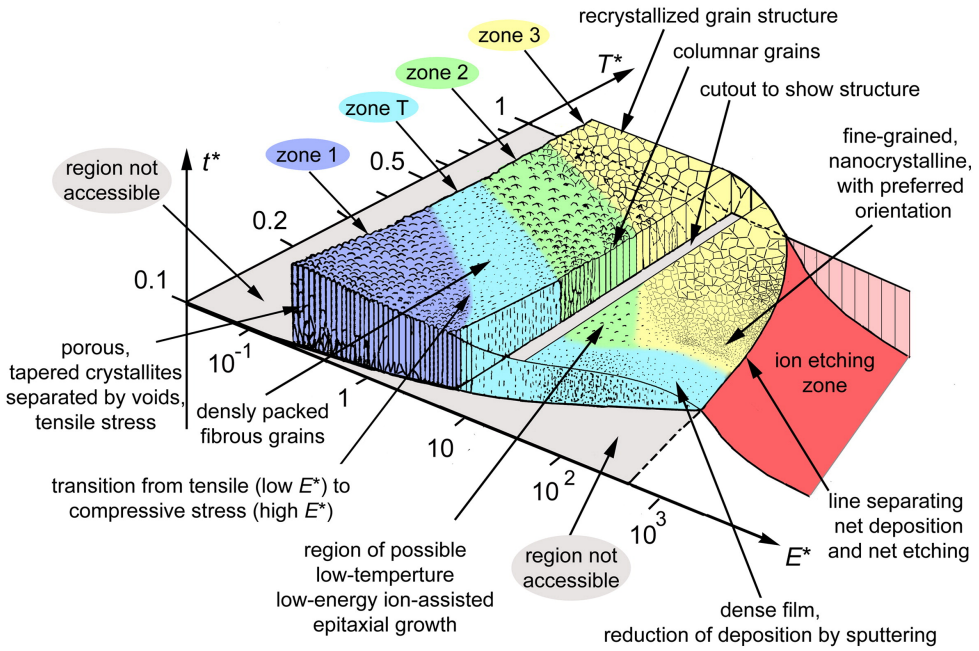

Figure 1.15 Structure zone model including the effect of ion etching. T* = Generalized temperature. Reproduced from [80].

grown on ZnO underlayers, and only a modest increase in grain size from 55 nm to 58 nm when going from Ar to Kr. Sagara *et al.* [84] showed no clear difference in grain boundary electron reflection (R factor as defined in the Mayadas-Shatzkes model) between both gases for thicker Ag films ($\sim$ 150 nm). Regarding film composition, studies using Secondary Ion Mass Spectroscopy (SIMS) and Rutherford Backscattering Spectroscopy (RBS) have evidenced a lower implantation of Kr in the film, which could then explain the lower resistivity. Regardless of the details of the effect of Kr as a plasmagenic gas (which remain not yet fully understood in the literature), this example shows how controlling the atomic weight of the atoms in the plasmagenic gas can lead to changes in the kinetic energy of backscattered neutral atoms and in the resulting film properties.

1.3.3 "Surfactants" in magnetron sputtering deposition

According to the definition - derived from the field of soft matter and adapted to film deposition - a "surfactant" substance adsorbs on the surface of the growing film in the monolayer or submonolayer concentration. It modifies the surface energies and the film growth mechanism, promoting a more 2D-like growth and a lower film roughness without being incorporated into the film itself. It should instead remain on the surface of the film ("float-out" behaviour) [18,87]. We will begin this section with an explanation of the effects of surfactants in homoepitaxial metal-on-metal growth (*i.e* a metal growing on the surface of the same metal). We will then analyse more recent studies focusing on metallic film growth on weakly-interacting substrates by sputtering deposition.

Surfactants in metal-on-metal homoepitaxy

Many works in the 1990's and early 2000's focused on the homoepitaxial growth of metallic thin films and the mechanisms by which surfactant substances manage to suppress island formation

and induce a layer-by-layer growth. They concluded that island formation is suppressed by inhibiting nucleation on top of pre-existing islands, and favouring the nucleation of a high surface density of nuclei on the substrate surface instead [88–95]. Several reasons have been put forward to explain this inhibition effect:

- increase of the activation energy for surface diffusion (E_D), which increases the nucleation density on the substrate surface (lower chance for an adatom to be captured by a pre-existing nucleus, higher chance of nucleating on the substrate);
- easier downwards inter-layer diffusion across steps (E_S), which reduces the mean adatom lifetime on top of an island and therefore its nucleation probability on top of the island [48, 91] ;
- modification of island shape: formation of ramified, less compact islands, with a higher fraction of step-edge sites compared to terrace sites, thus diminishing the adatom lifetime on the island surface.

The addition of sub-monolayer amounts of Sb on Ag(111) is a case study for these three surfactant effects on Ag/Ag(111) homoepitaxy. It has been shown that Sb adsorption on the Ag surface increases E_D for surrounding surface sites, diminishes the Ehrlich-Schwöbel barrier for inter-layer diffusion, and induces the growth of ramified ("dendritic") island shapes [89, 96, 97]. Similarly, Ferron *et al.* [91] made a detailed DFT study of the surfactant effect of Pb on Cu on Cu(111) homoepitaxy, which showed how adsorbed Pb almost completely block "hopping" diffusion of Cu atoms, which was the main diffusion mechanism on dense atomic planes.
With respect to the "float-out" behaviour expected in the case of a surfactant, the study by Meyerheim *et al* [92] focusing on Ni heteroepitaxy on Cu(111) surfaces with oxygen as a surfactant, is an example in which the formation of an "oxygen-rich subsurface region" after Ni growth was detected.

Surfactants for metallic film on weakly-interacting substrates

Metallic film growth on weakly-interacting substrates, such as oxides or 2D materials like graphene [98], do not follow the same scenario of metal-on-metal homoepitaxy. Instead, as previously explained, it is energetically favourable for the film to form metallic islands instead of 2D layers, to minimize the contact area with the substrate. From a kinetic point of view, upward inter-layer diffusion to the first atomic layer is improved by the weak interaction energy of the adatom with the substrate [99], and thus islands will form during the initial stages of film growth, well before the time needed for 2D monolayers to form and for nucleation on top of those monolayers to happen. Effective surfactants in these systems will therefore act upon the nucleation density, nanoparticle shape, and coalescence dynamics.

As previously shown, in the case of a 3D growth mode and under irreversible nucleation conditions, the island saturation density scales as $\left(\frac{F}{D}\right)^{\chi}$. Increasing the nucleation density on weakly-interacting surfaces can be achieved by decreasing surface diffusion D and increasing the atomic flux F. Romanyuk *et al.* [100] showed that the introduction of sub-monolayers of Sn before Ag deposition on Si(001) surfaces induced a roughly 8-fold increase in island density at an equivalent thickness of three monolayers of Ag. Assuming that the island density is directly related to nucleation density, they concluded that Sn addition led to an increase in nucleation density, although their data did not identify whether this increase in density was related to a decrease in surface diffusion or to an increase in the density of heterogeneous nucleation sites thanks to the adsorption of Sn. Another study by Fukuda *et al.* [101] looked at Ag sputtering deposition on Al-doped zinc oxide surfaces with pre-deposited (sub-)monolayers of a number of

transition metals. In this study, they looked at changes in the film percolation threshold, and found that some of the metals used (W, Mb, Zr, Ni) led to a decrease in this threshold thickness, presumably by creating additional nucleation sites on the oxide surface. In any case, we will note that since neither Sn nor any of the transition metals in Fukuda's work showed a "float out" behaviour, they do not fit our initial definition of a "surfactant".

Another important factor for the microstructural control of metallic thin films on weakly-interacting substrates is the control of the coalescence between growing islands. Rapid coalescence, which is expected for small islands during the initial stages of film growth, quickly leads to the fusion of the two initial islands with a final particle larger both in-plane and out-of-plane and with a shape closer to the equilibrium one. However, if island coalescence is somehow slowed-down, then it is possible to induce a phenomenon called "partial coalescence". As formalised by Jeffers *et al.* [102], this inhibition of island coalescence corresponds to an increase in the average time it takes for two particles to completely coalesce (τ_{coal}). When this time is shorter than the average time it takes for two particles to impinge on each other due to island growth and/or island diffusion on the substrate surface ($\tau_{impinge}$), more and more particles will impinge on groups of slowly-coalescing particles, thus creating irregular and elongated island shapes. The process is illustrated in Figure 1.16, showing the formation of 3D spherical particles when $\tau_{coal} < \tau_{impinge}$ (*i.e. complete coalescence*), and of elongated irregular particles due to inhibited coalescence when $\tau_{coal} > \tau_{impinge}$ (*i.e. partial coalescence*). This increase in τ_{coal} and the onset of partial coalescence normally occurs during film growth when the particles are large enough that they lose much of their driving force for coalescence (this is referred to as the "elongation transition" [102–104]), but it can also be caused by a surfactant. In practice, the onset of partial coalescence promotes in-plane growth of islands, and elongated "worm-like" islands that can form a percolated network at a lower thickness. Jamnig *et al.* [105,106] showed how the co-sputtering of Cu, Au, Al, Ti, Cr and Mo in small quantities alongside Ag leads to inhibition of island coalescence (*i.e.* higher τ_{coal}) and thus the formation of elongated particles, compared to pure Ag deposition at equivalent nominal thicknesses. This strategy allows for the deposition of thinner, continuous and conductive films, but it does not meet *stricto sensu* our original definition of a surfactant since the metallic impurities are incorporated into the film, and there is no "float-out" mechanism nor way to eliminate them after deposition. Still, it exemplifies how island coalescence play a paramount role in the evolution of film microstructure and how inhibiting it can lead to a more 2D-like film growth.

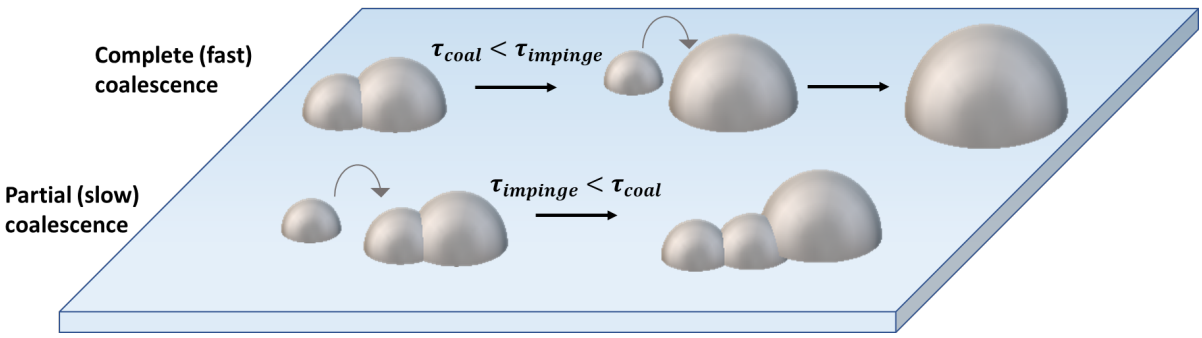

Figure 1.16 Illustration of "complete" and "partial" coalescence phenomena.

In conclusion, the ways in which these surfactants affect film growth vary depending on the system and the particular atomic processes they act upon, such as inter- and intra-layer surface

diffusion or island coalescence. Still, in some of the above-mentioned examples, the strategies do not fully meet our initial definition of a surfactant substance, since they introduce impurities to the film. Ideally, one should aim at finding substances that manage to affect the metallic film growth and microstructure without incorporating into the film making them more alike their soft-matter counterparts. In this respect, gas additives are appealing candidates. They can be easily added to the deposition chamber, left to interact - either in their fundamental state or activated by the plasma - with the growing film by adsorption, and then desorb from the film. We will finish this section on surfactants for magnetron sputtering deposition by examining the existing literature on the effect of N_2 and O_2 on Ag growth.

Effects of N_2 addition during Ag deposition

N_2 gas has been extensively used as an additive, mixed with Ar, in Ag film deposition by magnetron sputtering. On oxide substrates, its has been shown to produce thinner and smoother but continuous Ag films [41, 107–112]. N_2 is known as a very inert gas because of the very strong N-N triple bond in the molecule ($\sim$ 9.8 eV, or 945 kJ/mol [113]). Also, the enthalpy of formation of silver nitride is large and has been estimated at 314.4 kJ.mol^{-1} [114]. Both facts explain the reported apparent lack of reactivity of nitrogen towards Ag when used as an additive during magnetron sputtering deposition. For instance, Pierson *et al.* [107] and Kawamura *et al.* [115, 116] found only diffraction peaks characteristic of metallic Ag in films when deposited with N_2 addition, even for pure N_2. This begs the question, how nitrogen can even interact with the growing film and impact its growth mechanism. Of course, species activated in the sputtering plasma can be more reactive than the N_2 molecule in its fundamental state. Studies, mostly using optical emission spectroscopy, have shown that species present in an Ar:N_2 plasma during magnetron sputtering include excited N_2 molecules (N_2^*) and a relatively small quantity of atomic N resulting from the dissociation of N_2 molecules. The dissociation requires a high electron density and energy in the plasma, which can be achieved by increasing the applied power or by adapting the value of $\%N_2$; higher $\%N_2$ will increase the overall concentration of all N and N_2^* species in the plasma, but will also reduce the number of electrons with sufficient energy to dissociate N_2 [117–120].

The adsorption of atomic N at the surface of Ag has been studied theoretically and experimentally. *Ab initio* simulations have concluded at an exothermic adsorption of atomic N on Ag(111) surfaces [121–129], with an adsorption energy at the optimal adsorption site of $\sim$ 2.02 eV/atom. This positive value contrasts with the negative (and thus unfavourable) adsorption energy of -0.02 eV for a N_2 molecule [126, 128]. In addition, Yun *et al.* [130] have shown theoretically that the surface energy of Ag(111) and Ag(100) decreases almost linearly with the coverage in N (Figure 1.17). While the bare most compact surface Ag(111) is more stable than Ag(100), they even found that N-covered Ag(100) becomes more stable than the N-covered Ag(111) at a given coverage. N dissolution in the bulk, on the other hand, is highly unfavourable energetically [131]. Experimentally, there is only one report on N-adsorption on Ag(111) [131]. It evidenced a quite low-recombinative desorpion temperature starting around 350 K. On the other hand, scattering experiments of N atoms on Ag(111) [124, 129] have evidenced a surprisingly very efficient Eley-Rideal recombination mechanism between adsorbed N atoms and incoming N to form desorbing N_2 molecules [124, 127, 132]. This mechanism is even faster than the thermal recombinative desorption as observed by Carter *et al.* [131]. As will be shown later (Chapter 3 and 5), this fast and efficient desorption mechanism coupled with the very unfavourable bulk diffusion of N atoms will be key aspects in the N_2 surfactant effect during Ag magnetron sputtering deposition.

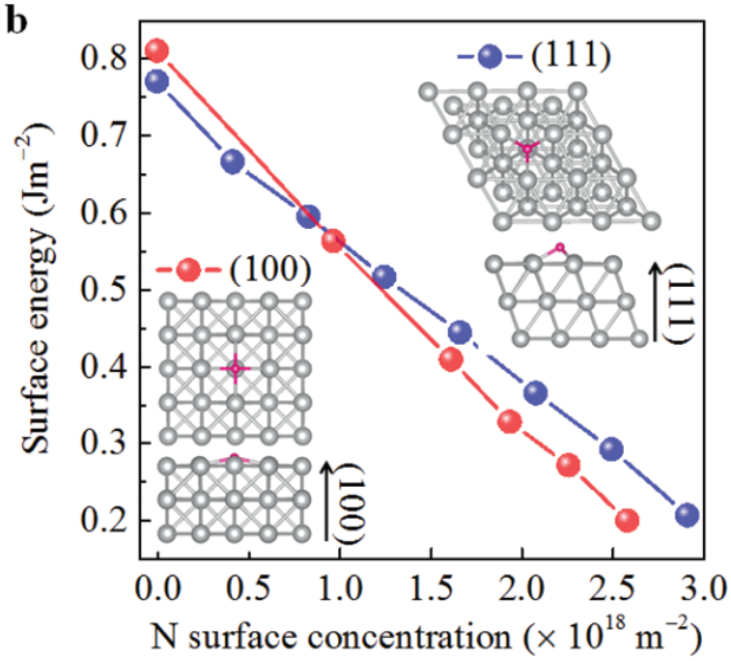

Figure 1.17 *Ab initio* calculated changes in surface energies of Ag(111) and Ag(100) as a function of the surface concentration of N atoms, which occupy interstitial-octahedral sites at the surfaces (insets). Reproduced from Reference [130].

To explain an earlier coalescence induced by N_2 addition during sputtering, the inhibition of island coalescence have been put forward [130]. Jamnig *et al.* [111] also proposed a selective deployment of N_2 gas during the initial stages of Ag growth on SiO_2 to avoid the observed loss of crystallinity and the increase in resistivity in thicker films. When deposited on an amorphous substrate (SiO_2) under pure Ar, Ag thick and continuous films (above 10-20 nm in thickness) adopt a preferentially, still not perfect, (111) texture since this corresponds to the most compact and stable Ag orientation. We note that some works have shown a more random orientation for Ag islands during the initial growth stages on SiO_2 [133]; as shown before, the energy liberated during coalescence drives the reorganisation towards more stable (111) orientation. The situation appears to be different when N_2 is added to the plasma. A structural study has been conducted by Kawamura *et al.* [116] for Ag films deposited under pure N_2 gas. They found a change in texture with a roughly 55/45 (111)/(200) peak intensity ratio in thick deposited Ag films. Somehow, this is in line with the simulation results of Yun *et al.* [130] which predicted that the Ag(100) plane becomes energetically favoured over the (111) one upon atomic N adsorption.

Effects of O_2 addition during Ag deposition

The addition of O_2 during magnetron sputtering deposition of Ag [134–138] has been extensively studied in the past two decades. O_2 efficiently speeds up the percolation on crystalline and amorphous oxide substrates, and even on flexible polymers. Several hypotheses have been put forward to explain this findings.

All studies based on photoemission and diffraction agree with a complex oxidation chemistry which depends on O_2 concentration in the sputtering gas and goes from the formation of Ag sub-

oxides to a more or less crystallized and stoichiometric Ag_2O-like film [58,107,134–136,138–140]. This oxidation process requires the formation of activated oxygen species in the plasma, most likely atomic oxygen resulting from O_2 dissociation [140] (O=O bond energy: $\sim$ 5.5 eV, or 498 kJ/mol [113]) as shown by the increase of plasma reactivity upon radio-frequency irradiation [141]. By adsorbing at the surface of growing islands, oxygen could modify the surface/interface energetic balance and favour wetting in the thermodynamic sense [135] as demonstrated by the decrease of contact angle with oxygen activity in melted sessile drop measurements [142,143]. One of the first works put forward a role of O_2 on the nucleation via a reduction of Ag diffusion at the substrate surface [135]. Other reports based on *ex situ* imaging ruled out any impact on the island density but concluded that a change in coalescence dynamics is induced by adsorbed oxygen [133, 137, 138, 144]. In the model of Jeffers *et al* [102, 145], the transition from isolated islands to a percolated film is controlled by the balance between the growth rate of individual particles from the incoming atomic flux, and the rate of island coalescence *i.e.* the recovery of the equilibrium shape after impingement between two islands. Thus by changing diffusion barriers, in particular at step edges (the so-called Ehrlich-Schwöbel barrier), and/or by impacting the ratio of facet orientations [146, 147], oxygen can induce partial coalescence and elongated object shapes that lead to a faster apparition of an interconnected network. A similar role of oxygen produced by migration from oxygen-rich Ag [148] or ZnO [149, 150] seed layers towards the growing film was also proposed. To avoid compromising the properties of interest through the O incorporation at the growth front, low concentrations [135, 136, 138] or specific strategies for O_2 gas deployment at the initial stages of growth [111, 138, 148] are required just like in the case of N_2.

Despite previous studies pinpointing important effects such as earlier percolation and film oxidation [134–138], the precise role of O_2 addition at the various stages of growth and the actual chemical state of oxidized species remain blurry. In fact, the well-known instability and reactivity of oxidized Ag compounds with the atmosphere [151–155] cast some doubts on the *ex situ* characterizations that are often used to study growth dynamics. For instance, beyond the impact of the usual protective film capping (if any) on species adsorbed at the film surface, fine chemical state analysis and quantification by depth profiling photoemission faces the question of differential sputtering and mixing artefacts. This blur overlaps with the intricate landscape of Ag 3d and O 1s core level binding energies in oxidized Ag [152–154, 156–166]. In addition, post-deposition evolution is systematically overlooked.

1.3.4 Control of film growth using the substrate surface

One last type of strategy for film growth control comes from the substrate surface, through its intrinsic nature and the use of "wetting" or "buffer" layers.

Wetting or buffer layers

"Wetting" or "buffer" layers are thin continuous underlayers deposited on the substrate surface before Ag growth. These buffer layers are usually ultra-thin (in the range of a few nm). Typically made of transition metals, their oxides, or semiconductors, they affect the interface energies of the resulting system by replacing weak film-substrate bonds with stronger film-wetting layer and wetting layer-substrate bonds. Therefore, they are sometimes referred to as "adhesion" layers, to emphasize their positive impact on the mechanical properties. They give rise to an earlier percolation as a lower interface energy will lead to better wetting for the metallic nanoparticles

during the initial growth stages and an increased activation energy for surface diffusion. To distinguish them from "seed" layers, which are typically in the sub-monolayer range and labelled as part of the "surfactant" category, we will consider buffer layers as thick films for which the contact between the substrate and the deposited film is non-existent or almost completely avoided. Examples of wetting layers for Ag film magnetron sputtering in the literature include Ge [167–171], W [172], Al_2O_3 [173], Ti [168, 174, 175], Sn [100] and Cu [176]. In particular, Fukuda *et al.* [101] studied the effect of Ni, Cr, Nb, Zr, Mo, W and Ta underlayers on glass and showed, depending on the buffer metal, a drastic impact on Ag film percolation. Although following the same Volmer-Weber growth mode as noble metals on a thermodynamic point of view, these metals with a high melting temperature have a large supersaturation during growth that induces their nearly 2D growth. Nevertheless, the use of buffer layers is often limited due to their detrimental effect on the final film properties such as optical transmittance or resistivity.

Zinc oxide (AZO) underlayers for Ag growth

One special wetting layer in Ag film deposition is zinc oxide. It is by far the most commonly used underlayer in the production low-E glazings. This material occurs naturally as the mineral zincite and crystallizes in a hexagonal wurtzite lattice (space group $P6_3mc$) under ambient conditions when deposited by sputtering. Its lattice parameters are $a = 3.2495$ Å and $c = 5.2069$ Å, and its density is 5.605 g.cm^{-3} [177]. As seen in Figure 1.18, the structure can be described as two interconnecting sublattices of Zn^{2+} and O^{2-}, with each Zn^{2+} surrounded by a tetrahedra of O^{2-} and vice-versa.

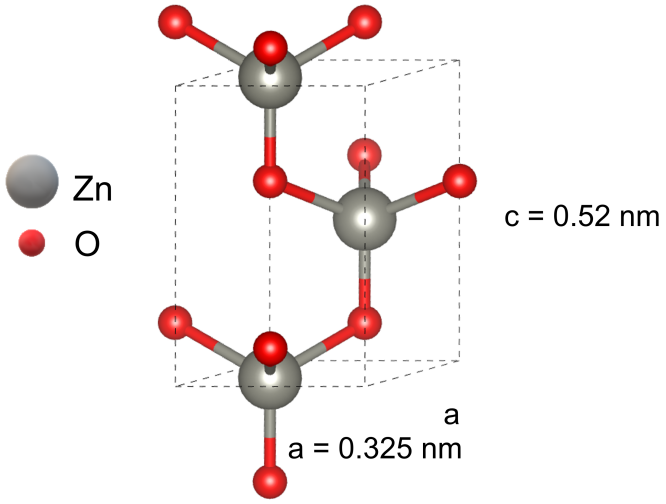

Figure 1.18 Unit cell hexagonal ZnO wurtzite lattice.

ZnO is a semi-conductor with a large band gap of 3.4 eV and a moderate intrinsic conductivity (carrier density of $\sim 10^{16}$ cm^{-3} [178]). Doping makes it a suitable candidate for transparent conducting electrodes. Al-doping is often used to bring the carrier concentration up to the order of 10^{20} cm^{-3} [179, 180]. This higher conductivity allows to use DC magnetron sputtering to deposit it. The truncation of ZnO along the c-axis leads to the appearance of polar (0001) surface, either Zn or O-terminated. Their stabilisation mechanism remain debated, although intrinsic defects (such as vacancies) and hydroxylation seems to play a critical role [181, 182].

The interest of ZnO (or AZO) thin films as seed underlayers for Ag film deposition lies in the epitaxial relationship at the interface. In fact, ZnO thin films tend to be polycristalline but with a pronounced out-of-plane texture along the c-axis direction [183–185]. On top of the (0001) oriented grains of ZnO, Ag preferentially grows along the [111] direction. Although the 30°-rotated in-plane lattice orientation has the lowest lattice mismatch (3 %), only the hexagon-hexagon epitaxy (Ag(111)[1$\bar{1}$0] ‖ ZnO(0001)[100]) is observed despite a much larger value (-11%) [53, 181, 186, 187] (see Figure 1.19). Initially explained by the existence of a coincidence lattice site, Benedetti *et al.* [188] suggested that this specific epitaxy is driven by the polar steps on the surface with an alignment of the dense row of Ag along them. Considering the theoretical surface energies for ZnO(0001) and Ag(111) (1.0-3.0 J.m^{-2} and 1.12 J.m^{-2}, respectively [44, 189]), a 2D Frank Van-der-Merwe ("layer-by-layer") growth mode is even expected. In fact, the formation of flat-top (111) islands has been observed by small-angle x-ray scattering during evaporation on O- and Zn-terminated ZnO(0001) surfaces [181, 186, 187]. In parallel to strong (111) Ag film texture [190], magnetron sputtering deposition studies also reported a lower percolation threshold, a lower film resistivity, a better crystallinity and wetting for Ag films on ZnO underlayers than on SiO_2 [12, 53, 191–193].

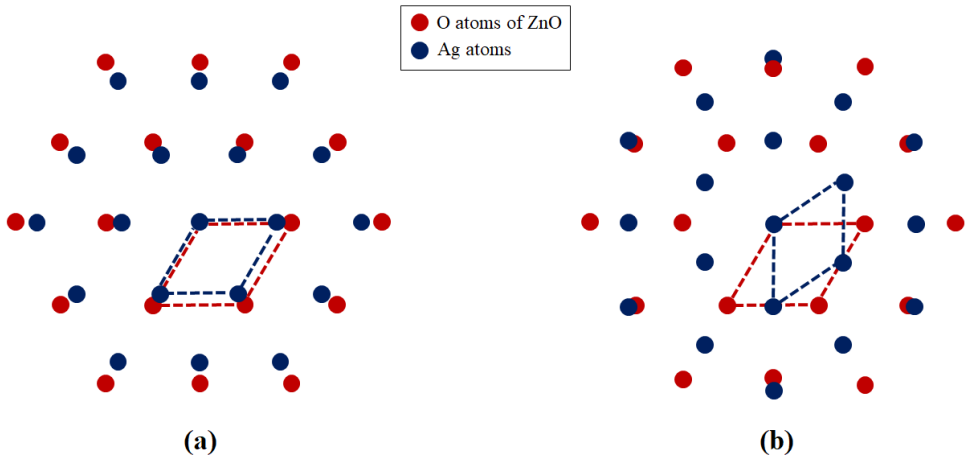

Figure 1.19 Illustration of the in-plane epitaxy at the Ag(111)/ZnO(0001) interface: (a) hexagon on hexagon and (b) 30°-rotated orientations.

Most studies on the effect of N_2 and O_2 on the growth of Ag have been performed on ZnO sublayers [39, 40, 130, 194–196]; they have mostly focused on the surfactant effect of the gas, and not on the interplay between these latter and the beneficial role of ZnO. In this work, after introducing the surfactant effects of N_2 and O_2 in the case of an amorphous substrate (Chapter 3 and 4), we will analyse, in Chapter 5, the way in which those effects translate (or not) to the case of Ag deposition on ZnO underlayers.

1.4 *In situ* and real-time characterizations of film growth

Throughout this chapter, thin film growth was described as an ensemble of elemental atomic processes occurring in response to a flux of atoms arriving at the substrate surface, with their dynamics changing throughout the different stages of film growth (nucleation, growth, coalescence, percolation, continuous and uniform film formation). Studying these processes directly would require techniques with atomic-scale resolution in real-time, such as electron microscopy

or near-field microscopies. These techniques are, however, limited in their application for our purpose, since they have severe limitations and are usually incompatible with magnetron sputtering deposition (presence of a plasma, deposition pressure, plasmagenic gas, rate of deposition...). Instead, the other approach is the real-time monitoring of different averaged properties of the growing film throughout the deposition process. The idea is to link their evolution to the atomistic mechanisms and stages of film growth. For instance, the "film percolation" corresponds to the formation of a non-continuous yet conductive film. Thus, real-time film resistance measurements should therefore detect a more or less drastic increase in film conductivity at this stage. This is an example of the kind of tool that we will refer (and use !) throughout this work as a "real-time" measurement. In the literature, they are also named "*in situ*", although in our case we will keep this term specifically for techniques performed *after* deposition but with no contact between the film and the atmosphere between deposition and characterization.

Regarding the variety of real-time techniques reported in the literature, many of them rely on optical monitoring. This is the case, for instance, of UV-visible ellipsometry or differential reflectivity spectroscopy. They are quite useful for following the initial stages of film growth (nucleation, growth, coalescence), where the growing film is composed of a series of isolated particles, through the analysis of their plasmonic resonances [197–201]. Another example is the monitoring of film stress via the curvature of the wafer induced by film deposition. It has been extensively used to characterize all stages of film growth which are associated to specific tensile/compressive evolutions of stress [42, 202–210]. For instance, zipping of grain boundaries upon coalescence induces a rise in tensile stress in the film. Tools for film stress monitoring and models, such as the ones developed by E. Chason [211], have rendered data analysis much more accessible and agile. At last, x-ray synchrotron-based techniques relying on absorption or scattering can provide access to structural and nanometre-scale informations in real-time during growth [212–216].

1.5 Conclusion

Many strategies for the control of Ag film growth on oxide surfaces have been reported in the literature. The use of "surfactant" substances, in particular, can promote a more 2D growth by affecting the nucleation density, the diffusion rate, the coalescence dynamics or the particle equilibrium shape. Ultimately, understanding the way in which these surfactants act on the growing Ag film would be of great importance for the deposition of thinner, more conductive films for applications such as Low-E glazing products. As shown in previous reports, the use of gas additives, such as N_2 and O_2, is particularly promising to promote a more 2D growth mode in an easy way without compromising too much film resistivity. Still, many of the previous reports suffer from the inherent limitations of *ex situ* characterizations that cast doubt on some interpretations. As such, many questions still remain on the prevailing effects of gas addition. Finally, with the use of ZnO wetting layers being widespread in industrial settings, it would also be interesting to study the interplay between the substrate effect and the gas effect.

This thesis work will try to tackle these questions using a combination of real-time, *in situ* and *ex situ* characterization techniques to study Ag film growth during magnetron sputtering deposition. A comparison will be drawn between amorphous ("SiO_x") and crystallized (AZO) substrates.

Chapter 2

Materials and methods

Table of contents

The first section of this chapter will present the technical aspects of the sputtering deposition experiments performed throughout this thesis, providing details on the experimental setup and the substrates. The following sections will describe the different characterization techniques, which are divided into three categories: (i) real-time measurements, (ii) *in situ* measurements, and finally (iii) *ex situ* measurements. No detailed reminder about the basics of each technique will be given; instead, only details specific to the present study will be presented.

2.1 Thin film deposition

2.1.1 The MISSTIC experimental setup

Magnetron sputtering deposition was performed using the "MISSTIC" (**M**ultilayer and **I**nterfaces **S**puttering deposition on **ST**ructured substrates and **I**n situ **C**haracterization) experimental setup at the "Surface du Verre et Interfaces" laboratory (CNRS/Saint-Gobain Research Paris, Auvervilliers). A side-view photograph of the vessel is shown in Figure 2.1.

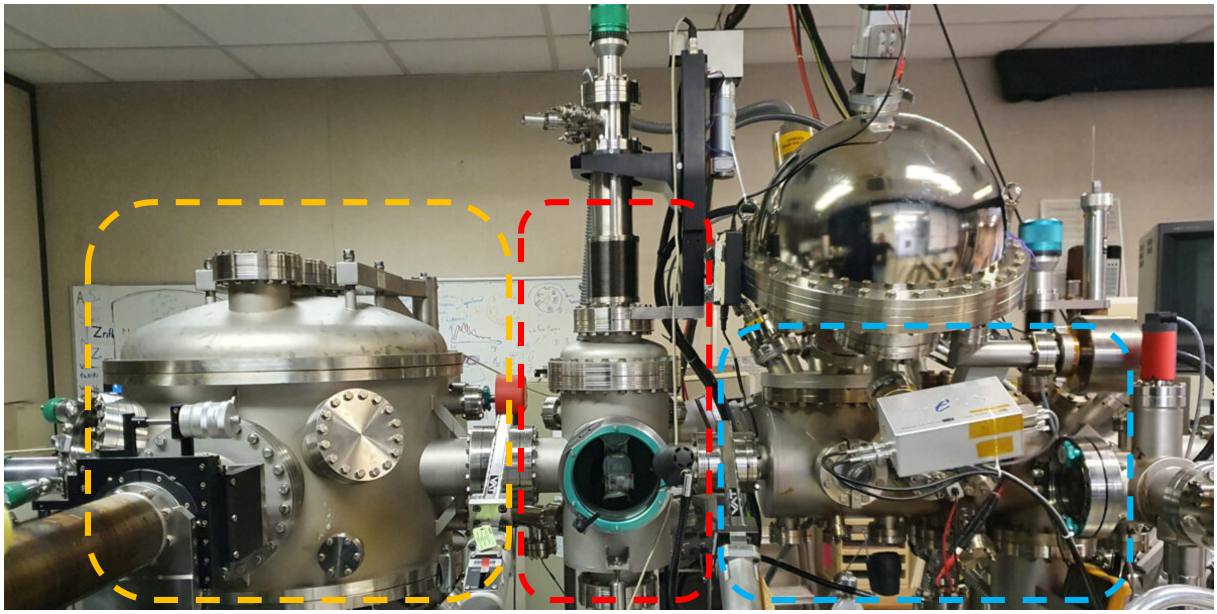

Figure 2.1 Side-view photograph of the MISSTIC deposition vessel. The three main parts of the setup are: Yellow: the magnetron sputtering and real-time measurement chamber; Red: the load-lock chamber; Cyan: the *in situ* analysis chamber equipped with an XPS spectrometer (Phoibos 100 analyzer).

This setup consists of a magnetron sputtering deposition vessel connected under vacuum via a load-lock chamber to an analysis chamber. Each part can be isolated from the adjacent one using high-vacuum gate valves, which allow to vent the isolated part to insert a substrate or for maintenance. Mechanical arms allow for sample transfer under vacuum between each chamber.

Inside the MISSTIC sputtering chamber (Figure 2.1, in yellow), a sample holder can be positioned above one of three magnetron sputtering targets using a mechanical arm which can be moved remotely. Each position (named M1, M2 and M3 hereafter) hosts a circular target with a diameter of $\sim$ 2 inches and a thickness of 3 mm. Each target is also equipped with a shutter mechanism that can be remotely opened and closed, to control the start and the end of a deposition experiment. The target-substrate holder distance was kept constant at 15 cm for M2 and

12 cm for M1 and M3. Figure 2.2 shows a diagram of the MISSTIC deposition chamber, with the three magnetrons and the mechanical arm that moves the substrate between the three positions.

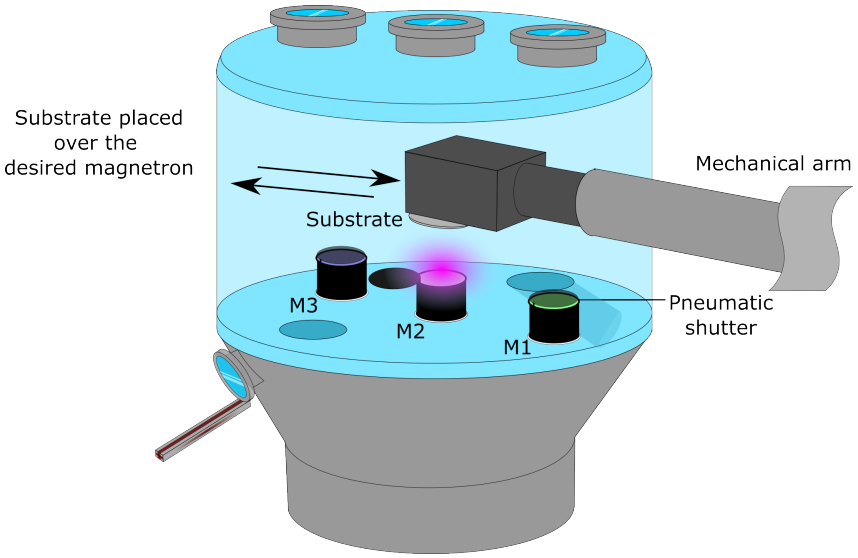

Figure 2.2 Illustration of the MISSTIC deposition chamber. The sketch shows the three magnetrons (M1, M2 and M3), each of them being equipped with a shutter to control deposition duration. The mechanical arm moves the substrate above the three positions.

The deposition chamber is pumped using both a primary oil pump and a Pfeiffer Vacuum turbomolecular pump (HIPace 800M, capacity(N_2): 790 L/s). The former can decrease the chamber pressure down to $\sim 10^{-2}$ mbar, while the latter allows to go down to a base pressure of $< 1 \times 10^{-8}$ mbar. When performing deposition experiments, the total pressure inside the chamber was monitored using a VAT PM-5 adaptive pressure controller, and its value was set between 1 and 25 μbar by opening or closing a throttle valve placed in front of the turbomolecular pump, modifying its pumping capacity. A second mechanical arm, opposite to the main one, has four Cu connector pins on its end and is used for real-time film resistance measurements (see Section 2.2.1 below for more details). Gases used in this work are research-grade Ar, O_2, and N_2 ($> 99.999\%$ purity), and were pumped directly into the vessel either as a pure gas or as mixture using two PR 4000 mass flow meters (from MKS). The maximum flow value for Ar was 50 sccm, whereas for O_2 and N_2 this value reached 22 sccm. Two PFC 1500 DC electrical sources from Hüttinger provided power to the magnetron target in direct current (DC) mode and were used for the sputtering of Ag and AZO (always set up in M2 and M1 positions, respectively). A third PFG 600 RF source, also from Hüttinger, providing power in radio-frequency (RG) mode was used for the sputtering of a dielectric Al_2O_3 target.

The load-lock chamber is located at the center of the setup (Figure 2.1, in red) and connects the sputtering and analysis chambers. High-vacuum valves can be closed to isolate one or both of these chambers from the load-lock, for introducing or retrieving samples after deposition. Lastly, the analysis chamber - pumped by a combination of an ion pump and a turbo-molecular pump down to a base pressure $\sim 10^{-9}$ mbar - hosts an XPS spectrometer for surface chemical characterization.

2.1.2 Substrates

Si substrates (n-doped, (100)-oriented wafers purchased from Neyco, thickness 280 μm, 2 in in diameter, quadratic roughness < 2 nm) were used as provided without specific treatment prior to film deposition; their native "SiO_x" oxide layer (~ 2 nm in thickness) makes them a suitable model for silica glass, while avoiding charge effects in photoemission spectroscopy.
Fused silica wafers purchased from NEYCO (2 in in diameter, thickness ~ 1 mm, quadratic roughness <0.5 nm according to manufacturer) were used for XRD analysis likewise without any specific surface treatment.
Amorphous, surface-oxidized silicon nitride (SiN_x) membranes were employed for *ex situ* Transmission Electron Microscopy experiments, since those membranes are transparent to high-energy electrons (> 30 kV). These membranes purchased from TED PELLA Inc. consist of small circular Si wafers (~ 3 mm in diameter) with nine 15 nm-thick amorphous silicon nitride "windows" each. Each square window had a lateral length of 0.1 mm. These membranes were mounted onto fused silica wafers using high-vacuum tape (Kapton) for deposition.

2.1.3 Sputter deposition conditions

Unless otherwise specified, all deposition experiments were performed under a total pressure of 2 μbar, with a total gas flux of 50 sccm. The sputtering power was kept constant at 50 W by the electrical DC or RF source; this amounts to a power density of 2.47 W/cm^2. Prior to any deposition, a 10 min-long pre-sputtering phase was performed using the same conditions as the subsequent experiment, but with the substrate stored in the load-lock. This pre-conditioning stage ensures that any impurities on the target surface are sputtered before deposition, and stabilizes its composition, especially when working with gas mixtures involving O_2 or N_2. For depositions under a mixture of Ar with another reactive gas (either O_2 or N_2), the composition of the gas flow will be denoted hereafter as $\%X_2$ (X = O or N) following Equation 2.1:

$$\%X_2 = \frac{flow_{X_2}}{flow_{Ar} + flow_{X_2}}. \tag{2.1}$$

Values for $\%X_2$ in this thesis work ranged from 0% to 40%, aside from a single exception in which a $100\%O_2$ deposition was performed with only 22 sccm of O_2 introduced into the vessel in order to get a photoemission reference of a highly-oxidized Ag film. Furthermore, no detectable hysteresis was observed when increasing $\%O_2$ and $\%N_2$ from 0% to 40% and down again.

Growth rates $\mathcal{R}$ were systematically calibrated for each gas mixture by depositing a thick Ag film (~ 50 nm) on a Si wafer previously marked with an ink line (Figure 2.3). The part of the Ag film deposited on top of the ink line was then etched *ex situ* in an ultrasonic ethanol bath to reveal a trench, the height of which could later be measured by atomic force microscopy (AFM). Five measurements at different points of the trench were performed in each case, and the average was taken as the trench height. $\mathcal{R}$ was then calculated by dividing this value by the deposition time.
By assuming a constant deposition rate over time, the nominal film thickness t, as used hereafter, was defined by the product of $\mathcal{R}$ and the deposition time. We note that this "nominal film thickness" is not equivalent to the actual film thickness measured by techniques such as AFM: it corresponds to the thickness of a theoretical, flat and uniform Ag film with the same total deposited mass as the deposited film. Especially for films below the percolation threshold, this model equivalent film will be very far from reality since the actual film will be composed of isolated particles. Still, we will use this abstract "nominal thickness" (t) notation throughout

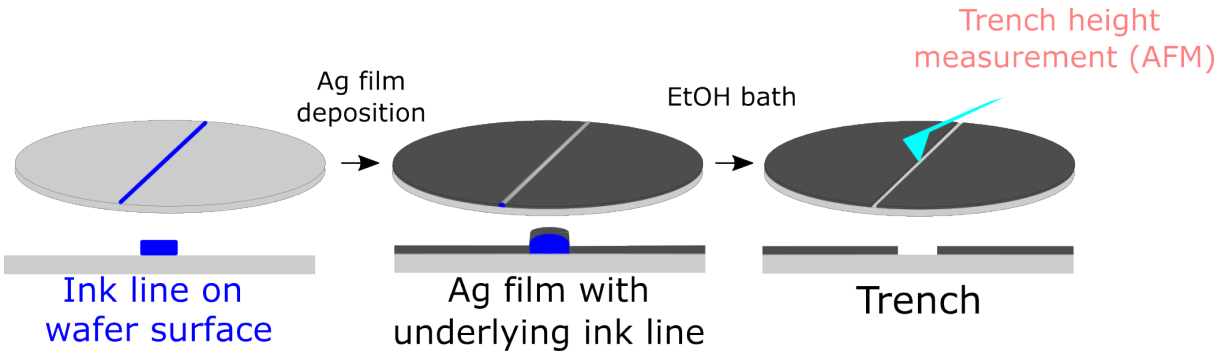

Figure 2.3 Illustration of the procedure for the deposition rate measurement. A trench is created by depositing Ag on a Si wafer surface with an underlying ink line, and then etching the Ag on top with an ethanol ultrasound bath. The height of the trench is measured using AFM.

this work since it is widespread in the literature and easy to work with.
Values of $\mathcal{R}$ for different Ar:O_2 and Ar:N_2 mixtures are shown in Table 2.1.

Table 2.1 Deposition rate values for different Ar:O_2 and Ar:N_2 mixtures. All conditions were calibrated for a total deposition pressure of 2 μbar, a total gas flux of 50 sccm and a deposition power of 50 W.

X% value	O_2 (nm/s)	N_2 (nm/s)
0%	0.55	0.55
4%	0.54	0.54
10%	0.50	0.52
20%	0.48	0.50
25%	0.47	-
30%	-	0.48
40%	0.45	0.45

2.2 Real-time film characterizations

Real-time measurements, namely electrical film resistance and reflectivity spectroscopy, were performed simultaneously inside the MISSTIC sputtering deposition vessel during deposition. These techniques provide valuable insights on the different growth stages of Ag films (nucleation, growth, coalescence, percolation, continuous film formation) and thus will be widely exploited throughout this thesis work. Since they do not interfere with each other, the two resulting data sets (one for each real-time technique) were collected in parallel and were analysed independently.

2.2.1 Electrical film resistance

The two electrode measurement system

Real-time film resistance measurements in MISSTIC are carried out using a two-electrode setup [12,217]. Before actual film growth, two 200 nm-thick linear Ag electrodes (size 31×2 mm^2) separated by 25 mm are deposited onto a Si wafer using a metal mask, under typical Ag sputtering conditions (2 μbar, 50 W, 50 sccm Ar). The wafer with the pre-deposited electrodes is

then taken out of the vacuum chamber via the load-lock chamber and placed in a custom substrate holder, with four Cu pin female connectors. The sample holder pins and the electrodes on the surface of the wafer are wired using 0.5 mm-thick cables and conductive silver paste. A photograph of the sample holder ready to be transferred into the sputtering chamber is shown in Figure 2.4.

Figure 2.4 A photograph of the custom sample holder with Cu connection pins used for real-time resistance measurements with a Si wafer with the pre-deposited Ag electrodes. Two pins are connected to each electrode via 0.5 mm-thick cables, whose adhesion and connection to the electrodes is obtained using conductive silver ink.

Once inside the sputtering chamber, the mechanical arm controlling the sample holder is carefully maneuvered so that the female pins of the sample holder can fit into the male pins on the second mechanical arm in the MISSTIC sputtering chamber (located opposite to the first arm). This manoeuvre is illustrated in Figure 2.5 and the pin connectors in Figure 2.6.

The connectors are brought into contact above the M2 position, which is the magnetron holding the Ag target. When the sample holder is in place and a proper electrical connection between the male and female pins of the holder and the mechanical arm is established, the deposition experiment can start and the real-time film resistance data are recorded by a custom-made device (Alciom company) directly connected to a computer for data storage and analysis.

Film resistance data analysis

The film resistance system developed by Alciom measures the resistance $R_{\square}^{m}$ of the area of the Si wafer between the Ag electrodes by imposing a 2 kHz AC current and measuring the voltage drop. Data in this thesis work were recorded with a sampling frequency of 10 Hz - corresponding to one point every ~ 0.05 nm - and were later corrected using an external calibration against an *ex situ* 4-point measurement [12,217] (RT-3000/RG-80N system from Napson; see Section 2.4.3), to obtain the corrected sheet-resistance value $R_{\square}$ according to the following equation:

$$R_{\square} = 1.44 \times R_{\square}^{m} + 1.04.$$

This correction compensates for the geometry of the measurement [12, 217].

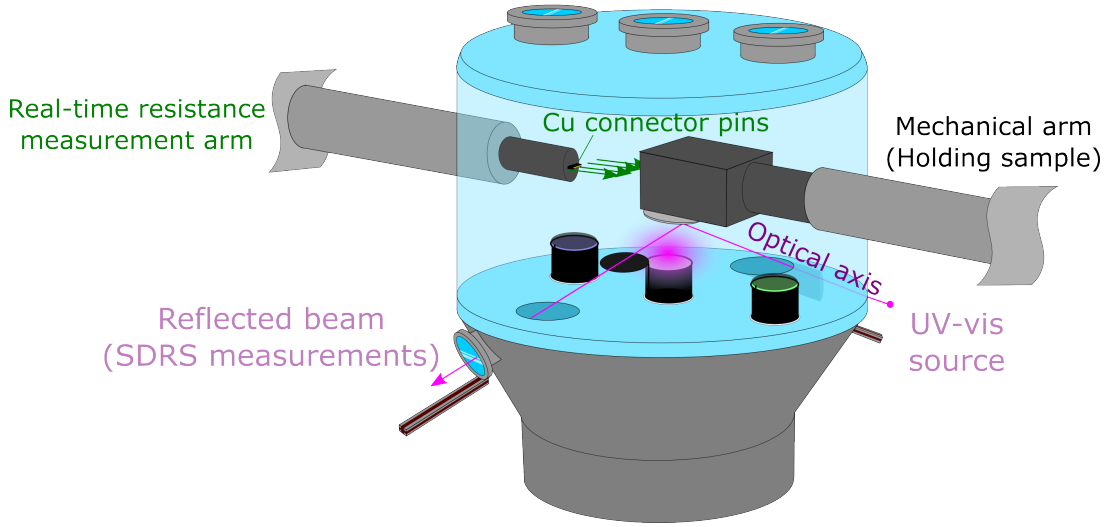

Figure 2.5 Illustration of the real-time measurements in the MISSTIC deposition chamber. **Film resistance:** we see the approach between the mechanical arm holding the substrate, and the opposite arm for resistance measurements. The contact between connectors in each mechanical arm is illustrated by the green arrows. **SDRS:** the UV-vis beam enters the deposition chamber via a silica viewport, is specularly reflected by the substrate at an angle of 45°, then exits the chamber by another viewport. A Wollaston prism then separates the beam into its s and p-polarized components, and each component is collected by a lens plugged on an optical fiber and a UV-vis spectrometer.

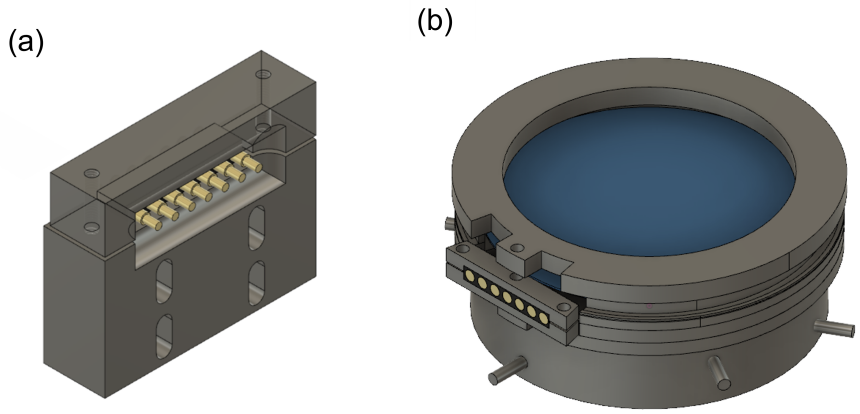

Figure 2.6 (a) The male Cu pin connectors located at the end of the second mechanical arm inside the MISSTIC deposition chamber. (b) The sample holder for real-time film resistance measurements, with the female Cu pin connectors on the side.

Figure 2.7 shows an example of a real-time film resistance measurement during the deposition of Ag on a Si wafer substrate under 4%O_2. The different stages of film growth are shown in the graph to illustrate the correlation between film resistance and its morphology evolution.

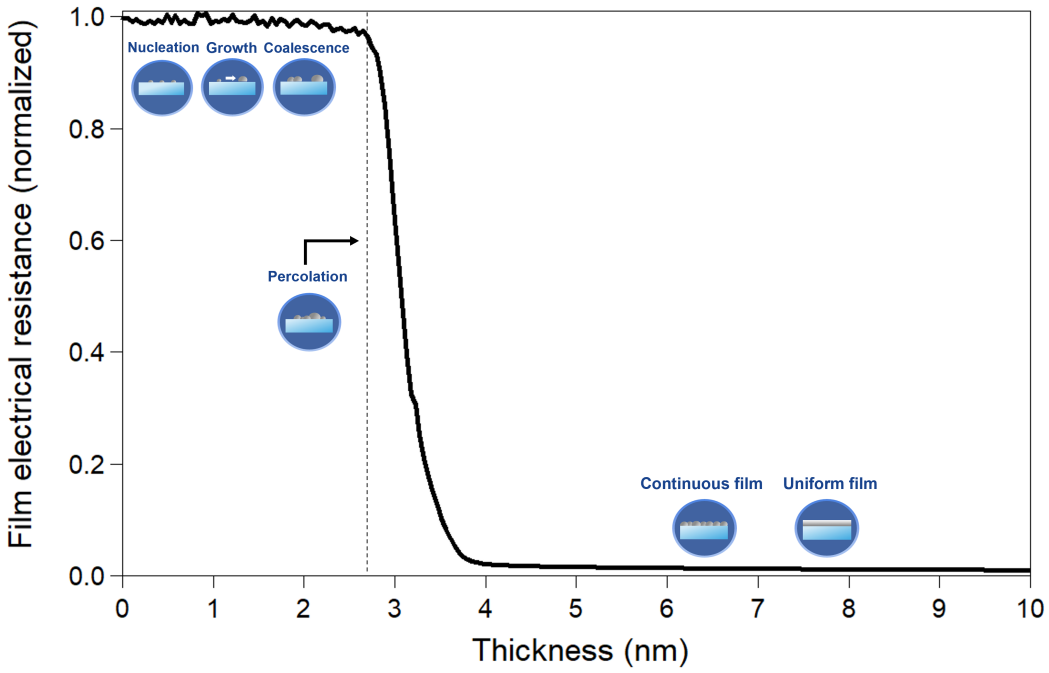

Figure 2.7 Example of a typical resistance vs nominal deposited thickness curve, measured in real-time during an Ag deposition experiment on a Si substrate and under a 4%O_2 gas mixture. Data are normalized to resistance before growth.

In a typical real-time film resistance measurements during Ag deposition, the starting value of $R_\square$ is relatively high, since the Si wafers (as well as AZO underlayers used in Chapter 5) are poor conductors compared to metallic Ag films. This high resistance value remains nearly constant during the initial stages of film growth, during which the film is composed of isolated Ag nanoparticles. These initial stages correspond to nucleation, nanoparticle growth, and generalized particle coalescence. It is only when an electric path across the film is established that the film resistance drastically and suddenly decreases. The corresponding thickness is known as the percolation threshold thickness, and will be denoted as t_p hereafter.

Film resistivity $\rho(t)$ was obtained from the real-time data by multiplying $R_\square$ by the corresponding nominal film thickness $\rho(t) = R_\square(t) \times t$ [217]. $\rho(t)$ is a quantity intrinsic to the film, regardless of the amount of matter [217]. It differs from the value of the bulk of the material as it depends on the film microstructure (contributions from film interfaces and grain boundaries, as explained in Chapter 1). We note however, that before the formation of a continuous film $t < t_p$, the value for ρ is artificial and is not characteristic of the film. It even increases linearly before the percolation threshold, because of the multiplication of the constant substrate resistance by the linearly increasing film thickness. For this reason, when comparing the film resistivity ρ between different deposition conditions, values at $t = 20$ nm were taken as a reference for each experiment, to make sure that the value for every experiment corresponds to a uniform film.

Finally, instead of using $R_\square(t)$ or $\rho(t)$ vs t plots, the percolation threshold thickness is much

more accurately determined in practice by multiplying $R_{\square}$ by t^2, yielding the resistivity-thickness product ($\rho(t) \times t$) [37]. Indeed, instead of a step-like decrease in resistance, the $\rho(t) \times t$ versus t plot reaches a maximum at t_p. Figure 2.8 shows an example of such a plot for a deposition under pure Ar.

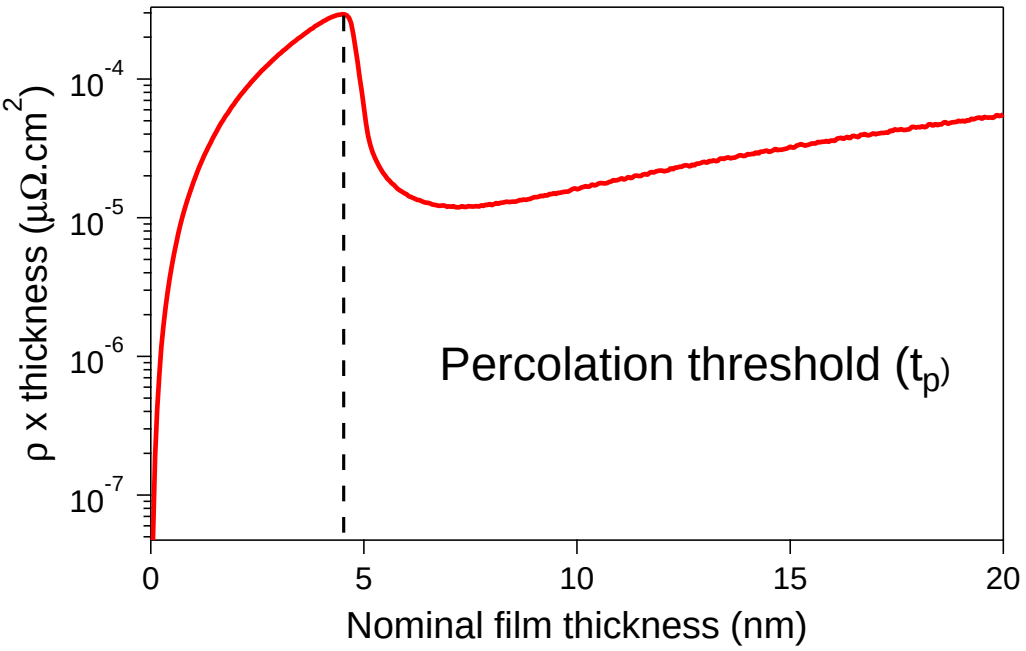

Figure 2.8 Example of $\rho(t) \times$ t vs t evolution for a deposition under pure Ar. The maximum of the plot corresponds to the thickness threshold t_p for the formation of a percolated Ag film.

2.2.2 Surface Differential Reflectivity Spectroscopy (SDRS)

In parallel to the real-time film resistance measurements, the initial stages of Ag growth (nucleation, growth and coalescence) were probed by UV-vis Surface Differential Reflectivity Spectroscopy (SDRS). Through the excitation of plasmon resonances, this optical technique is especially suitable for following the initial stages of film growth, in order to obtain information concerning the morphology of growing islands.

Experimental setup and data acquisition

The SDRS setup [199, 218] used in the MISSTIC deposition chamber can be seen in the illustration in Figure 2.5. The parts involved in the real-time SDRS measurements are shown in purple.
UV-vis light (wavelength 275-820 nm or photon energy 1.5-4.5 eV) emitted by a deuterium-halogen lamp located outside the sputtering chamber is first collected into an optical fiber and focused on the sample through a series of lenses and a transparent fused silica viewport at an incidence angle of 45°. The incident light beam and the different optical components encountered along the optical path are shown in more detail in Figure 2.9. The specularly reflected beam exits the chamber via a second fused silica viewport, and is split by a $BaBO_3$ Wollaston prism in its s (perpendicular to the incident plane) and p (parallel, respectively) polarization states.

The two beams are then collected and analysed separately by two grating broadband UV-vis spectrometers (from Avantes) to record the relative variation of the sample reflectivity $\frac{\Delta R}{R}$ with respect to the signal recorded on the bare substrate prior to deposition. These spectra are also corrected from source drift through an ancillary spectrometer directly connected to the lamp by an optical fiber. Most of the beam paths are inside solarized fibers. Throughout this thesis work, the acquisition rate for SDRS spectra was about 15 spectra.s^{-1}, with each spectrum consisting of an average of 25 measures with an integration time of 2.5 ms. Such a fast acquisition is fully compatible with the Ag growth rate of about 0.5 nm.s^{-1} leading to one spectrum per 0.033 nm.

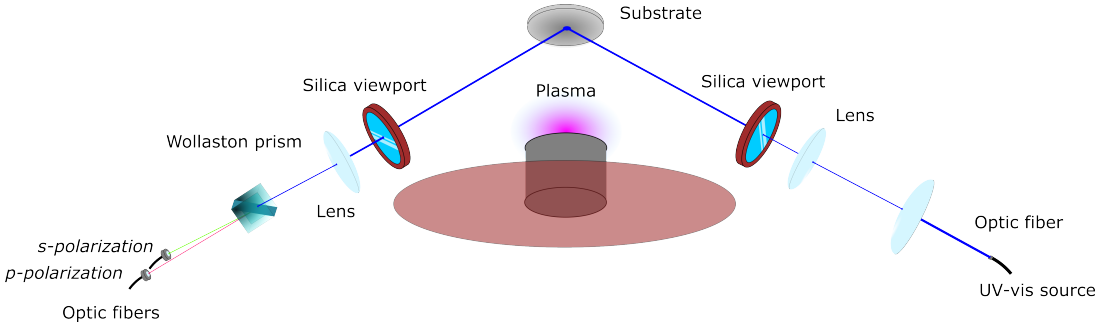

Figure 2.9 Illustration of the optic path and the involved optical components for a SDRS measurement. The beam enters the deposition chamber via a silica viewport, is specularly reflected by the substrate at an angle of 45°, then exits the chamber by another viewport. A Wollaston prism separates the beam into its s and p-polarized components (perpendicular and parallel to the incidence plane, respectively), and each component is collected by a lens plugged on an optical fiber and a UV-vis spectrometer.

Principle of SDRS and excitation of plasmon modes

As was previously shown [199, 200], the variation of the SDRS signal during Ag deposition is mainly driven by the excitations of the different modes of plasmon resonances in the metallic nanoparticles present in the initial stages of film growth. The interaction of the free electrons of the metal with the electric field of the incident electromagnetic wave of a UV-vis beam excite collective oscillations. This phenomenon is known as Localized Surface Plasmon Resonance (LSPR), and for nanoparticles, it manifests itself as a partial extinction of the incident beam due to absorption and scattering. For very small metallic objects *i.e.* with a diameter much smaller than the wavelength of the incident light, this extinction is mainly driven by absorption, the cross-section of which $\sigma_{abs}(\omega)$ is directly proportional to the imaginary part of the nanoparticle polarizability tensor $\alpha(\omega)$. The resonance frequencies given by the poles of $\alpha(\omega)$ will be strongly dependent on nanoparticle shape while their intensities will scale, not only with the volume of the object, but also with their oscillator strength [200, 219]. This quantity scales mainly with the aspect ratio of the object [200].

For a metal with an isotropic surface energy, the equilibrium shape of a nanoparticle on a dielectric substrate can be approximated by a truncated sphere as given by the Yound-Dupré approach. Compared to a sphere in an homogeneous medium, the anisotropic nature of the truncated shape as well as the electrostatic coupling with the substrate induces a break in symmetry between collective electron oscillations along different directions. Two main plasmonic modes, corresponding mainly to dipolar oscillations of the electron cloud, are then present: (i)

one perpendicular to the substrate, and (ii) one parallel to it. Their excitations will depend on the direction of the incident electric field and therefore on the polarization of the incident beam. In s-polarization with an electric field perpendicular to the incident plane and parallel to the substrate surface, only the parallel mode can be excited. In p-polarization with an electric field in the plane of incidence, both modes can be excited by the two projections of the electric field (perpendicular and parallel to the substrate surface). The resonance condition for each of these modes being different, they lead to two different peaks [200] in the $\frac{\Delta R}{R}$ spectra. For Ag, one of these peaks located at a lower photon energy is strictly positive and corresponds to the parallel plasmon mode; the second peak located at higher energy and strictly negative, present only in *p*-polarization, corresponds to an excitation perpendicular to the substrate.

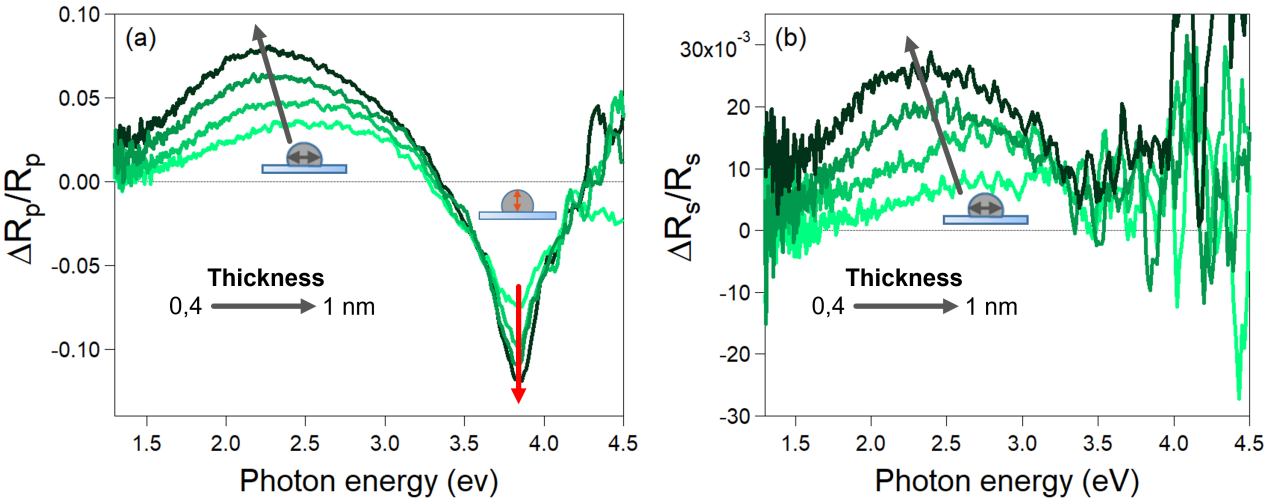

Figure 2.10 Evolution of SDRS spectra for increasing deposited Ag thickness under 4%O_2, measured in (a) p- and (b) s-polarization. The directions of excitations *i.e.* of the induced dipole are given schematically in the graphs.

Figure 2.10 shows a typical example of $\frac{\Delta R}{R}$ spectra measured in (a) *s*-polarized and (b) *p*-polarization during Ag growth on SiO_2. The evolution of the signal is assigned to the change in size, density and shape of Ag nanoparticles on the substrate during the initial stages of film growth. The aim when using SDRS measurements is thus to link these spectral features (intensity, position and shape) to the evolution of film morphology as a function of deposition conditions. To do so, simulations of SDRS spectra, as detailed below, are required.

SDRS dielectric simulations

SDRS experiments were supplemented by dielectric simulations with regular arrays of truncated sphere/spheroid shapes using the *GranFilm* software [220,221]. Fresnel coefficients, in particular in reflection, are calculated in the framework of the excess fields and surface susceptibilities of Bedeaux and Vlieger [222]. For particles with a radius much smaller than the wavelength of the incident light, these quantities depend mainly on the tensor of polarizability of the nanoparticles, which is calculated by solving the electrostatic Laplace equation in a fixed geometry of truncated sphere [222,223] or spheroid [224]. To do so, a multipolar expansion of the electrostatic potential is used and boundary conditions of continuity are matched on the various interfaces using the trick of image point expansion at the interface with the substrate. The remaining boundary conditions on the sphere surface is projected onto the complete set of spherical harmonics leading

to an infinite linear set of equations for the expansion coefficients of the potential. This set is truncated at a high multipolar order at which potential convergence is reached [223] and solved numerically. The first dipolar expansion coefficient is nothing else than the particle polarizability. This quantity is then renormalized by particle-particle electrostatic coupling, either at dipolar or quadrupolar order, on an ordered lattice of objects. Resonances appear as the eigenvectors of the matrix system when dielectric absorption is switched off [219,225]. Beyond particle geometry, the main inputs are the tabulated dielectric constants of the various materials [226]. A similar approach was developed also to describe the case of core-shell truncated particles [227].

Without going up to a quantitative fit of SDRS spectra [145, 228–230], simulations with the *GranFilm* package were performed in *p*-polarization for Ag truncated spheres with a 2 nm radius on a semi-infinite SiO_2 or ZnO substrate (Figure 2.11), in order to pinpoint the main effects on the optical response of changes in (i) Ag nanoparticle aspect ratio A_r (diameter/height) (Figure 2.11-a), (ii) Ag nanoparticle density ρ_s (Figure 2.11-b) and (iii) the formation of an "Ag_2O" shell of thickness t_s (Figure 2.11-c). In the first two cases, the sphere truncation and lattice spacing were varied, while in the last case the relative shell thickness was continuously increased to mimic an oxidation process. Since the *GranFilm* program cannot take the presence of a thin film between the Ag particles and the semi-infinite substrate into account, the calculated electrostatic interaction was taken with an infinite SiO_2 substrate, and then all differential reflectivity spectra were then normalized to the reflectivity of Si so as to compare simulation and experiments. Simulations were performed at constant deposited thickness, except in Figure 2.11-c, to highlight variations related to oscillator strength [199, 200]. To account for experimental widths due to finite-size effects and size/shape distributions, an *ad hoc* broadening [227, 229] was included to qualitatively match the experimental widths via a convolution with a Gaussian function (with a FWHM of 0.4 eV and 0.1 eV for the parallel and perpendicular directions, respectively). Bulk dielectric functions of Ag, SiO_2, Ag_2O [226, 231] were used for the simulations.

In brief, as can be seen in Figure 2.11-a, and as previously described in depth [199, 200, 219, 224, 225, 229, 230, 232], particle flattening (Figure 2.11-a) induces a sizeable red-shift and intensity increase of the low-energy in-plane parallel plasmon resonance peak. The effects on the high-energy out-of-plane perpendicular plasmon resonance peak are the opposite, though less pronounced in magnitude. Similar trends are observed with the increase of particle surface density (Figure 2.11-b), but with a more moderate effect on the low-energy in-plane resonance peak [225]. Lastly, thickening of the oxide shell red-shifts the position of both peaks and decreases their intensities [227] (Figure 2.11-c). This last effect is related to a lower fraction of polarizable metallic Ag in the nanoparticles. Qualitativley, the trend observed here for an oxide is the same for any dielectric material on top of a metallic core. At last, qualitative similar results are obtained on ZnO.

These *Granfilm* simulations allowed for qualitative interpretation of SDRS spectra for different deposition conditions as a consequence of a combination of effects, including changes in nanoparticle aspect ratio, changes in particle surface density and formation of dielectric shells.

Integrated s-polarized signal

Change in morphology are often probed in plasmonics through the energy position of resonances. But intensity also brings information of the morphology through the oscillator strength as seen in Figure 2.11. In differential reflectivity, it can be demonstrated [200, 219] that the signal is directly proportional to the product of the film thickness and the imaginary parts of the particle

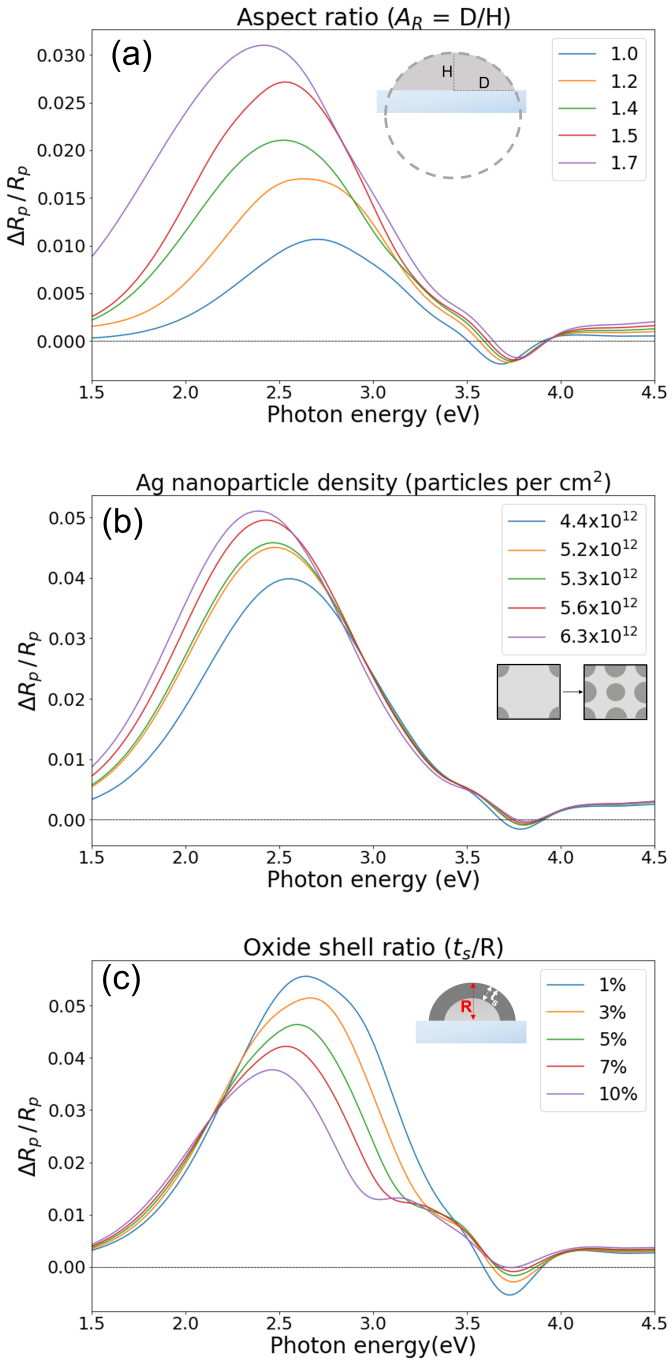

Figure 2.11 Simulated p-polarized SDRS spectra for Ag truncated spheres arranged in a square lattice on SiO_2/Si. Effect of a change in (a) aspect ratio (diameter/height), (b) particle density, (c) oxide shell thickness. In the last two cases, a hemispherical shape was used. An *ad hoc* broadening was included to match with experimental widths (see Section 2).

polarizabilities (normalized to their volume). In other words, this means that the SDRS signal is indeed directly proportional to absorption. As previously shown [200], the integrated SDRS signal in s-polarization defined as

$$\mathcal{A}_s(t) \propto \frac{1}{t} \int \frac{\Delta R_s}{R_s}(\omega, t) \frac{d\omega}{\omega}. \tag{2.2}$$

is directly proportional to the oscillator strength of the parallel plasmon mode. This later, as it is well-known in plasmonics, is directly proportional to the particle aspect ratio A_r (diameter/heigh) nearly whatever the metal/dielectric and the particle shape. Thus $\mathcal{A}_s(t) \propto A_r$ is a fair and sensitive indicator of the evolution of particle wetting.

As an example for the use of $\mathcal{A}_s(t)$ as a tool to follow wetting, Figure 2.12 shows the results during Ag deposition under $0\%O_2$ and $4\%O_2$ conditions. Since values for $4\%O_2$ are consistently higher than for $0\%O_2$ during the whole deposition, this shows that Ag particles have improved spreading under an oxygenated gas mixture. This will be an important result which will be studied in more detail in Chapter 4.

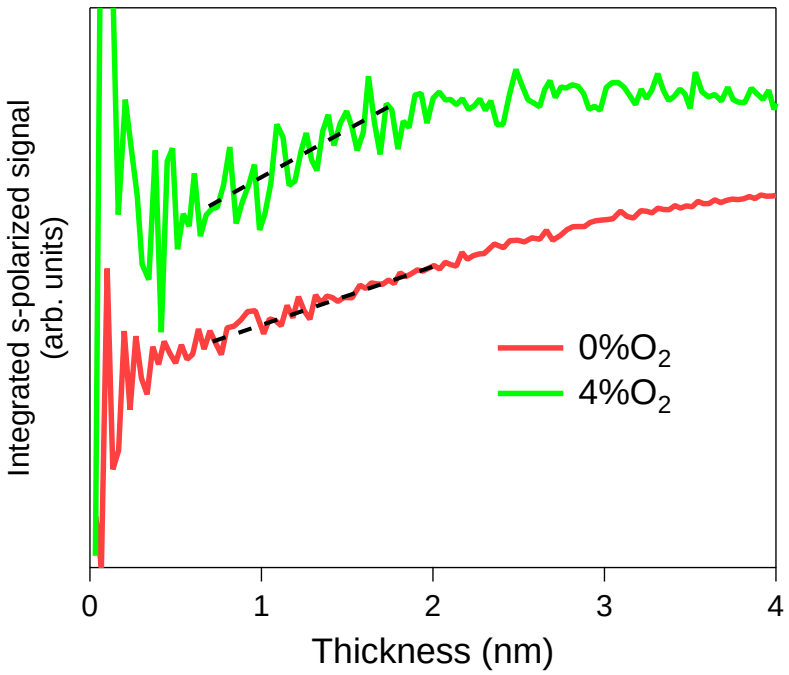

Figure 2.12 Integrated $s-$polarized signal $\mathcal{A}_s$ as a function of the deposited thickness for Ag growth under 0% and $4\%O_2$. Dotted lines in the linear region for $\mathcal{A}_s(t)$ (coalescence stage) are shown as a guide for the eye.

Furthermore, the change in $\mathcal{A}_s(t)$ and therefore of aspect ratio reflects also the growth process itself. A transition between particle growth at fixed equilibrium shape (during nucleation and growth) and early coalescence regimes is observed at a threshold thickness t_c (the coalescence threshold thickness) corresponding to a minimum of the $\mathcal{A}_s(t)$ curve. This initial "U-shape" evolution of $\mathcal{A}_s(t)$ is observed systematically for vapour deposition of metals on dielectrics [200], but is often blurred in magnetron sputtering deposition by the signal/noise ratio (due to the comparatively faster deposition rate in sputtering). After this threshold, the coalescence stage is

characterized by a linear increase of $\mathcal{A}_s(t)$ with thickness, the slope of which depends on growth conditions and the extent of the lateral spreading of nanoparticles. In Figure 2.12, at $t = 1$ nm, the linear regime for $\mathcal{A}_s(t)$, characteristic of generalized coalescence, is reached. The higher slope for $4\%O_2$ is then associated with a faster spreading of the particules in 2D compared to $0\%O_2$.

2.3 *In situ* film characterization and treatment

In situ means inside the MISSTIC experimental setup after deposition. Transfers between the different chambers are performed under vacuum, with the advantage that any evolution of film morphology or of chemical characteristics due to the contact with air is avoided. The most important technique of this category that was used throughout this thesis work is X-ray Photoemission Spectroscopy (XPS). Such an advantage is decisive when studying the effect of adsorbates (O or N herein) at the surface of the film. It avoids (i) a step of capping to protect the film that, for sure, modify them and (ii) the uncertainties brought by sputtering profilometry in photoemission (preferential sputtering and mixing effects). *In situ* XPS was also used for study the effect of plasma exposure during the first seconds of sputter deposition on the substrate surface itself.

2.3.1 X-ray Photoemission Spectroscopy (XPS)

In situ X-ray Photoemission Spectroscopy (XPS) was performed in the MISSTIC analysis chamber (Figure 2.1-in cyan) with a Phoibos 100 hemispherical analyser (from SPECS) equipped with 5 channeltron detectors under non-monochromatic Al Kα excitation (XR50 from SPECS). The binding energy (BE) scale was calibrated on the Ag 3d 5/2 core level of a thick metallic Ag film ($E_B = 368.1$ eV). Spectra were recorded at a pass energy of 15 eV and for an emission angle of 24.5 deg. The acquired core level regions throughout this thesis work included Ag 3d, O 1s and N 1s, which were used to obtain information on the chemical state of Ag in the deposited films and the nature of the oxidized species that were formed during film deposition. C 1s was also recorded, to detect the presence of other carbon impurities at the film or substrate surface, in particular the formation of carbonates. Finally, Si 2p, Zn LMM, C 1s, O 1s and N 1s regions were measured in the case of chemical studies of the substrate surface state (Si wafer and AZO underlayers) and of very thin Ag films for which the substrate signal is not completely damped. It is worth noticing thar Ar used as the main plasmagenic gas was never detected in the films by XPS.

All the measured spectra were analysed with the *I4P Igor Pro* package [233]. For the case of partially oxidized films (which will be frequently encountered in Chapters 4 and 5), Ag 3d spectra were decomposed as a sum of two peaks, one corresponding to metallic Ag, and a second one shifted by about 0.5 eV corresponding to "oxidized Ag". No better fit could be obtained with more components. An active Tougaard-type background [234] was used, and source satellites [235] were accounted for during the fit process. A Doniach-Sunjic asymmetric line shape was used for the metallic Ag peak, with an asymmetry parameter of 0.05, whereas a Voigt profile was used for the oxidized one. For both peaks, the Lorentzian full-width at half maximum (FWHM) was fixed at the Al-Kα_1 source emission line (0.58 eV) [235] while the Gaussian FWHM counterpart of the profile was assigned to instrumental broadening and distribution of chemical shifts. The branching ratio and the spin-orbit splitting of Ag 3d doublet was kept fixed at the theoretical (2/3) and the tabulated (6 eV [236]) values, respectively. Assuming an homogeneous film (although not the case; see Chapters 4 and 5) with a $Ag^0_{1-y}Ag^{\delta+}_y$ composition, the

fraction y of oxidized silver was obtained from the ratio of peak areas in the Ag 3d decomposition.

Fit of O 1s spectra, on the other hand, was used to scrutinize the nature of the oxygen species at the surface of the film that were formed during film deposition, as well as to quantify their relative fraction. It was performed using a series of Voigt peaks which Lorentzian FWHM was kept at the source broadening. Due to the low resolution of the non-monochromatized x-ray excitation, the binding energies value (E_B) of each species was taken from literature and kept constant; also a common Gaussian FWHM was used for all of them. The background was accounted by an active Shirley one. More details on the nature of these oxygen species will be given in the respective Chapters 4 and 5.

In addition to the fit of the O 1s core level, a global average stoichiometry AgO_x of the analyzed film surface region could be deduced from the ratio of the total O 1s/Ag 3d areas, assuming a uniform film and using inelastic mean free paths in metallic silver. The quantification of the AgO_x stoichiometry was performed after correcting the corresponding areas from photoionization cross section [237] and analyzer transmission function [238] using TPP2M inelastic mean free path [239, 240] in metallic silver ($\lambda^{Ag}_{Ag3d} = 1.6$ nm and $\lambda^{Ag}_{O1s} = 1.43$ nm). Both results (oxidized Ag fraction y and the global average stoichiometry x) could then be combined to deduce the average charge δ transferred per Ag atom, using the balance $2x = \delta.y$, *i.e.* by assuming an O^{2-} charge state.

Beyond model bias, the error bars of such an analysis are of ± 0.1 eV for binding energy and of ~ 10 % for area quantification.

2.3.2 Surface plasma treatment

The impact of the exposure of the sample (wafer surface or thin metallic nanoparticle film) to a reactive plasma in the initial deposition stages was mimicked by exposing *in situ* a sample to a plasma ignited on an alumina target (M3 magnetron position) using a radio-frequency excitation (power 50 W). The substrate holder was place above the M2 position, so not in direct line of sight of the M3 plasma. The uptake of the sample in O or N and the decrease of its carbon contamination were analysed by photoemission. Due to the intrinsic very low deposition rate of alumina in these conditions (0.007 nm/s), the offset substrate position and the short exposure time, aluminium signal was below the detection limit of XPS after plasma treatment.

2.4 *Ex situ* film characterizations

Finally, *ex situ* characterizations were performed outside the MISSTIC setup; to do so, samples have to be exposed to the atmosphere before and during the analysis. To avoid contamination and ageing from this exposure to air, films were systematically protected with a capping layer previous to ventilation and extraction from MISSTIC. The choice of the capping layer was done based on a series of tests on 20 nm-thick Ag films deposited under 25%O_2 on Si wafers. Indeed, it was noted that storage under air of these oxidized films led to a decrease in film resistance as recently reported and discussed by Jeong *et al.* [151]; this phenomenon is related to the decomposition of unstable oxides in the film (whose formation will be discussed in Chapter 4). This decrease in resistance under air storage was used as a criterion for the choice of the capping layer; the slower the decrease the better the capping. The following capping layers were tested:

- No capping layer (reference);
- AZO (5 nm);

- AZO (10 nm);
- Ti (3 nm);
- AZO (10 nm) + Ti (3 nm).

After removal from MISSTIC, and thus exposure to air, the initial film resistance for each film was quickly measured using a Napson 4-point resistance measurement (as explained below Section :4-point-resistance). Over the following days, all films were kept in the laboratory exposed to air, and their resistance was periodically measured. Figure 2.13 shows the evolution of the film resistance (normalized to their respective starting value) with time as a function of the capping layer nature. The resistance of the unprotected film consistently decreased with time. After

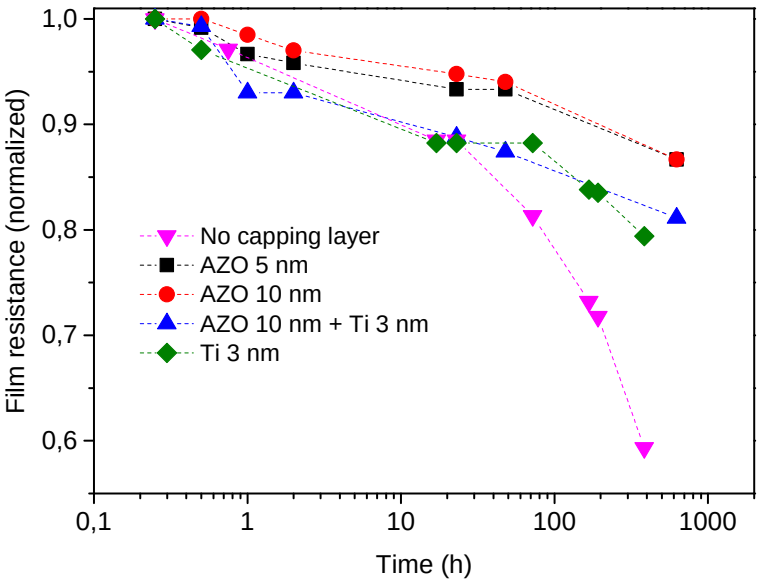

Figure 2.13 Evolution of normalized sheet resistance for a series of 20 nm-thick Ag layers deposited on Si wafers under 25%O_2 for different capping layers.

roughly 24 h, its resistance value had decreased by 11% and after 15 days, by 40%. Looking at the capped layers, the 5 nm AZO and 10 nm AZO capping films were the best-performing ones since the resistance only decreased by 5 or 7% after 24 h and by only 14% after 15 days. Considering that vacuum conditions have been systematically used to store films for a long period of time (more than a few hours), AZO was chosen as an effective capping layer for temporary exposure to the atmosphere. Between the two tested thicknesses, it was deemed safer to use a 5 nm-thick films so as to avoid increasing the total thickness of the stack more than necessary for *ex situ* measurements, in particular Transmission Electron Microscopy.

To conclude, a 5 nm-thick AZO layer (deposited under pure Ar at 50 W in DC mode from a ceramic target) was then chosen as the capping layer for all *ex situ* characterizations.

2.4.1 Transmission electron microscopy (TEM)

In order to determine the impact of different deposition conditions on film morphology, samples at an equivalent nominal thickness of 0.6 nm were analysed by Transmission Electron Microscopy (TEM). The Scanning Transmission Electron Microscope acquisitions in High Angle Annular

Dark Field (STEM-HAADF) were performed in plane-view mode on the Titan THEMIS (ThermoFischer Scientific) of the PANAM platform (C2N, Palaiseau, France), a part of the TEMPOS Equipex. It features a 200 keV high-brilliance XFEG gun with a Cs corrector on the condenser system allowing 80 pm of lateral resolution.

Films for TEM analysis were deposited on amorphous silicon nitride membranes (described in a previous section), whose oxidized surface mimics the amorphous native oxide layer of Si (SiO_x). The selected nominal deposited Ag thickness ensures that all films, regardless of their deposition conditions, are well below t_p and consist of disconnected nanoparticles. Right after Ag film deposition, all samples were capped with a 5 nm-thick-AZO layer. Samples were synthesized as close as possible to TEM analysis, and stored under vacuum conditions between deposition and analysis to minimize ageing. Figure 2.14 illustrates a 0.6 nm-thick Ag film deposited on a Si_3N_4 membrane being analyzed by TEM.

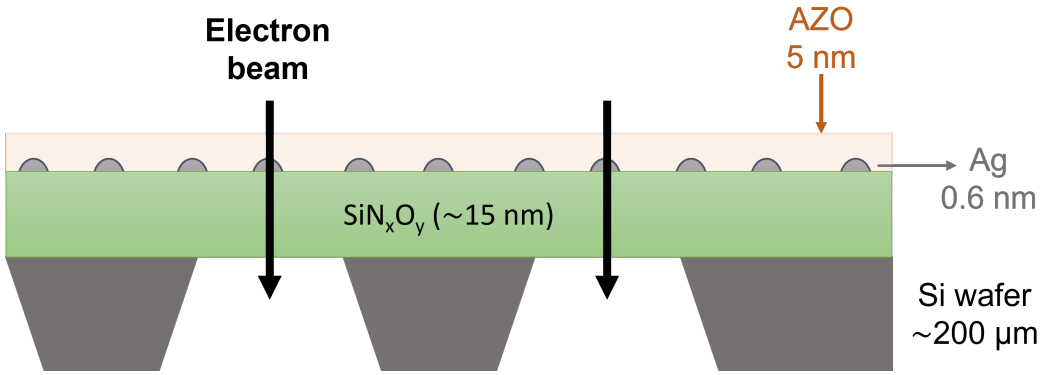

Figure 2.14 Illustration of a 0.6 nm-thick Ag film deposited on a Si_3N_4 membrane during TEM analysis. The value of $t = 0.6$ nm ensures that all films, regardless of deposition conditions, are below the percolation threshold.

STEM-HAADF images were analysed with a *Python* image analysis script from the Scikit-image library, coupling (i) a "Blob-Log" algorithm to detect Ag particles as bright "blobs" against a dark background, and (ii) a watershed procedure for finding their edge and thus their in-plane shape. Figure 2.15 shows an example for a 0.6 nm-thick Ag deposition under $0\%O_2$, alongside the result from the image analysis.
Information on the Ag nanoparticles such as mean radius and surface density can be extracted from such an analysis using several STEM-HAADF images. As explained in the following chapters, only the particle density was actually exploited since capping may change particle size and aspect ratio.

2.4.2 X-Ray Diffraction (XRD)

Structural analysis with X-Ray Diffraction (XRD) was used to obtain information on the crystallinity and texture of the polycristalline Ag films grown under different conditions. All samples for XRD analysis had a Ag film thickness of 20 nm and were capped with a 5 nm-thick layer of AZO to avoid ageing when exposed to air outside of MISSTIC; the exposure to air was minimized and always < 24 h. Moreover, films were deposited on bulk fused silica wafers instead of Si wafers to avoid overlap between peaks of interest and the multiple diffraction Si(100) signal in the $2\theta = 30 - 35$ deg range [241].

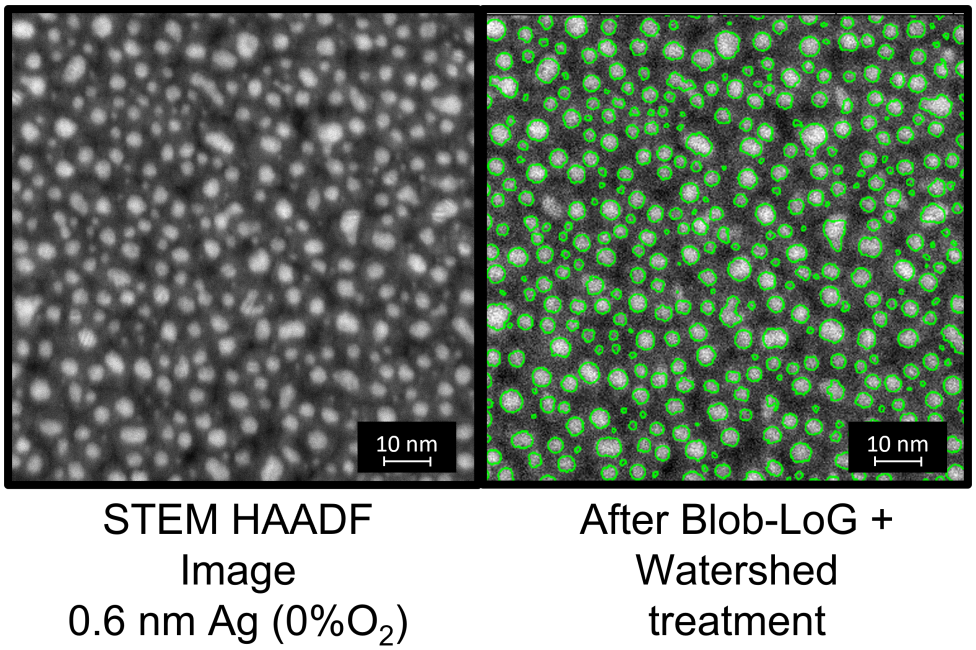

Figure 2.15 Example of a STEM HAADF image of a Ag deposit made of nanoparticles. Left: original STEM HAADF image. Right: after treatment with Blob-Log and Watershed algorithms for finding the Ag nanoparticle positions and edges.

Ex situ Bragg-Brentano and in-plane grazing incidence X-Ray Diffraction (in-plane GIXRD) analyses were performed using a Bruker D8 Advance diffractometer for the former and a Rigaku Smartlab diffractometer for the latter. During an XRD measurement in the Bragg-Brentano geomtery, atomic planes whose normal is perpendicular to the substrate surface will diffract the X-Rays, whereas for GIXRD it will be atomic planes with their normal parallel to the substrate surface (Figure 2.16 a and b). We shall therefore refer to these two geometries by their given names, or using the terms "out-of-plane" and "in-plane" respectively in the context of this thesis work.
The incidence angle for the in-plane GIXRD (Figure 2.16-b) was set at 0.5 deg, which is just above the critical angle for total reflection. A copper Kα source was used, with no monochromator. Spectra were analyzed and compared to data from XRD databases (ICDD PDF4+) using the Bruker Diffrac.Eva Suite. The coherent domain size D_{coh} (the so-called "Debye-Scherrer" size) was obtained from the FWHM of peaks after a peak fitting procedure with Voigt profiles.

2.4.3 4-point resistance measurements

Sheet resistance for different thin film stacks were measured at room temperature with a Napson PEL 3000 apparatus. It consists of 4 in-line equidistant probes [217] that are pressed in the stack (Figure 2.17). The two outer probes inject and collect the current, whilst the two inner probes detect the associated voltage drop. A weight on top of the measurement head ensures proper electrical contact between the probes and the film by pressing them down in the film. For a very thin film with $t \ll s$ (which is clearly the case for our nanometric thin-film stacks; Figure 2.17), the value of the injected current and resulting voltage drop are linked to the film electrical resistance by the following expression:

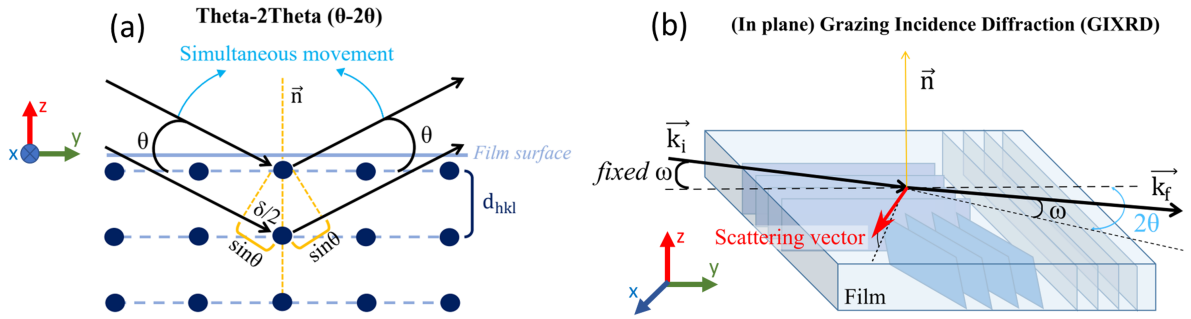

Figure 2.16 Illustration of (a) Bragg-Brentano (or out-of-plane geometry), and (b) GIXRD (or in-plane) XRD measurement geometries.

$$R_{\square} = \frac{\pi}{\ln 2}\frac{\Delta V}{I}$$

Sheet resistance was measured at different spots for each sample to calculate an average stack resistance.

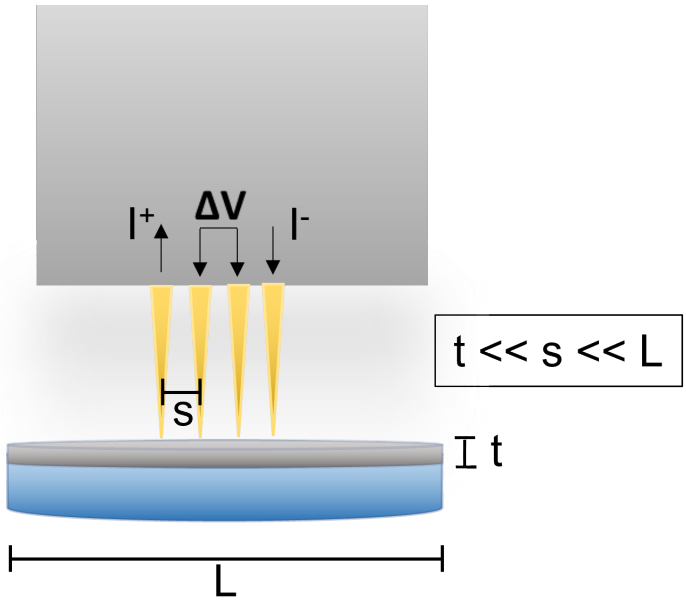

Figure 2.17 Illustration of a collinear 4-point film resistance measurement. In the used apparatus, $s = 1.5$ mm.

Chapter 3

Effect of N_2 addition on Ag sputtering deposition on SiO_x substrates

The effect of N_2 addition during magnetron sputtering deposition on the growth and properties of Ag films will be studied in this chapter. Results from real-time and *in situ* measurements will show the important role of N_2 as a "surfactant" gas, improving the Ag nanoparticle wetting on the substrate during the initial growth stages and inducing a lower percolation threshold thickness.

Table of contents

3.1 Deposition conditions

Throughout this chapter, all Ag deposition conditions others than gas composition (Ar:N_2 mixture) will be kept constant, with a power of 50 W in DC mode, a total pressure of 2 μbar and a total gas flow of 50 sscm. Gas composition was varied between 0% and 40%N_2. A 10 min-long pre-sputtering stage was performed prior to any growth. Unless otherwise specified, all depositions in this chapter were carried out on Si wafers whose SiO_x native amorphous surface oxide mimics a glass surface. Film resistance and SDRS measurements were carried out in real-time during deposition and in parallel.

3.2 Film morphology from real-time measurements

3.2.1 Film resistance measurements

As shown in Figure 3.1, the percolation threshold thickness t_p decreases from $\sim$ 6 nm down to $\sim$ 3 nm when the N_2 flow increases from 0%N_2 to 40%N_2.

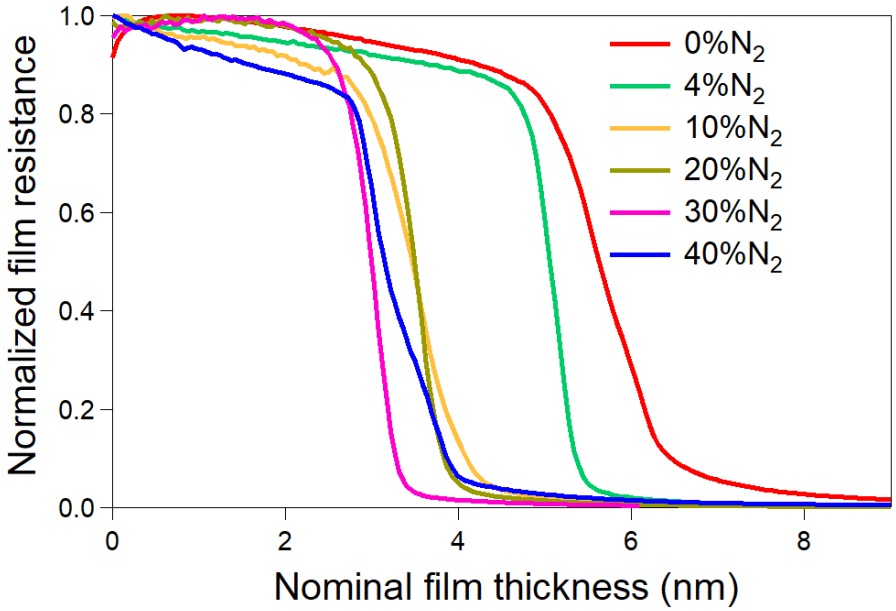

Figure 3.1 Evolution of film sheet resistance $R_\square$ during Ag deposition on SiO_x/Si substrates as a function of %N_2 in the gas flow. Data are normalized to the initial value before opening the shutter in front the target. The drop in $R_\square$ corresponds to the formation of a percolated and conductive film.

The value of t_p even reaches a minimum of 2.7 nm at 30%N_2 (Figure 3.2-a). Such an early percolation is in agreement with previous observations both for N_2 gas addition [110, 111, 130, 242]. This decrease in t_p occurs in parallel to a 26% increase in the continuous film resistivity ρ at t = 20 nm, from 6.7 to 8.5 $\mu\Omega$.cm (Figure 3.2-b). Since the films are already continuous by this stage, the increase in resistivity must be explained by changes in the film microstructure or chemistry.

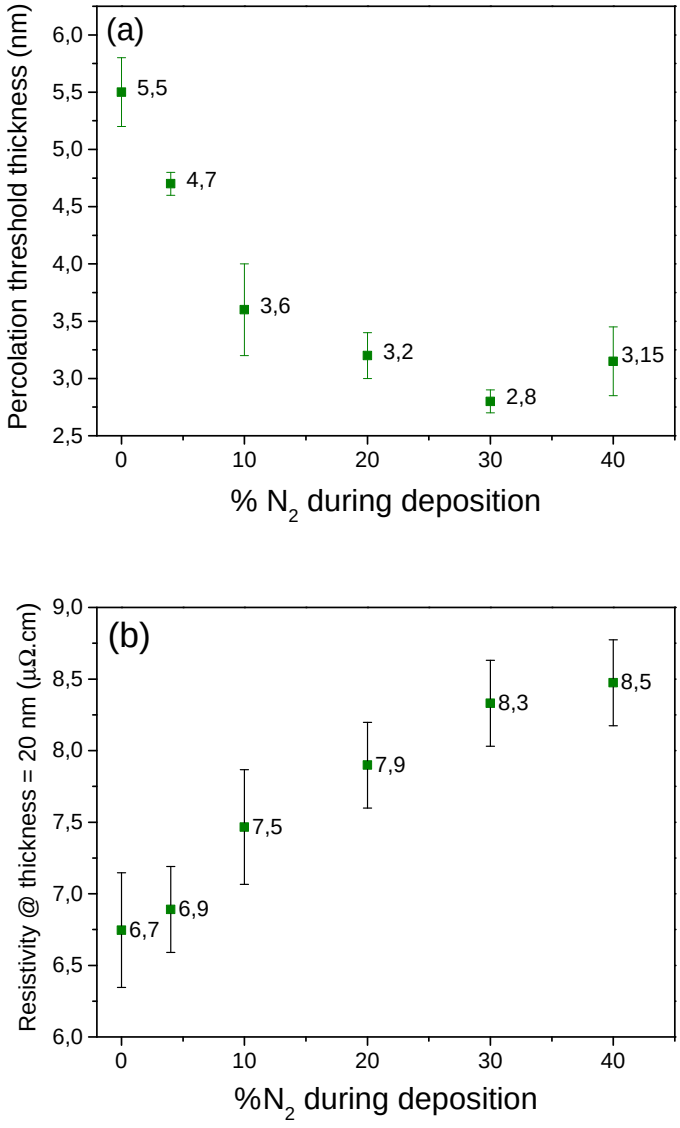

Figure 3.2 (a) Percolation threshold thickness t_p and (b) film resistivity $\rho(t = 20\,\text{nm})$ for different $\%N_2$ during deposition. Values correspond to an average over several experiments and the error bars to the corresponding standard deviations.

3.2.2 SDRS measurements

In parallel to film resistivity measurements, Ag deposition was followed using real-time SDRS to characterize Ag nanoparticles during the initial stages of film growth. Figure 3.3 shows the integrated signal $\mathcal{A}_s(t)$ in s-polarization for deposition under different Ar:N_2 mixtures.

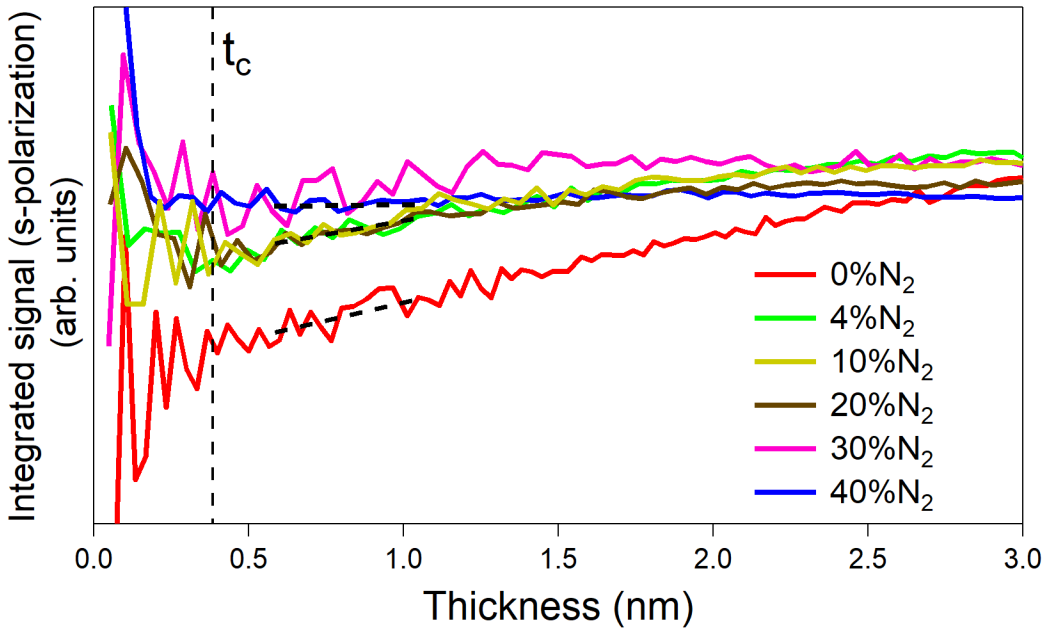

Figure 3.3 Integrated signal $\mathcal{A}_s(t)$ of s-polarized SDRS spectra as a function of deposited thickness. The vertical line shows the approximate threshold for coalescence onset t_c while the dotted lines is a guide to the eye showing the difference in slope in $\mathcal{A}_s(t)$ evolution.

For all $\%N_2 > 0$ conditions, the value of $\mathcal{A}_s(t)$ is higher than under pure Ar ($0\%N_2$). This quantity being a reliable reporter of the evolution of aspect ratio A_r [200], this finding indicates more flattened particles when N_2 is used. Despite noise in the data due to the division of two small quantities (see Equation 2.2 in Chapter 2), this observation holds in the regime of isolated islands, before the onset of coalescence t_c that corresponds to the increase of the integrated signal. Interestingly, with increasing $\%N_2$, $\mathcal{A}_s(t)$ reaches the constant plateau value much faster. This plateau finds its origin in the limited integration range of the red-shifted plasmon resonance [200] (see Figure 3.4).

Figure 3.4 shows the corresponding measurements in p-polarization at three equivalent nominal thicknesses: 0.6 nm, 1 nm, and 2 nm. According to Figures 3.1 and 3.3, such values roughly match the end of the isolated particles growth regime (0.6 nm), and more advanced particle coalescence (1 nm and 2 nm). As a reminder from Chapter 2, the observed spectra are characteristic of the excitation of plasmon resonances in nanoparticles with (i) a negative dip at high photon energy associated to the dipole perpendicular to the surface and (ii) a positive feature at low-energy associated to the dipole parallel to the surface. The latter being more sensitive to any evolution of morphology, in particular particle density, aspect ratio and formation of a core-shell structure, the discussion will mainly focus on this low-energy peak.

Analysing the trends for the p-polarised spectra, for very thin Ag films (0.6 and 1 nm; Figures 3.4-

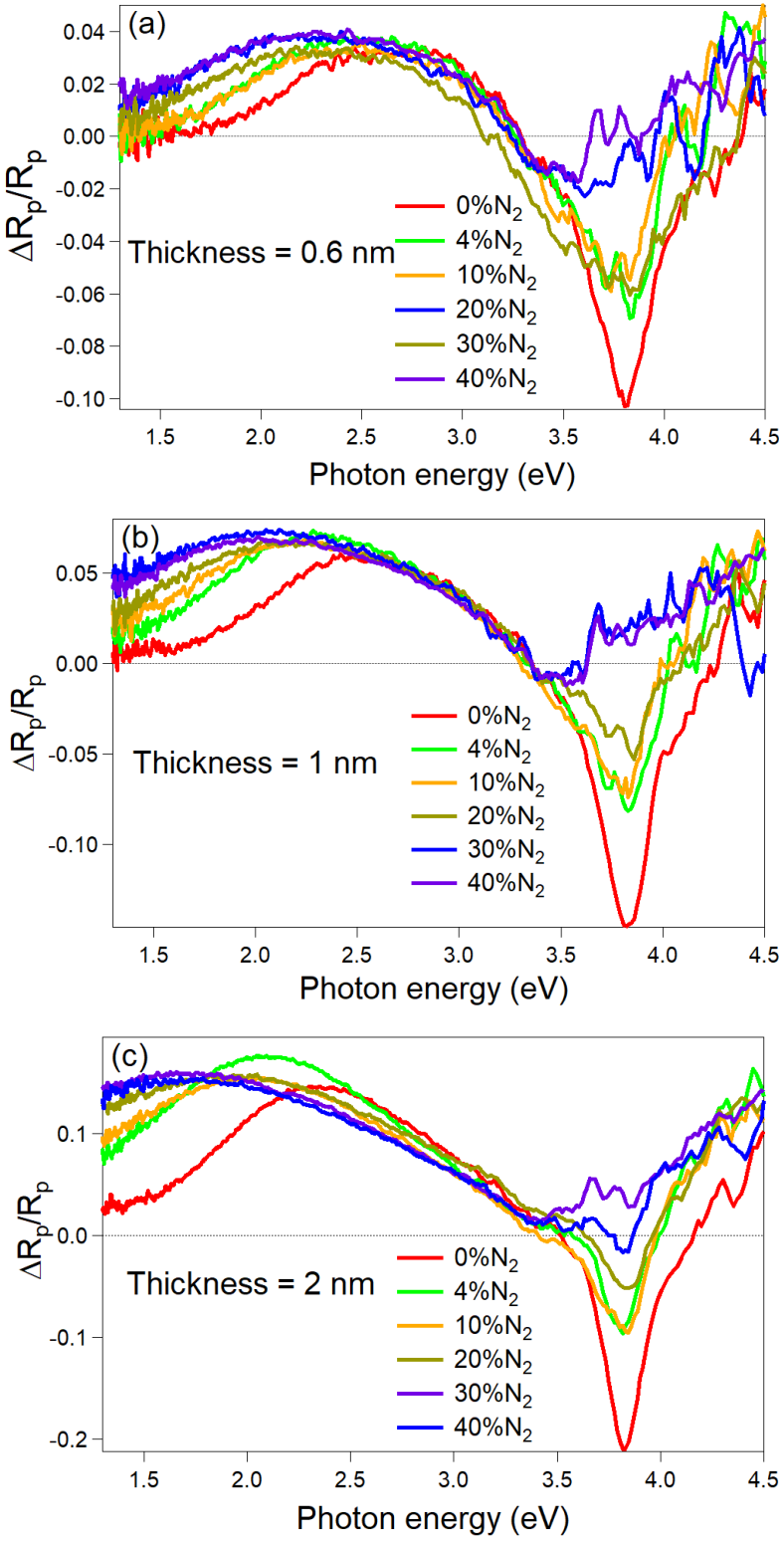

Figure 3.4 SDRS spectra in p-polarization for different $\%N_2$ during deposition, corresponding to a nominal deposited thickness of (a) 0.6 nm, (b) 1 nm and (c) 2 nm.

a,b) the addition of N_2 leads to a red-shift, an intensity increase, and a broadening of the low-energy resonance peak. The change is nearly already set up at $4\%N_2$ and poorly evolves above this value. Particle flattening can explain this shift in the SDRS spectra (as shown in the *GranFilm* simulations in Chapter 2) and, in turn, the decrease in film percolation threshold thickness t_p in Figure 3.2-a, since flattened particles with a more pronounced 2D shape would impinge on each other and form a conductive percolated network faster than more rounded, 3D ones. Reduced metal surface energy due to atomic N adsorption as predicted by first principles calculations [130] could be the driving force for such a better wetting of nanoparticles at the growth stage before coalescence (see Figure 1.17 in Chapter 1).
The analysis differs somewhat at a thickness of 2 nm (Figure 3.4-c). In this case the addition of $4\%N_2$ red-shifts and enhances the low-energy resonance, while a further increase of $\%N_2$ keeps on shifting the peak but at the expense of its intensity and in a way nearly independent of $\%N_2$ for values greater than 10%. According to the *GranFilm* simulations in Chapter 2, this trend could be explained by the formation of a core-shell structure consisting of a metallic Ag core and a dielectric shell. This latter may very well be the result of atomic N adsorption on the surface of Ag nanoparticles. Also, it would explain why the peak does not shift further for higher $\%N_2$ values, since the effect will be limited to N adsorption on the exposed Ag surface. To illustrate this effect, Figure 3.5 shows the simulated trends for p-polarized spectra expected for the formation of a dielectric shell on the surface of metallic Ag nanoparticles, both at the expense of the total mass of Ag in the nanoparticle (Figure 3.5-a) and at constant total mass of Ag (Figure 3.5-b).
Looking at the simulated spectra in Figure 3.5, we notice that while the formation of a shell generates a red-shift of the low-energy parallel plasmon resonance in both cases, no decrease in intensity is observed at constant Ag core size with increasing shell thickness t_s. The decrease in peak intensity is therefore related to the decrease in the Ag mass. Moreover, the effect is quite pronounced even for minute changes in shell thickness [227] in the range of a few percent of nanoparticle radius, a change that would correspond to an atomic thickness for nano-sized particles. Thus, in principle, plasmonics is not only sensitive to an actual change in chemistry - as will be shown latter for O_2 (Chapter 4) - but also to the presence of adsorbates in the monolayer range.

3.3 *In situ* photoemission analysis (XPS)

3.3.1 Photoemission analysis of 20 nm-thick Ag films

The potential chemical interaction between Ag and N was explored by XPS. Figure 3.6 shows the Ag 3d, N 1s, O 1s and C 1s core-level regions [243] measured *in situ* on 20 nm-thick Ag films, grown under different $\%N_2$ conditions. Unlike previous reports in the literature where a capping layer was present [41,111,130], the use of *in situ* XPS gives direct access to the chemistry of the free surface and avoids potential desorption of species induced when depositing a capping layer. For all $\%N_2$, the Ag 3d spectra (Figure 3.6-a) perfectly overlap, with no change in peak position or line shape that would otherwise indicate an evolution in the chemical state of the metal. In parallel, no peak is visible in the N 1s core level range (Figure 3.6-b), ruling out the presence of N in the film within the sensitivity of photoemission. It is worth noting that the plasmon multiple-loss satellite of the Ag 3d core level peak at $E_B \simeq 398-400$ eV should not be misinterpreted as the signature of residual traces of trapped N as done in Reference 41. No significant O 1s signal that could be due to gas impurities is visible (Figure 3.6-c) and only adventitious carbon contamination at $E_B = 284.5$ eV (Figure 3.6-d) is present, ruling out the formation of

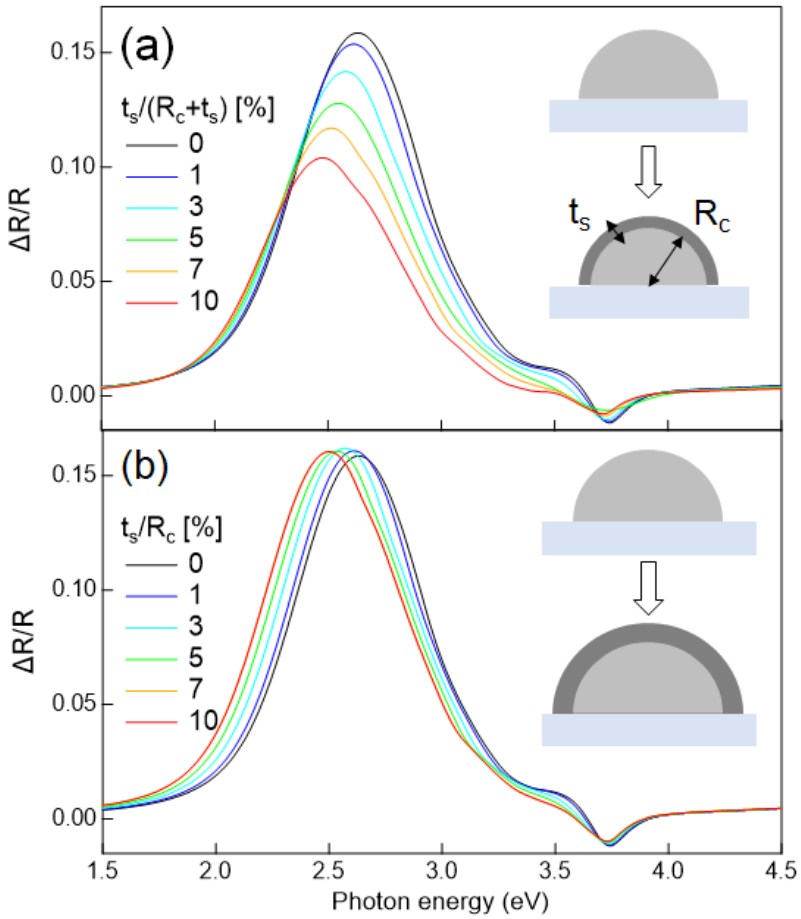

Figure 3.5 Simulated p-polarized SDRS spectra for core-shell hemispheres arranged on a square lattice on SiO_2/Si. Evolution upon varying the shell thickness t_s at (a) the expense of the core size R_c and (b) at constant core size. The dielectric function of metallic bulk Ag was used for the core while the index of refraction of the shell was fixed arbitrarily at 2. The parallel plasmon is broadened *ad hoc* by 0.3 eV [229, 230] and the particles are electrostatically coupled at quadrupolar order. The film thickness amounts to about 1.6 nm as in the ageing experiments of Figure 3.8.

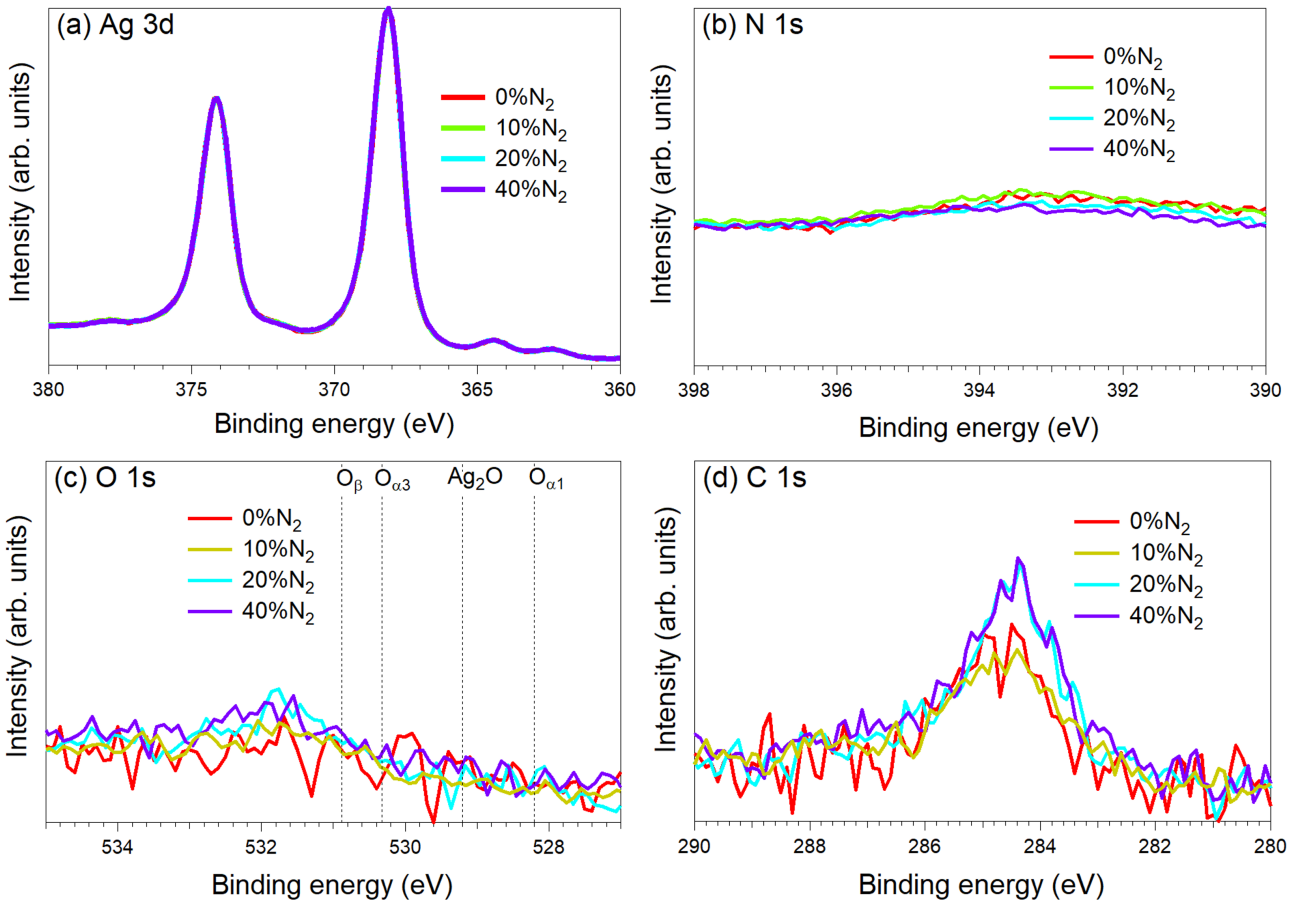

Figure 3.6 XPS spectra of 20 nm-thick Ag films after growth under different $\%N_2$ conditions. Core-level regions: (a) Ag 3d, (b) N 1s, (c) O 1s, (d) C 1s. The slight bump in Figure b corresponds to a plasmon satellite of the Ag 3d core-level. In Figure c, reported peak positions for Ag-O moieties are shown for reference.

any spurious compound at the film surface. Lastly, photoemission (not shown) does not evidence any trace of N at the surface of a pure 20 nm-thick Ag film (deposited under pure Ar) and exposed to a 40%N_2 plasma ignited on a nearby alumina target during 90 s (*i.e.* more than two times the growth duration); this rules out any role of the film growth process itself in the observed lack of N. All these findings indicate that the addition of N_2 during Ag sputter deposition does not lead to any detectable change in film surface chemistry. This observation confirms the conclusions from previous works on Ag deposition under similar conditions, which reported a lack of chemical reactivity of Ag towards N [41, 111, 130]. This is also in agreement with the lack of stable bulk silver nitride compounds [244] and the energetically unfavourable dissolution of N in the Ag subsurface predicted by first principle atomistic simulations [130].

In the absence of chemistry, other microstructural factors should be put forward to account for the worsening of film resistivity observed with N_2 as compared to pure Ar (Figure 3.2-b). We will come back to this point later in the chapter. Up to now, only the surface chemistry of relatively thick and continuous Ag films ($t = 20$ nm) has been explored. At this point, we could wonder whether N_2 in the plasma could modify the surface chemistry of the SiO_x substrates during the initial stages of film growth, and in turn impact the resulting Ag film.

3.3.2 Effect of N_2 plasma treatment on the SiO_x substrate

Having a value of only a few nanometres at the studied photoelectron kinetic energies [240], the probing depth of photoemission does not allow us to explore the film/substrate interface in the case of the previous 20 nm-thick Ag films. To explore the chemical impact of the N_2-rich plasma on the wafer surface itself before Ag film percolation, the SiO_x substrate surface was exposed during 3 s to a plasma ignited in front of an alumina target. Such a short duration of exposure to the plasma corresponds to an equivalent Ag deposited thickness of ~ 1.5 nm during growth, well below the percolation threshold.

The substrate was analysed by XPS before and after this treatment. Figure 3.7 summarizes the evolution before and after plasma treatment, with pure Ar (0%N_2) and 40%N_2 in the deposition chamber. As seen in the shifts of the Si 2p (Figure 3.7-a) or O 1s (not shown) core-levels, both gases induce an upward band bending of about 0.4 eV. At the same time, plasma exposure reduces the adventitious C 1s peak intensity (Figure 3.7-b). A new signal is observed in the N 1s core-level region (Figure 3.7-c) after treatment with 40%N_2. It parallels a broadening on the low-binding energy side of the SiO_x component in Si 2p; this is characteristic of silicon nitride [243]. Quantification (see Chapter 2 for methodology) shows that both uptakes amount to about a monolayer, *i.e.* an equivalent thickness of 0.2 nm. This nitridation of the wafer, beyond the band bending observed also with pure Ar that seems characteristic of C removal, demonstrates that activated N species are actually present in the plasma and that they strongly interact with the substrate surface during the time scale of film growth. This finding explains the observations in previous works of an N signal at the substrate interface by secondary ion mass spectroscopy that escaped the sensitivity of depth-profiling *ex situ* photoemission [111, 130].

Despite the presence of activated N species in the plasma, the lack of a N 1s fingerprint on the Ag film surface contradicts a number of surface science experiments [131] and atomistic calculations [121–123, 130, 245] on the interaction of atomic N with Ag(111) and Ag(100) orientations. These studies all agree on a favourable N adsorption, which is not observed in our case. However, a quite low recombinative desorption temperature of 350 K was found on Ag(111) [131], suggesting that a poorly stable N adsorbate could be present only dynamically at the surface of

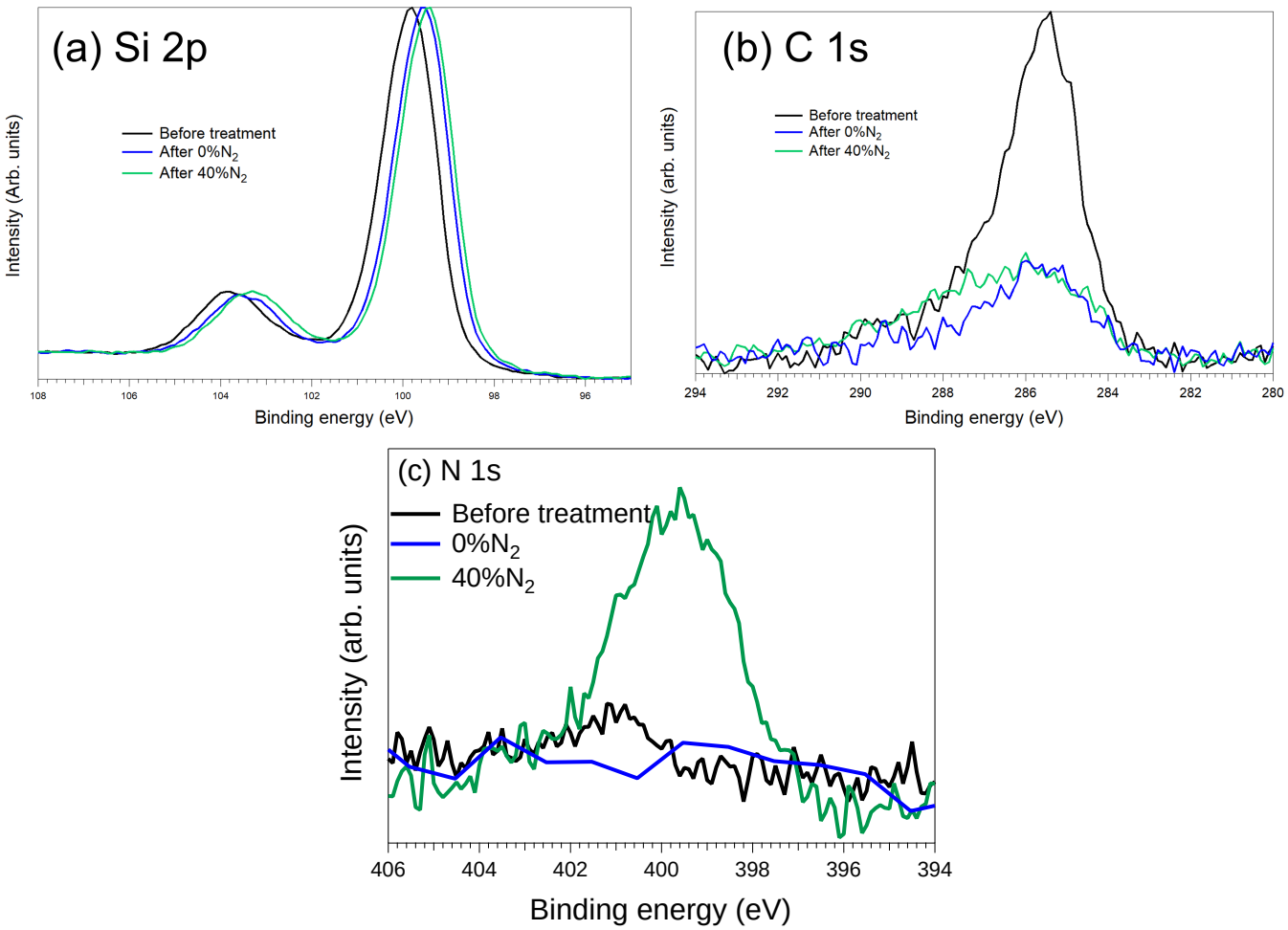

Figure 3.7 Evolution of Si wafer core levels after a 3 s plasma treatment ignited on an alumina target for the indicated gas composition: (a) Si 2p, (b) C 1s,(c) N 1s.

Ag in the present experiments and quickly desorb as N_2 after deposition. This hypothesis is in line with a surprisingly efficient Eley-Rideal mechanism of recombinative desorption upon direct impact of N on N-Ag(111) [124, 132]. Finally, x-ray or electron induced decomposition during photoemission acquisition - a unmonochromated source is used in our case - as observed for gold nitride [246] cannot be completely ruled out despite the short time scale of the measurement. Beyond this potential spurious effect, the lack of any N 1s core level fingerprint in thick Ag films makes the core-shell optical scenario invoked to explain a better wetting unlikely unless adsorbed N at the Ag surface is unstable once the growth is stopped. Still, the nitridation of the wafer surface demonstrates the presence of activated N species in the plasma, in the form of atoms or ions that can react with the film or be implanted in it. To investigate these apparently conflicting results, post-deposition ageing of Ag films was investigated by SDRS.

3.4 Post-deposition evolution of Ag nanoparticles by SDRS

Figure 3.8 shows the evolution of SDRS spectra in p-polarization over a time scale of an hour under vacuum after gas evacuation ($p \sim 5.10^{-7}$ mbar). The evolution of 1.6 nm-thick Ag films deposited under pure Ar and under 20%N_2 conditions are compared. Spectra were corrected from the drift of the light source using an ancillary spectrometer [199]. The noticeable evolution of the SDRS signal highlights the post-deposition film instability that is often overlooked. In addition to this, Figure 3.9 shows the evolution of the integrated SDRS signal in s-polarization, for the same films and conditions as in Figure 3.8.

For the film grown under pure Ar, both peaks in the p-polarized spectra get closer in energy and poorly evolve in intensity. These trends are characteristic of a slight dewetting of nanoparticles, *i.e.* a decrease of A_r towards more rounded objects, although the slight intensity increase of the low energy resonance (Figure 3.8-a) does not match fully theoretical expectations (see *GranFilm* simulations in Chapter 2). Argon adsorption is obviously ruled out and an evolution of particle density by Ostwald ripening is unlikely owing to the short time scale of most of the change (roughly 1 min from Figure 3.8-a). In contrast, the evolution differs at 20%N_2. Both peaks in the p-polarization SDRS spectra increase in intensity and come closer in energy with time, but with a slower evolution after the end of film deposition compared to 0%N_2 (Figure 3.8-b). According to qualitative dielectric simulations using *GranFilm*, such a finding can only be assigned to the desorption of N species from the surface of the nanoparticles. Indeed, dewetting cannot account, by any means, for the observed increase in intensity for both resonances, although its presence cannot be fully ruled out either. This conclusion is further reinforced by the increase of $\mathcal{A}_s(t)$ with time (Figure 3.9) for the sample deposited under 20%N_2, since pure dewetting would decrease the particle aspect ratio (and thus the value of $\mathcal{A}_s$). Moreover, according to Figure 3.9, the phenomenon occurs over a time scale of 15 mins. This time is longer than what is required to transfer and analyse the sample by photoemission, potentially explaining the lack of traces of N on the film surface after deposition. Finally, as shown by comparing the simulated evolution of SDRS spectra caused by shell growth at the expense of the metallic core and at constant core thickness (Figure 3.5-a and b, respectively), the change of SDRS intensity upon N adsorption/desorption implies a charge transfer between Ag and N, or in other words, a loss of metallic character of Ag.

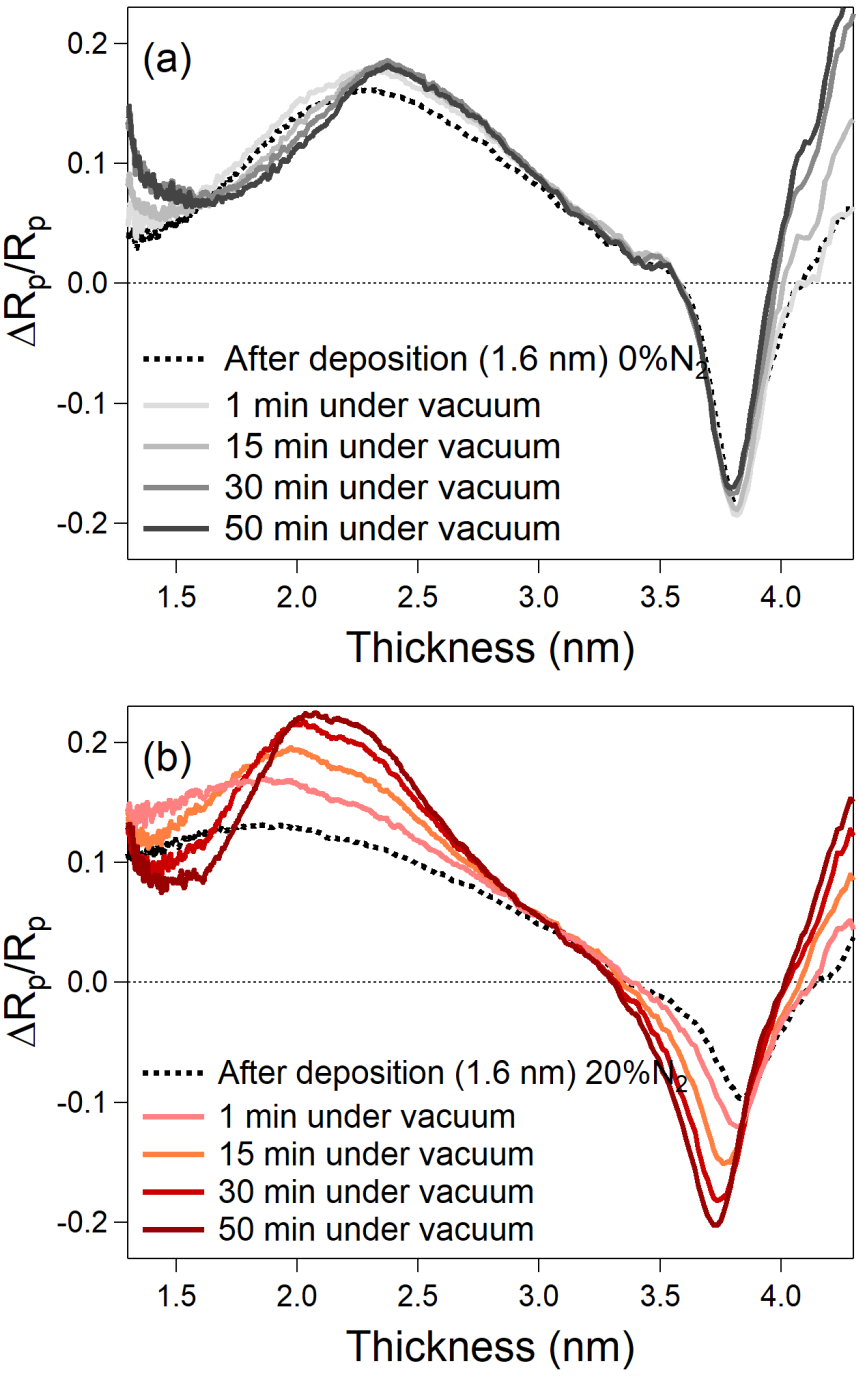

Figure 3.8 Post-deposition evolution under vacuum of p-polarized SDRS spectra for 1.6 nm-thick Ag films deposited under (a) 0%N_2 and (b) 20%N_2. Duration after the end of the growth is indicated in the figure.

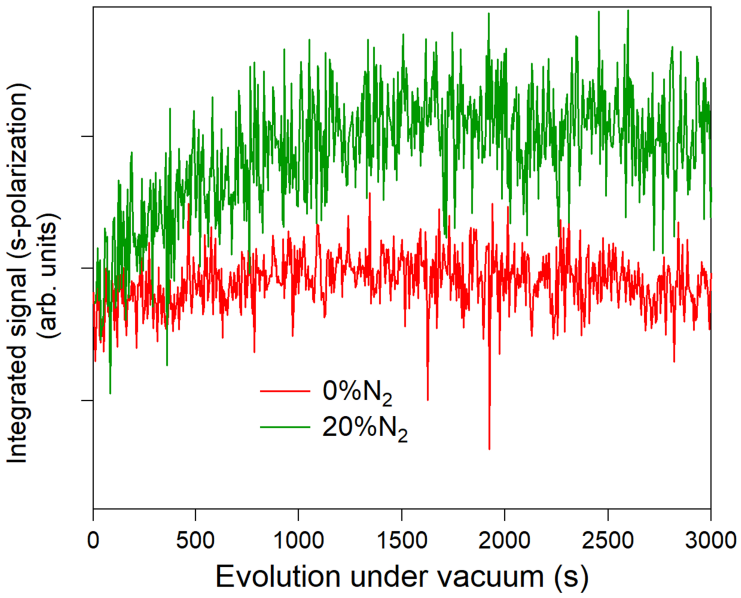

Figure 3.9 Post-deposition evolution of the integrated SDRS signal in s-polarization for 1.6 nm-thick Ag films deposited under 0% and 20%N_2.

3.5 *Ex situ* measurements

3.5.1 Ag nanoparticle STEM-HAADF imaging and particle density

Photoemission experiments revealed that exposure of the SiO_x substrate to a N_2-rich plasma modifies its surface chemistry, with a decrease in carbon impurities and an uptake in N in the form of Si-N bonds. *Ex situ* STEM-HAADF imaging was therefore used to further investigate the effect of this nitrogenated plasma on the initial stages of film growth on a 0.6 nm-thick Ag film capped with AZO (Figure 3.10). Based on the evolution of the integrated SDRS signal $\mathcal{A}_s(t)$ (see Figure 3.9) and on the percolation thresholds (Figure 3.2-a), at such a nominal thickness all films are still in the initial stages of growth of isolated nanoparticles before the beginning of coalescence, which corresponds to the rise of $\mathcal{A}_s(t)$ [200].

At first sight, no clear-cut change in morphology shows up with increasing %N_2, in contrast with previous reports that focused more on late coalescence [41, 130]. Image analysis using the BlobLog and Watershed algorithms revealed a $\sim$ 30% increase in particle density from $4.4\,10^{12}$ cm^{-2} for 0%N_2 to $5.7\,10^{12}$ cm^{-2} for 40%N_2 (Figure 3.11). Further interpretation of TEM imaging, particularly the evolution of aspect ratio from average size and mean thickness, was not pursued as it may be hindered by encapsulation and uncertainties on film thickness, unlike particle density measurements.

3.5.2 Film structure from *ex situ* x-ray diffraction

XRD structural analysis was performed on 20 nm-thick Ag films deposited under different %N_2 conditions on bulk fused silica wafers. For all %N_2, XRD diffractograms in both the Bragg-Brentano (out-of-plane) and GIXRD (in-plane) configuration (Figure 3.12-a and b, respectively) only show peaks corresponding to metallic face-centred cubic Ag, wurtzite ZnO from the capping layer, and a large feature around $2\theta = 22°$ assigned to the amorphous silica substrate.

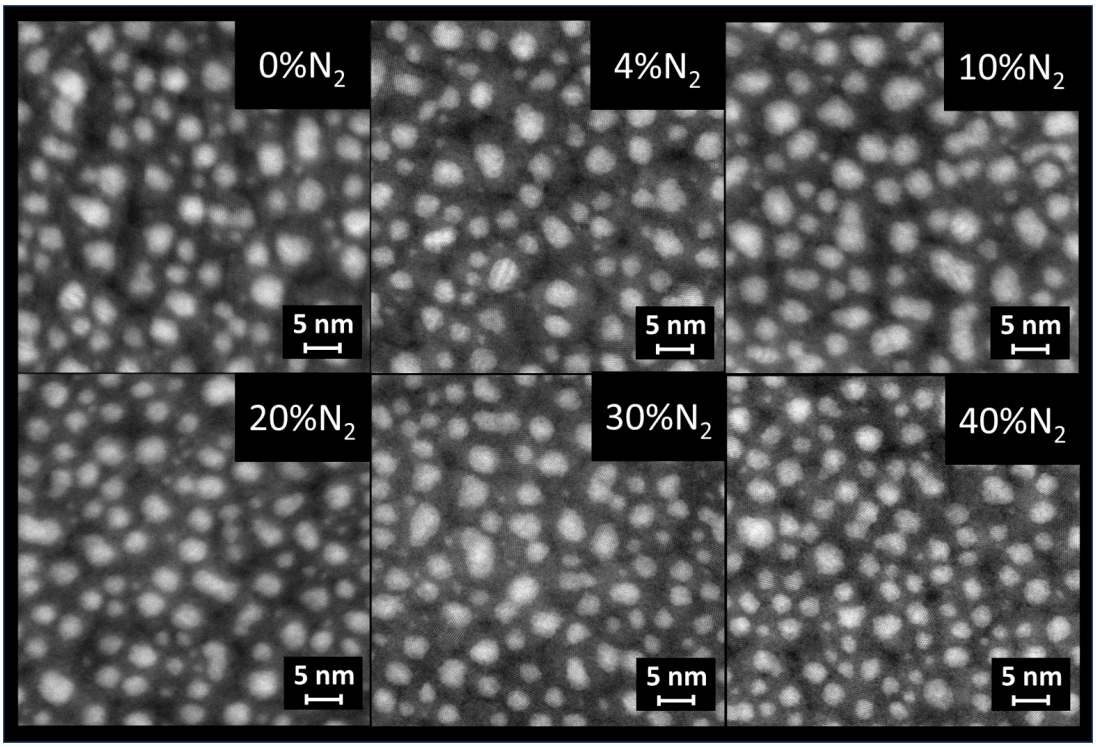

Figure 3.10 STEM-HAADF imaging of 0.6 nm-thick Ag films deposited on amorphous, surface-oxidized silicon nitride (SiN_x) membranes at increasing $\%N_2$. The scale bar corresponds to 5 nm.

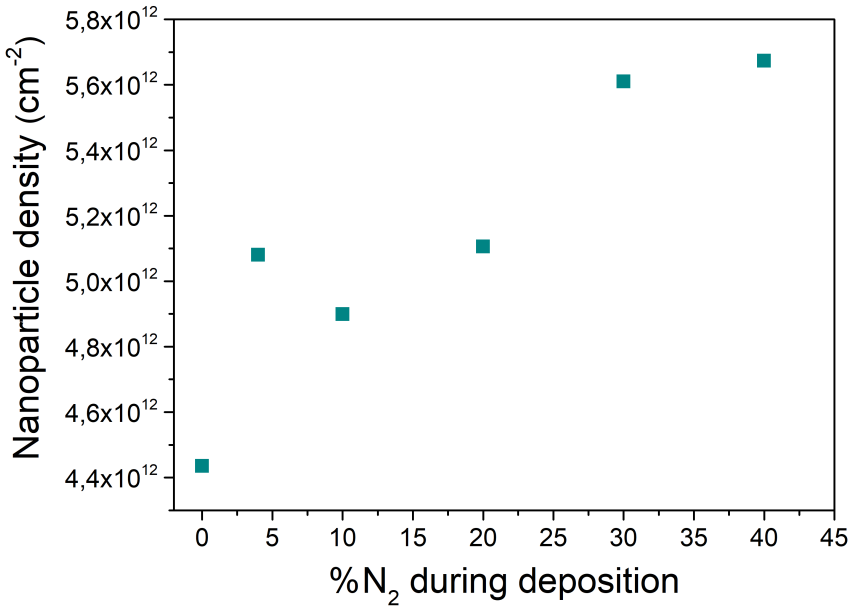

Figure 3.11 Evolution of the nanoparticle density with the fraction of N_2 in the gas flow. Values are deduced from TEM image analysis at the same equivalent thickness (0.6 nm).

Despite the out-of-equilibrium conditions of sputtering deposition, no silver nitride formation is observed [130, 244].

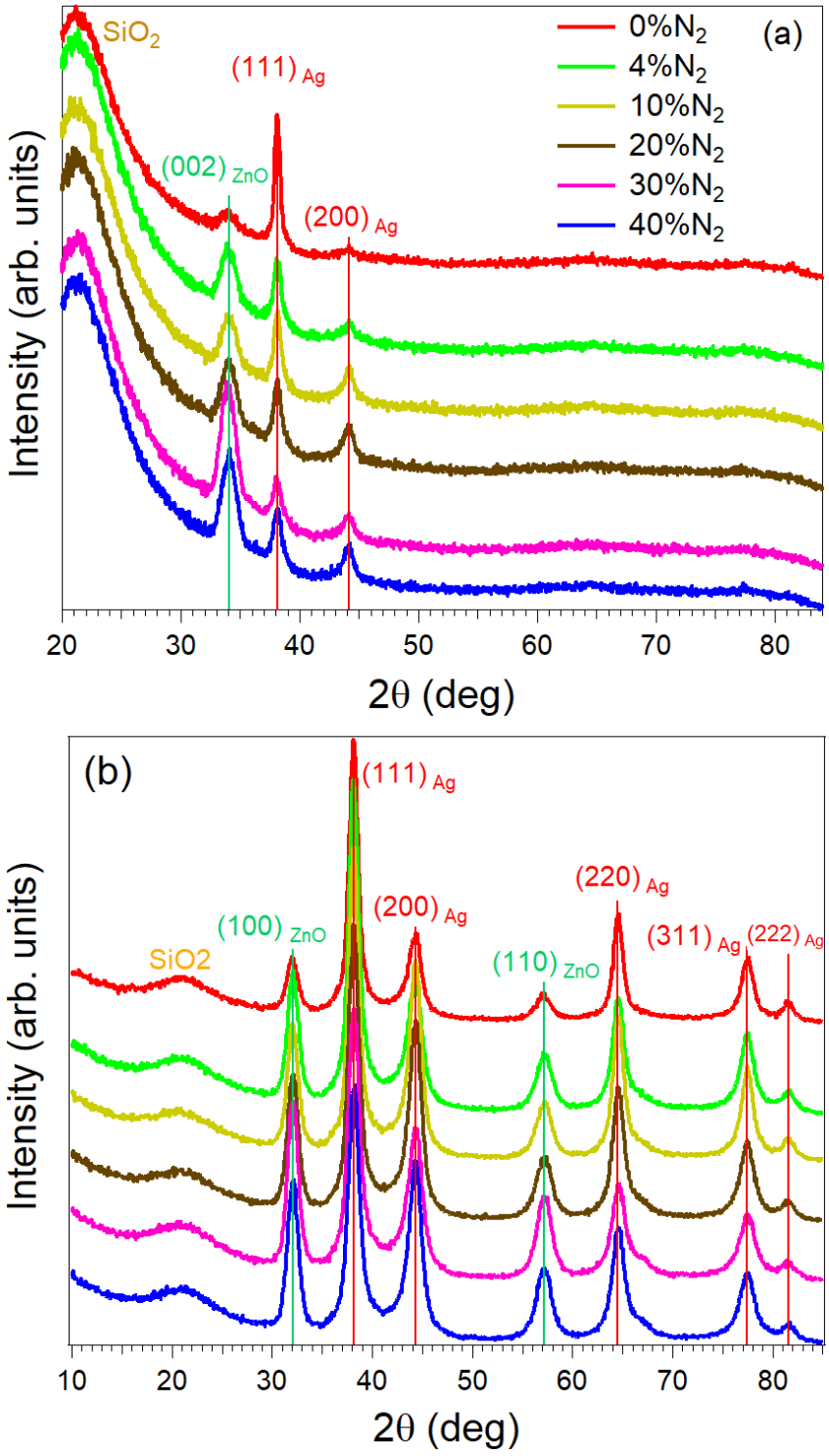

Figure 3.12 XRD diffractograms in (a) Bragg-Brentano and (b) GIXRD geometry of 20 nm-thick Ag films deposited under different $\%N_2$. Vertical bars indicated the expected bulk positions of the diffraction peaks.

As seen in Figure 3.12-a, the Ag films appear to be only (111)-(100) textured along the growth direction (out-of-plane). Starting from the classical favoured (111) stacking under pure Ar characterized by an intense (111) peak and a weak (200) reflection, the texture evolves with increasing $\%N_2$ towards more [100]-oriented grains. This also reflects in the relative evolution of (220) and (200) peaks in the grazing-incidence (in-plane) scans (Figure 3.12-b). In parallel, as expected for an amorphous substrate, the film is not textured in-plane since all Ag allowed reflections are present. To rationalize this, fitting all peaks with Voigt profiles gave the corresponding Debye-Scherrer sizes from peak full-width at half-maximum (Figure 3.13-a) and the relative crystallite volume from peak areas (Figure 3.13-b) after correction from the relative intensities for a powder [247] (*i.e.* from structure factors, reflection multiplicity, Lorentz-polarization factor and beam footprint).

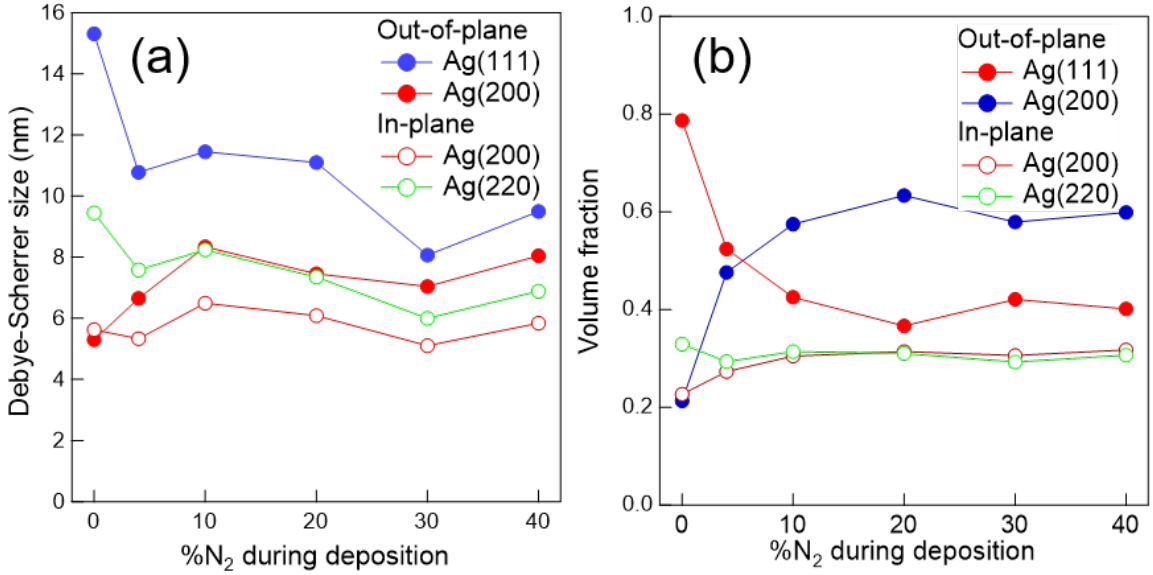

Figure 3.13 (a) Debye-Scherrer sizes $D = \frac{0.9\lambda}{\cos(2\theta)\Delta(2\theta)}$ from peak full-width at half-maximum $\Delta(2\theta)$ in the out-of-plane (Bragg-Brentano) and in-plane (GIXRD) configurations. (b) Film texture or volume fraction from ratio of the areas of all visible peaks after correction from intensities expected from a powder sample [247].

The out-of-plane Debye-Scherrer size (D_{coh}) of [111]-oriented-crystallites decreases at the expense of [100] ones. But both are much smaller than the film thickness when N_2 is used showing a deterioration of film crystallinity. Meanwhile corresponding in-plane sizes of those domains (derived from the widths of (220) and (200) Bragg peaks, whose normals to the corresponding diffracting planes are perpendicular to the [111] and [100] directions) poorly evolve with $\%N_2$ (Figure 3.13-a). In passing, their similar broadening partly supports the underlying assumption of correct Bragg spot integration behind the out-of-plane texture analysis through only the Bragg-Brentano scan. In parallel to this size evolution, the film texture changes from a dominant (111) out-of-plane orientation under pure Ar to a 40/60 % (111)/(100) mix for $40\%N_2$ with a minor impact in-plane (Figure 3.13-a). As grain boundaries between (111) and (100) crystallites lead to a strong structural mismatch in the vertical direction, this explains the worsening of the final film resistivity with $\%N_2$ despite an earlier percolation (Figure 3.2-b). To circumvent the issue, a solution is to deploy the N_2 gas in the initial stage of film growth as done in Reference [111].

Initially suggested by Kawamura *et al.* [116] to achieve films with the unusual (100) Ag orientation on an amorphous glass substrate by sputtering deposition, this surprising effect of N_2 on continuous film texture was also reported on SiO_x upon increasing (i) N_2 content in the gas flow in References 107, 242 or (ii) the film thickness at constant $\%N_2$ in Reference 130; in Reference 111, only a loss of out-of-plane (111) texture was observed as the (200) peak is hardly visible. Assuming the presence of adsorbed N at the surface of Ag, this change in texture with $\%N_2$ matches the calculated reversal of surface energies between N-covered (111) and (100) Ag surfaces with N surface concentration [130] (see Figure 1.17 in Chapter 1). Higher N_2 flow favours an enhanced N_2 dissociation and higher dynamical coverage, and in turn a larger fraction of (100) facets. Similarly, when N_2 is present, Yun *et al.* [130] observed an initial increase of the proportion of (111)/(100) oriented crystallites before a decay after the onset of percolation. This might be explained by a kinetic competition between (i) the metal-metal aggregation by diffusion that favours a (111) stacking for a face-centred cubic metal, (ii) the substrate decarbonation and nitridation and (iii) the starting of N adsorption on Ag(111) surfaces as theoretically expected from an energetic point of view at low coverage [130].

3.6 Discussion on the N_2 surfactant effect

The addition of N_2, even in small quantities, in the Ar plasma provokes an outstanding decrease in percolation threshold thickness (51%) but at the expense of final film resistivity (Figures 3.2 -a and b).

Looking at the chemical state of the deposited films, N is not detected on the surface of as-grown Ag films by *in situ* photoemission experiments. N_2 adsorption being excluded owing to its filled orbital structure and its large triple-bond energy, only species activated by the plasma can be at the origin of the phenomenon, most probably atomic N. Indeed, other activated species such as N_2 ions would temporally implant on the Ag film surface and once neutralized, the resulting molecule would immediately desorb. The hypothesis of atomic N adsorbates is supported by *ab initio* atomistic calculations that all predict (i) an energetically stable N adsorbate at the Ag surfaces with a adsorption energy above 2 eV/atom [121–123, 130, 245] and (ii) an energetically unfavourable dissolution in the bulk [130] in line with the strong positive enthalpy of formation of Ag nitride (314 $kJ.mol^{-1}$ or 3.25 eV/atom [244]). While the nitridation of the substrate bears witness to the presence of such activated N species, the lack of any trace of N 1s signal on thick Ag films can be explained by a fast recombinative desorption at room temperature. This picture is supported by the large post-deposition evolution of SDRS plasmonic signal (Figure 3.8) suggesting the disappearance of a shell on top of a metallic core. In addition, experiments by Carter *et al.* [131] on N/Ag(111) showed that the recombinative desorption process, that already starts around 350 K, is not of second order and therefore not limited by the surface diffusion of adsorbed N, but rather by the concerted lifting of induced surface reconstruction and N_2 molecule desorption. Thus, the dynamic N coverage that is present during growth is limited first of all by the amount of dissociation of N_2 in the plasma (*i.e.* the $\%N_2$ value), and by the surprisingly efficient reported recombinative desorption of N upon direct impact of another N atom [124, 132] (*i.e.* an Eley-Rideal mechanism).

To rationalize the 51 % decrease in percolation threshold thickness when adding N_2 (Figure 3.2-a), changes in particle saturation density ρ_s and aspect ratio A_r can be put forward. In parallel to a delayed coalescence upon impingement, denser or flatter initial particles all give rise to an earlier percolation. Assuming a scaling $t_p \propto t_c$ between the electrical percolation threshold t_p and

the thickness for the onset of coalescence between nanoparticles t_c, one finds: $t_p \propto t_c \propto D_c^3 \rho_s / A_r$, where D_c the in-plane size of particles at coalescence start. Since particles are in contact with each other at coalescence, $D_c \propto \rho_s^{1/2}$ so that $t_p \propto 1/(\rho_s^{1/2} A_r)$. Thus one can estimate the expected variation of t_p from the variation of A_r and ρ_s:

$$\frac{\Delta t_p}{t_p} = -\frac{\Delta A_r}{A_r} - \frac{1}{2}\frac{\Delta \rho_s}{\rho_s}. \tag{3.1}$$

The change in density of $\frac{\Delta \rho_s}{\rho_s} = +28$ % from 0 to 40 %N_2 found by TEM (Figure 3.11) accounts only for roughly one third of the observed evolution of t_p. Assuming equilibrium before coalescence, particle shape can be tackled by thermodynamics of surface/interface energies. Young-Dupré's equation for a truncated sphere (Chapter 1) allows linking the variation of A_r to that of the contact angle θ_c, of the adhesion energy $W_a = \gamma_s - \gamma_{fs} + \gamma_f$, and of the metallic film surface energy γ_f through:

$$\begin{aligned} W_{adh} &= \gamma_f(1+\cos(\theta_c) \\ \frac{\Delta A_r}{A_r} &= -\frac{\sin\theta_c \Delta\theta_c}{1-\cos\theta_c} \qquad (3.2) \\ \frac{\Delta W_a}{W_a} - \frac{\Delta \gamma_f}{\gamma_f} &= -\frac{\sin\theta_c \Delta\theta_c}{1+\cos\theta_c}. \qquad (3.3) \end{aligned}$$

Of course, forgetting cristallographic anisotropy of Ag surface energies by assuming a truncated sphere equilibrium shape [248] is a first approach of the problem that nevertheless grasps the present physics. This anisotropy between (111) and (100) orientations is modest on bare surfaces ($\frac{\gamma_{(100)}-\gamma_{(111)}}{\gamma_{(111)}} \simeq +3$ %) but strongly enlarges upon N adsorption ($\frac{\gamma_{(100)}-\gamma_{(111)}}{\gamma_{(111)}} \simeq -50$ %) [45,130]. Starting from an equilibrium contact angle of $\theta_c \simeq 130°$ for Ag/SiO_2 [200,249] and assuming that adhesion energy is not modified by the interaction of N with the substrate, the calculated drastic decrease of surface energy [130] of $\frac{\Delta \gamma_f}{\gamma_f} \simeq -75$ % for both (111) and (100) orientations with N coverage (see Figure 1.17 in Chapter 1) would lead to a modest $\Delta\theta_c = -20°$ (Equation 3.3) and $\frac{\Delta A_r}{A_r} = +16$ % (Equation 3.2). So $-\frac{\Delta A_r}{A_r} - \frac{1}{2}\frac{\Delta \rho_s}{\rho_s} = -30$ % accounts only for a fraction of the observed $\frac{\Delta t_p}{t_p} = -51$ % (Equation 3.1). Beyond kinetic hindering of reshaping that could be already present during the growth of isolated nanoaparticles, a delayed coalescence should be invoked to explain the remaining part of the change in t_p. Evidence of this could be found in the much faster increase of $\mathcal{A}_s(t)$ towards a plateau value in the coalescence regime (Figure 3.3). Beside the modification of surface Ag diffusion by a N adsorbate, a likely explanation can be found in the competition between the growth of [111] and [100]-oriented islands as testified by the change in film texture (Figure 3.13-b) and the increase in surface energy anisotropy with N adsorption [130]. Their coalescence is structurally impeded.

Finally, the observed change in texture from (111) to (100) as a function of %N_2 (Figure 3.13-b) or as a function of film thickness [107,130,242] finds its origins in the crossover between (111) and (100) surface energies with N coverage [130] (see Figure 1.17 in Chapter 1). The anisotropy goes from a small value of a few % in favour of (111) orientation (that agrees with the experimental microscopy observation of the Wulff-Kaischew equilibrium shape [45]) to around 50 % in favour of (100) orientation. During the initial stages of film growth (nanoparticles), several factors combine to yield an initial growth of [111] oriented islands on SiO_x [130]: (i) the consumption of activated N by the substrate surface itself, (ii) the more favourable (111) interfacial energy, and (iii) the competition between metal-metal aggregation and the N adsorption at Ag surface. As the fraction of wafer surface covered by the metal and the availability of N or potential

(100) facets for adsorption increase, the N-covered (100) facets overcome the (111) ones. The impingement of islands with different orientations results into an incomplete coalescence and an earlier percolation but at the expense of poor grain boundaries for electrical transport. This scenario shows the benefit of the strategy of gas deployment at the beginning of the growth to benefit from earlier percolation while avoiding the detrimental transition between orientations for resistivity. This drawback can be turned into an advantage to grow Ag films on amorphous substrate with an unusual (100) orientation [116] or to achieve epitaxial and continuous Ag(001) films on MgO(001) [250] at very small thickness.

To conclude, N_2 appears to behave as a "surfactant" during sputtering deposition of Ag. It is immiscible in Ag and its adsorption decreases the surface energy of the metal thus favouring flattening. Nevertheless, the origin of its impact on the percolation threshold seems to results from a interplay between a better wetting, a change in saturation density and a delayed coalescence in which the orientation-dependent impact of N on energetics plays a role.

3.7 Conclusion

The effect of N_2 during sputtering growth of Ag on an amorphous substrate was revisited using a combination of real-time and *in situ* measurements. Increasing the $\%N_2$ in the gas flow led a sizeable decrease of the percolation threshold but at the expense of film resistivity. According to *in situ* photoemission, N is absent from the film and its surface. However, substrate nitridation and decarbonation proves the presence of activated N species in the plasma, probably atomic N that covers dynamically the metal but desorbs once the growth is stopped as seen by plasmonics. This adsorbate decreases the surface energy of the metal, thus inducing a flattening during the island growth. This enhanced wetting cannot explain on its own the observed decrease in percolation threshold thickness. One should invoke a contribution from the change in particle density and from a delayed coalescence. The latter is assigned to the competition between (111) and (100) oriented particles that ends up in an evolution of film texture and a worsening of film resistivity. As a result, nitrogen displays all the characteristics of a "surfactant" for Ag growth. It is immiscible, floats at the surface, modifies the surface energy and desorbs easily but it stabilizes (100) more than (111) orientations, which ends up increasing the film resistivity. Of course, these specific characteristics seem to preclude the systematic use of N_2 as a surfactant for metals having a stronger chemical interaction with N.

Chapter 4

Effect of O_2 addition on Ag sputtering on SiO_x substrates

Using the knowledge acquired from the study of N_2 addition during Ag sputtering on SiO_x (Chapter 3), this chapter will explore the case of O_2. We will underline the similarities between both gases as "surfactants" for Ag sputtering on an amorphous surface, as well as their differences which stem mainly from the increased reactivity of O_2 relative to N_2. In this respect, *in situ* XPS measurements will prove to be of great relevance to better shed light on the complex oxidation chemistry of Ag films sputtered under oxygenated plasmas.

Table of contents

4.1 Deposition conditions

Deposition conditions in this chapter are analogous to those of Chapter 3, with O_2 gas instead of N_2. Briefly, Ag growths were carried out under 2 μbar of total pressure in DC mode with a power of 50 W. A 10 min-long pre-sputtering step was performed before any deposition to clean the target. Films were deposited on as-supplied Si wafers just like in the previous chapter without any specific surface preparation. These wafers have a layer of native amorphous oxide on their surface, which will be referred to as "SiO_x". $\%O_2$ values were varied from 0% to 40% and an XPS reference film was deposited at 100%O_2 (but at a total flow of 22 sscm).

4.2 Film morphology from real-time measurements

4.2.1 Film resistance measurements

Figure 4.1 shows the evolution of the normalized real-time resistance all along the Ag growth for different $\%O_2$ conditions. In all cases, as for N_2, a sharp drop which corresponds to the percolation threshold thickness t_p is observed between 3 and 6 nm.

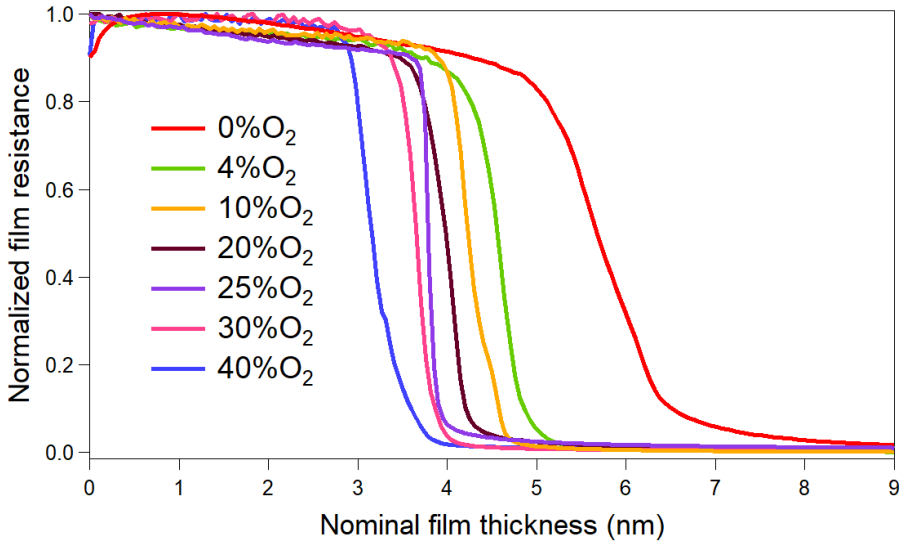

Figure 4.1 Real-time film resistance during Ag deposition on a SiO_x/Si wafer as a function of the $\%O_2$ in the sputtering gas flow. Data are normalized to the value prior to shutter opening.

From these data, the change in t_p (Figure 4.2-a) and film resistivity ρ (Figure 4.2-b) at $t = 20$ nm with increasing $\%O_2$ was obtained.

Values for t_p decrease from 5.4 down to 3.0 nm with $\%O_2$, while ρ at $t = 20$ nm increases over tenfold from 7.9 up to 84 $\mu\Omega.cm$. While these findings appear to be similar to those for N_2 in terms of trends, a closer inspection of Figure 4.2 shows at least two regimes of $\%O_2$. At very low O_2 flow, between 0% and 4%, a sharp decrease of 20% in t_p is observed (from 5.4 nm to 4.3 nm) without any significant impact on the final resistivity at $t = 20$ nm. At higher $\%O_2$ values, t_p keeps decreasing while ρ rises linearly. This change in trend with $\%O_2$ seemingly indicates a change in growth and/or oxidation regime. This first analysis of real-time resistance measurements already points at a key difference between the two gases since the effect of N_2

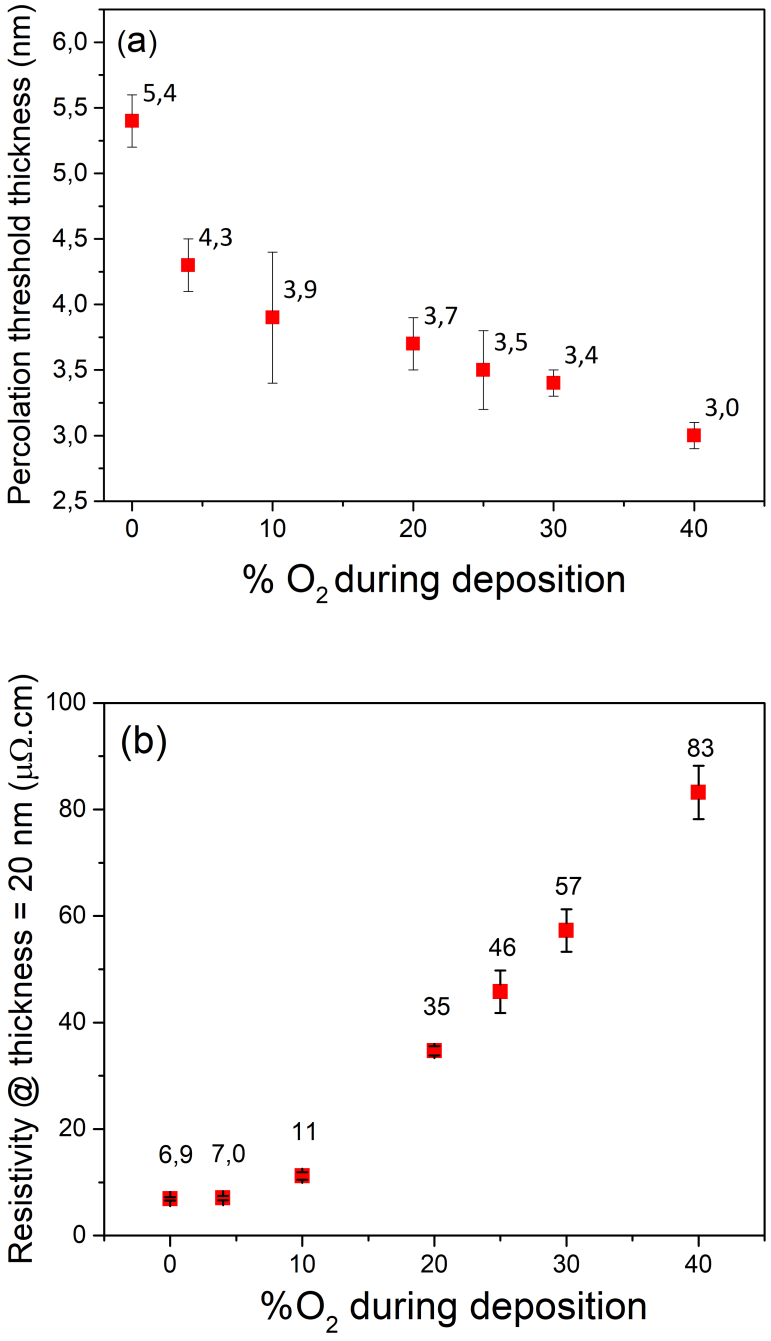

Figure 4.2 (a) Percolation threshold thickness t_p and (b) film resistivity ρ for $t = 20$ nm obtained from real-time film resistance measurements for different $\%O_2$ conditions. Values and error bars shown correspond to the mean value and standard deviation over several experiments.

was more gradual and monotonous (Chapter 3).

4.2.2 SDRS measurements

Real-time SDRS measurements were systematically carried out in parallel to film resistance acquisitions to scrutinize the initial stages of film growth at different $\%O_2$ conditions. Figure 4.3 shows the comparison between p-polarized spectra for different $\%O_2$ at given nominal thicknesses of (a) $t = 0.6$ nm and (b) $t = 3$ nm. These values were chosen based on t_p (Figure 4.2-a), so that films were not yet percolated and thus composed of a mixture of isolated and coalescing nanoparticles.

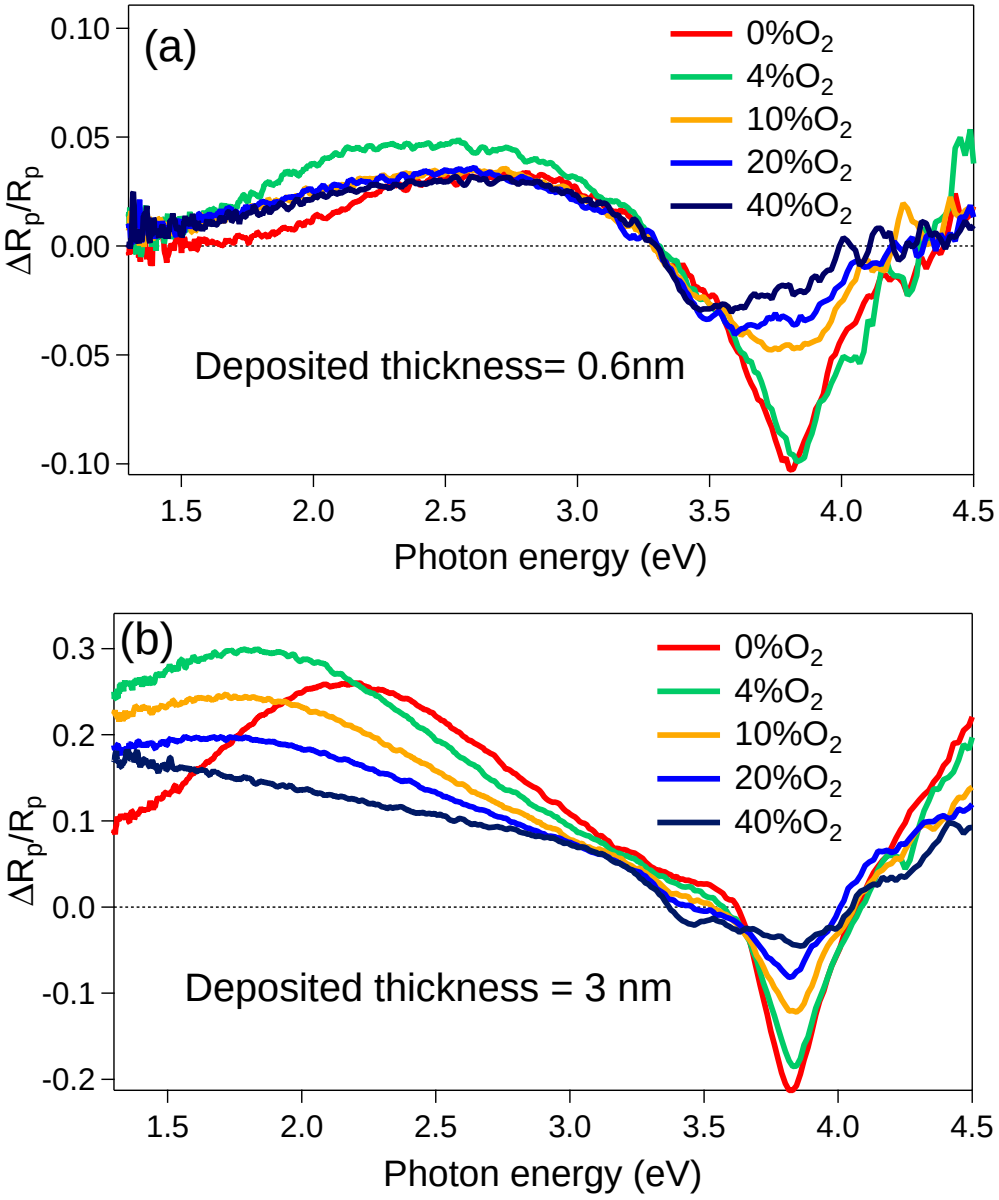

Figure 4.3 Evolution of the p-polarized SDRS spectra for different $\%O_2$ during deposition at a nominal deposited film thickness of (a) 0.6 nm and (b) 3 nm.

The *p*-polarized SDRS spectra were analysed in a manner analogue to the N_2 study (Chapter 3), by looking at the variation in position and intensity of the low-energy plasmon peak and comparing these trends with the *Granfilm* dielectric simulations.

- **SDRS spectra at $t = 0.6$ nm:** increasing $\%O_2$ from 0 to 4% leads to an increase in intensity and a red-shift of the low-energy peak. Peaks for $\%O_2 \geq 10\%$ have lower intensities and mostly overlap.
- **SDRS spectra ar $t = 3$ nm:** the trends in the SDRS spectra at $t = 3$ nm are more obvious. Increasing the value of $\%O_2$ from 0 to 4% leads once again to a red-shift and intensity increase of the low-energy peak, and a clear trend is now observed from 10% up to $40\%O_2$, with the low-energy peak decreasing more and more in intensity while also being more red-shifted.

According to the *Granfilm* simulations (shown in Chapter 2), the increase in intensity and red-shift observed at low $\%O_2$ values is consistent with an increase in Ag nanoparticle aspect ratio A_r. In other words, the Ag nanoparticles are on average "flattened" when deposition is performed under $4\%O_2$. We note that the same effect was observed for N_2 over a wider range of $\%N_2$ values (Chapter 3), but in the present case, this "flattening" effect is only observed for very low gas flows (*i.e.* $4\%O_2$). The new trend at higher $\%O_2$ (red-shift and a decrease in intensity) is compatible with the formation of a core-shell structure with a metallic Ag core and an oxidized shell. Moreover, this effect is more pronounced at higher thickness (*i.e* at $t = 3$ nm rather than $t = 0.6$ nm). This point will be explored in a later section on *in situ* XPS chemical characterization for increasing film thickness.

As a support to the previous observations, and to highlight the evolution of A_r [200], SDRS signal in s-polarization was also integrated (Figure 4.4) up to late coalescence where $\mathcal{A}_s(t)$ saturates because of the limited spectral integration range of the plasmon peak (> 1.5 eV) (the proportionality between $\mathcal{A}_s(t)$ and A_r is valid only when integrating the whole plasmon width over the available frequency windows). For all stages of growth, the larger $\mathcal{A}_s(t) \propto A_r$ signal clearly evidences a better nanoparticle wetting when O_2 is added to the gas flow.

4.3 *In situ* photemission analysis (XPS)

The oxidation of Ag is one of the key factors in explaining the effects of O_2 addition on the growth and final properties of sputtered films. Thus *in situ* XPS was performed after deposition in order to detect and characterize Ag-O compound formation. As we shall see, photoemision is quite relevant in distinguishing between different kinds of Ag-O moities. Before detailing our results, we will start with a literature review on the chemistry of oxygen at the Ag surface from a point of view of photoemission.

4.3.1 Oxygen species on Ag surfaces: a complicated history

One important aspect to underline is that the determination of the precise chemistry of an oxidized or partially oxidized Ag surface is no easy task in photoemission, mostly because of the existence of different AgO_x bulk compounds and the abundance of surface/subsurface O species, the structures of which are often ill-defined or poorly known [251]. Overlap between the spectroscopic fingerprints of the corresponding moities and instrumental limitations often hinder the ability to distinguish or accurately detect them.

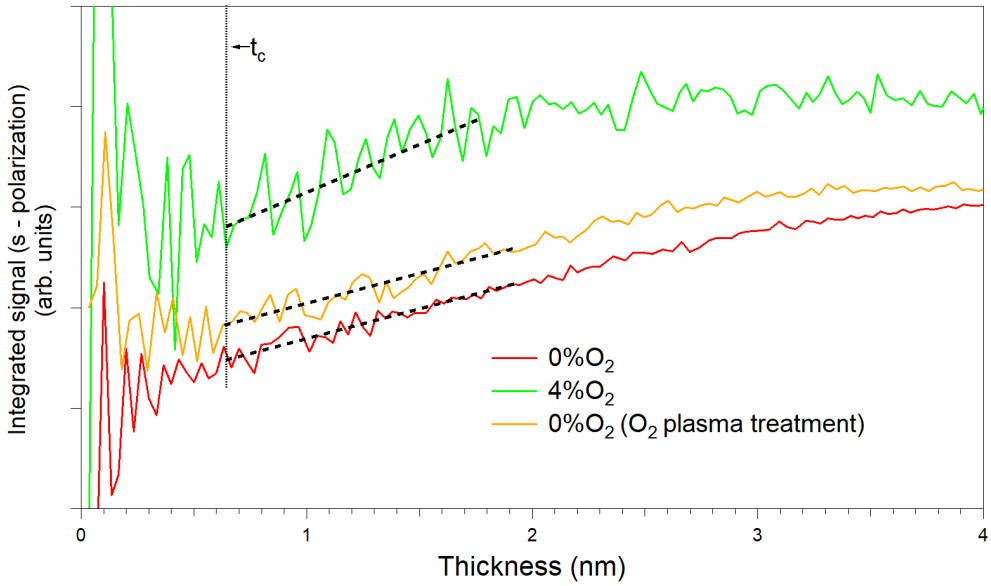

Figure 4.4 Integrated value $\mathcal{A}_s(t)$ (Equation 2.2 in Chapter 2) of the s-polarized SDRS spectra for $0\%O_2$ [without (red line) and with $40\%O_2$ wafer plasma pre-treatment (orange line)] and $4\%O_2$ on a native wafer. Trends similar to 4 $\%O_2$ are found at higher oxygen flow (not shown for clarity). The vertical dotted line points to the onset of coalescence t_c.

The best documented bulk Ag oxides include Ag_2O, the most stable polymorph, and the lesser known AgO oxide [164, 165]. These compounds differ in terms of atomic structures. The cubic cuprite Ag_2O involves O anions in a four-fold Ag^+ tetrahedral coordination, whereas the monoclinic AgO is a mixed-valence compound, with an average Ag oxidation state of +2 but involving a dismutation on the two Ag sites, with Ag^+ in a linear coordination and Ag^{3+} in square-planar one. The unstable +3 pure oxidation state of Ag has only been reported in exotic compounds such as Ag_2O_3, although their syntheses require harsh oxidizing environment such as anodic treatment or ozone exposure [152–154, 162, 252, 253]. Spectroscopic characterization of the bulk silver oxide compounds is blurred by the formation of carbonates at their surfaces upon exposure to air, and by their poor thermal stability [152–154, 156–158, 161, 165, 254] that prevent any faithful in-vacuum preparation procedure. Spectroscopic distinction between Ag^+ and Ag^{3+} in AgO is not even clear-cut in the literature, with many reports describing a broad Ag 3d peak that accounts for the two crystallographic sites. Binding energies for Ag^0 and Ag^+ oxidation states in metallic Ag and Ag_2O are reported, respectively, at $E_B(Ag\,3d) = 368.1 \pm 0.15$ eV and $E_B(Ag\,3d) = 367.7 \pm 0.3$ eV; $E_B(O\,1s) = 529.2 \pm 0.35$ eV [152–154, 156–162] [163–165]. These reported values and standard deviations result from an average over the above quoted literature on oxidized Ag. The negative chemical shift for Ag 3d peaks observed upon oxidation may seem counter-intuitive at the first sight, since in principle the reduction of the density of valence electrons upon oxidation decreases the electrostatic screening by the nucleus thus increasing the binding energy. The explanation for the particular case of Ag stems from the lack of on-site sensitivity to oxidation in Ag and a complex final state effect [156, 255]. The hierarchy of bulk thermodynamic stability follows Ag > Ag_2O >AgO > Ag_2O_3; in principle, thermodynamics even predicts the instability of all Ag oxides in vacuum at room temperature [155, 164, 252]. Even in studies using direct photoemission from *in situ* oxidized Ag (a procedure that escapes the inherent problem of surface contamination due to air exposure [159, 163, 164, 166]), the

spectroscopist faces the formation of suboxides AgO_x whose atomic structures are almost never determined.

Several oxygen moieties with distinct stability in temperature have been reported during oxidation of metallic Ag single crystal surfaces with molecular O_2 at high temperature [159, 166, 254, 256–260]. Adsorbed oxygen has reportedly been produced in surface science studies also upon NO_2 adsorption and decomposition [261,262] or via a dedicated atomic-O thermal cracking source [263]. Physisorbed O_2 partly dissociates upon heating leaving behind an atomic species labelled $O_{\alpha 1}$ that desorbs above 580 K. This species, observed at low chemical potential in many surface science experiments, is associated with orientation-dependent $p(4 \times 4)$ reconstruction [128, 264–267] at Ag(111) surface; it is associated with a relatively high charge transfer with Ag as reported by Rocha *et al.* [166]. Increasing the O_2 exposure and/or heating the Ag surface leads to the migration of oxygen into the bulk and the creation of a partial equilibrium with the surface species. This so-called O_β subsurface species polarizes the surface Ag-O bond, creating different moieties from a spectroscopic point of view *i.e.* $O_{\alpha 3}$. At even higher chemical potential, in particular near-atmospheric pressure and high-temperature, the Ag surface strongly restructures leading to a strongly-bound and thermally stable subsurface O_γ oxygen species in conjunction with a $O_{\alpha 2}$ moiety at its surface. This Ag oxidation pathway requiring high-pressure dosing due to the very low-sticking coefficient of O_2 [140,256] can also be sped-up by exposing the Ag surface to atomic oxygen from a dedicated source [160, 162, 263] or in the course of reactive sputtering deposition [140].

To sum up, upon increasing oxygen chemical potential and in the course of reactive sputtering deposition (where atomic oxygen will be present in the plasma), the formation of O moieties follows the schematic pathway:

$$\begin{aligned} O_{\alpha_1}(s) &\rightarrow O_\beta(b) + O_{\alpha_3}(s) \rightarrow O_\gamma(b) + O_{\alpha_2}(s) \\ &\rightarrow O_{Ag_2O}(b) \rightarrow O_{AgO}(b) \end{aligned} \tag{4.1}$$

where the labels $(s), (b)$ stand for "surface" and "bulk or subsurface", respectively. Besides the use of their different desorption temperatures and thus bonding, these O species are often identified via their O 1s photoemission fingerprints. Often overlapped, they are reported at [159, 166, 254, 256–260, 263]: $E_B(O_{\alpha 1}\, 1s) = 528.1 - 528.4$ eV, $E_B(O_\beta\, 1s) = 530.8 - 531.0$ eV, $E_B(O_{\alpha 3}\, 1s) = 530.1 - 530.4$ eV, $E_B(O_\gamma\, 1s) = 529.5 - 529.7$ eV, $E_B(O_{\alpha 2}\, 1s) = 529.1 - 529.2$ eV.

In our case, the O_β and $O_{\alpha 3}$ species were observed when a metallic 15 nm-thick Ag film was exposed to a 10%O_2 gas mixture for one hour without any assistance from plasma or heating, as shown in Figure 4.5. Exposure resulted in a very small increase of the O 1s signal in the energy range expected for O_β and $O_{\alpha 3}$ moities due to the very low sticking coefficient of O_2 on Ag, whilst no shift was observed for the Ag 3d spectrum. In parallel, only adventitious carbon of aliphatic nature increased in the C 1s region ($E_B = 284.5$ eV). This result suggests that O_β and $O_{\alpha 3}$ have a "molecular" origin instead of an "atomic" one, and leads to a lower charge transfer to Ag than the previously mentioned $O_{\alpha 1}$ species as no shift of Ag 3d is observed. The fact that these species are observed by simple exposure to molecular O_2 without heating is in agreement with the works of Campbell [254, 256, 268].

To conclude, exposure to O_2 at low temperatures leads to a small sticking and to the formation of the weakly-oxidizing O_β and $O_{\alpha 3}$ species, whilst sample heating and/or the use of atomic O sources (such as a dedicated source or a plasma) enables O_2 dissociation and facilitates the

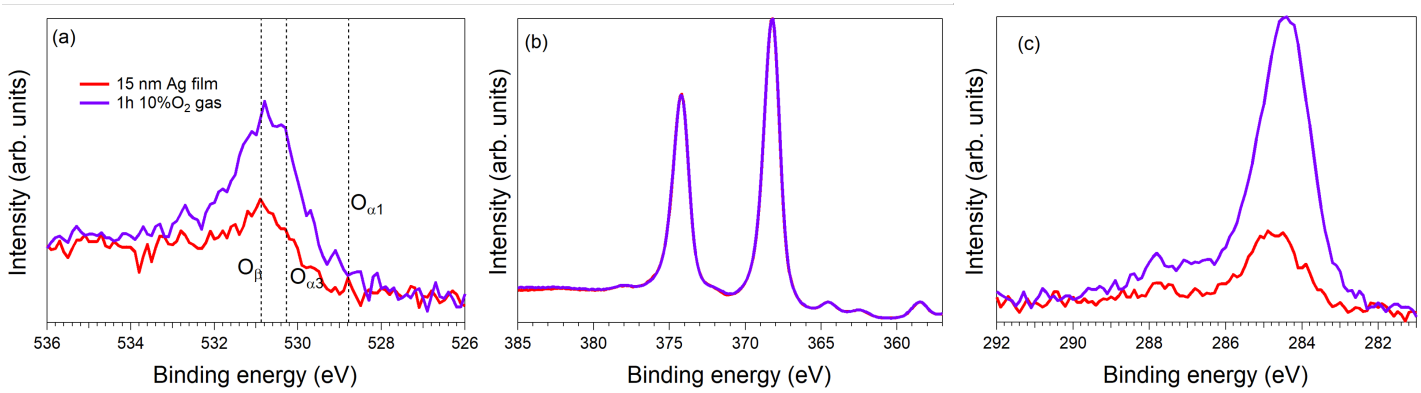

Figure 4.5 *In situ* XPS spectra of (a) O 1s, (b) Ag 3d and (c) C 1s core levels, for an as-deposited 15 nm-thick Ag film before and after a 1 hour exposure to 10%O_2 gas.

formation of reconstructed Ag surfaces, leading to the highly oxidizing $O_{\alpha 1}$ species. Based on this spectroscopic panorama of Ag bulk and surface oxide species, we can begin our analysis of the results of *in situ* XPS analysis.

4.3.2 Photoemission analysis of 20 nm-thick Ag films

20 nm-thick Ag films deposited under different %O_2 conditions, from 0%O_2 to 40%O_2, were analysed by *in situ* XPS (Figure 4.6). Spectroscopic results were supplemented by an extra deposition under pure O_2 gas (100%O_2-22 sscm) as a reference. The thickness value of 20 nm ensures that the signal corresponding to the substrate is completely damped and that only the Ag film surface composition is analysed. It also allows for direct comparison with real-time film resistivity measurements described in the previous section. Unlike N_2, it is clear that O_2 addition leads to major changes in the Ag 3d core level line shape and to the emergence of new features in the O 1s region (Figure 4.6).

For low %O_2 condition, between 0 and 4%, the O 1s spectra is poorly impacted with only a very slight increase in intensity in the binding energy region corresponding to the O_β and $O_{\alpha 3}$ species. These O 1s contributions cannot be entailed by a Ag_2CO_3-like carbonate species which is close in binding energy ($E_B = 530.5 \pm 0.3$ [152,154,157,158]) since the observed C 1s binding energy ($E_B = 284.5$ eV) does not correspond to carbonates ($E_B = 287.6-288$ eV [152,154,157,161,269]). Any contribution from hydroxyl groups or adsorbed water (due to gas contamination) can also be safely ruled out, as they peak at $E_B > 531.5$ eV [161,269,270] and are not observed in the present data. Besides, no shift is observed in the Ag 3d spectra. All these results are similar to those for the exposure of a metallic Ag film to molecular O_2 gas (Figure 4.5), where only the weakly oxidizing O_β and $O_{\alpha 3}$ species were detected and no $O_{\alpha 1}$ was observed. *In situ* XPS results seem to suggest that at very low O_2 flux, oxidation of Ag is driven by the interaction with molecular O_2 and without any significant oxide formation.

Increasing %O_2 leads to sizeable changes in XPS spectra. In parallel to the increase of a new main O 1s feature at $E_B \sim 529.2$ eV (Figure 4.6-a), the binding energy of the Ag 3d 5/2 peak (Figure 4.6-b) shifts continuously from $E_B = 368.1$ eV down to $E_B = 367.7$ eV when going from 10%O_2 to pure O_2 (100%O_2). Both extreme E_B values are in close agreement with reported values for Ag^0 and Ag^+ oxidation states in metallic Ag [$E_B(Ag\,3d) = 368.1 \pm 0.15$ eV] and

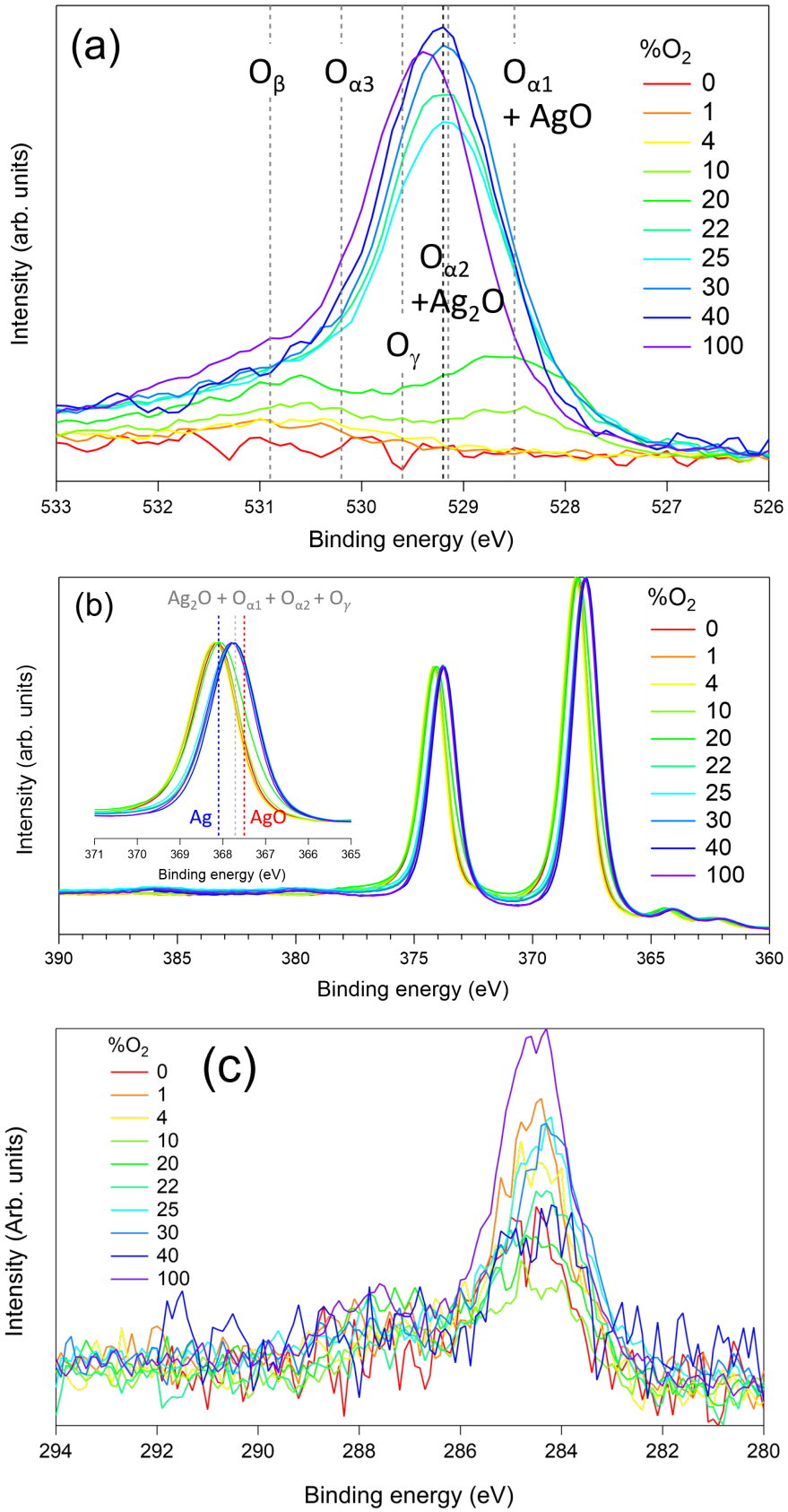

Figure 4.6 *In situ* XPS measurements of 20 nm-thick Ag films deposited under different %O_2, for binding energies corresponding to the (a) O 1s, (b) Ag 3d, and (c) C 1s core levels. Vertical lines show tabulated values for different bulk oxides and (sub)surface oxygen species (see text for explanation). The inset of figure-b zooms on the evolution of the Ag 3d 5/2 peak. Spectra are normalized to the background in the case of O 1s and C 1s, and to the same scale for Ag 3d.

Ag_2O [$E_B(Ag\,3d) = 367.7 \pm 0.3$ eV; $E_B(O\,1s) = 529.2 \pm 0.35$ eV] [152–154, 156–162] [163–165]. Furthermore, two trends appears at higher values of $\%O_2$. O 1s core level of films deposited under 10% and 20%O_2 show peaks corresponding to a mixture of $O_{\alpha 1}$ species and of the pair of $O_\beta/O_{\alpha 3}$ species. The increasing presence of $O_{\alpha 1}$ means that the film is more and more oxidized, even if it remains mostly metallic Ag judging by how the centroid of the Ag 3d 5/2 peaks at $E_B = 368.1$ eV. Finally, for films deposited at $\%O_2 > 20\%$, a new major component emerges at $E_B \sim 529.2$ eV in the O 1s spectra. It is assigned to the formation of an Ag_2O-like compound, and not to the O_{α_2} moiety, since its companion O_γ peak (see Equation 4.1 is never observed in the peak fits (see below). The film is now mostly oxidized, since the centroid for the Ag 3d 5/2 peaks shifts for $\%O_2 > 20\%$ towards $E_B = 367.7$. Peak fitting of these XPS spectra will be later discussed in order to quantify the composition of these partially oxidized Ag films.

Before going on, a comment should be made on the assignment of the peak at $E_B = 528.4$ eV as a $O_{\alpha 1}$ moiety. Indeed, based the spectroscopy of known and reported bulk oxidized Ag species, this binding energy could also be linked to the formation of an AgO oxide. The problem with this assignment is that this peak is observed for relatively low $\%O_2$ values (between 10% and 20% especially), whilst higher $\%O_2$ yield Ag_2O as the major product. Since Ag is more oxidized in AgO than in Ag_2O as previously explained, it seems thermodynamically unlikely that increasing the $\%O_2$ would produce AgO before Ag_2O. Moreover, the spectroscopic fingerprints of AgO found at $E_B(Ag\,3d) = 367.5 \pm 0.4$ eV and $E_B(O\,1s) = 528.5 \pm 0.4$ in the literature do not fit our findings under pure O_2 ($100\%O_2$). Based on these arguments, the peak at $E_B = 528.4$ eV is assigned to the $O_{\alpha 1}$ species and not to AgO bulk oxide.

At last, despite the *in situ* transfer, a slight carbon contamination of a fraction of Ag(111) monolayer (~ 0.3) was present at the surface of all samples. Its presence does not entail the following discussion as its binding energy corresponds to adventitious hydrocarbons ($E_B = 284.5$ eV) and not C-O bonds ($E_B = 286 - 288$ eV [243]) or even Ag carbonates ($E_B = 287.6 - 288$ eV [152,154,157,161,269]). No other contaminants, particularly implanted Ar, were detected by XPS.

4.3.3 Evolution of O species and Ag stoichimoetry from XPS spectral fit

The procedure for the Ag 3d and O 1s peak fitting was previously explained in Chapter 2. The identification of different oxide species was based mainly on the analysis of O 1s core level spectra.

As illustrated in the examples of Figure 4.7-a,b, for 20 nm-thick films grown under different $\%O_2$ conditions, a consistent fit could be systematically achieved for all O 1s spectra using a sum of Voigt peaks corresponding to all the bulk and surface species reported in the literature. Owing to the poor resolution of the non-monochromated source and the large number of fit parameters, the binding energies of the Voigt peaks were kept fixed (at previously discussed E_B literature values) while a common Gaussian broadening was used for all of them. Figure 4.8-a shows the obtained evolution of the relative areas of all the fitted components as a function of $\%O_2$ at $t = 20$ nm.

Regarding the analysis of the Ag 3d core level, the reported chemical shift of Ag 3d upon oxidation [260], that spans from -0.35 to -0.6 eV with respect to metallic Ag, is less sensitive to the formed species or bulk compounds (Figure 4.6-b, inset). Therefore, no attempt was made to distinguish the contributions from Ag atoms bonded to different O species, especially those in Ag_2O and those bonded to $O_{\alpha 1}$. The Ag 3d core level was thus fitted with only two compo-

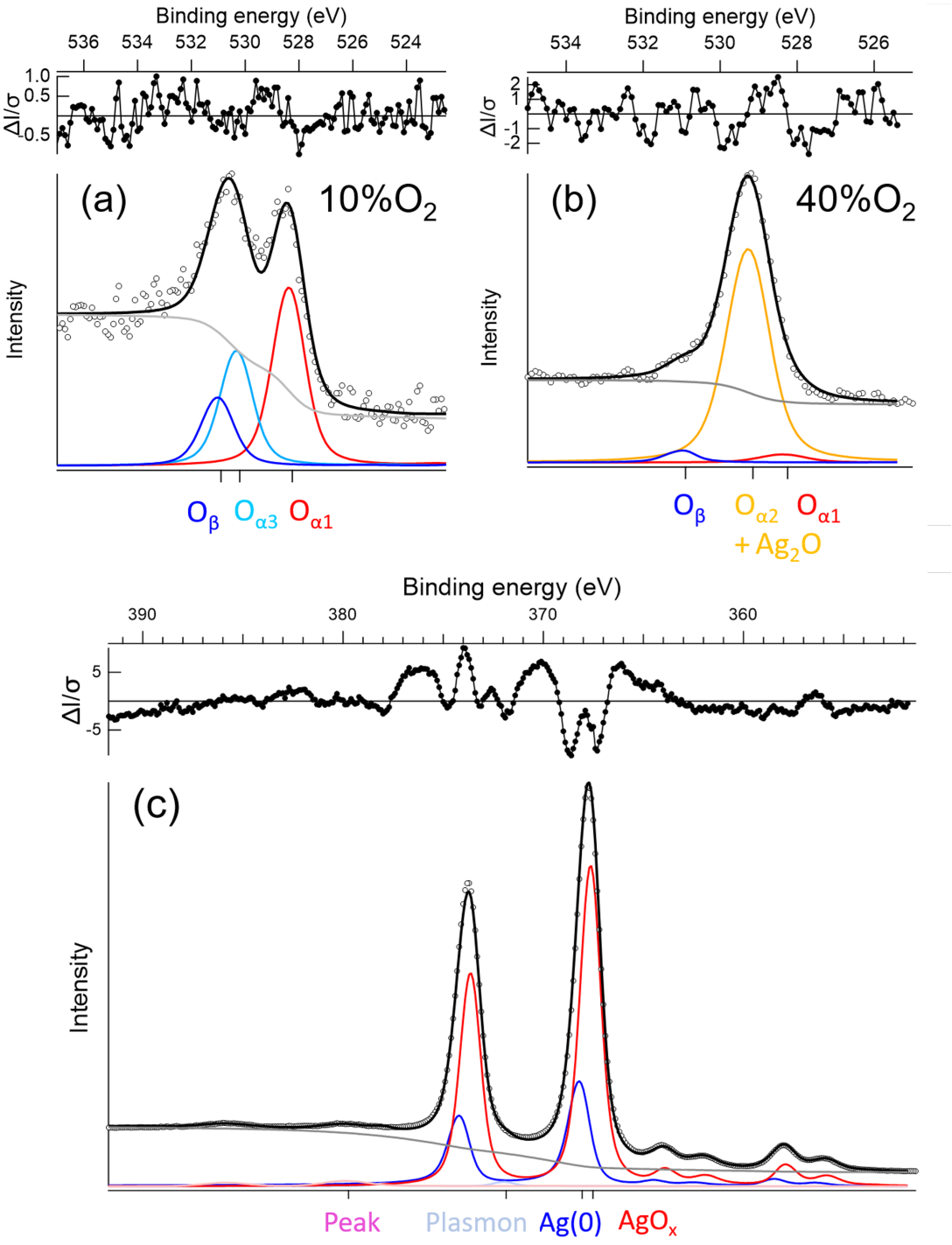

Figure 4.7 Examples of fits of core level peaks of 20 nm-thick films grown under different $\%O_2$: (a) O 1s ($10\%O_2$), (b) O 1s ($40\%O_2$), (c) Ag 3d ($30\%O_2$). See text for explanation. Data (circles), fit (black line), background (grey line) and various components (colored lines as indicated below) are shown. The residuals normalized to error bars taken as the square-root of intensity are shown in the top scale.

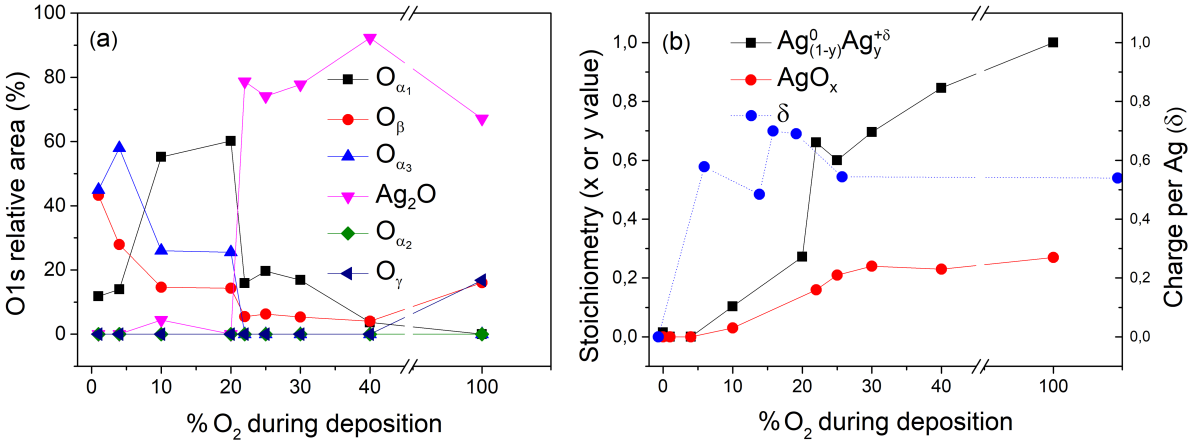

Figure 4.8 Photoemission analysis of 20 nm-thick films as a function of $\%O_2$: (a) evolution of the relative areas of all O 1s components (see text for explanations) and (b) changes in (i) global stoichiometry AgO_x from O 1s/Ag 3d relative peak areas (red symbols), (ii) fraction $Ag^0_{1-y}Ag^{\delta+}_y$ of oxidized Ag component from the Ag 3d core level spectra fits (black symbols) and (iii) the charge transferred δ per Ag atom (blue symbols). The error bars are of the order of 10 %. An uniform film hypothesis is used for the analysis.

nents, as exemplified in Figure 4.7-c, one for metallic Ag at fixed $E_B(Ag^0) = 368.1$ eV, and a second generic component for oxidized silver, that was found shifted by about -0.5 ± 0.1 eV at E_B=367.7 eV. For spectra involving a large fraction of metallic Ag, a bulk plasmon loss shifted by about 3.85 eV had to be taken into account in the Ag 3d profile as well as a similar feature but shifted by 12 eV for oxidized silver (see Figure 4.7-c). In addition, the global average film stoichiometry AgO_x, the fraction $Ag^0_{1-y}Ag^{\delta+}_y$ of oxidised silver Ag and the average charge per oxidized Ag atom δ were also calculated using the procedure explained in Chapter 2. All three quantities (y, x and δ) are displayed in Figure 4.8-b for 20 nm-thick films.

For $\%O_2$ values below 10% (Figure 4.8-a), oxidation proceeds via a mixture of O_{α_1}, O_β and O_{α_3} moieties, in which the main species O_β and O_{α_3} evolve in parallel as expected (see Equation 4.1). The interpretation is further reinforced by the quantification of the total (O_{α_1}+O_{α_3}) O 1s signal. Considering it as coming from only surface species, the total coverage is always found well below the Ag(111) monolayer (< 0.8); on the other hand including O 1s signal at $E_B = 529.1 - 529.2$ eV (*i.e.* interpreting the signal as O_{α_2} instead of Ag_2O) leads to unphysical coverage well above the monolayer.
The increase from 10% to 20%O_2 leads to the replacement of O_β/O_{α_3} moieties by O_{α_1} and to a higher fraction of oxidized Ag as seen in the higher value of δ (Figure 4.8-b). Such a highly oxidic nature of $O_{\alpha 1}$ has already been pointed out in Reference 166 which reports a $Ag^{\delta+}/O$ value as more than 20 times higher than for O_{α_3}-O_β.
The sharp transition observed above 20%O_2 (Figure 4.8) corresponds to the appearance of an O 1s component at $E_B = 529.2$ eV and a noticeable change in stoichiometry and in fraction of oxidized Ag. The new O 1s peak is assigned to the formation of an Ag_2O-like compound, and not to the O_{α_2} moiety, since its companion O_γ peak is never observed (see Equation 4.1). Interestingly, not present at lower $\%O_2$, a not- clearly assigned spin-orbit split "plasmon-like" feature at $E_B = 379.6$ eV, shifted by +12.3 eV from metallic Ag 3d, goes with the appearance

of this Ag_2O-like compound. In contrast, the plasmon loss in metallic Ag, shifted by +3.85 eV, has to be accounted for only below ~ 20 $\%O_2$.

Even for deposition under pure O_2, the global stoichiometry AgO_x, including all O species, remains surprisingly well below the $x = 0.5$ value expected for Ag_2O, while the charge transferred per Ag atom only goes up to roughly 0.6, far from the expected value of 1 for pure Ag_2O (Figure 4.8). The key to understanding this observation lies in the non-homogeneous film composition along its thickness.

4.3.4 Film composition gradients

Figure 4.9 shows the example of XPS spectra for Ag films of different thicknesses deposited under $10\%O_2$. It is clear from these results that the Ag film composition varies with increasing thickness. In particular, the shift of the Ag 3d 5/2 peak towards lower binding energy shows how Ag is more and more oxidized with increasing film thickness.

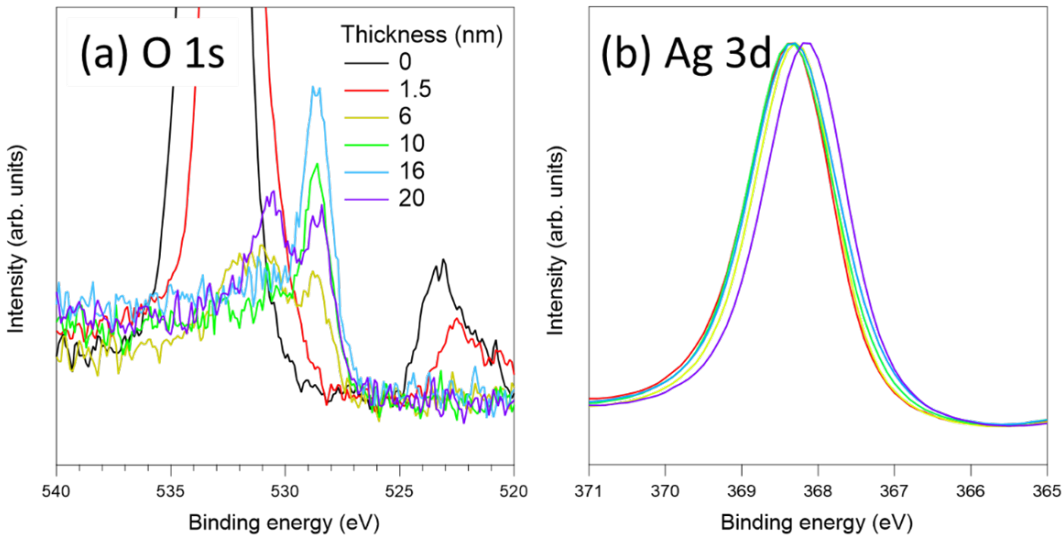

Figure 4.9 Change in (a) O 1s and (b) Ag 3d 5/2 core level spectra for Ag films with nominal thicknesses for films deposited under $10\%O_2$.

To further study this phenomenon, film composition was characterized along the film thickness for three representative O_2 flow conditions: $4\%O_2$, $10\%O_2$ and $40\%O_2$. Thickness values were chosen in order to span the different stages of Ag film growth: (i) disconnected Ag island growth on the surface, (ii) near the percolation threshold thickness, and (iii) a final thickness above percolation (see Figures 4.2 and 4.4). The evolution of chemical states with increasing film thickness was analysed by fitting core levels similarly to the 20 nm-thick films. For thickness values below the photoelectron escape depth of $3\lambda \sim 5$ nm, an extra O 1s component at $E_B = 532$ eV corresponding to an SiO_x peak from the substrate surface had to be accounted for, due to the metal film discontinuity and/or to the fact that its signal is only partially damped by the film (see example Figure 4.10). Results for the evolution of the different O 1s components with increasing thickness are shown in Figure 4.11, and those for the fraction $x - y$ of oxidized Ag stemming from Ag 3d spectral analysis are shown in Figure 4.12.

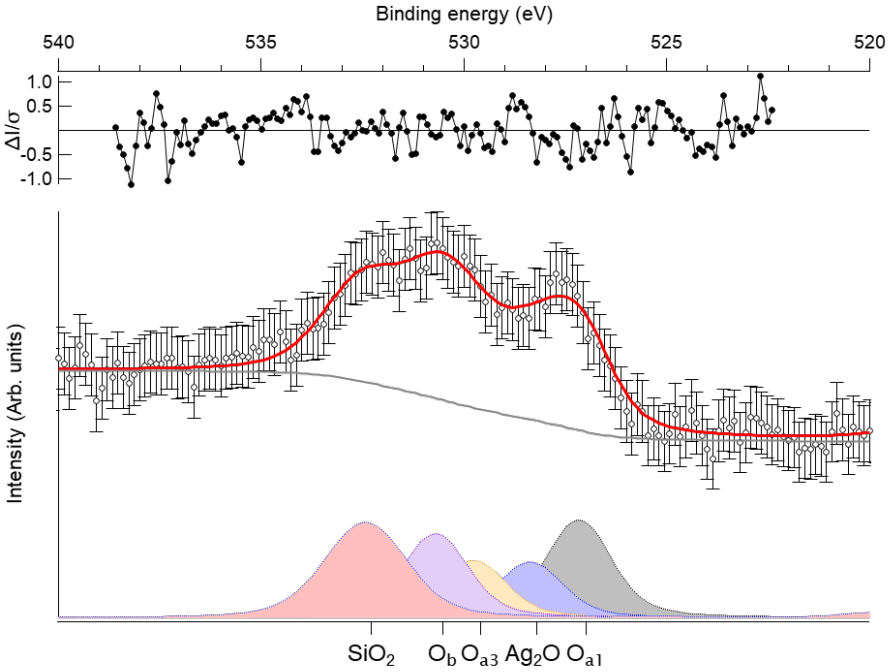

Figure 4.10 Example of O 1s core level decomposition of a 6 nm-thick Ag film grown under $10\%O_2$ including the signal from the SiO_x substrate.

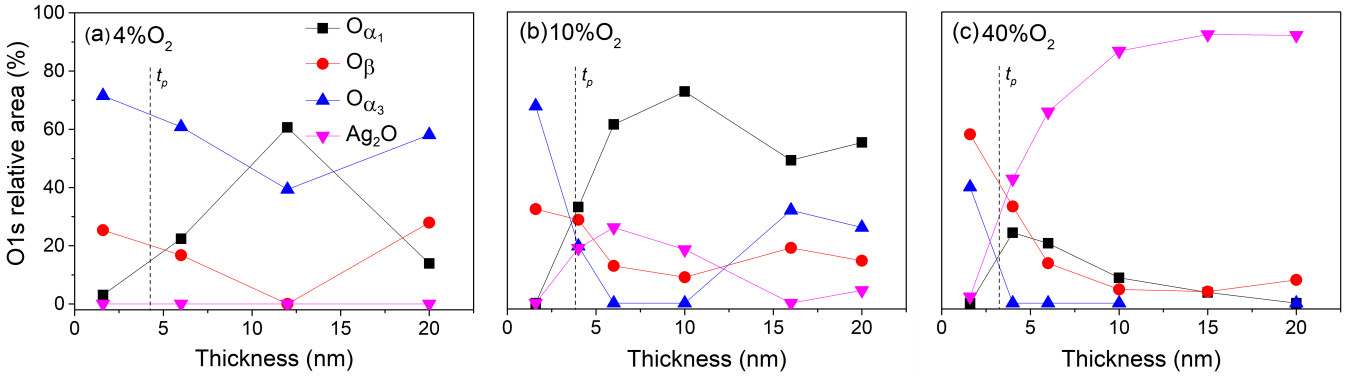

Figure 4.11 Evolution of the relative area of all O 1s components (see text for explanations) as a function of film thickness, for depositions at (a) $4\%O_2$, (b) $10\%O_2$, and (c) $40\%O_2$. The vertical dotted line corresponds to percolation threshold. The error bars are of the order of 10 % of the value.

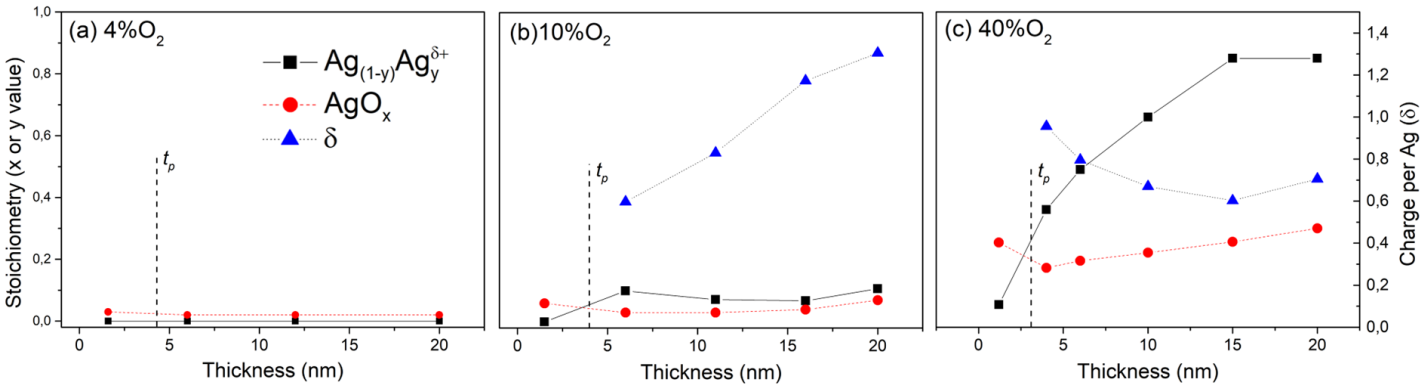

Figure 4.12 Evolution of film stoichiometry and charge per Ag atom as a function of film thickness, for depositions under(a) 4%O_2, (b) 10%O_2, and (c) 40%O_2. Values shown correspond to film characteristics x, y and δ as previously defined (see Figure 4.8-b).

While no evolution of the Ag 3d spectrum with increasing thickness is observed for 4%O_2, O_β and $O_{\alpha 3}$ moieties evolve in parallel as expected from equation 4.1. The $O_{\alpha 1}$ signal also increases after percolation before decreasing for the 20 nm-thick film. The evolution of these species will not be analysed in detail, since the O 1s signal for films deposited under 4%O_2 is very low thus increasing the uncertainty of the fitting procedure. We will simply conclude that the only occurring species in these films are the $O_{\alpha 1}$ and $O_\beta/O_{\alpha 3}$ moieties, with no detectable change in the Ag 3d core level region which is consistent with our measurements for 20 nm-thick films.

In contrast, the change in film stoichiometry with increasing thickness at 10% and 40%O_2 (Figure 4.12) is clearer, and showcases how a gradient in Ag oxidation state sets up during deposition. The film is more metallic at the interface with the substrate and its oxidized fraction increases with thickness before reaching a steady state. The phenomenon is faster and more pronounced at 40%O_2 than at 10%O_2. In fact, modulo the XPS probing depth, the transition from a predominantly metallic to an oxidized film starts roughly at the film percolation thickness (see Figure 4.11 and 4.12), and the above-mentioned plateau (steady state) is presumably reached when a continuous film is formed. Unlike previous hypotheses on formation of Ag suboxides in parallel to metal [58, 107, 135, 136, 138–141, 144, 155, 271], these results reflect a composition gradient that is correlated to the film morphology. A likely explanation for this composition gradient and its dependence on the percolation threshold thickness involves a competition between favourable Ag clustering on the SiO_x surface (due to the very weak substrate-metal interaction energy and fast ad-atom diffusion) and Ag oxidation by direct impinging of activated O species from the plasma [140, 141] via an "Eley-Rideal" mechanism. Indeed, a "Langmuir-Hinshelwood" scenario involving oxygen adsorption and surface diffusion is impeded by the competition with substrate oxidation/decarbonation, which occurs during the initial stages of film growth when substrate coverage by the film is still not complete (*i.e.* before the formation of a continuous hole-free film). We will now look in more detail at the interaction between the Ar:O_2 plasma and the substrate surface itself, which will add another piece to the explanation of the gradual oxidation of Ag with film thickness.

4.3.5 Effect of O_2 plasma treatment on the SiO_x substrate

Oxidation of the SiO_x/Si substrate during the initial stages of film growth was scrutinized using *in situ* photoemission analysis (Figure 4.13) before and after Ar:O_2 plasma (40%O_2) exposure in front of an alumina target (see Chapter 2 for more details).

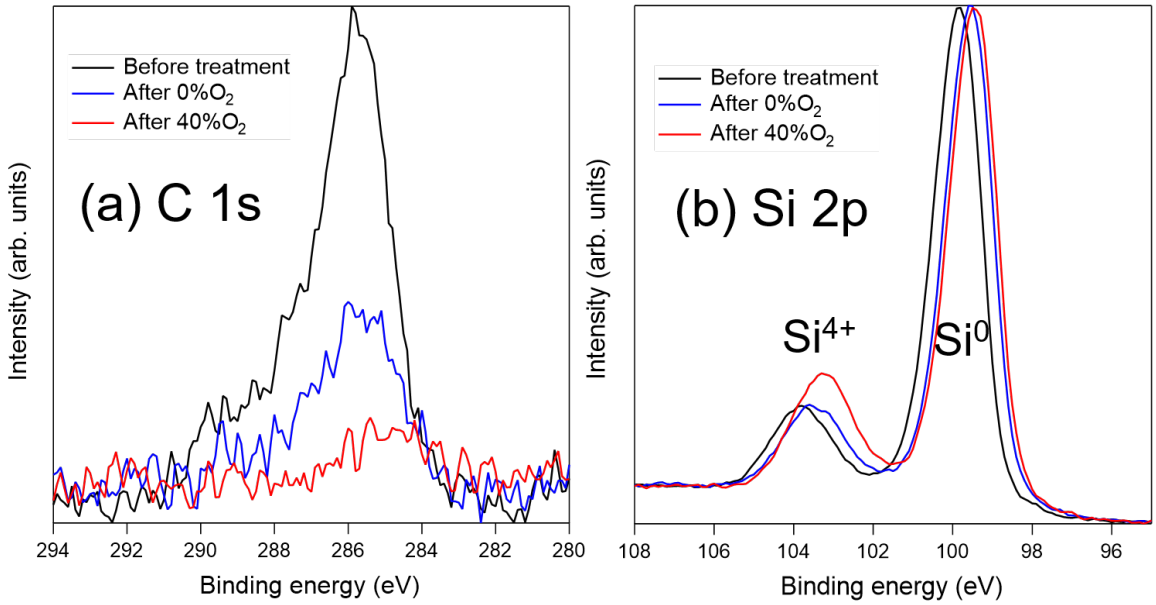

Figure 4.13 Evolution of core levels after a plasma treatment of the Si wafer surface in a pure Ar plasma (0%O_2) and a 40%O_2 mixture: (a) C 1s and (b) Si 2p. The time scale of plasma treatment (3 s) is equivalent to a deposited thickness of $t \sim 1.5$ nm.

For the explored exposure duration (3 s corresponding to $\sim$ 1.5 nm during deposition), the plasma treatment is accompanied by (i) a nearly complete reaction of plasma-activated O species with carbonaceous contamination surface species, unlike the case of a pure Ar plasma (Figure 4.13-a), and (ii) a SiO_x layer thickening of about 0.2 nm (ratio Si^{4+}/Si^0 2p), alongside a sizeable Si upward band bending of 0.4 eV (Figure 4.13-b). Due to this competing mechanism of surface oxidation, the oxidation rate of Ag should increase with surface coverage and reach a stationary value at a thickness value above film percolation, in particular when no more substrate surface is exposed, *i.e.* for a continuous film.

Lastly, the exposure of a deposit of metallic Ag nanoparticles (t = 1.5 nm) to O_2 alone gives rise to only a modest uptake of O_β and O_{α_3} species, and no band bending in the wafer (Figure 4.14). On the contrary, when activated species are present in the plasma even at low %O_2, substrate and Ag particles actually oxidize as demonstrated by the increase of the Ag_2O photoemission fingerprints and the more sizeable shift of the Si 2p core level than after exposure to a pure Ar plasma (Figure 4.14). After an exposure of 90 s to the plasma, the rise of the AgO_x stoichiometry up to $x = 0.1$ at 4%O_2 and to $x = 0.42$ at 20%O_2, which is much higher than during growth (Figure 4.12) (even for growth under 100%O_2, for which $x = 0.28$) and close to the expected value of $x = 0.5$ for Ag_2O, demonstrates that the Ag oxidation phenomenon promoted by activated O species in the plasma is not really impeded, and that the presence of metal during growth is a consequence of a kinetic competition. This point is confirmed by

SDRS (Figure 4.15); while nanoparticles seem insensitive to exposure to an Ar plasma, their plasmonic response clearly fades away with oxidation under the oxygenated plasma.

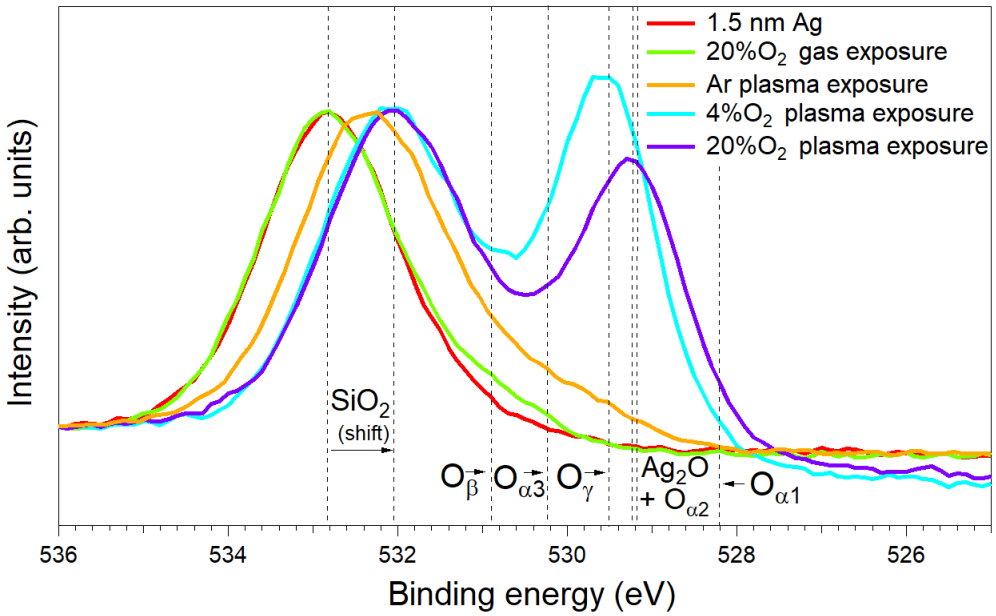

Figure 4.14 Evolution of O 1s core level of a 1.5 nm-thick Ag film deposited under pure Ar (red line) induced by an 90 s exposure (i) to molecular O_2 (green line) and (ii) to a plasma generated on a nearby alumina target with 4%O_2 (violet line) and 20%O_2 (blue line). The dotted vertical lines correspond to the binding energies of the different expected O species.

Finally, to assess the impact of substrate interaction with reactive oxygen species, the Ag growth under pure Ar on a native oxide-covered substrate was compared to that on a wafer pre-treated by exposure to a 40%O_2 plasma for 3 s (Figure 4.16). While no difference on percolation threshold t_p was observed (not shown), optics does not evidence a significant change in aspect ratio, as evidenced through the evolution of $\mathcal{A}_s(t)$ (see Figure 4.4). TEM image analysis showed no change in particle density.

4.4 *Ex situ* measurements

4.4.1 Ag nanoparticle STEM HAADF imaging and particle density

In order to clarify the main impact of O_2 on Ag film morphology during the nanoparticle growth stage, films deposited on amorphous silicon nitride SiN_x membranes were imaged by STEM plane views at the same 0.6 nm thickness but for different %O_2 conditions (Figure 4.17). This thickness value ensures a deposit in the growth stage and with saturated particle density, roughly before the generalized coalescence threshold t_c as shown by the $\mathcal{A}_s(t)$ signal in Figure 4.4.
Image analysis using the BlobLog and Watershed algorithms (see Chapter 2) led to a non-linear increase in particle density ρ_s (Figure 4.18) with a nearly constant lateral size of approximately 2 nm. Unfortunately, unlike particle density, uncertainties in deposited thickness and modification of particle shape by encapsulation do not allow to comment reliably the evolution of aspect

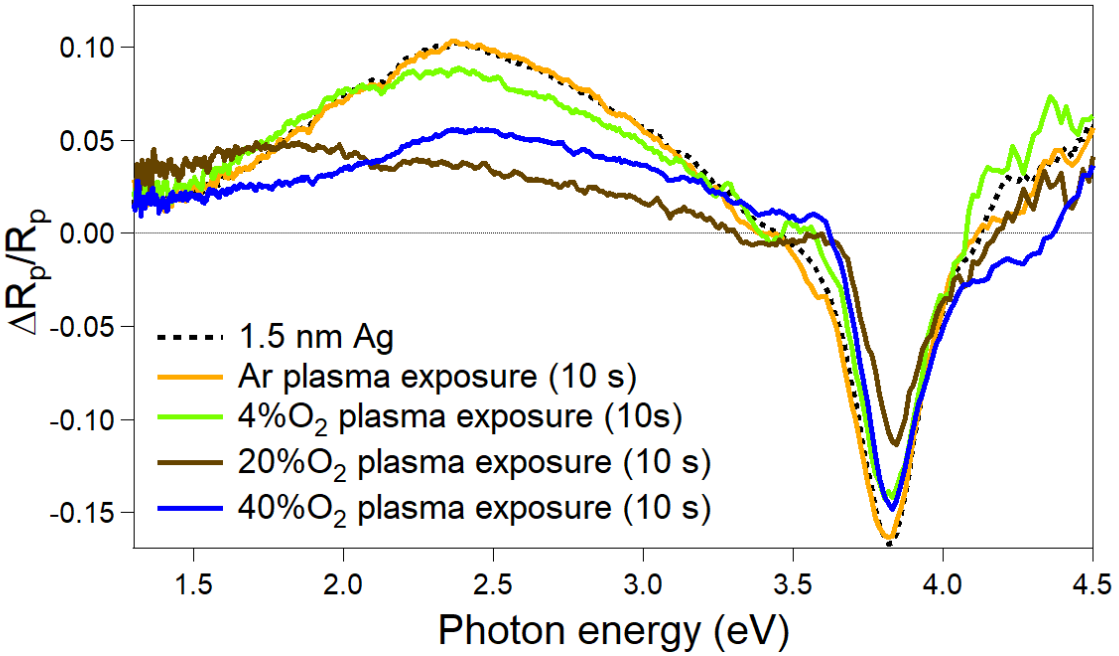

Figure 4.15 Same film treatment as in Figure 4.14 but followed by SDRS after a 10 s exposure to plasma of (i) pure Ar *i.e.* $0\%O_2$ (orange line) and (ii) $4\%O_2$, $20\%O_2$ and $40\%O_2$ (green, brown, blue lines, respectively).

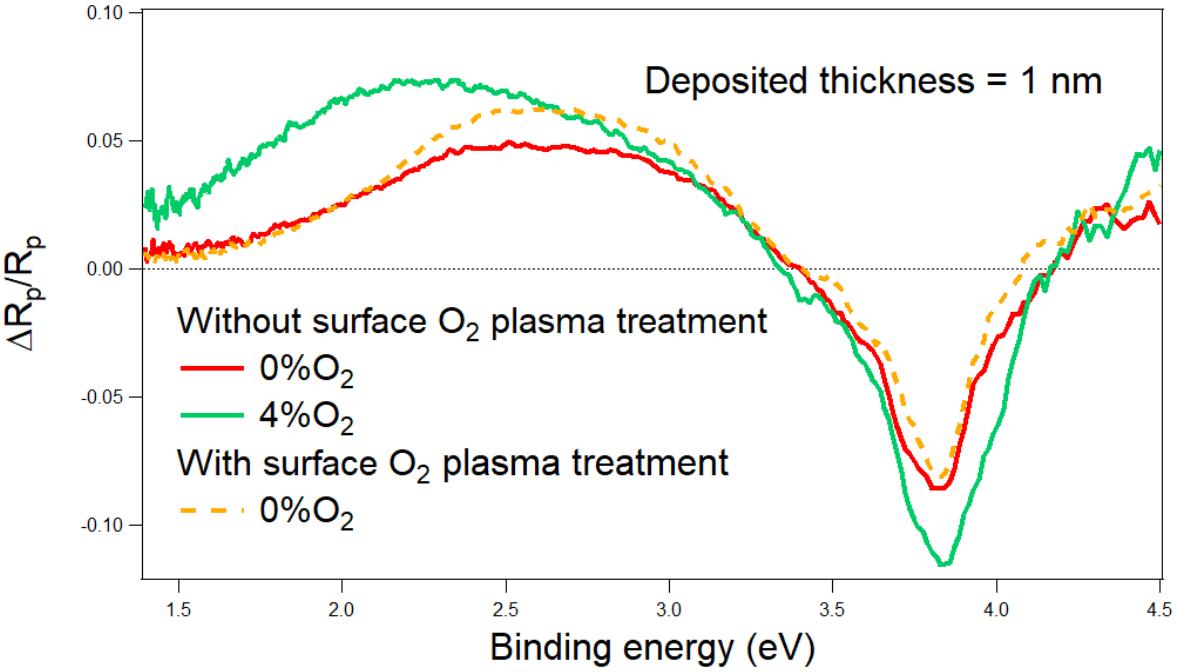

Figure 4.16 Comparison of p-polarized SDRS spectra for 1 nm-thick films deposited under (i) pure Ar ($0\%O_2$) without (red line) and with (orange dotted line) 3 s-long substrate plasma pre-treatment and (ii) under a gas mixture with $4\%O_2$.

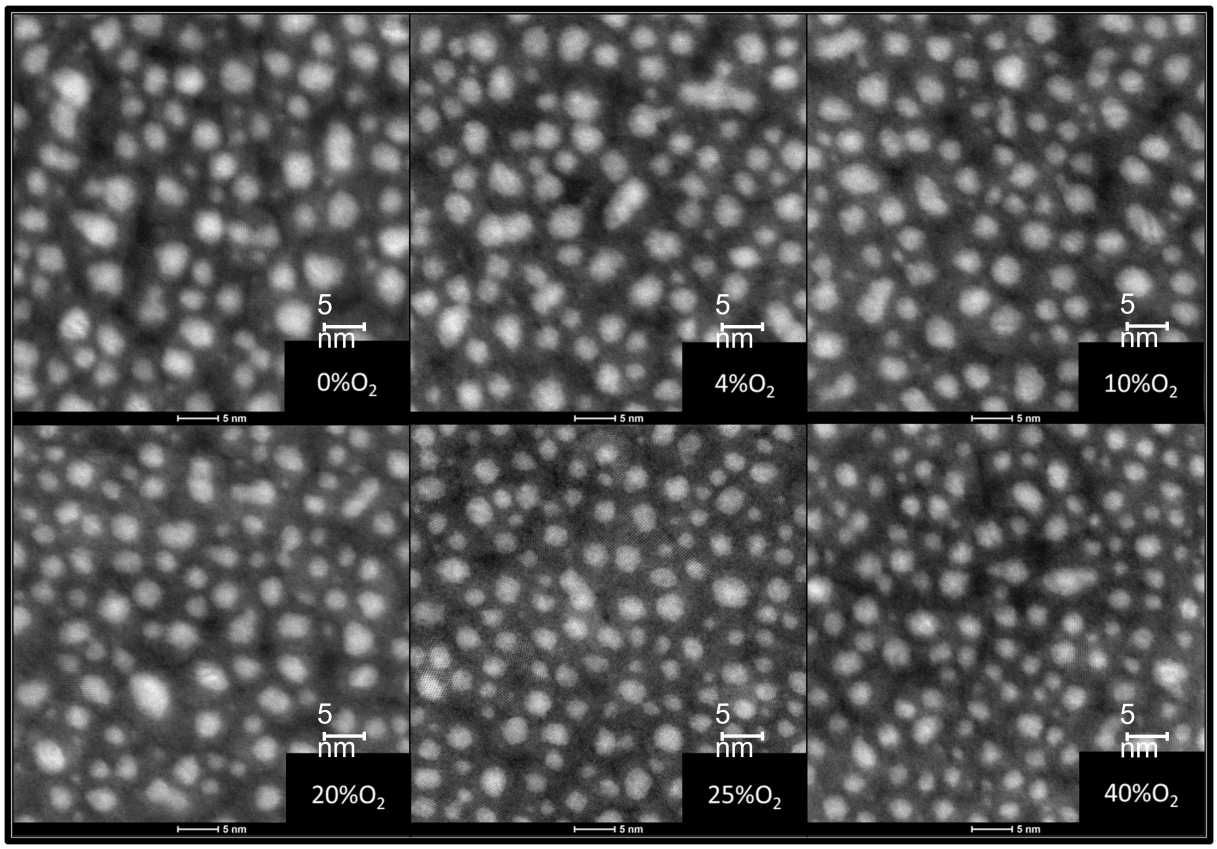

Figure 4.17 Examples of STEM-HAADF images taken at $t = 0.6$ nm-thick Ag films grown under different $\%O_2$ conditions.

ratio from mass conservation.

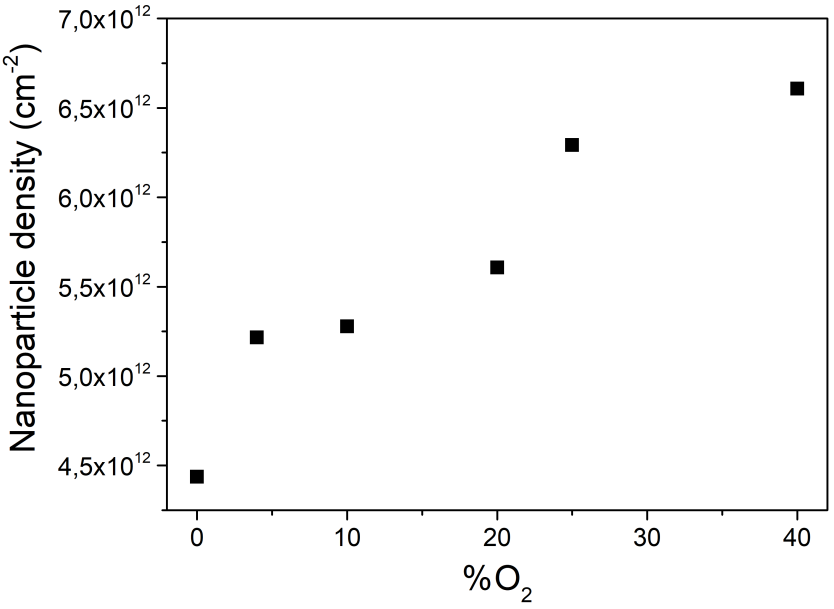

Figure 4.18 Particle density as obtained from TEM image analysis of 0.6 nm-thick Ag films grown under different $\%O_2$.

4.4.2 Film structure from *ex situ* x-ray diffraction

Photoemission results were supplemented by *ex situ* out-of-plane Bragg-Brentano and in-plane grazing incidence XRD measurements for 20 nm-thick Ag films deposited under different $\%O_2$ conditions on bulk fused silica wafers (Figure 4.19).
Compared to bulk atomic structure expectations, all diffractograms exhibit only Ag and ZnO wurtzite peaks, with a broad feature associated with amorphous SiO_2 from the silica wafer. The most intense (111) reflection of Ag_2O, expected at $2\theta \simeq 33°$, is absent in all diffraction geometries and for all $\%O_2$. The fortuitous overlap between $(111)_{Ag}$ and $(200)_{Ag_2O}$ reflections cannot hide textured Ag_2O grains, since the expected $(220)_{Ag_2O}$ peak along the perpendicular diffraction direction is not observed. Thus, the formed silver oxide does not appear to be crystalline, in agreement with similar studies of sputtering deposition [58, 150] although other studies have observed crystallized sputtered Ag_2O films [107, 134–136, 139, 271, 272]. Different film thicknesses, deposition kinetics and substrates may explain the discrepancy.

XRD peak positions, FWHMs and areas extracted from a global fit with Voigt line shapes have been translated into strain, coherent domain size D_{coh} (or Debye-Scherrer size) and volume ratio (Figure 4.20). The (001)-textured ZnO layer has a perpendicular D_{coh} close to its film thickness (4 nm) and shows an anisotropic distortion due to an in-plane compression stress. In comparison, the [111]-oriented Ag grains appear to be poorly strained, unlike the [100]-oriented grains which are in a tensile strain along both directions. D_{coh} obtained from all Ag peaks decreases with $\%O_2$ demonstrating a clear loss of crystallinity of metallic Ag. The most impacted peak is the out-of-plane $(111)_{Ag}$ which D_{coh} decreases from a value of ~ 15 nm close to the film thickness at $0\%O_2$ down to ~ 4 nm at $40\%O_2$. Surprisingly, a switch from out-of-plane texture from (111) to

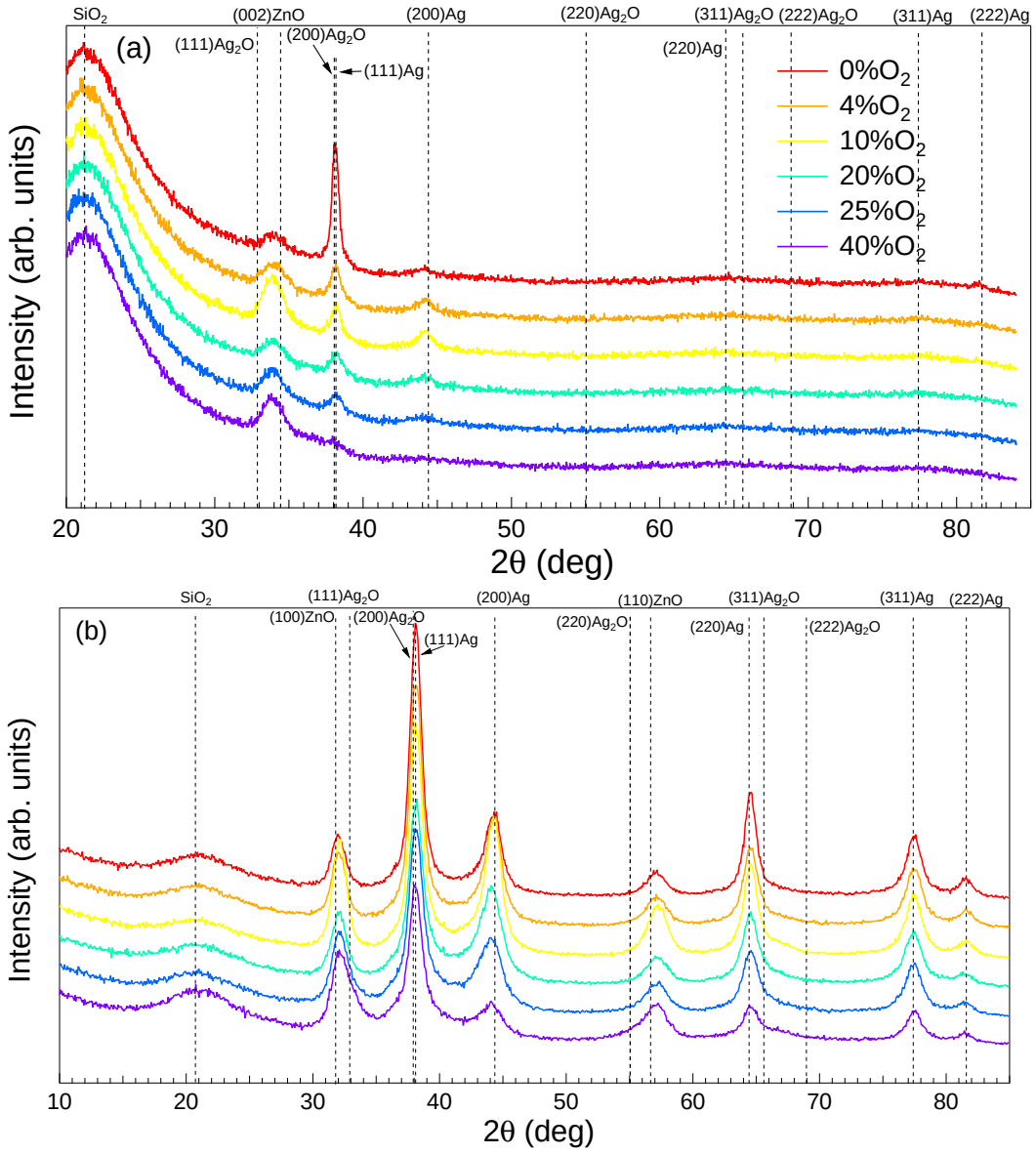

Figure 4.19 XRD measurements of 20 nm-thick films deposited on fused silica bulk substrates under different $\%O_2$ conditions: (a) Bragg-Brentano out-of-plane and (b) grazing incidence in-plane geometries. Vertical bars correspond to expected diffraction peak positions [247] for Ag, Ag_2O, ZnO and SiO_2.

(100) [58] (Figure 4.20-c) parallels the change in oxidation behaviour observed by photoemission at 10%O_2 (Figure 4.8).

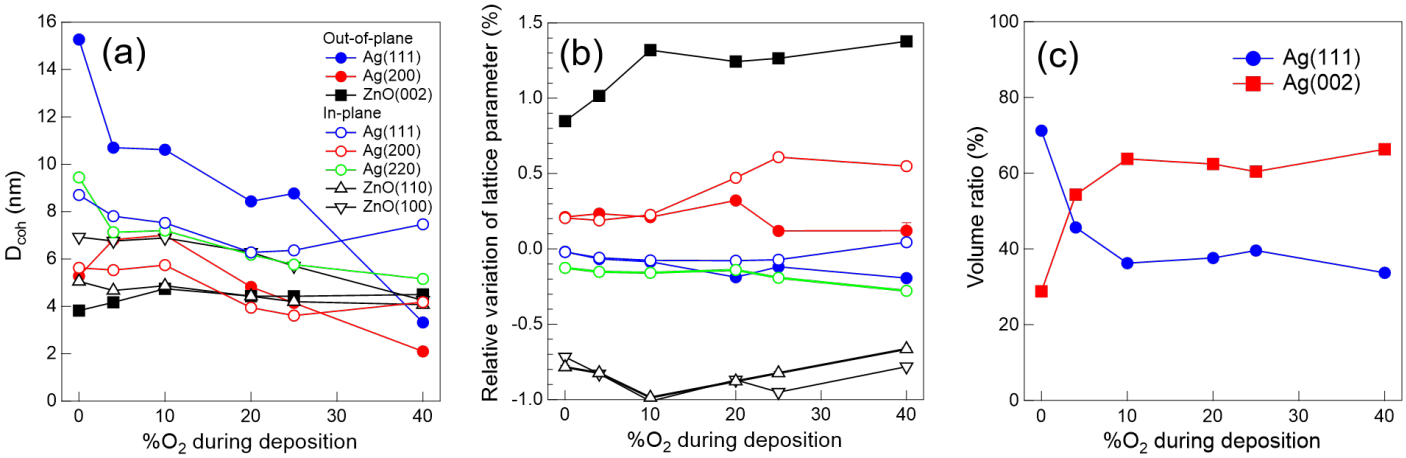

Figure 4.20 (a) Coherent domain sizes $D = \frac{0.9\lambda}{\cos(2\theta)\Delta(2\theta)}$ as deduced from the full-width at half-maximum $\Delta(2\theta)$ of the indicated peaks in the out-of-plane (Bragg-Brentano) and in-plane (GIXRD) configurations. (b) Strain or lattice parameter variation relative to bulk value obtained from the (2θ) position of the indicated peak. (c) Analysis of texture from out-of-plane XRD data: volume ratio as obtained by the fraction of $(111)_{Ag}$ and $(200)_{Ag}$ out-of-plane peak areas corrected from expected bulk powder intensities.

4.5 Discussion: the three %O_2 regimes

Based on all the results described in the previous sections, the effect of O_2 addition can be separated schematically into three regimes in terms of the % of O_2 flow during deposition: (i) a *low regime* (for %O_2 between 0 and 4%), (ii) an *intermediate regime* (for %O_2 between 10 and 20%), and (iii) a *high regime* (for %O_2 higher than 20%).

4.5.1 The low %O_2 regime: $0 \leq$ %O_2 ≤ 4

In this regime, a sizeable 20 % decrease of the percolation threshold t_p (Figure 4.2-a) is observed, from 5.4 nm at 0%O_2 to 4.3 nm at 4%O_2. This occurs with no significant impact on the final resistivity at $t = 20$ nm (Figure 4.2-b) despite a slight film crystallinity worsening (Figure 4.19). Regarding film composition, no clear trace of oxidation in the Ag 3d core level peak is present at any thickness within the sensitivity of photoemission spectroscopy (Figures 4.6-a and 4.12), in agreement with previous reports [111, 140]. The same conclusion is reached with the low intensity O 1s peak (Figure 4.11), its total area only leading to an AgO_x stoichiometry of $x = 0.02$ for 4%O_2. If for a 20 nm-thick continuous film, the major species are the O_β moiety (*i.e.* subsurface oxygen) and its companion surface $O_{\alpha 3}$ moiety (Figure 4.6-a), $O_{\alpha 1}$ goes through a maximum at $\sim$ 12 nm in thickness (Figure 4.11-a). This behaviour, observed even at higher %O_2 (Figure 4.11-b,c) seems to be related, within the probing depth of photoemission, to the percolation of the film and the fraction of film surface available for $O_{\alpha 1}$ adsorption or for oxidation (Ag_2O). Most likely, $O_{\alpha 3}$-O_β moities are related to the enhanced reactivity of undercoordinated sites

present in nanoparticles with molecular oxygen [166]; indeed, their respective O 1s peaks also appear after exposure of an Ag film grown under pure Ar (Figure 4.14 and Figure 4.5) to O_2 gas without plasma.

Based on the present data, different explanations can be put forward for the decrease in percolation threshold in this low $\%O_2$ regime. The first one is an increase in nucleation density [135,144]. Due to the 3D morphology, a substrate with a higher surface density of islands could in principle lead to a percolated network at a lower deposited thickness than a substrate with less numerous but larger islands. Assuming that t_p scales with the coalescence threshold t_c, at which generalized impingement between islands occurs,, one finds: $t_p \propto t_c \propto D_c^3 \rho_s / A_r$, where ρ_s is the saturation particle density during growth stage, A_r the equilibrium aspect ratio of particles (diameter/height) and D_c the in-plane size of particles at coalescence start. Since particles are in contact with each other at coalescence, $D_c \propto \rho_s^{-1/2}$ so that $t_p \propto 1/(\rho_s^{1/2} A_r)$. Thus, any variation of A_r or ρ_s translates into a variation of t_p as:

$$\frac{\Delta t_p}{t_p} = -\frac{\Delta A_r}{A_r} - \frac{1}{2}\frac{\Delta \rho_s}{\rho_s}. \tag{4.2}$$

However, TEM experiments (Figure 4.18) only show a moderate increase of ~ 10 % in particle density at thickness $t = 0.6$ nm (from $4.4\,10^{12}$ cm^{-2} to $4.9\,10^{12}$ cm^{-2}) when introducing $4\%O_2$, which should give rise only to a modest decrease of ~ 5 % for t_p. This value is far from the observed decrease of -20 % in t_p. In addition to this, a larger density of particles should induce an increased grain boundary density in the percolated film and thus a higher film resistivity [56,273] which is not observed experimentally (Figure 4.1-b). Thus, a change in nucleation density fails to fully explain by itself the observed drastic decrease in t_p.

The second explanation is an improved wetting of Ag islands in the initial stage of film growth, before coalescence. Flattened particles covering a larger fraction of the substrate surface should start impinging on each other at a lower deposited thickness. As shown in Figure 4.4, and despite noise in the measurement, the initial value of $\mathcal{A}_s$ and therefore the initial A_r in the growth regime before coalescence is larger when $4\%O_2$ is added. This particle flattening effect is also clearly evidenced in the SDRS spectra (Figures 4.3-a and b) by the red-shift and the increase in intensity of the parallel plasmon peak [200] between $0\%O_2$ and $4\%O_2$ at $t = 0.6$ nm. According to the $\mathcal{A}_s(t)$ evolution, at such an equivalent thickness, the film is indeed in the growth regime of isolated islands. This experimental SDRS trend is consistent with the qualitative *Granfilm* simulations shown in Chapter 2, while the change in particle density through particle-particle electrostatic coupling fails to account for the order of magnitude of the experimental red-shift of the parallel plasmon peak. Moreover, as it will be shown below for the high $\%O_2$ regime, a similar change in particle density is not always correlated with an earlier percolation threshold.

Particle flattening may be approached using thermodynamics through surface/interface energy considerations. For a truncated sphere equilibrium shape (*i.e.* ignoring crystalline anisotropy), the contact angle θ_c is driven by the balance between the particle surface energy γ_f, the substrate surface energy γ_s and the interface energy between the two materials $\gamma_f s$ via the Young-Dupré equation:

$$\begin{aligned} W_a &= \gamma_f(1+\cos\theta_c) \\ W_a &= \gamma_s + \gamma_f - \gamma_f s, \end{aligned} \tag{4.3}$$

where W_a stands for the adhesion energy. The variation ΔA_r of aspect ratio:

$$A_r = \frac{2}{1-\cos\theta_c} \tag{4.4}$$

induced by a change in contact angle $\Delta\theta_c$ reads:

$$\frac{\Delta A_r}{A_r} = -\frac{\sin\theta_c \Delta\theta_c}{1-\cos\theta_c}. \tag{4.5}$$

Thus, starting from a contact angle of $\theta_c \simeq 130°$, corresponding to the energetics of Ag/SiO_x [200, 249], a change in $\frac{\Delta t_p}{t_p} \simeq -20$ % due to $4\%O_2$ addition (Figure 4.2) would require a moderate change of $\Delta\theta_c \simeq -24°$ according to Equation 4.2 and ignoring the effect of density. Although not directly comparable in terms of temperature, this order of magnitude matches the variation of $\Delta\theta_c \simeq -20°$ observed in the low regime of oxygen activity on melted Ag sessile drop measurements [142, 143]. From an energetic point of view, this would require a variation of:

$$\frac{\Delta W_a}{W_a} - \frac{\Delta\gamma_f}{\gamma_f} = -\frac{\sin\theta_c \Delta\theta_c}{1+\cos\theta_c} \simeq 90\% \tag{4.6}$$

which can be achieved by a decrease of γ_f and/or an increase in W_a. This change in interface energetics W_a could be related to the impact of activated O species on the substrate itself, as seen in Figure 4.13 with the decrease of the C 1s fingerprint of carbonaceous contamination. Even if a slight increase of A_r is observed in the initial value of $\mathcal{A}_s(t)$ after plasma treatment, neither t_p (5.3 nm for a $0\%O_2$ growth on a plasma-treated wafer instead of 5.4 nm for an as-introduced one), nor the slope of evolution of $\mathcal{A}_s(t)$ in the coalescence regime (Figure 4.4), nor the parallel plasmon peak (Figure 4.16) at $t = 1$ nm are impacted by wafer surface plasma treatment before deposition. All these findings rule out a major impact on Ag wetting of a substrate "cleaning effect" by the plasma. On the other hand, oxygen adsorption at the surface of the Ag nanoparticles ($O_{\alpha 3}$) or in a subsurface form (O_β) as observed by photoemission (Figure 4.6 and Figure 4.11-a) is a likely explanation of this enhanced wetting. Nevertheless, the thermodynamic stability diagrams of O-adsorption at the surface/subsurface of Ag(111) [274] and Ag(100) [275] obtained by *ab initio* calculations show that a variation of surface energy $\frac{\Delta\gamma_f}{\gamma_f}$ of at best -40% can be achieved at the highest oxygen chemical potential, before the formation of bulk Ag_2O. This value is less than half of what is required by Equation 4.6.

Lastly, a delay in coalescence dynamics induced by oxygen adsorption could also explain the formation of elongated and irregular-shaped clusters instead of round-shaped islands and therefore an earlier percolation (Figure 4.2). Previously reported in the literature only via *ex situ* scanning electron microscopy imaging [150, 276], the phenomenon of partial coalescence appears clearly herein, when comparing $0\%O_2$ and $4\%O_2$, in the change in slope in the evolution of $\mathcal{A}_s(t)$ (Figure 4.4) and the match between the experimental and simulated SDRS line shapes at $t = 3$ nm (Figure 4.3-b) . A likely explanation lies in the observed switch of film texture from 70 % [111]-oriented to 65% [100]-oriented grains when O_2 is introduced in the plasma, as shown in Figure 4.20. Besides adsorbed O, the vertical interplanar distance mismatch between [111] (2.35 Å) and [100] (2.045 Å) oriented grains hinders their coalescence process. At $4\%O_2$, this structural impediment reaches a maximum with a 50-50% balance between both types of grains, not speaking about their random relative in-plane orientations. As predicted by first principle calculations, such a reversal of film texture could find its origin (i) in a more favourable isolated oxygen adsorption energy at a (100) rather than a (111) surface, associated to a much larger O surface diffusion barrier [277] ; and (ii) in a lower O-covered surface energy of (100) [275]

than (111) [274] surface at all O chemical potentials, which nearly compensates the difference in compacity between the two orientations.

To conclude, the earlier percolation induced by the $4\%O_2$ addition results from a combination of effects: (i) change in particle density, (ii) a better wetting before coalescence and (iii) a delayed coalescence due to oxygen adsorption. The last two mechanisms appear to be the most effective. Substrate "cleaning" by exposure to oxygenated plasma, on the other hand, does not seem to play a major role. The lack of clear-cut oxidation and the presence of only surface/subsurface O moities argue in favour of a "surfactant" mechanism of O_2 in this regime.

4.5.2 The intermediate $\%O_2$ regime: $10 \leq \%O_2 < 20$

While still being well below the measured value under pure Ar, the thickness at the percolation threshold only slightly decreases from 10 $\%O_2$ to $20\%O_2$ (Figure 4.2-a). Concurrently, the resistivity at $t = 20$ nm starts rising (Figure 4.2-b). Particle flattening and delayed coalescence are still at work just like in the low $\%O_2$ regime (Figure 4.3 and 4.4), alongside the effect of particle density increase, although more moderate than in the low O_2 regime (Figure 4.18).

Chemical analyses in the intermediate regime show a transition towards a component dominated by O_{α_1} species in 20 nm-thick film (Figure 4.8). In parallel, the fractions x and y of oxidized Ag slowly increase in this regime, even though the major fraction of the film still remains metallic (Figure 4.8). Following this uptake in O_{α_1} that denotes a more "oxidative" plasma [166], a gradient of composition develops across the film thickness before reaching a plateau value of $\simeq 8-10\%$ at 10 nm (Figure 4.12-b). In parallel, at intermediate thicknesses ($\sim$ 6 nm; Figure 4.11-b), a Ag_2O (or O_{α_2}) species is detected before completely vanishing in thicker films. These observations can be linked to a change in the oxidation behaviour of the exposed Ag surface that follows the growth mode of the film *i.e.* the transition from 3D particles to a continuous, uniform film. The case being clearer in high $\%O_2$ regime, it will be commented in the next section.

SDRS spectra at $t = 0.6$ nm (Figure 4.3-a) for $10\%O_2$ start differing from those corresponding to 4 $\%O_2$. The trend becomes clearer at $t = 3$ nm (Figure 4.3-b), with an overall decrease in intensity and a red-shift of both resonances. According to dielectric simulations (Chapter 2), these observations can be explained by the formation of a core-shell structure due to adsorbed oxygen. A similar trend is observed later in the high $\%O_2$ regime at $40\%O_2$ (see below). Thus, the initial stage of deposition is mainly governed by the growth of metallic nanoparticles with absorbed O at their surface in a core-shell like-configuration, that is the starting point for the gradual oxidation of the film with increasing thickness.

4.5.3 The high $\%O_2$ regime: $\%O_2 \geq 20$

The high $\%O_2$ regime is characterized by an abrupt increase of the oxide fraction AgO_x in the film stoichiometry at $t = 20$ nm (Figure 4.8-b), which stabilizes at $x = 0.26$ for $40\%O_2$, a value only slightly lower than for a deposition under pure O_2 ($x = 0.28$). From the Ag 3d core level, all Ag atoms appear to be in an oxidized state (Figure 4.8-a) at $t = 20$ nm. This occurs alongside a drastic change in film chemistry; above $20\%O_2$ at $t = 20$ nm, the O 1s core level is characteristic of an Ag_2O-like compound (Figure 4.8-a). Therefore, in agreement with previous reports [140], thick films deposited in the high O_2 regime appear to be mainly composed of a highly sub-stoichiometric oxide that is not crystallized (see Figure 4.19).

Both the percolation threshold and the film resistivity at $t = 20$ nm (Figure 4.2) follow a linear evolution from the intermediate regime. The increase in resistivity is consistent with the enhanced film oxidation, but also with the increase in nanoparticle density (Figure 4.18) that scales with the final grain boundary density in the percolated film. However, compared to resistivity expected for a pure oxide (59.3 Ω.cm for AgO and $3.3\,10^3 - 7\,10^8$ Ω.cm for Ag_2O) [107,139,278], the seven orders of magnitude lower value measured at $40\%O_2$ (57 $\mu\Omega$.cm) suggests that the $t = 20$ nm-thick film is not homogeneous. Indeed, a composition gradient across the layer thickness is clearly evidenced by the analysis of photoemission results (Figure 4.12-b,c).

Besides resistivity, SDRS and XRD measurements also raise the question of composition gradient in the film. Metal particles are required to observe a plasmon resonance at low thickness (Figure 4.3-a). At the start of deposition in the nanoparticle growth regime, the film is mostly metallic according to photoemission (Figure 4.12-c), thus explaining the presence of Ag metal peaks in $t = 20$ nm XRD patterns (Figure 4.19). These nanoparticles form through competitive mechanisms (i) of metal-metal clustering by fast Ag surface diffusion on silica and (ii) of oxidation, probably mainly by direct impact as the substrate itself reacts with activated-oxygen species (Figure 4.13). As the surface coverage increases, they further oxidize. Thus, the optical signature for the formation of an oxide shell on a metallic core (red-shift for the parallel plasmon peak alongside a decrease in intensity) is even more apparent in SDRS spectra at higher thickness values (Figure 4.3-b at $t = 3$ nm versus Figure 4.3-a at $t = 0.6$ nm). After percolation, and moreso after the formation of a continuous film, the oxide fraction reaches about half of its final value (Figure 4.12-c; $40\%O_2$; $t > 6$ nm). In this thickness regime, film growth takes place on a Ag-suboxide where Ag ad-atom diffusion is slowed down, and metallic Ag clustering is unlikely compared to SiO_x, given its higher adsorption energy. Moreover, the sticking coefficient of activated O species [140], and probably their diffusion lengths at the surface, increase. Thus, a change from an oxidation mechanism of "Eley-Rideal" to a "Langmuir-Hinshelwood" type due to the evolution of the film morphology leads to an oxidation gradient with (mostly) metallic Ag being deposited in the initial stages. This explains (i) the existence of an initial plasmonic signal (Figure 4.3-a), (ii) a reflectivity characteristic of a percolated film at $t = 3$ nm with a continuous increase in the near infrared, (iii) a low resistivity of the final film compared to a bulk oxide and (iv) the presence of Ag metallic XRD reflections, albeit less crystalline for higher $\%O_2$ conditions. The transition and the actual oxidation state of the film is governed by the balance between (i) the fraction of covered substrate (and thus the film morphology), (ii) the relative arrival rates of Ag and activated O species and (iii) their relative sticking coefficients and diffusion lengths on SiO_x and Ag-suboxide. The existence of the initial competition between metal clustering and oxidation is confirmed by the strong reactivity observed during post-growth exposure to a O-rich plasma ($20\%O_2$ in Figure 4.14); in principle, complete Ag oxidation is not really impeded. On the other hand, not even the growth under pure O_2 plasma is able to reach a stoichiometry close to Ag_2O ($x = 0.28$). Anticipated in the previous section, such a general scenario seems to be also at work in the intermediate regime of $\%O_2$, but to a lesser extent, as the content of activated species in the plasma is lower (Figure 4.12). The transition from metallic to more oxidized Ag (Figure 4.12) and the switch from $O_{\alpha 3}$-O_β to Ag_2O moities (Figure 4.11) correlate with the percolation threshold of the film.

All these observations rationalise the methodology of gas deployment in the early stages of film growth proposed in previous studies [111,138,148] to benefit from earlier film percolation while avoiding the deleterious impact of oxidation on film resistivity. But such a trick is not the panacea; it requires an apparatus-dependent optimisation as it relies on a subtle kinetic balance

between growth and oxidation rates.

4.6 Conclusion

In this chapter, the effects of O_2 addition during magnetron sputtering of Ag films was explored. It was shown that eventhough O_2 shares some similarities with N_2 (such as a decrease of percolation threshold, a loss of crystallinity, a change in texture and a resistivity increase with % in the gas flow), the magnitudes of trends are very different. In particular, O_2 differentiates itself from N_2 especially due to its higher reactivity. A rich chemistry between Ag and O was observed depending on the $\%O_2$, from adsorbates to the formation of suboxides. The impact of the latter on film resistivity was much more noticeable than for N_2 for which no compound is formed. Three $\%O_2$ regimes were distinguished. Firstly, at low O_2 flow ($0 \leq \%O_2 \leq 4$), a combined effect of (i) nanoparticle flattening and density increase in the initial stages of film growth, (ii) a delayed coalescence and (iii) a change in film texture from [111] to [100] can explain the strong reduction in the percolation threshold thickness. Neither clear-cut Ag oxidation nor film resistivity increase are observed. The observed change in surface/interface energy due to the formation of adsorbed $O_{\alpha 1}/O_{\alpha 3}$ and subsurface O_β moities on the growing nanoparticles was put forward to explain these findings. In the intermediate regime ($10 \leq \%O_2 < 20$), in addition to the particle flattening, to the onset of increase in resistivity and to a weaker decrease in percolation threshold thickness, $O_{\alpha 1}$ moieties become the main species of adsorbed oxygen. Finally, in the high regime ($\%O_2 \geq 20$), actual oxidation takes places in the form of an Ag_2O-like amorphous/not-crystallized compound and has a strong impact on resistivity. The found gradient of oxidation was explained by growth kinetics involving a complex balance between substrate reactivity, arrival rates of Ag and of activated O species, metal-metal aggregation, O diffusion, and film morphology.

Chapter 5

Effect of N_2 and O_2 addition during the sputtering growth of Ag films on AZO underlayers

In previous chapters (Chapters 4 and 3), the study of the effect of N_2 and O_2 addition during Ag film sputtering deposition on the amorphous, oxidized surface of a silicon wafer ("SiO_x"), revealed a number of more or less drastic consequences on the growth mechanism and the resulting properties of the Ag film. In this chapter, a new study will be carried out with the same gases but on a pre-deposited wurtzite c axis-oriented aluminium-doped zinc oxide (AZO) film. The use of these kinds of underlayers for the growth of Ag is widespread all across the glazing industry, where it is known to improve the quality of sputtered Ag films and therefore the efficiency of different products such as Low-E glazings. The objective of this chapter is to verify whether the previous conclusions on the effects of N_2 and O_2 gases on the Ag film growth (lower percolation threshold thickness, higher resistivity, oxide formation...) will be affected by the introduction of this new substrate surface.

Table of contents

5.1 The AZO underlayer: thickness and deposition conditions

In this chapter, we will be studying Al-doped Zinc Oxide (AZO) underlayers for the growth of Ag films. As previously discussed in Chapter 1, Al-doping increases the conductivity of ZnO, so that AZO thin films can be deposited directly using DC magnetron sputtering deposition from ceramic AZO targets. Although Al doping can modify the unit cell parameters [183, 279, 280], AZO films are still (0001) oriented in the out-of-plane direction and still act as an epitaxial template for Ag growth like pure ZnO films. Finally, the use of AZO underlayer also puts our work much closer to industrial applications in the glass industry.

AZO underlayers were deposited by DC sputtering from a ceramic target (ZnO/Al_2O_3, 98%/2%-weight by Neyco) on Si wafers right before each experiment. The composition of the target was constant for all experiments in this work as well as the deposition conditions (50 W, 2 μbar total pressure, 50 sccm total gas flux). In order to decide on the other remaining parameters for the AZO deposition protocol, namely film thickness and gas composition, three conditions and thicknesses were tested:

- **Condition 1:** 2 nm-thick AZO layer, deposited under 50 sccm pure Ar;
- **Condition 2:** 5 nm-thick AZO layer, deposited under 50 sccm pure Ar;
- **Condition 3:** 5 nm-thick AZO layer, deposited under 50 sccm $10\%O_2$.

The chosen thickness values are in the range that is typically used in industrial applications for Low-E glass production. Also, we note that increasing the AZO thickness results in an increase of roughness, a parameter which is not treated in this work [12, 281]. When comparing results from these three conditions, the selected criteria for choosing the optimal one were the minimization of the percolation threshold thickness (t_p) and the final resistivity (ρ) of a 20 nm-thick Ag film deposited on top. The procedure was as follows. For each of the three above-mentioned conditions, an AZO underlayer was first deposited on a Si wafer substrate with pre-deposited Ag electrodes (for the real-time resistance measurements). The sample was then stored in the MISSTIC load-lock chamber under vacuum during the pre-sputtering stage of the Ag target, to avoid any contact of the AZO with air. Finally, 20 nm-thick Ag films were deposited using standard conditions (2 μbar, 50 sccm pure Ar, 50 W DC), alongside real-time SDRS and resistivity measurements.

For each condition 1-3, p-polarized SDRS spectra for thicknesses between $t = 0.4$ nm and $t = 1$ nm are displayed in Figure 5.1, where they are compared to a direct deposition on a SiO_x surface (Si wafer surface, no underlayer) for $t = 1$ nm (dotted line). First of all, looking at the low-energy in-plane plasmon peak, we see that no matter the AZO deposition conditions, a strong red-shift coupled with an increase in intensity is observed with respect to Ag deposition on SiO_x. This is consistent with the presence of more flattened Ag nanoparticles at similar thickness, which is a well-known effect of AZO and a consequence of the lower AZO/Ag interface energy due to the epitaxial relationship between these two materials (see Chapter 1 for more details). On the other hand, no clear energy shift or change in intensity is found when comparing the spectra for the three AZO deposition conditions at an equivalent thickness. This demonstrates that varying the AZO deposition protocol, at least in the explored range, does not significantly impact the Ag nanoparticle aspect ratio or density.

Figure 5.2 reports the values of the percolation threshold thickness (t_p) and film resistance (ρ) at $t = 20$ nm for each of the deposition conditions. **Condition 1** (2 nm-thick film, deposition under pure Ar) is clearly less favourable from an Ag film quality perspective because of the

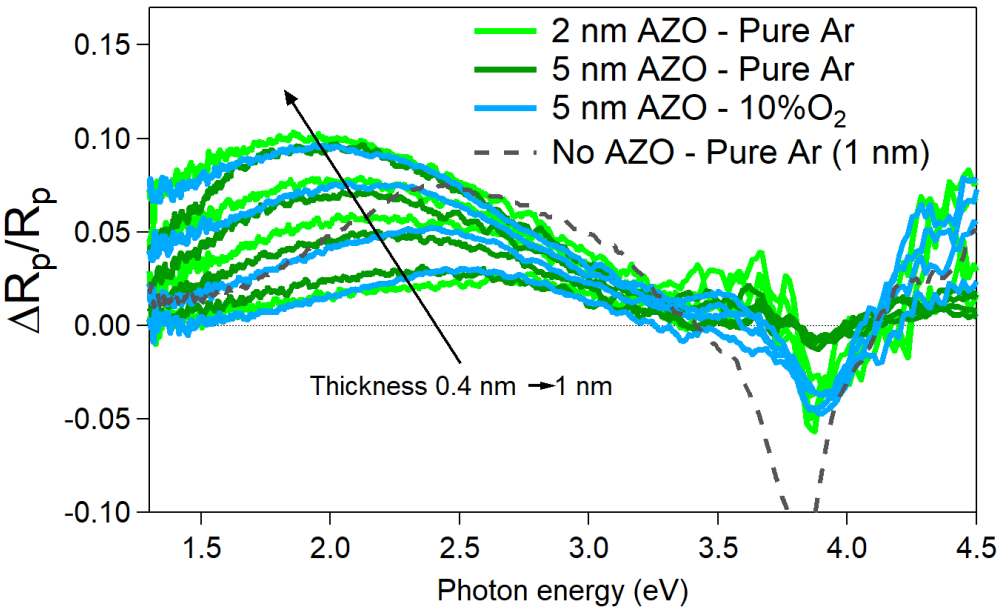

Figure 5.1 SDRS spectra in p polarization for each of the three tested AZO underlayer deposition conditions. Spectra are shown for Ag thickness values ranging from 0.4 nm to 1 nm. Spectra are compared to deposition of $t = 1$ nm Ag on SiO_x, with no underlayer (dotted line).

higher values of both t_p and ρ. Comparing the other two conditions, **Condition 2** (5 nm-thick film, deposition under pure Ar) has a lower t_p value, but at the expense of a higher value for ρ, whereas the opposite is observed for **Condition 3** (5 nm-thick AZO film deposited under 10%O_2). A similar study was done by Tsuda *et al.* [190] on the effect of the deposition conditions for a 15 nm-thick AZO underlayer, on the electrical properties and surface roughness of a 20 nm-thick Ag film deposited on top. This study only reported a slight variation in ρ ($\sim 0.1\ \mu\Omega.cm$) with increasing %O_2 (from 0% to 50%). On the contrary, film roughness was shown to change to a greater extent with increasing %O_2. In our case, however, we observed a roughly 1.4 $\mu\Omega.cm$ difference in the Ag film resistivity with %O_2. This sizeable difference could be explained by the different deposition conditions for the films (pressure and power) and by different values of film roughness, since thinner (5 nm) and therefore less rough films [281] are used in the present work. However, as it was already said, it is outside the scope of the present work to analyse the role of AZO film roughness in depth, and as such we will not go further into this analysis.

Based on these results, and since one of the objectives of this study is the development of a new strategy combining gas and substrate effects for lowering the Ag percolation threshold t_p and obtaining thinner and more conductive Ag films, it was decided to choose **Condition 2** (5 nm-thick AZO film under pure Ar) as the standard deposition condition for the AZO underlayer. We considered this choice to be the most sensible one because this condition yielded the lower t_p value, and therefore it gave us the chance to explore the full extent to which the percolation threshold could be decreased by reactive gas addition. Moreover, AZO deposition under pure Ar gas avoids the problem of over-oxidation of the substrate layer and potential O diffusion to the Ag layer from an O-rich AZO film as previously suggested by Jeong *et al* [150].

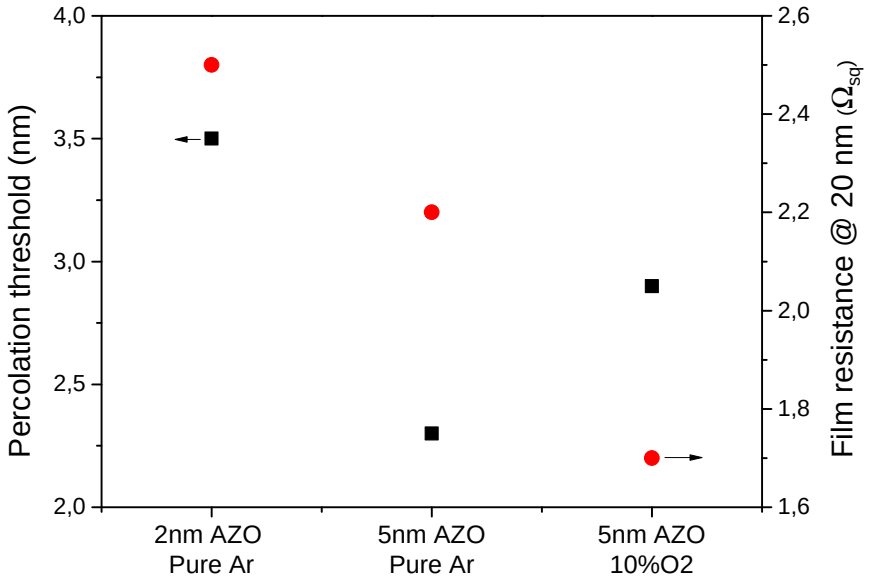

Figure 5.2 Percolation threshold thickness and film resistance at $t = 20$ nm for each of the tested conditions for AZO deposition.

5.2 Ag film deposition on AZO underlayers: effect of N_2 addition

The effect of N_2 addition on the growth of Ag films was studied in the same way as it was for deposition on SiO_x (*i.e* the native oxide on the surface of a Si wafer) in previous chapters. An AZO underlayer was deposited before each experiment using the conditions described above, and stored under vacuum during the pre-sputtering of the metal target prior to Ag film deposition. We will analyse the results from real-time, *in situ* and *ex situ* characterizations for Ag deposition on the AZO underlayer with increasing $\%N_2$ conditions, and compare those results to those from our study on SiO_x in Chapter 3.

5.2.1 Film resistance measurements

Values for the percolation threshold thickness t_p for increasing $\%N_2$ values are shown in Figure 5.3-a and compared to the SiO_x case (from Chapter 3).

As expected, the film percolation threshold for $0\%N_2$ is reached at a lower thickness when Ag is deposited on an AZO underlayer rather than on SiO_x. The 3.1 nm decrease in t_p between the two substrates is comparable to that measured in Q. Hérault's thesis work [12] (3.4 nm). It is a consequence of the improved wetting of Ag nanoparticles on AZO compared to SiO_x due to a lower interface energy, which is itself explained by the epitaxial relation between Ag(111) and the (0001) surface of the c-axis oriented AZO crystallites. This improved wetting was already apparent in the SDRS results of Figure 5.1 and will also be obvious later on when analysing STEM HAADF images of Ag nanoparticles. In short, flattened particles on AZO will impinge upon each other during film growth and form a conductive network sooner than the round and more spherical particles observed on SiO_x.

We will now look in more detail at the evolution of t_p (Figure 5.3-a) for increasing $\%N_2$. A slight increase in t_p is first observed when going from 0% to $4\%N_2$, which is followed by a decrease in t_p down to a minimum value of 1.3 nm at $30\%N_2$, an exceptionally low thickness value for a conductive thin Ag film. Increasing the N_2 flux above ~ 10 % decreases the value for t_p for both substrates AZO and SiO_x. The slight increase in t_p between 0% and $4\%N_2$ on AZO contrasts with the decrease of roughly 1 nm observed on SiO_x. This anomalous behaviour of t_p at $4\%N_2$ will be discussed in the following sections by combining results from SDRS, XRD and TEM analysis.

Another trend for which an interesting comparison can be made between the two substrates is the Ag film resistivity ρ at $t = 20$ nm (Figure 5.3-b). For $0\%N_2$, $\rho = 5.5\ \mu\Omega.cm$ and $\rho = 7.9\ \mu\Omega.cm$ for deposition on AZO and on SiO_x, respectively. The value of ρ for deposition on AZO is in line with results from Tsuda *et al.* [190], who reported values between 4.0 and 6.0 $\mu\Omega.cm$ for Ag films deposited on 15 nm-thick AZO underlayers grown under similar conditions. With increasing $\%N_2$, ρ increases for both substrates, almost in parallel and with a difference that is roughly constant and close to $\sim 1\mu\Omega.cm$. This observation lets anticipate that the origin for the deterioration in film resistivity is the same for both substrates *i.e.* intrinsic to the film growth itself, and not dictated by the interface. This hypothesis will be further developed and put to the test with the rest of the data in later sections.

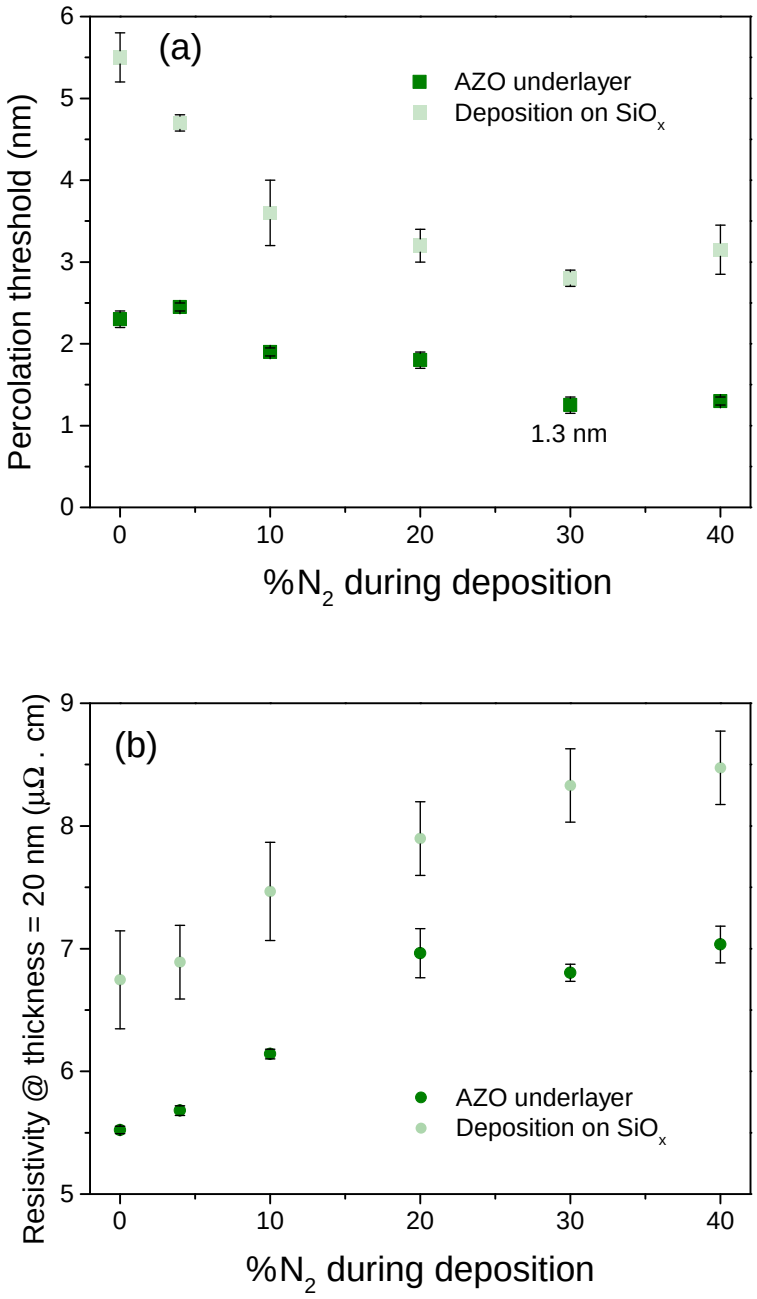

Figure 5.3 (a) Ag percolation threshold thickness t_p and (b) film resistivity ρ at $t = 20$ nm measured for different $\%N_2$ conditions for deposition on AZO underlayer. Results are compared to the SiO_x case. Values and error bars shown correspond to the mean value and the standard deviation several experiments (at least two for each condition).

5.2.2 SDRS measurements

p-polarized SDRS spectra for Ag films with nominal thickness values of 0.4 nm and 0.6 nm (*i.e* before film percolation, which does not occur below $t = 1.3$ nm for any of the studied conditions) are shown in Figure 5.4 for different values of $\%N_2$. The thickness values are chosen lower than those used for the study on SiO_x surfaces (0.6-2 nm), so as to remain in the nanoparticle regime before percolation and to avoid the parallel plasmon peak centroid from red-shifting too far into the infra-red region, outside the spectral range of the spectrometer. Once again, this shift is merely a consequence of the improved nanoparticle wetting on AZO, like it was observed in Figure 5.1 for deposition under $0\%N_2$.

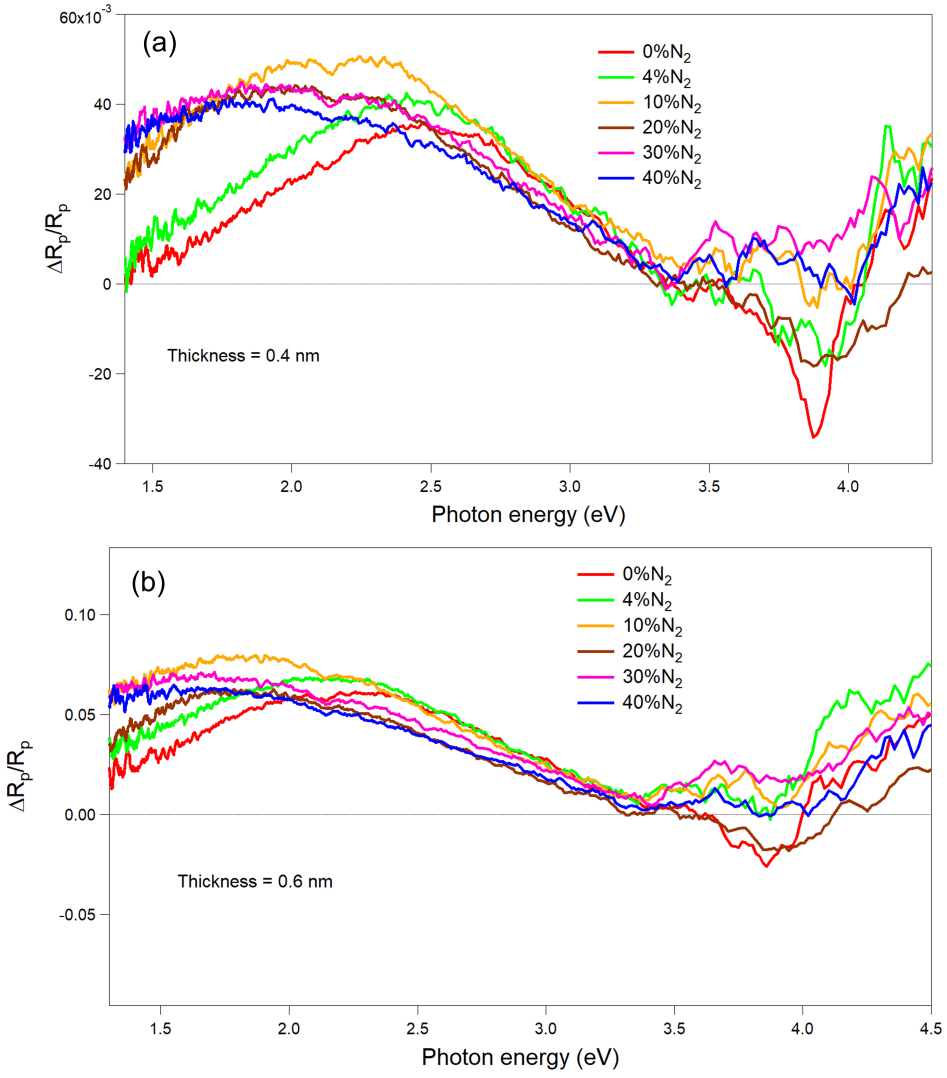

Figure 5.4 p-polarized SDRS spectra for different $\%N_2$ during deposition of Ag/AZO at a nominal deposited film thickness of (a) $t = 0.4$ nm and (b) $t = 0.6$ nm.

Looking at the low-energy resonance peaks in the SDRS spectra of Figure 5.4, the parallel plasmon peak red-shifts and increases in intensity when $\%N_2$ goes from 0% up to 10%. This change is consistent with a progressively higher particle aspect ratio (*i.e.* particle "flattening"), and is observed for both thickness values $t = 0.4$ nm and $t = 0.6$ nm. We note that for deposition on

SiO_x, the low-energy feature reached an intensity maximum at $4\%N_2$, not at $10\%N_2$. Further increasing the nitrogen content above $10\%N_2$ still leads to a red-shift, but alongside a decrease in intensity of the parallel plasmon peak, just like on SiO_x. On AZO, unlike on SiO_x, the decrease in intensity for the low-energy peak is observed even for films as thin as $t = 0.4$ nm.

SDRS data are further supported by the integrated values $\mathcal{A}_s(t)$ of the s-polarized SDRS spectra for different $\%N_2$ conditions (Figure 5.5). While the value of $\mathcal{A}_s(t)$ for $\%N_2 \geq 10\%$ is consistently higher than the value for $0\%N_2$, the integral for $4\%N_2$ is essentially equal to that for $0\%N_2$ throughout the whole deposition. $\mathcal{A}_s(t)$ being a descriptor of nanoparticle aspect ratio, this trend suggests an effect on the nanoparticle aspect ratio for $\%N_2$ above a certain threshold of nitrogen. This could be a key factor in explaining the anomalous behaviour of t_p at $4\%N_2$ (Figure 5.3), which escaped the otherwise decreasing trend of t_p with increasing $\%N_2$. In short, since the particles are already flattened at $0\%N_2$ because they are deposited on AZO, the effect of N_2 at low concentration ($4\%N_2$) is less impactful than it was for SiO_x.

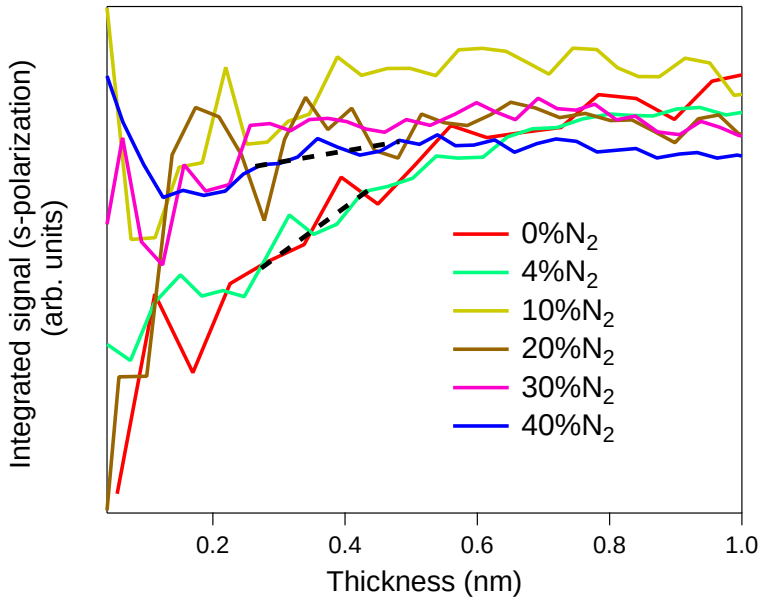

Figure 5.5 Integrated s-polarized SDRS signal for Ag deposition on AZO underlayers for different $\%N_2$. Due to a low signal-to-noise ratio at the very beginning of the deposition, the minimum of the $\mathcal{A}_s(t)$ which would otherwise indicate the onset of generalized coalescence is not visible. Dotted black lines are shown as a guide to the eye to compare the relative evolutions.

To explain the role of N_2 in the change in aspect ratio of the Ag/AZO nanoparticles, we will look further into the presence (or lack thereof) of adsorbed N species on the Ag surface in the next section using *in situ* XPS.

5.2.3 *In situ* XPS measurements for 20 nm-thick films

Figure 5.6 shows the *in situ* XPS spectra for 20 nm-thick Ag films deposited under different $\%N_2$ conditions.

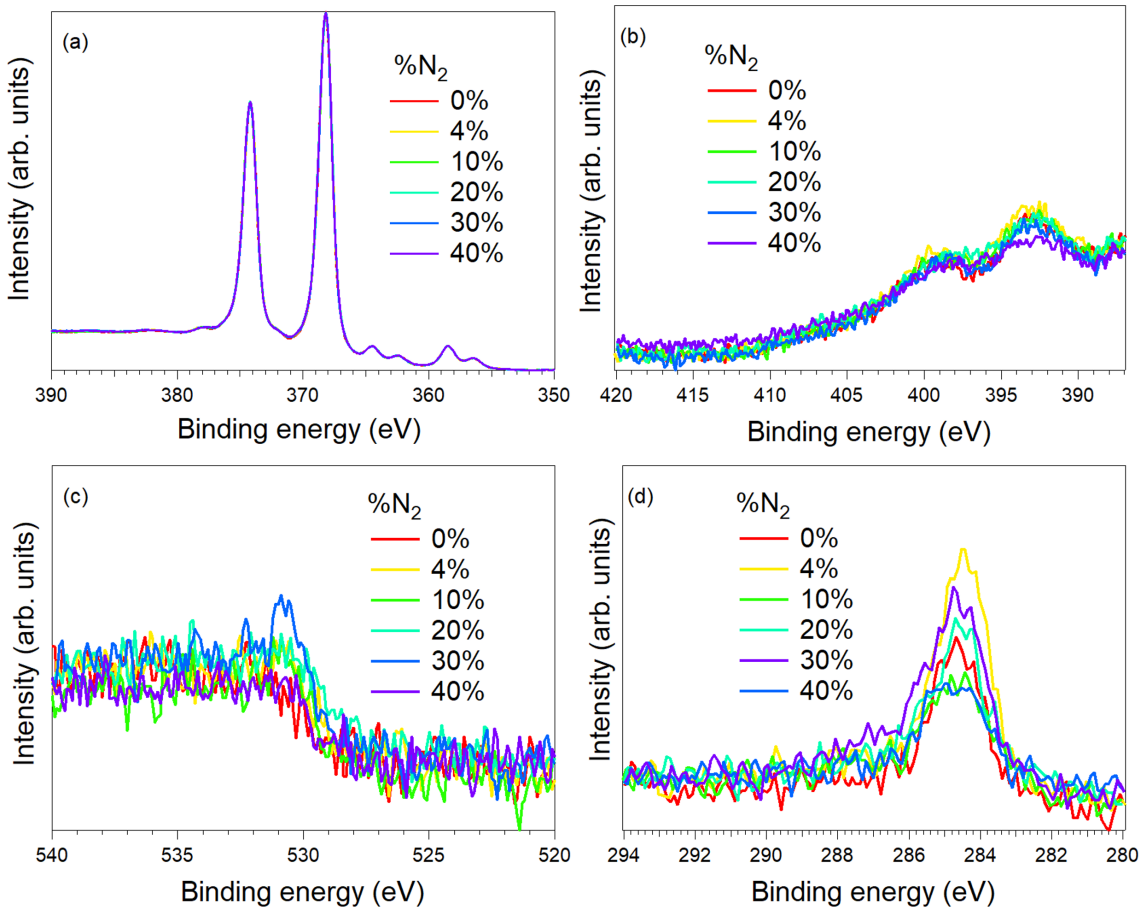

Figure 5.6 XPS core level spectra of Ag films ($t = 20$ nm) deposited on an AZO underlayer under different $\%N_2$ conditions: (a) Ag 3d, (b) N 1s, (c) O 1s and (d) C 1s. Spectra were normalized to the same scale for Ag 3d and to background for the other core levels.

Results for Ag film chemistry are very similar to those observed for deposition on SiO_x in Chapter 3. The perfect overlap of the Ag 3d core level peaks (Figure 5.6-a) rules out any change in the chemical state of Ag. This is further reinforced by the absence of evolving features in the N 1s core level region, which only shows the multiple plasmon losses of Ag 3d. The visible C 1s signal corresponds to adventitious carbon of aliphatic nature at $E_B = 284.5$ eV, ruling out the presence of compounds such as carbonates at the film surface. Finally, the lack of peaks in the O 1s core level spectra excludes any significant spurious oxidation of the Ag film. The observed step in the spectra could be due to the excitation of Ag 3p 5/2 core level by the Kβ satellite of the Al-Kα x-ray source; however, the expected shift of 69.7 eV of the Kβ line would give rise to a peak around 534.3 eV - slightly shifted from the present finding (Figure 5.6-c).

In conclusion, photoemission results support the presence of metallic silver and rule out the presence of Ag-N bonds for all $\%N_2$ conditions.

5.2.4 Surface plasma treatment of AZO with N_2 plasma

The effect of the exposure of the AZO underlayer to a plasma during the initial stages of film growth was explored by XPS following the same procedure as in Chapter 3. Figure 5.7 shows XPS spectra before and after a 3 s-long exposure of AZO to a plasma ignited on an Al_2O_3 target for $0\%N_2$ and $40\%N_2$.
All gas compositions diminish the surface carbon contamination on the film to a similar extent (Figure 5.7-c), thus increasing the intensity of the substrate components (spectra without rescaling not shown). In parallel, N_2 (but not Ar) induces an upwards band bending as seen in the consistent shifts of all the AZO substrate features *i.e.* Zn 2p, Zn LMM Auger line, and O 1s (not shown). This is assigned to a reaction of the AZO layer with plasma-activated N species. Its direct signature appears both as a new component in the N 1s core level region (Figure 5.7-d), and through the disappearance of the under-oxidized Zn component (Figure 5.7-a,b). To evidence the latter, the Zn LMM Auger line (Figure 5.7-a) is the best indicator as the energy shift between metallic (Zn^0) and oxidized (Zn^{2+}) zinc is larger than that observed for the Zn 2p core level [181]. The case is illustrated in Figure 5.8 with the Zn LMM region of metallic zinc thick deposit and of a ZnO(0001) single crystal [282].
The amount of oxidation of Zn upon plasma treatment can be obtained from the ratio of areas between the Auger line and the difference spectra before and after plasma treatment (Figure 5.7). Accounting for the mean free path $\lambda = 2$ nm at $E_K = 900$ eV in ZnO [239], it corresponds to a thickness of ~ 0.2 nm.

5.2.5 STEM-HAADF imaging analysis of Ag nanoparticles

The effect of the presence of N_2 during the island stage of film growth (*i.e.* before percolation) was studied using STEM-HAADF imaging. The analysed stacks consisted of a 5 nm-thick AZO underlayer, a 0.6 nm-thick Ag layer (*i.e* well below percolation in all cases), and a final 5 nm-thick AZO capping layer, all of them deposited on amorphous SiN_x TEM membranes. Figure 5.9 displays a selection of HAADF TEM images obtained for different $\%N_2$ conditions during Ag deposition.

Compared to images of a direct deposit on the oxidized amorphous SiN_x TEM membranes (shown in Chapter 3) in which case nanoparticles have rounded spherical shapes, one immediately sees that nanoparticles deposited on AZO are more irregular in shape. This is even more striking at higher $\%N_2$, when particles appear more and more elongated and irregularly-shaped.

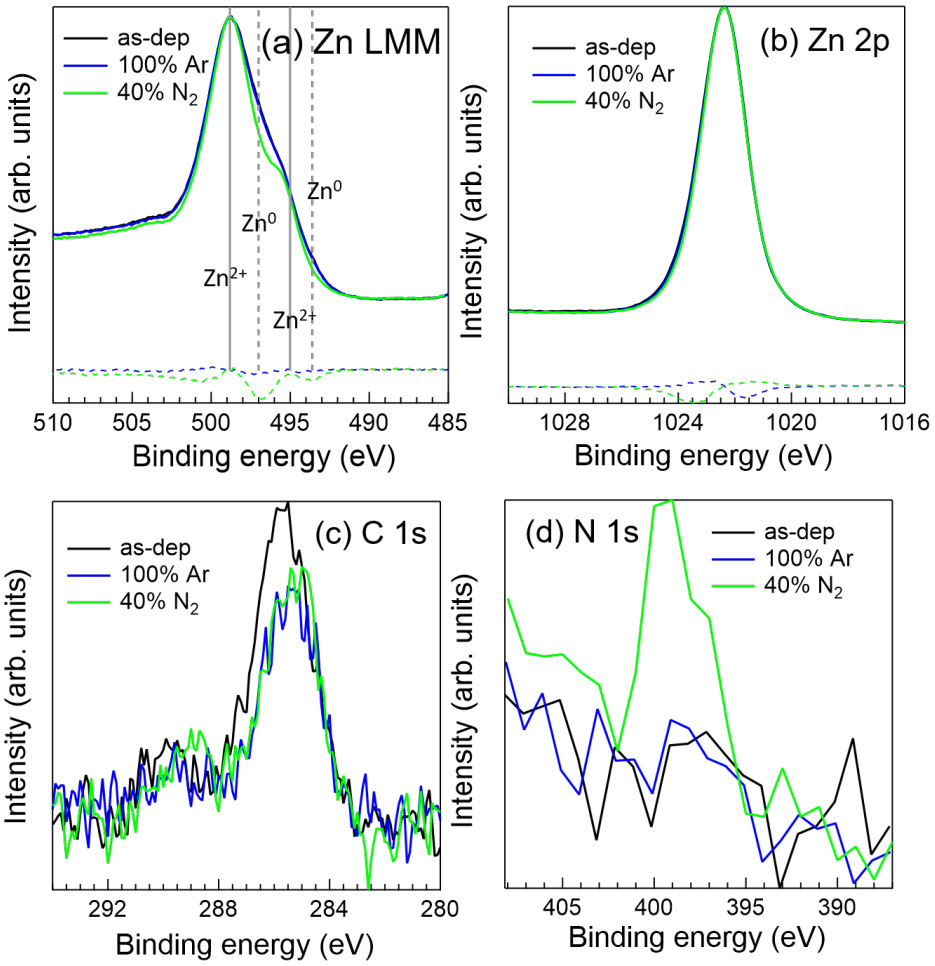

Figure 5.7 Photoemission spectra of AZO layers after a 3 s-long plasma treatment in front an Al_2O_3 target for the indicated gas composition: (a) Zn LMM Auger line; (b) Zn 2p; (c) C 1s; (d) N 1s. In Figures a-b, peaks have been shifted and rescaled to the same intensity while in Figures c-d, they have been aligned to the same background. In Figures a-b, the difference with the spectrum of the as-deposited material is shown as a dotted line at the bottom of the graph.

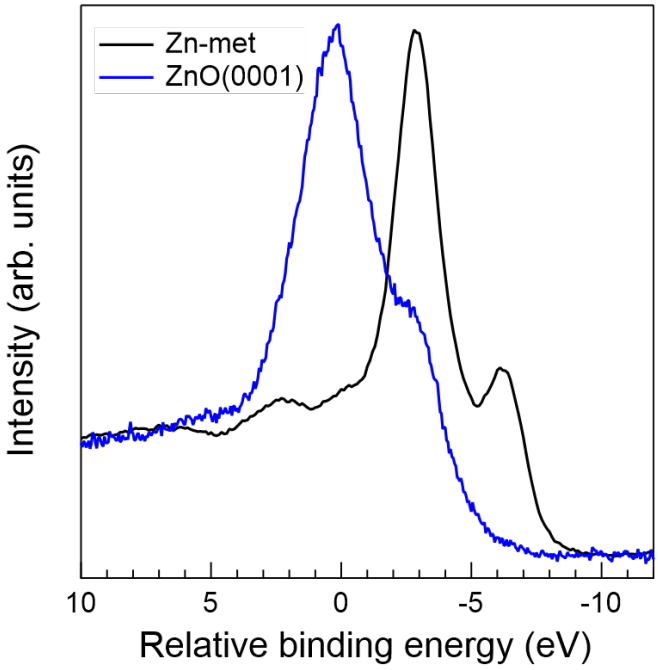

Figure 5.8 LMM Auger line from references of metallic zinc (black line) and oxidized zinc (blue line) in a ZnO(0001) single cristal.

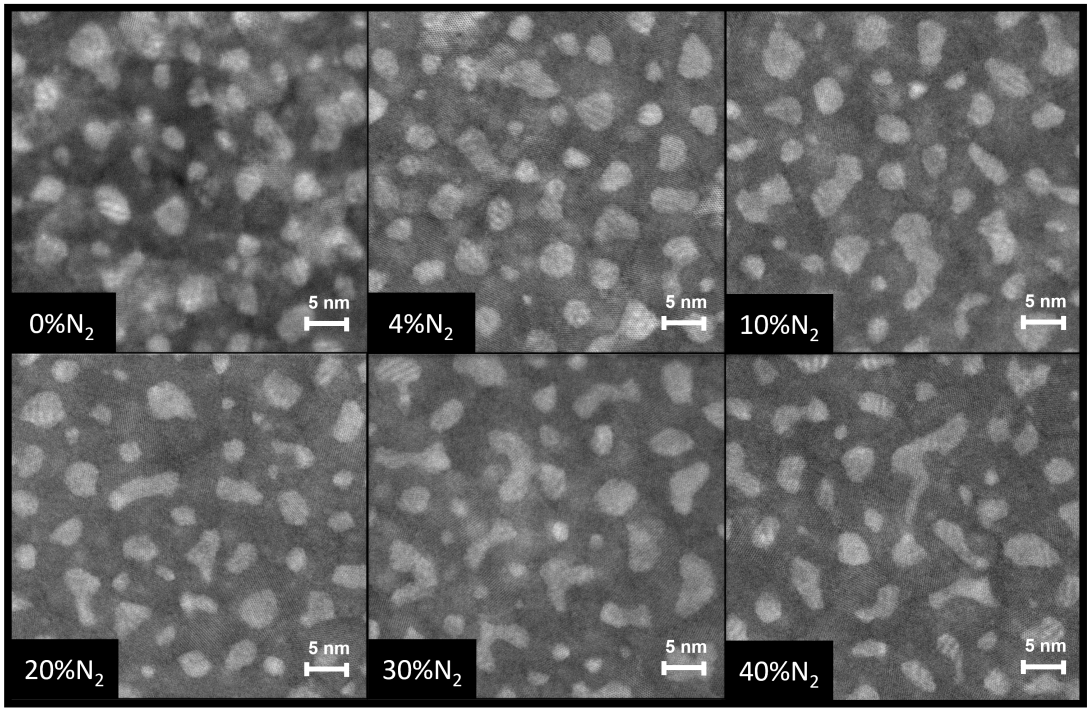

Figure 5.9 Examples of HAADF TEM images of 0.6 nm-thick Ag films deposited under different $\%N_2$ on AZO underlayers. A second 5 nm-thick AZO capping layer was deposited on top right after Ag deposition.

The development of such objects is a tell-tale sign of the onset of partial coalescence as described by Zhao *et al.* [144] and formalised in the work of Jeffers [102]. Partial coalescence was already explained in Chapter 1. As a brief reminder, this mechanism involves the inhibition of particle coalescence leading to an increase in the average time it takes for two particles to completely coalesce (τ_{coal}). When this time becomes larger than the average time it takes for two particles to impinge on each other due to particle growth ($\tau_{impinge}$), then more and more particles will impinge on groups of slowly-coalescing particles, creating island clusters with irregular and elongated island shapes instead of the round, 3D islands obtained in the case of complete coalescence.

Further image analysis was performed to extract the evolution of particle density for each $\%N_2$ condition. These results are shown in Figure 5.10, alongside results for deposition directly on the SiN_x membrane. Values start at 2.1×10^{12} cm^{-2} for deposition under $0\%N_2$, which is al-

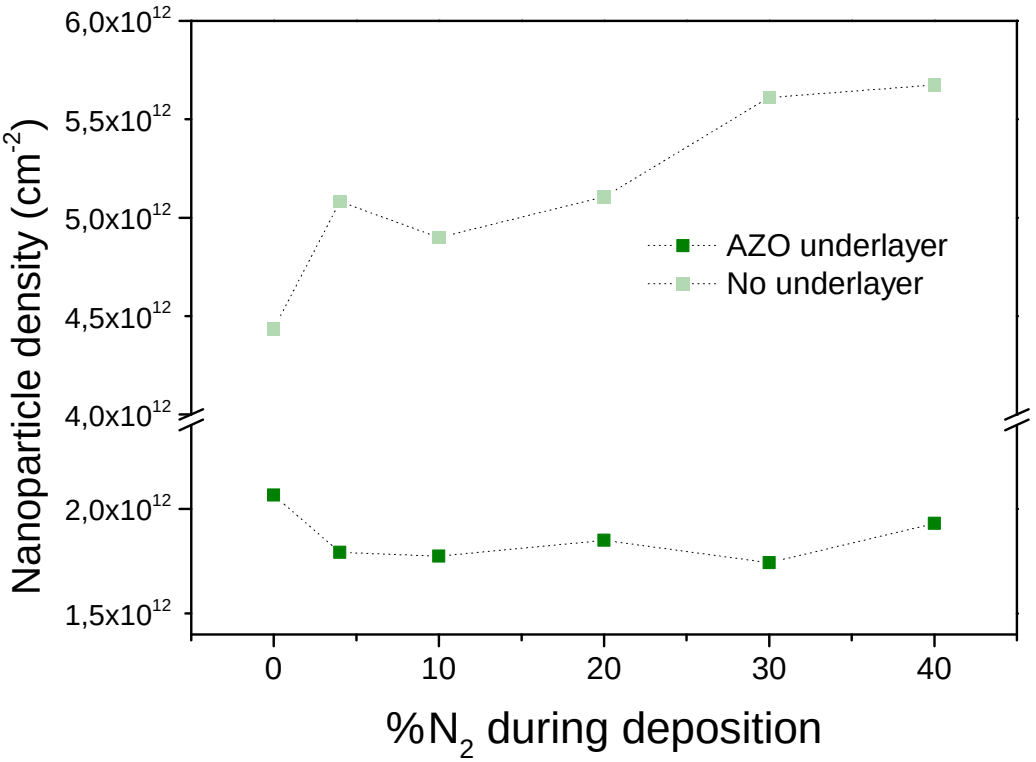

Figure 5.10 Ag nanoparticle surface density from STEM image analysis of 0.6 nm-thick Ag films deposited on AZO underlayers. Values obtained under the same conditions but for deposition directly on the oxidized TEM SiN_x membrane surface are also shown for comparison.

ready lower than for deposition on the bare, oxidized SiN_x membrane (4.4×10^{12} cm^{-2}). As the nucleation stage is most probably heterogeneous in these conditions, and therefore linked to the density of surface impurities and nucleation sites [12, 22], one could conclude at different density of defects and impurities (*i.e* different density of nucleation sites) between AZO and the bare TEM membrane to explain this difference in particle density between substrates. Another likely explanation is a more advanced coalescence at such a thickness on AZO than on SiO_x as a consequence of better wetting. This is clear when comparing the evolution of $\mathcal{A}_s(t)$ on AZO

(Figure 5.5) and on SiO_x (Chapter 3) for any of the $\%N_2$ conditions. For increasing $\%N_2$, the particle density appears to be nearly constant with $\%N_2$, with a slight initial drop at $4\%N_2$ and uptake at $40\%N_2$. The initial drop in particle density could be due to the analysis algorithm treating coalescing particles as a single object, artificially decreasing the value of particle density in the process.

Another possible explanation for the elongated Ag nanoparticle shapes on AZO could be a preferential nucleation and growth along the AZO grain boundaries. This should, however, be observed under all $\%N_2$ conditions, and not uniquely at higher nitrogen fluxes. Anyway, to test this hypothesis, a series of STEM-HAADF images were taken on samples deposited under the same conditions but using an amorphous Al_2O_3 capping layer. Unfortunately, this material has a much lower deposition rate than AZO (0.007 nm/s, compared to 0.16 nm/s for AZO). To achieve the same final thickness for the capping layer (5 nm), the Ag nanoparticles are exposed to the bombardment of high-energy species from the plasma for a longer time when using Al_2O_3, which makes them evolve in shape and adopt a round shape, closer to equilibrium, as shown in Figure 5.11. This evolution in nanoparticle shape excludes any meaningful morphological analysis, which was the initial goal for this experiment. The value for particle density is 1.43×10^{12} cm^{-2}, which is a value that lies in the range observed in Figure 5.10, but is still lower than the value for $0\%N_2$ with an AZO capping layer. Improved surface diffusion of the Ag atoms and islands thanks to the energy transfer during collisions of energetic particles could be responsible for increased dynamic coalescence and this decrease in particle density. Nonetheless, this experiment demonstrates the difficulties of reliable *ex situ* TEM image analysis for such a mobile material as Ag; on the one hand, uncapped films are prone to ageing upon atmosphere exposure, while on the other hand capping may also impact morphology, especially when energetic species from a plasma are present.

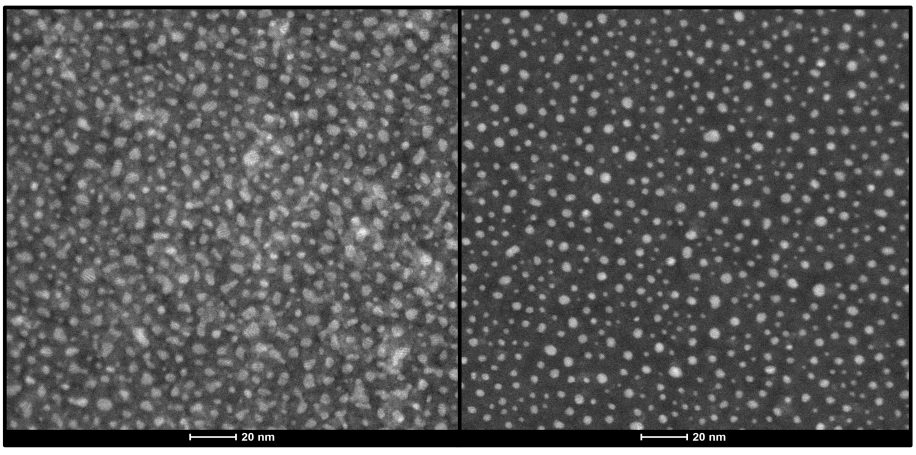

Figure 5.11 STEM-HAADF images taken from 0.6 nm-thick Ag films deposited on 5 nm AZO underlayers and capped with (a) 5 nm of AZO or (b) 5 nm of Al_2O_3.

5.2.6 XRD film analysis of 20 nm-thick films

Figure 5.12 shows XRD diffractograms for 20 nm-thick Ag films deposited on 5-nm AZO underlayers, on top of fused silica wafers. The stacks were capped with a 5 nm-thick AZO layer and the diffractograms were measured in out-of-plane Bragg-Brentano and in-plane GIXRD geometries. In all cases, only peaks relative to fcc metallic Ag and wurtzite AZO are observed. Contrary to

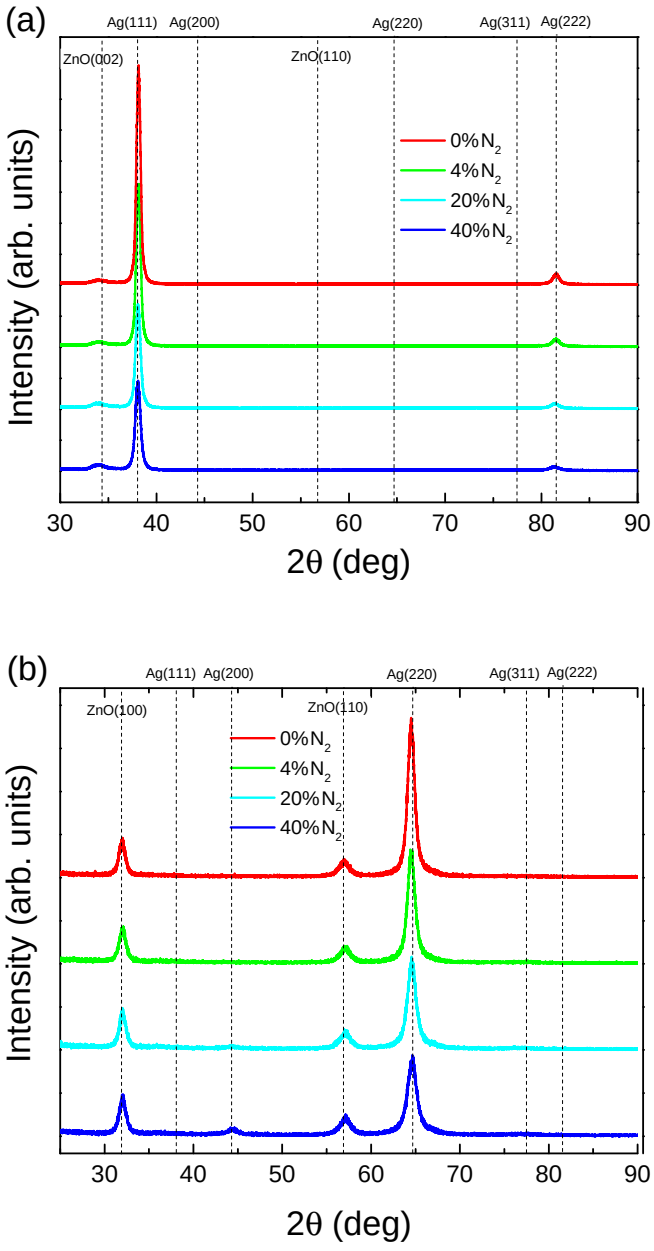

Figure 5.12 XRD diffractograms measured in (a) Bragg-Brentano and (b) in-plane grazing incidence geometries on 20 nm-thick Ag films deposited under different $\%N_2$ conditions.

previous results on SiO_x (Chapter 3), the initial Ag film at $0\%N_2$ is highly textured along the [111] direction due to the favourable epitaxy on [001]-textured AZO underlayer [53,186,187,190].

However, the cristallinity of Ag is worsened when increasing $\%N_2$, as demonstrated by the decrease of the out-of-plane and in-plane coherent domain sizes (D_{coh}, Figure 5.13-a). The value for D_{coh} along the normal to the film starts close to the nominal film thickness (17 nm instead fo 20 nm), and then slightly decrease down to 14 nm for $40\%N_2$. This is a moderate change in D_{coh} when compared to previous results, especially for O_2 addition during Ag deposition on SiO_x (Chapter 4) where a decrease from 15 nm down to 4 nm was observed. In-plane D_{coh} data show a decrease from 12 nm down to 8 nm. This should directly contribute to a higher resistivity of the Ag film (Figure 5.3-b). In short, diffraction results show that the crystallinity of the (111)-textured Ag film on AZO worsens with increasing $\%N_2$.

Although not visible in Bragg-Brentano geometry, a new Ag(200) peak appears in GIXRD above $20\%N_2$ (Figure 5.13-b). This is in line with observed change of texture from [111] to [100] for Ag that was put forward in the case of SiO_x and explained by a lower surface energy of a N-covered Ag(100) surface than that of Ag(111) surface. In the case of AZO, the change in texture is delayed compared to SiO_x, probably owing to the Ag(111) epitaxy on AZO(0001) that stabilises this orientation. In fact, such a change of orientation from [111] to [100] was observed at larger thickness in reference [116].

To conclude, N_2 addition leads to a "moderate" worsening in film crystallinity for deposition on AZO compared to SiO_x. The change in film texture, previously observed for deposition on SiO_x at much lower $\%N_2$, was practically not observed on AZO. Instead, the film maintains its (111) out-of-plane texture throughout the entire range of $\%N_2$ used in this work. Nevertheless, traces of (100) orientation start appearing at the highest $\%N_2$.

5.2.7 Discussion on the effects of N_2 addition during Ag deposition on AZO

The use of an AZO underlayer for Ag thin film deposition is known to induce an increased wetting of the Ag nanoparticles during the initial growth stages, leading to a decrease in the percolation threshold thickness. Due to its role as a template for heteroepitaxial Ag growth, it also induces a strong Ag(111) texture, improving film crystallinity and reducing crystalline mismatch at the grain boundary regions of the polycristalline Ag film. The concomitant reduction of grain boundary density (due to particle flattening) and the improvement of their crystalline quality (due to epitaxy) reduce film resistivity [53] compared to a deposition on SiO_x [190, 192, 283]. In accordance with previous reports [12, 53, 190], all of the above-mentioned reported effects of an AZO underlayer appear in our results for $0\%N_2$. However, because of AZO, we note that these positive effects sought with the use of a "surfactant" are already present even before any N_2 is added to the deposition chamber.

Based on these observations, we can now look in more detail at the actual impacts of N_2 gas addition. A monotonous decrease of the percolation threshold t_p, all the way down to a minimum of 1.3 nm (Figure 5.3-a), is observed for $\%N_2 \geq 10\%$. However, no decrease was measured for low nitrogen flux ($4\%N_2$) unlike for SiO_x, where a noticeable change from 5.5 nm to 4.7 nm was found (Chapter 3). SDRS measurements showed that particles are already flattened for $0\%N_2$ compared to SiO_x (Figure 5.1) and according to the values of the integrated s-polarized SDRS spectra $\mathcal{A}_s(t)$ (Figure 5.5), the addition of $4\%N_2$ does not lead to a sizeable increase in aspect ratio. STEM HAADF images showed a $\sim 13\%$ decrease in nanoparticle surface density when increasing $\%N_2$ from 0 to 4% instead of an increase like it had been observed for SiO_x. This decrease in density may be caused by the image analysis algorithm treating slowly-coalescing elongated particle clusters (due to the onset of partial coalescence) as a single particle. So we will

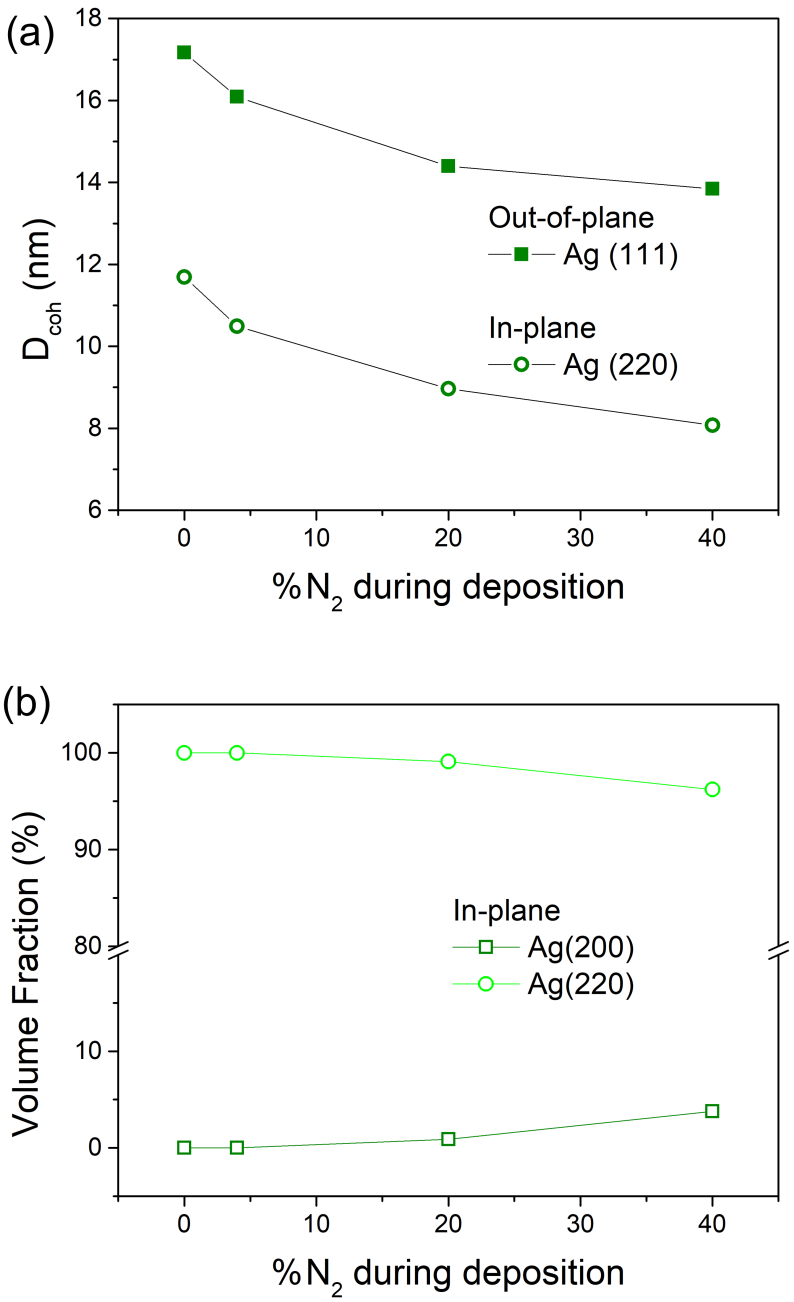

Figure 5.13 Diffraction from 20 nm-thick Ag films as a function of $\%N_2$ during growth. (a) Coherent domain sizes D_{coh} determined from the width of the Ag(111) peak in Bragg-Brentano out-of-plane geometry and the Ag(220) peak in in-plane grazing incidence geometry. (b) Volume fractions calculated from the integrated Ag peak areas in GIXRD diffractograms.

not use it to estimate an expected change in t_p like we did in Chapter 3. In short, the anomalous behaviour at 4%N_2 for the percolation threshold on AZO could be explained considering that Ag nanoparticles are already flattened on AZO substrates (compared to SiO_x), and thus the addition of a small flux of N_2 does not lead to any sizeable particle flattening and decrease in t_p.
For higher values of %N_2 ($\geq$ 10%), experimental trends for AZO are more comparable to those for SiO_x. Values for t_p decrease in both cases. But on AZO, the Ag nanoparticle surface density images stays practically constant with increasing %N_2 (Figure 5.10) as seen by STEM HAADF. So an impact of N_2 on particle aspect ratio can be put forward to explain this decrease in t_p; indeed SDRS measurements evidenced further particle flattening for 10%N_2, probably due to a more efficient N_2 dissociation and N adsorption at the Ag surface. In parallel, STEM HAADF images showed that Ag nanoparticles became more irregular and elongated (Figure 5.9) under these conditions. The appearance of such shapes is a sign of the onset of partial coalescence in agreement with the observations by Yun *et al.* [130] for Ag deposition on ZnO under similar conditions ($\sim$ 25%N_2). Partial coalescence requires an inhibited coalescence and/or a faster rate of particle impingement. Whereas Yun *et al.* claimed that the inhibited particle coalescence was a consequence of the crystalline mismatch between coalescing (111)-oriented particles caused by the incorporation of N_2 gas, our XPS data completely ruled out the presence of N in the film. In parallel, our XRD spectra showed only a slight change in texture at the highest %N_2 conditions with the appearance of a (200) peak in the GIXRD spectra. The difference between the two works can be explained considering that our XRD spectra were measured at t = 20 nm, whilst Yun *et al.* used much lower film thicknesses, leaving little room for texture evolution during film growth. We can propose an alternative explanation for the onset of partial coalescence based on the presence of adsorbed atomic N species, just like for SiO_x. The lack of N in photoemission can be linked to reversible adsorption of atomic N at the surface of the Ag nanoparticles, blocking Ag surface diffusion and thus inhibiting particle coalescence upon contact by "facet-migration" [30].

Finally, the increase in film resistivity for Ag on AZO mimics the trend observed for SiO_x, with the film on AZO always being lower in resistivity (Figure 5.3-b). At t = 20 nm, XRD measurements show a progressive loss of crystallinity for both substrates *i.e.* a decrease of coherent domain size (Figure 5.13-a), whilst the loss of film (111) texture on SiO_x with increasing %N_2 is not present on AZO up until 40%N_2 (but only in the in-plane orientation; see Figure 5.13-b). This is a consequence of the epitaxial relation of Ag with the underlying (0001)-oriented AZO layer; the higher in-plane texturation of the Ag films on AZO leads to less reflecting grain boundaries and thus a lower film resistivity [53].

5.3 Ag film deposition on AZO underlayers: effect of O_2 addition

The addition of O_2 was already shown to have a major impact on the Ag film growth, microstructure and - especially - composition, for Ag deposition on SiO_x. For AZO underlayers, some effects will be analogous to those found for N_2 while others will be completely different and will even differ from those observed for SiO_x.

5.3.1 Film resistance measurements

As shown in Figure 5.14-a, for a low O_2 flux (4%O_2), the addition of O_2 gas seems to slightly increase the Ag percolation threshold. However, given the size of the error bar and the general dispersion of the data for O_2 compared to N_2 (see Figures 5.3-a versus 5.14-a), we will only go as far as to conclude that there is no decrease in t_p. Whatever the interpretation of the result for 4%O_2, the lack of a sharp drop in t_p is in stark contrast with results for deposition on SiO_x, for which the addition of 4%O_2 led to a sizeable decrease (>1 nm) in t_p (the "low %O_2 regime", as explained in Chapter 4). Further increasing the O_2 flux above 10% leads to a decrease in t_p, with a minimum average value of 1.8 nm being reached at 30%-40%O_2. This is comparable to the results for N_2, even a lowest value was achieved for N_2 ($t_p = 1.3$ nm for 30%N_2 on AZO).

With increasing oxygen flux into the deposition chamber, film resistivity at $t = 20$ nm increases in a similar way to that for a deposition on SiO_x (Figure 5.14-b). The total increase in film resistivity is over tenfold, much higher than the one corresponding to N_2 addition. Furthermore, the difference between resistivity values for deposition on AZO and SiO_x fluctuates around $\simeq 2.5$ $\mu\Omega$.cm, with the film deposited on AZO always being lower in resistivity. It had already been concluded for SiO_x that this drastic increase of ρ was due to the contribution of Ag suboxides produced during film growth (Chapter 4). But such variations in resistivity could be linked not only to film composition, but also to structural aspects of the Ag film. Both contributions will be analysed in this chapter.

5.3.2 SDRS measurements

Looking at the SDRS spectra in p-polarization for $t = 0.4$ nm and $t = 0.6$ nm (Figure 5.15-a,b) for Ag deposition under increasing %O_2 conditions, we see trends that resemble those observed for Ag deposition on SiO_x. Namely:

- Increasing %O_2 from 0% to 4% first induces a red-shift coupled with an increase in intensity of the low-energy parallel resonance peak, compatible with Ag nanoparticle "flattening" according to *Granfilm* simulations (Chapter 2);
- Further increasing %O_2 to 10% and higher leads to an even greater red-shift of the low-energy peak, coupled with a decrease in intensity; this is compatible with the formation of an oxide shell on the surface of the "flattened" Ag nanoparticles.

Interestingly enough, both effects (particle flattening and formation of an oxidized shell) are already present at very low deposited thicknesses ($t = 0.4$ nm and $t = 0.6$ nm) on AZO underlayer. This was not quite the case on SiO_x (Chapter 4). At $t = 0.6$ nm, the SDRS spectra showed the effect of particle flattening for 4%O_2, but it did not show the increasing effect of the oxide shell formation for higher %O_2 values; the spectra for %$O_2 \geq 10$% were bunched up and practically superimposed with each other. A higher film thickness ($t = 3$ nm) was necessary to detect the increasing effects of oxide shell formation in SDRS. Back in Chapter 4, this was explained by

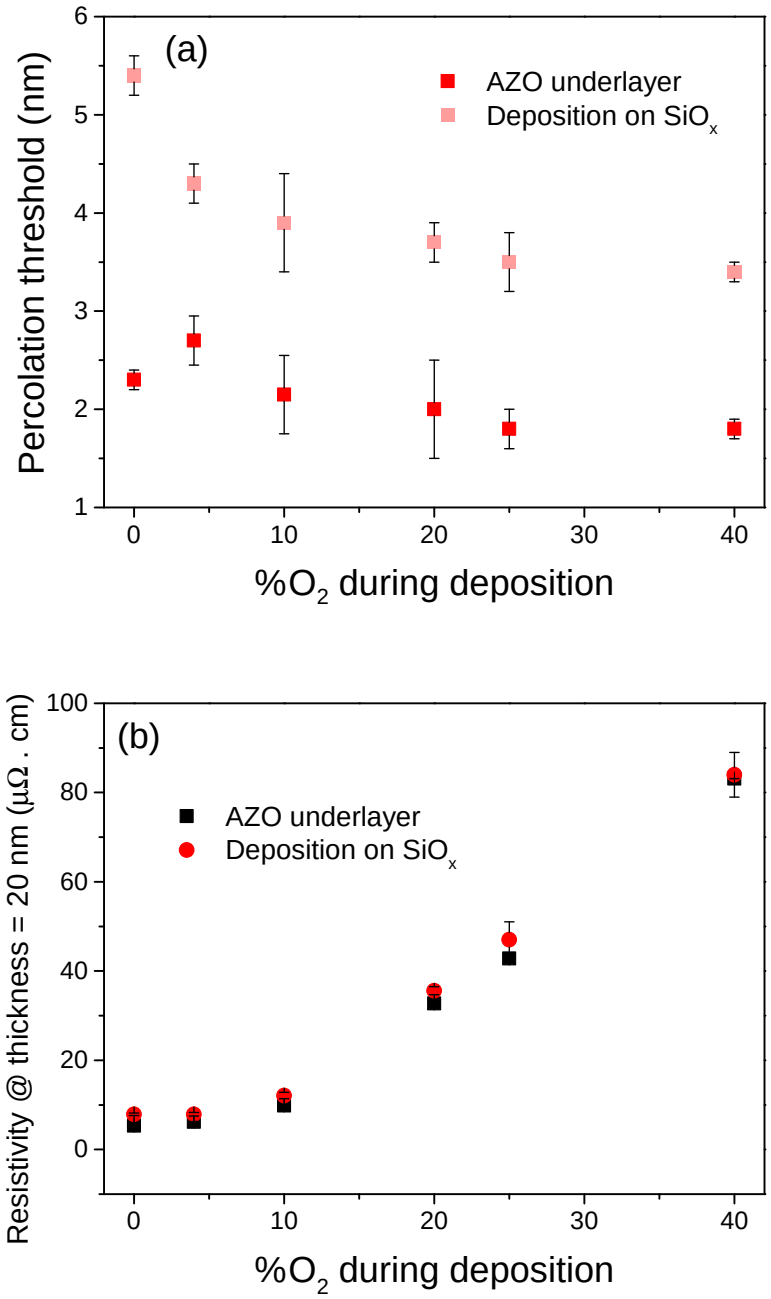

Figure 5.14 Evolution of (a) the percolation threshold thickness t_p and (b) film resistivity ρ at $t = 20$ nm for different%O_2 conditions for Ag deposition on AZO underlayer. Values and error bars correspond to the mean and standard deviation over several experiments (at least two for each condition).

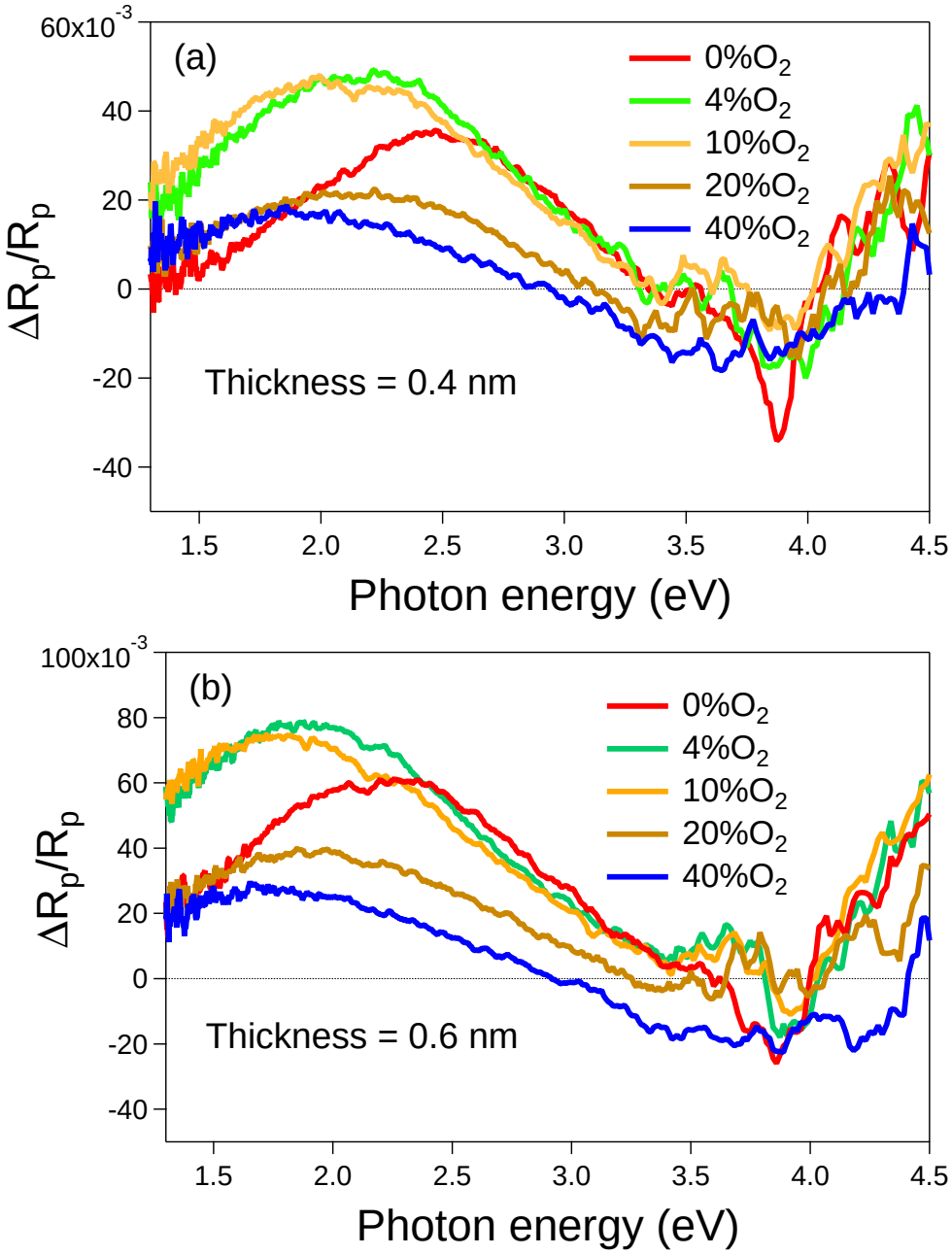

Figure 5.15 SDRS spectra in the p-polarization for Ag films deposited on AZO underlayers under different $\%O_2$ conditions. Spectra correspond to a deposited nominal thickness of (a) $t = 0.4$ nm and (b) $t = 0.6$ nm.

the presence of an "oxidation gradient" along the Ag film thickness, with the fraction of oxidized Ag at the surface becoming higher with increasing film thickness. In the case of AZO, the fact that we can already see the effect of nanoparticle oxidation at small thickness ($t = 0.4$ nm and $t = 0.6$ nm) is a sign that Ag films are already more oxidized at lower thickness on this substrate. Later in this section, we will analyse the oxidation gradient in the AZO case and compare it to results for deposition on SiO_x.

The integrated intensity of the s-polarized signal $\mathcal{A}_s(t)$ was also calculated for Ag deposition on AZO. Unfortunately, the data shown Figure 5.16 have a low signal-to-noise ratio and thus trends are unclear. $\mathcal{A}_s(t)$ increases with thickness at 0%, 4% and 20%O_2 but is constant at 40%O_2, and the behaviour is simply unclear at 10%O_2. We must keep in mind that in the case of Ag deposition on AZO, the parallel-plasmon peak is already red-shifted compared to deposition on SiO_x, and will be even more red-shifted with increasing %O_2. The peak will thus be located very close to the integration limit of the spectrometer used for the SDRS measurements (see Figure 5.15-c). Because of these instrumental limitations and the low signal-to-noise ratio, we will not comment the $\mathcal{A}_s(t)$ data any further in this chapter.

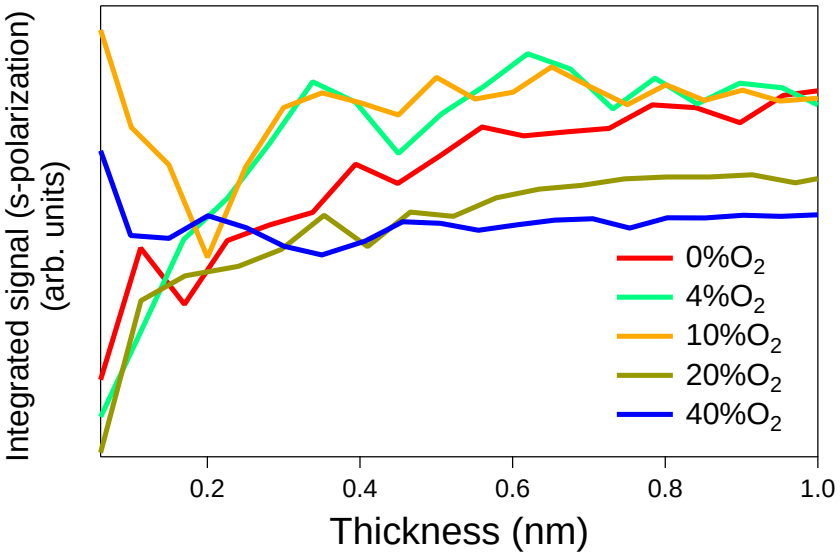

Figure 5.16 Integrated *s*-polarized signal from the SDRS spectra for Ag films deposited on AZO underlayers under increasing %O_2.

5.3.3 *In situ* XPS measurements for 20 nm-thick films

In situ XPS spectra for 20 nm-thick Ag films deposited on AZO underlayers are shown in Figure 5.17. Increasing %O_2 leads to an energy shift of the Ag 3d 5/2 core level (Figure 5.17-a) from $E_B \simeq 368.2$ eV down to $E_B \simeq 367.7$ eV. This shift is essentially the same as the one observed for deposition on SiO_x (Chapter 4), and corresponds to an evolution from metallic Ag towards an increasingly oxidized film. The O 1s core level spectra (Figure 5.17-b) show the presence of different components appearing with increasing %O_2. $O_{\alpha 1}$ species are observed for low %O_2 flux values (4%O_2), and a dominating peak at $E_B \simeq 529.2$ eV corresponding to Ag_2O is observed at %$O_2 \geq 10$%. This evolution contrasts with the results of deposition on SiO_x where a "low-%O_2 regime" was observed at 4%O_2, with neither Ag_2O nor $O_{\alpha 1}$ species being detected by XPS, but only O_β and $O_{\alpha 3}$ moities corresponding to surface and subsurface

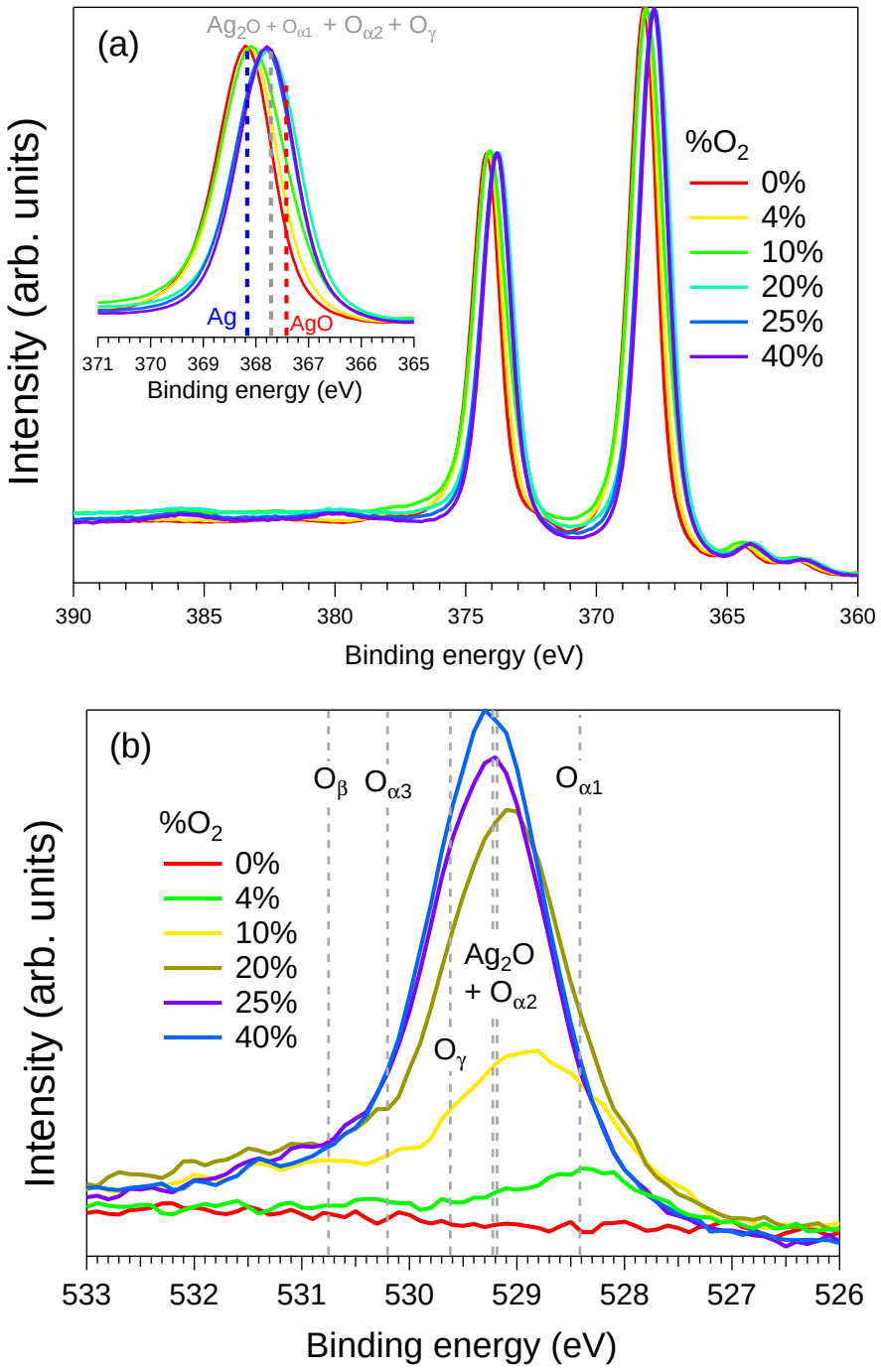

Figure 5.17 *In situ* photoemission core level spectra for Ag films (t = 20 nm) deposited on AZO underlayers under different $\%O_2$ conditions: (a) Ag 3d, (b) O 1s and (c) C 1s.

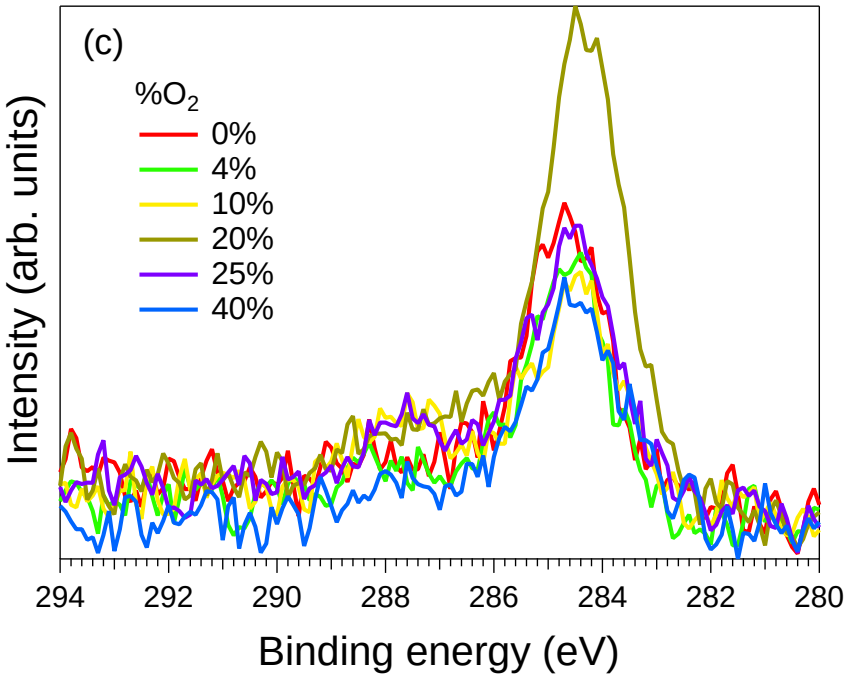

Figure 5.17 **Continued** *In situ* XPS core level spectra for Ag films ($t = 20$ nm) deposited on AZO underlayers under different $\%O_2$ conditions: (a) Ag 3d, (b) O 1s and (c) C 1s.

adsorbed O without charge transfer with Ag. On AZO, oxide species and the related shift in the Ag 3d spectra were detected even at $4\%O_2$. Finally, the only peak present in the C 1s spectra (Figure5.17-c) corresponds to an adventitious carbon uptake during sample transfer inside the MISSTIC setup; no carbonate peak is observed under any condition.

Photoemission spectra for the Ag 3d and O 1s core levels were fitted using the same method as for the study of Ag deposition on SiO_x (see Chapter 2 for more details). As a reminder, the Ag 3d spectra were decomposed into two components, one corresponding to metallic Ag at $E_B = 368.1$ eV, and a second one corresponding to oxidized Ag ("AgO_x") with a E_B value shifted by -0.5 ± 0.1 eV. Components for the O 1s core level were fitted using Voigt peaks but with E_B fixed at tabulated values for each oxygen species.

Figure 5.18 shows the analysis for 20 nm-thick Ag films deposited on AZO underlayers. At $4\%O_2$, the O 1s spectrum is dominated by the $O_{\alpha 1}$ species, which results in a slight increase in the fraction y of the oxidized Ag component in the Ag 3d spectrum. For $\%O_2 \geq 10\%$, Ag_2O becomes the major component of the O 1s spectrum with a corresponding increase in the oxidized component y in the Ag 3d spectrum. These trends qualitatively match the previous observations for Ag deposition on SiO_x in the so-called "intermediate $\%O_2$" regime for $4\%O_2$ on AZO, later transitioning to the "high $\%O_2$" regime for $\%O_2 \geq 10\%$ on AZO. On the other hand, the "low $\%O_2$" regime is not present on AZO. Even at $4\%O_2$, $O_{\alpha 1}$ species and the corresponding oxidized Ag fraction y (albeit small) are detected.

Now that the main trends for the composition of 20 nm-thick films on AZO have been established, we can compare these results in more detail with those for Ag deposition on SiO_x.

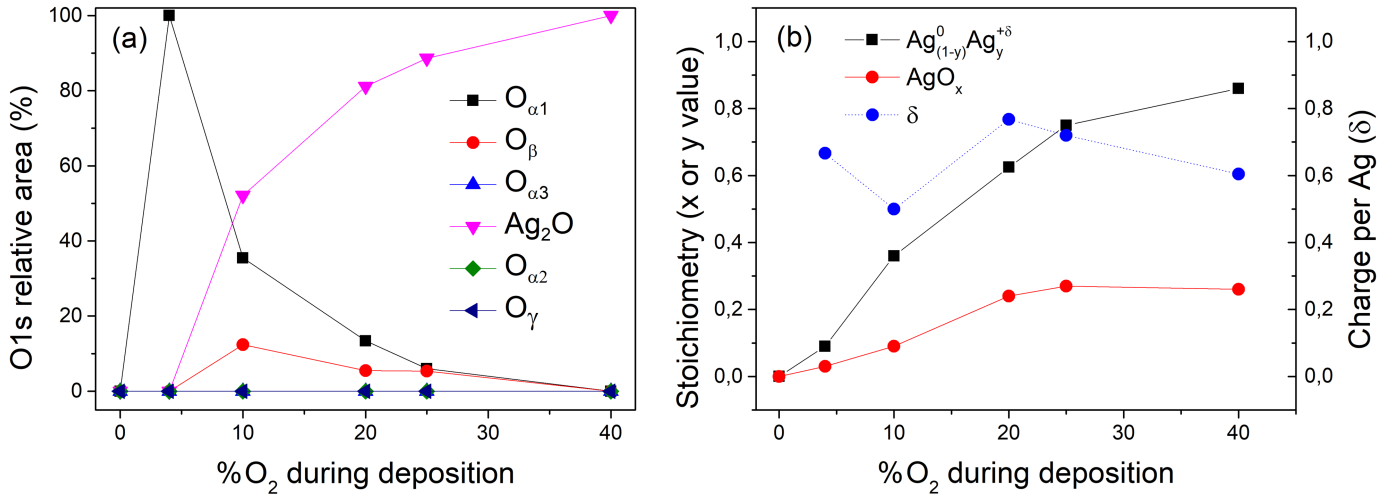

Figure 5.18 Results of core level fits for 20 nm-thick Ag films deposited on AZO underlayers as a function of $\%O_2$: (a) O 1s with the relative area for each O species; (b) Ag 3d with the values of the fraction $Ag^0_{1-y}Ag^{\delta}_{y}$ of oxidized Ag in the film, of the global AgO_x stoichiometry from the ratio between the total O 1s and Ag 3d peak areas and the average charge per Ag atom δ.

Figure 5.19 shows a comparison between the values of (a) y and (b) x parameters on the two substrates, SiO_x and AZO. The values for y are consistently higher for Ag films on AZO, with

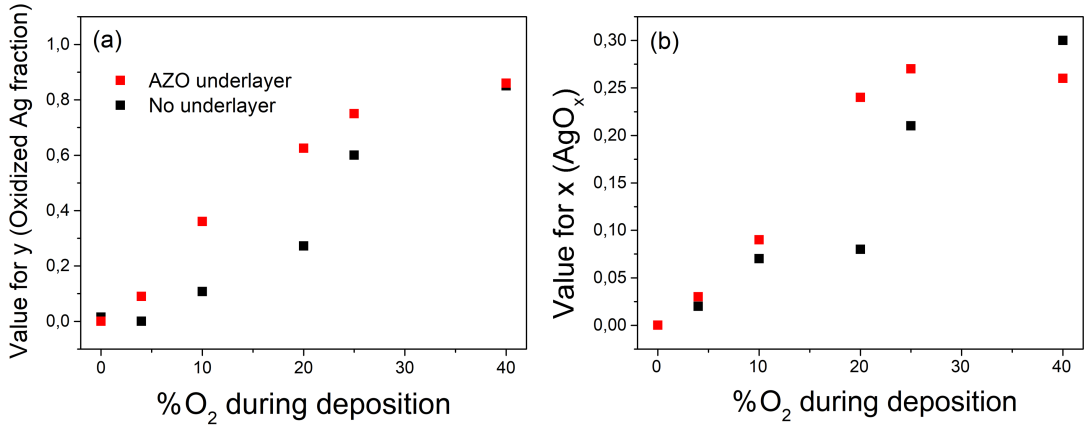

Figure 5.19 Comparison between the (a) y (oxidized Ag fraction), and (b) x (AgO_x average stoichiometry) values for 20 nm-thick Ag films deposited on SiO_x and on an AZO underlayer.

the difference between the two substrates being especially large at $10\%O_2$ and $20\%O_2$. This can be understood through the major species in the O 1s spectra for $10\%O_2$ and $20\%O_2$ on each substrate: $O_{\alpha 1}$ (*i.e* a surface oxide) is the main species for Ag films on SiO_x deposited under $10\%O_2$ and $20\%O_2$, whereas Ag_2O is the main species for Ag films on AZO. $O_{\alpha 1}$ species are reportedly unstable [151] and located at the surface of the films [284, 285], whereas Ag_2O is a more stable oxide that can accumulate in the bulk of the film. Therefore, formation of Ag_2O

contributes to a higher value of y for the film on AZO, increasing the gap between the two substrates. For $\%O_2 \geq 20\%O_2$, where Ag_2O is the major component of the film for both substrates, the gap in the y values between the two substrates narrow, particularly at $40\%O_2$ in which case an almost identical value of y is reached for AZO and for SiO_x. The film stoichiometry AgO_x tells a similar story, with the x values for Ag films on AZO being always higher than for Ag films on SiO_x. This is especially true for $20\%O_2$, in which case the gap in x is very large.

Films deposited under $4\%O_2$ show an interesting behaviour. While the y value is equal to zero for a film deposited on SiO_x, the corresponding x value is higher than zero and close to that of the film deposited on AZO. The explanation lies in the oxidizing nature of the O species in the film. The calculation of x involves integrating the entire O 1s core level spectrum, which includes a variety of oxygen species both "oxidizing" (*i.e.* $O_{\alpha 1}$) and "non-oxidizing" (*i.e.* O_β and $O_{\alpha 3}$). The latter contribute to the value of x, but not to the value of y since no charge transfer is observed in the Ag 3d spectrum and thus the oxidized Ag fraction does not increase. The rise in the value for x for the film deposited on SiO_x is thus mostly related to the accumulation of "non-oxidizing" species on the film; this was one of the defining properties of the so-called "low $\%O_2$ regime" in Chapter 4. In the case of AZO, however, we observe the accumulation of the oxidizing $O_{\alpha 1}$ species and a higher value of y even when the total x value (total O intake) remains equal to SiO_x. This is similar to what we observed in Chapter 4 for the so-called "intermediate $\%O_2$". Only in this case, this regime occurs at $\%O_2$ as low as 4%.

In conclusion, only the "intermediate" and "high" $\%O_2$ regimes are present when an AZO underlayer is used, and the lower limits for these regimes are skewed towards lower $\%O_2$ values. On top of this, photoemission shows that the nature of the O species on Ag during film growth varies depending on the substrate, with a higher fraction of oxidizing species ($O_{\alpha 1}$ and Ag_2O) being formed when the AZO underlayer is used.

5.3.4 Film composition gradients

The composition gradient along the film thickness for Ag films deposited on AZO was studied using the same procedure for Ag deposition on SiO_x: $4\%O_2$, $10\%O_2$ and $40\%O_2$ conditions were analysed, with thickness values between 0 and 20 nm. Figure 5.20 shows the analysis of the O 1s core level spectra with the relative fraction of each O species with increasing film thickness. Figure 5.21 shows the values for y (fraction of oxidized Ag), x (global "AgO_x" stoichiometry) and the average charge transferred per Ag atom δ obtained from the analysis of the Ag 3d core level. In all three cases, the abnormally high values of x and δ for the lowest film thickness are simply an artefact of the O 1s peak fit due to the presence of the overwhelming contribution from the substrate that can not be reliably accounted for during data treatment.

Values for y increase with increasing film thickness and seem to eventually reach a plateau. For $4\%O_2$, this increase in the fraction of oxidized Ag is linked to the formation of $O_{\alpha 1}$ species, whereas for $40\%O_2$ it is linked to the formation of Ag_2O. In the case of $10\%O_2$, $O_{\alpha 1}$ is the dominant species for intermediate thicknesses ($t = 4 - 10$ nm), and then decreases in favour of Ag_2O when approaching a film thickness of 20 nm. The plateau in this case is also less defined. One important observation we can make by looking at Figure 5.21 is that compared to the oxidation gradient for films deposited on SiO_x (Chapter 4), the starting values for y for very thin films ($t < 1.6$ nm) are consistently higher for Ag films deposited on AZO. In other words, the Ag films are more oxidized in the early stages of film growth when Ag is deposited on an AZO

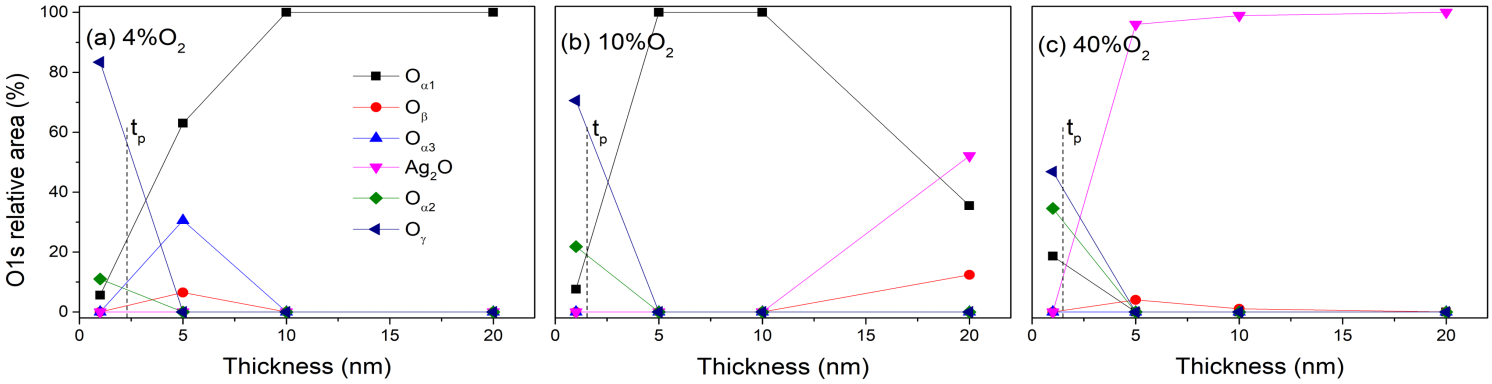

Figure 5.20 Results from the decomposition of O 1s core level spectra with the relative fraction of each O species with increasing film thickness for three representative $\%O_2$ conditions.

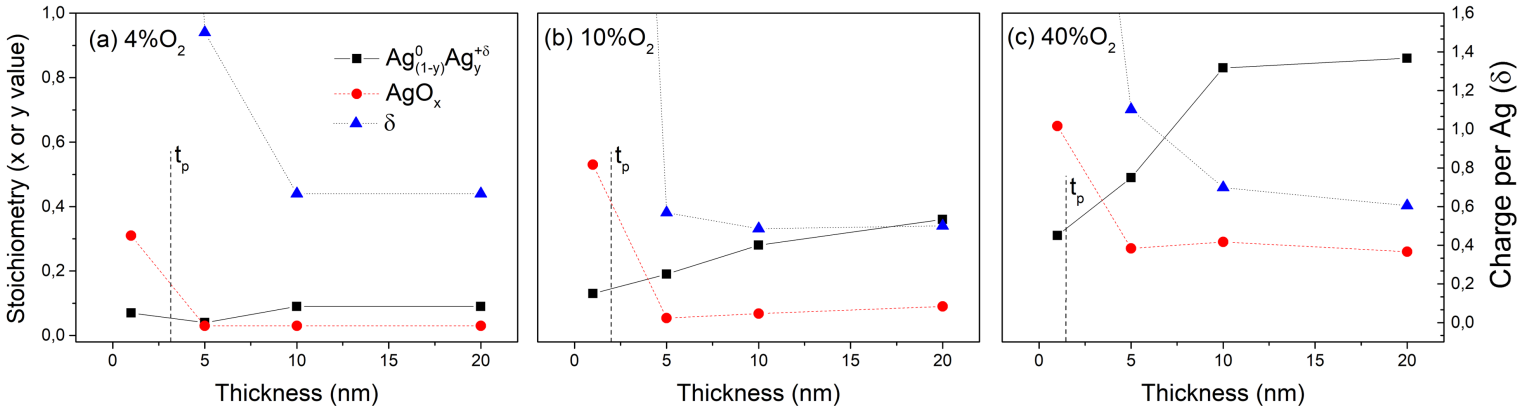

Figure 5.21 Results from the decomposition of the Ag 3d core level spectra for increasing film thickness and three representative $\%O_2$.

underlayer. This is a key difference between deposition on SiO_x and on AZO, and showcases differences in the dynamics of surface oxidation of the film during Ag growth.

5.3.5 Surface plasma treatment of AZO with O_2 plasma

Figure 5.22 shows the XPS spectra before and after 3 s-long exposure of a 5 nm-thick AZO layer to a plasma ignited on an Al_2O_3 target, at $0\%O_2$ and $40\%O_2$. Results for $40\%N_2$ plasma are also shown for comparison.

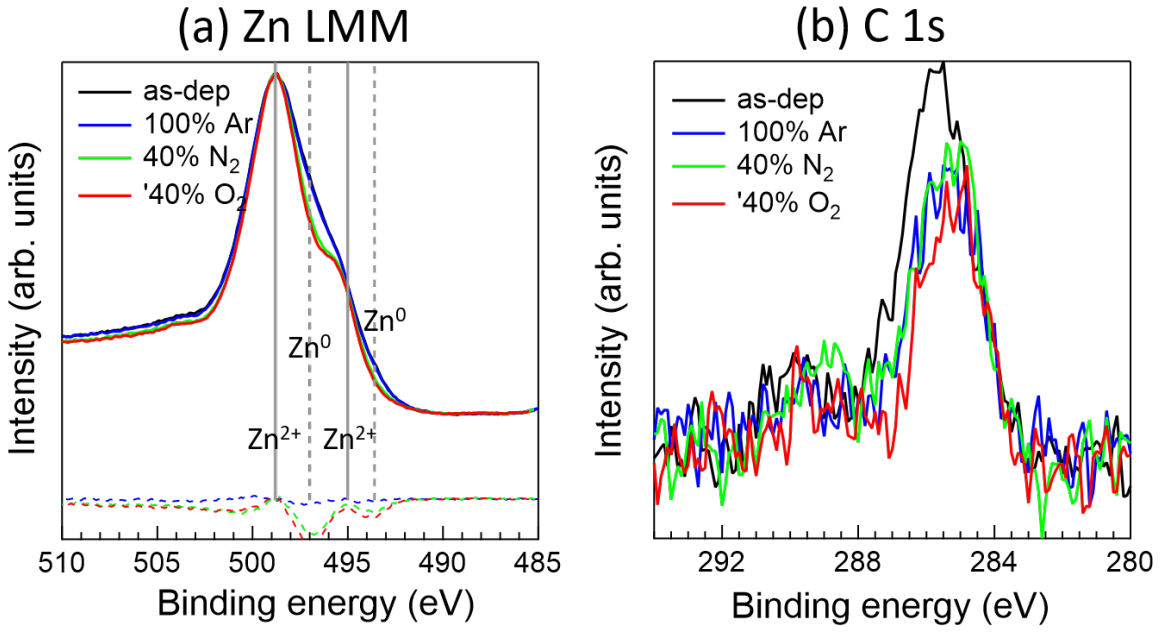

Figure 5.22 Pphotoemission spectra of AZO underlayers after a 3 s plasma treatment in front an Al_2O_3 target for the indicated gas composition: (a) Zn LMM Auger line and (b) C 1s. Spectra are shifted and overlapped for Figure a and aligned to background for Figure b. Dotted lines in Figure a corresponds to subtracted spectra using the as-deposited spectrum as reference.

The treatment with the O_2-rich plasma has similar effects to the N_2-rich one, *i.e.* and upward band bending (not shown), an increase of the oxidized Zn fraction at the AZO surface (Figure 5.22-a) and a decrease of carbon contamination (Figure 5.22-b). It appears that the kind of carbon impurities present at the AZO surface are "cleaned" by the energetic/reactive species of the plasma during the initial stages of Ag deposition regardless of the gas composition. The remaining C 1s peak after plasma treatment may correspond to a C uptake during the sample transfer to the XPS chamber.

5.3.6 STEM-HAADF imaging analysis of Ag nanoparticles

A selection of STEM HAADF images of 0.6 nm-thick Ag films deposited under different $\%O_2$ conditions on AZO underlayers are shown in Figure 5.23.
Ag nanoparticles are noticeably more irregular in shape and elongated at higher $\%O_2$ conditions, which can be ascribed to partial coalescence like in the case of N_2 addition. Elongated, irregular nanoparticles should impinge on each other and form a percolated network faster than spherical,

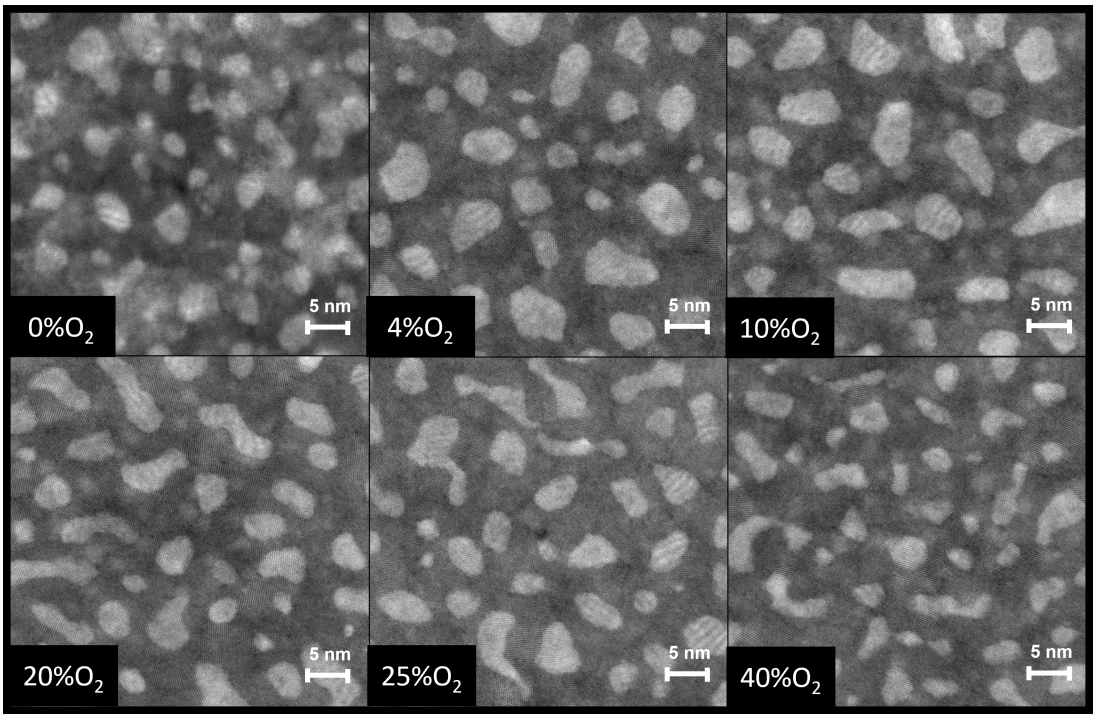

Figure 5.23 Examples of HAADF TEM images of 0.6 nm-thick Ag films deposited under different $\%O_2$ on AZO underlayers.

3D-like particles, thus reducing the value for t_p.

Figure 5.24 displays the corresponding change in particle density with $\%O_2$ obtained from image analysis and compares it to the case of direct Ag deposition on an oxidized amorphous SiN_x membrane surface. The evolution of particle density on an AZO underlayer with O_2 is very similar to that observed with N_2 (see Figure 5.10). After an initial drop when increasing the oxygen flux from 0% to 4%, the surface density of the nanoparticles remains almost constant for increasing $\%O_2$ and finally shows a small increase at $40\%O_2$.

5.3.7 XRD film analysis of 20 nm-thick films

Figures 5.25 show the *ex situ* XRD diffractograms for 20 nm-thick Ag films deposited on AZO underlayers, in the out-of-plane Bragg-Brentano and in-plane GIXRD geometries. Only peaks corresponding to wurtzite ZnO and cubic fcc Ag are present in both configurations, in accordance with results for Ag deposition on SiO_x. No extra-peaks due to Ag_2O are visible. Unlike deposition on SiO_x, however, there is a clear out-of-plane texture along the [111] direction which does not change with increasing $\%O_2$. The value of D_{coh} (Figure 5.26-a) for Ag(111) out-of-plane peak starts at $0\%O_2$ with a value close to film thickness (20 nm), and then decreases with higher $\%O_2$ conditions down to 8 nm, showing a deterioration of film crystallinity. Like for N_2, in-plane diffractograms involve mainly a (220) peak corresponding to an (111) out-of-plane texture. A small peak appears at $2\theta \simeq 36°$ at high $\%O_2$ conditions, which might correspond to a highly-strained (111) in-plane Ag peak. In parallel, the D_{coh} value (Figure 5.26-a) of the in-plane Ag(220) peak decreases from ~ 12 nm down to ~ 7 nm at $40\%O_2$. The corresponding Ag(220) volume fraction seems to decrease at higher $\%O_2$ as shown in Figure 5.26-b in favour of (presumably) the highly-strained (111) and (200) planes, although the peak broadness and

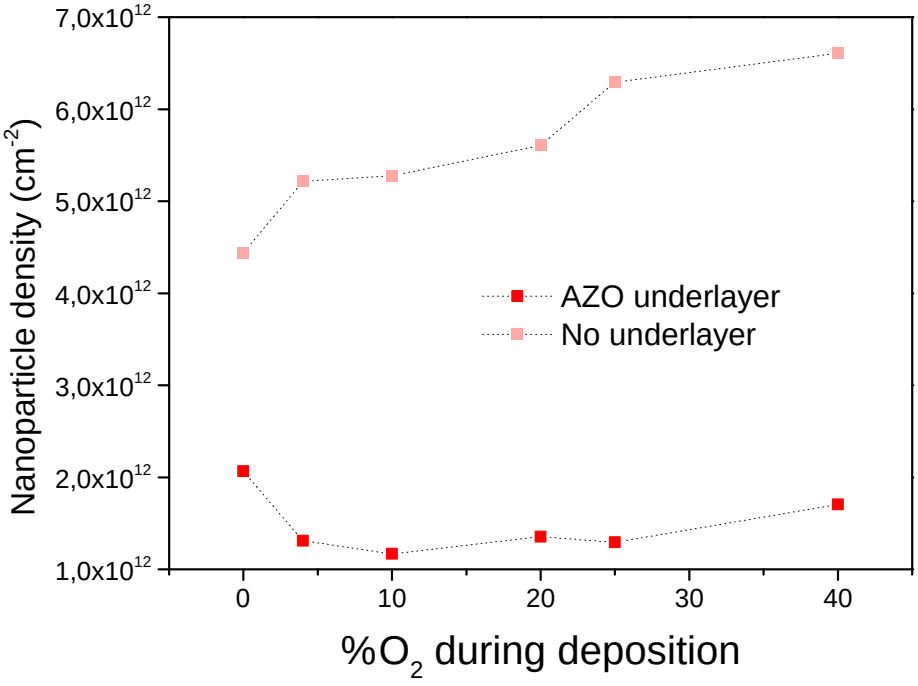

Figure 5.24 Change in Ag nanoparticle surface density from the image analysis of the TEM-HAADF images of 0.6 nm-thick Ag films deposited on AZO underlayers. Values for Ag nanoparticles deposited on amorphous SiN_x membranes without underlayer are shown for comparison.

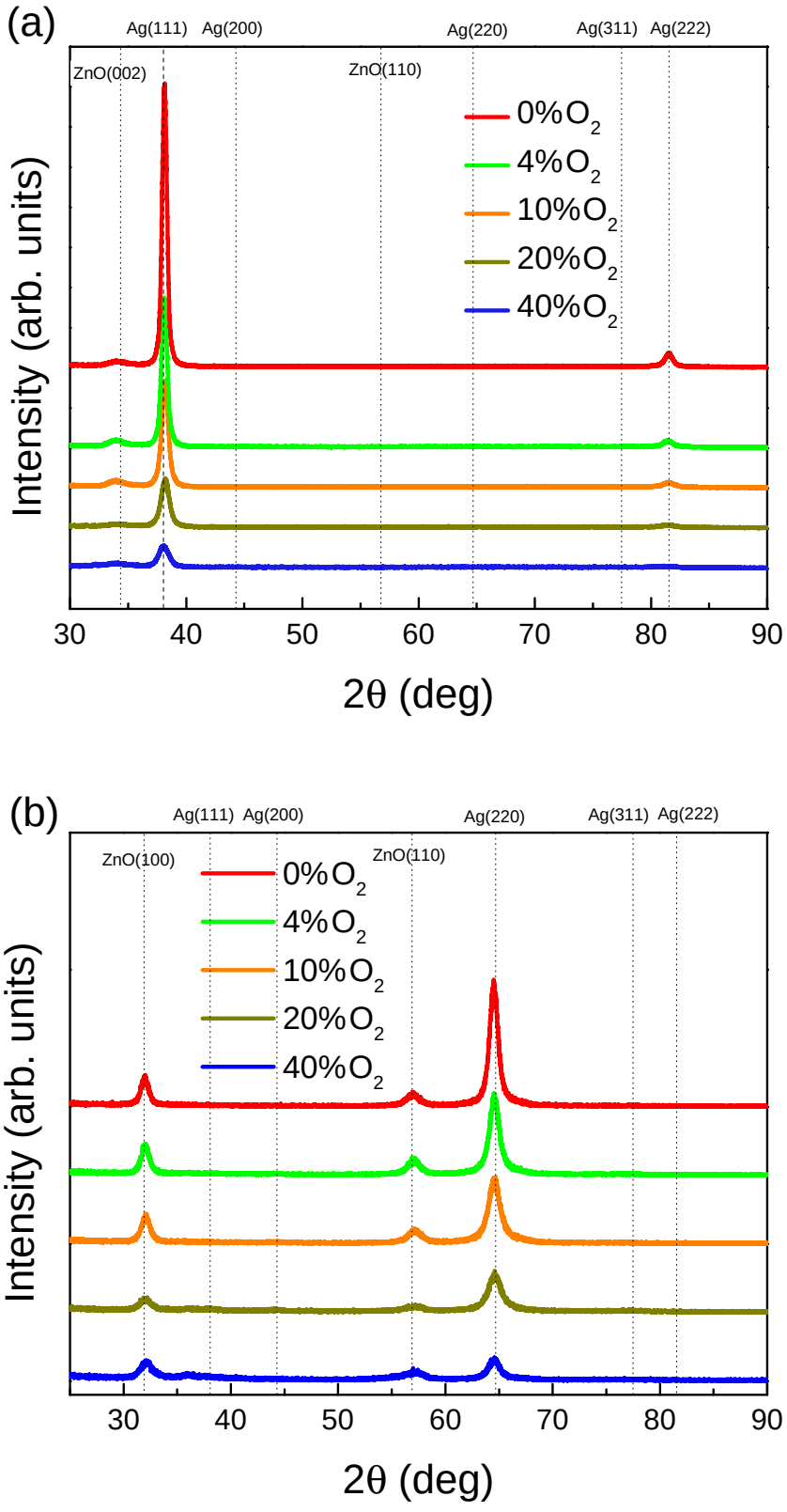

Figure 5.25 *Ex situ* XRD diffractograms measured in (a) the Bragg-Brentano and (b) the in-plane grazing incidence geometries on 20 nm-thick Ag films deposited under different $\%O_2$ conditions on AZO underlayers. A second AZO layer ($t = 5$ nm) was added as a capping layer to prevent ageing.

assignment uncertainty cast a shadow on this particular result.

5.3.8 Discussion on the effects of O_2 addition during Ag deposition on AZO

Similar to the findings for N_2, addition of O_2 during Ag deposition on AZO led to no significant change in t_p for $4\%O_2$, followed by a decrease down to 1.8 nm in line with results for SiO_x. Nevertheless, at $4\%O_2$, SDRS spectra in p-polarization do show signs of flattening of the Ag nanoparticles. Unfortunately, this finding cannot be supported by integrated values of the s-polarization SDRS signal due to the poor signal-to-noise ratio. STEM HAADF images show a $\sim$ 36 % decrease in nanoparticle density at $t = 0.6$ nm. In this case, we can only assume that the changes in aspect ratio and eventual onset of particle coalescence are not strong enough to induce a decrease in t_p for $4\%O_2$. For higher $\%O_2$ values, t_p decreases because of inhibited coalescence by the adsorbed O species at the nanoparticle surfaces which leads to partial coalescence. Such an adsorbate is detected by XPS, in the form of $O_{\alpha 1}$ and Ag_2O species.

Film composition measurements show that the Ag films deposited on AZO are more oxidized than their SiO_x counterparts (Figure 5.19). This difference is present even for very thin films; at $t = 0.4$ nm, SDRS spectra already show signs of the formation of an oxidized shell on the Ag nanoparticles (Figure 5.15), and a higher value of y for very thin films is observed for the film composition. The difference between the oxidation dynamics of Ag on both substrates could be linked to their different wetting properties and an higher diffusion barriers for Ag on AZO (Chapter 1). Assuming an "Eley-Rideal" mechanism for Ag oxidation by activated O species in the plasma, the already flattened particle shape and the likely slower diffusion of Ag on an AZO surface than on SiO_x mean that more Ag will be exposed and subject to oxidation from the plasma. Finally, the structure of the Ag film could also play a role; according to the literature, the formation of $O_{\alpha 1}$ species originate from an O-induced reconstruction at Ag(111) surface. With films deposited on AZO showing a strong [111] out-of-plane orientation due to the favourable epitaxial relation with the AZO underlayer, we can expect the fraction of $O_{\alpha 1}$ species in the films to be higher on AZO under similar exposure conditions to an oxygenated plasma. This could explain the higher y at $4\%O_2$ on AZO; in this case the film is highly [111] textured out-of-plane and $O_{\alpha 1}$ are the main species, compared to SiO_x for which the texture is lost to a certain extent and O_β and $O_{\alpha 3}$ are the main species.

Film resistivity increases with $\%O_2$ on both substrates, with a nearly constant difference of about 1 $\mu\Omega.cm$, in favour of AZO. Compared to N_2, the over-tenfold increase in resistivity is caused by the oxidation of the film. Surprisingly though, it would seem like the higher fractions of oxidized Ag y for films on AZO (Figure 5.19) do not translate into a higher value of ρ compared to SiO_x. Another explanation for this constant gap in resistivity between AZO and SiO_x could involve film crystallinity; since the Ag films on AZO are strongly textured along the [111] direction, the lower mismatch between grains result in less-reflecting grain boundaries [53] and an overall lower resistivity for films on AZO.

5.4 Conclusion

The main objective in this chapter was to study the effect of the superposition of two different growth control strategies for the magnetron sputtering deposition of Ag thin films: N_2 or O_2 gas addition and the use of an AZO underlayer. Both, on their own, are known to affect the growth of the Ag film, but their interaction is not yet completely understood.

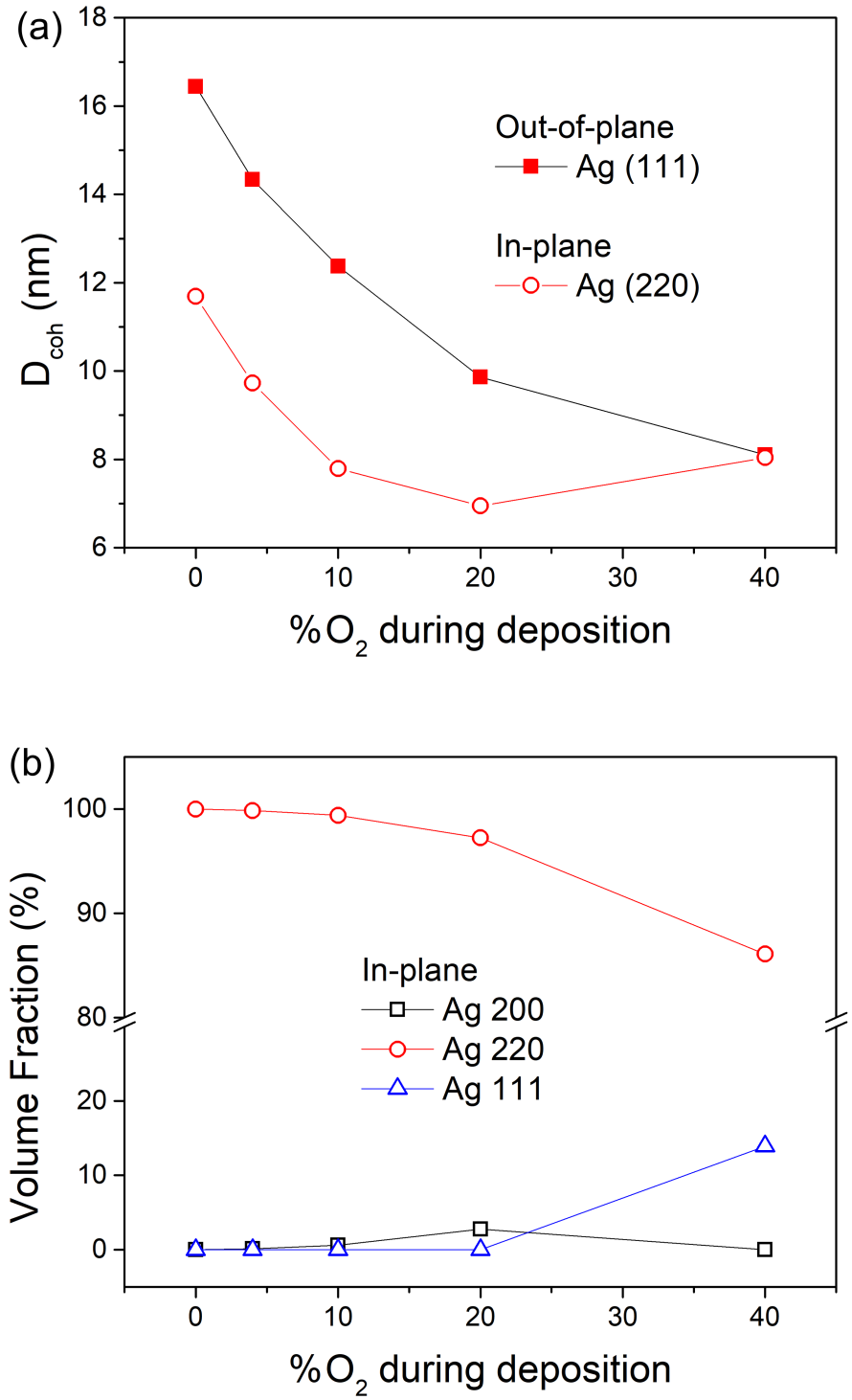

Figure 5.26 Analysis of XRD diffractograms of 20 nm-thick Ag films for increasing $\%O_2$: (a) Coherent domain size obtained from the widths of Ag(111) peak in Bragg-Brentano (out-of-plane) geometry and of the Ag(220) peak in grazing incidence (in-plane) geometry. (b) Volume fraction calculated from the integrated peak areas of the GIXRD diffractogram.

Results for low gas flux values (4%N_2 or 4%O_2) showed that, since particles in the initial growth stages are already "flattened" when using an AZO underlayer, this cancels the effects of gas addition and thus t_p barely changes. This is in contrast with the very weakly-interacting SiO_x substrate, for which particles are more rounded. For higher values of added gas flux, the observed decrease in t_p is much more comparable to that for SiO_x. It can be assigned to an increase in aspect ratio and the onset of partial coalescence. This latter could be the result of a loss in particle crystallinity at the beginning stages hindering plane alignment, but also a consequence of atomic N or O adsorption - or oxide formation - inhibiting coalescence mechanisms that rely on surface diffusion. Finally, the worsening of film conductivity at higher gas flux on AZO is quite comparable to the trend observed on SiO_x, with an almost constant difference in film resistivity between both substrates. An explanation purely based on the crystalline structure of the film would imply that loss of crystallinity causes an increase in resistivity, whilst the better texturation of the films on AZO leads to a lower value because of less-reflecting grain boundaries. However, oxidation still plays a role, since it is the major factor explaining the much higher increase in resistivity with O_2 than with N_2. Between substrates though, the oxidized fraction (y) does not seem to play a determining role, since the difference in resistivity between substrates does not really depend on the fraction of oxidized Ag.

In conclusion, the use of AZO underlayers for thin Ag film deposition has a series of effects on the initial stages of film growth (nucleation, growth and coalescence) of the Ag film that affect the resulting film properties. When used alongside a gas additive such as N_2 or O_2, the effect of the substrate can interefere with that of the gas additive, and in some cases compensate it. An example is given by the case of low gas flow (N_2 or O_2) being rendered ineffective at reducing t_p, since the Ag nanoparticles in the initial growth stages are already flattened on AZO. Using higher gas flux values though can still work for decreasing t_p thanks to a combination of particle flattening by the substrate and the onset of partial coalescence, which can lead to exceptionally low values for the percolation threshold (1.3 nm for 30%N_2). At last, chemical analysis showed differences in the Ag oxidation dynamics which could be assigned to the role of AZO substrate on the fraction of the surface covered by the film. This leads to more oxidized Ag films on AZO underlayers than on their SiO_x counterparts, especially in the initial stages of film growth.

Conclusions and perspectives

Understanding the mechanisms behind Ag thin film growth during magnetron sputtering deposition is of paramount importance both from a fundamental and industrial point of view, since it can lead to the development of new ways for tailoring film growth and properties through the process parameters. This is of great relevance in different applications for which the deposition of thin, but still continuous and highly-conductive films is required. The case of Ag-based Low-E glazings, where $\sim$ 10 nm-thick Ag films are used, is an example where a trade-off between transparency in the visible and infra-red reflection has to be found. The main bottleneck to overcome with Ag is the inherent thermodynamic trend of 3D growth of this metal on weakly-interacting substrates such as oxides. One possible strategy to tackle this limitation is the use of so-called "surfactant" gas additives, like N_2 and O_2, to force a more 2D-like growth and produce a thinner, more conductive film.

This manuscript started out with a general overview on the fundamentals of thin film growth during physical vapour deposition with an emphasis on magnetron sputtering. We presented usual models describing the thermodynamic and kinetic aspects of film growth, with a focus on metallic film growth on weakly-interacting substrates, and then on the particular case of Ag deposition on oxides such as silica (*i.e.* glass surfaces). We found that thermodynamic aspects (surface/interface energies) drive to a large extent the preference for 3D Ag growth, the so-called "Volmer-Weber" growth mode. However, since atom gas supersaturation near the substrate surface leads to "out-of-equilibrium" growth conditions, kinetic aspects of film growth are also of great relevance. Our kinetic description involved exploring the main elementary atomic processes happening in each of the stages of film growth (nucleation, growth, coalescence, percolation, continuous and finally uniform film formation). This led, in the second part of the chapter, to review the literature about the levers for controlling these mechanisms and eventually inducing a more 2D-like film growth. This objective is underpinned by the common microstructural traits that favour the highest film conductivity: (i) low density of poorly-reflecting grain boundaries, (ii) low surface roughness and (iii) low density of defects and good crystallinity. We evidenced the fact that most of the reported strategies for growth control have drawbacks that are hardly compatible with glazing applications, including a loss in transparency, a loss in infrared reflectance and an incorporation of impurities into the film. We singled out the use of "surfactant" gas additives, however, as a promising strategy, since they can affect film growth while also "floating out" and remaining on the film surface, instead of incorporating into the bulk of film.
As such, through the use of a combination of real-time, *in situ* and *ex situ* characterization techniques, the first objective of this thesis was to understand the "surfactant" effect of N_2 and O_2 gas additives during Ag deposition on an amorphous SiO_x substrate, which was used as a baseline "reference" substrate. This initial study helped us understand how these gases can be used for promoting a 2D growth and producing thinner, conductive Ag films. The second objective was to look at the interplay between this "surfactant" effect from the gas additives and the use of an epitaxial AZO underlayer, which is widely used in both academia and industry.

The second chapter described the experimental techniques available in the "MISSTIC" deposition set-up that were used all along this thesis. They were divided into real-time measurements (*i.e* during film deposition), *in situ* measurements (*i.e* after deposition but with vacuum transfer between deposition and analysis) and *ex situ* measurements (*i.e* outside the vacuum chamber). In particular, it was discussed how real-time techniques, such as film electrical resistance and SDRS, allow for the detection of the nominal thickness thresholds of the different stages of film growth.

The third and fourth chapters were dedicated to the study of the effects of N_2 and O_2 addition on the growth of Ag films on the native amorphous oxide layer of a Si wafer ("SiO_x"). This baseline substrate, compatible with photoelectron spectroscopy, was chosen as a "model" surface for glass surface. While a low flow (4% of the total) of both gases led to a strong decrease in percolation threshold ($\geqslant 1$ nm) thanks to a combination of increased particle density, increase of particle aspect ratio in the initial stage of isolated islands and delayed coalescence, the behaviour changes at higher gas flow and is instead mostly driven by the chemical interaction between each gas and Ag. While SDRS results for N_2 addition were consistent with the reversible adsorption of atomic N from the plasma, *in situ* XPS analyses showed that the interaction with O_2 follows a complex scenario with the formation of different O-species and Ag (sub)oxides in the film and on its surface. A gradient of composition sets up in the thickness of the film, which we attributed to the competitive mechanisms of metal aggregation and oxidation. XRD analysis showed that addition of either gas resulted in a loss in crystallinity (more pronounced in the case of O_2) and a progressive change in film texture from (111) to (100). In short, this study showed that while these gas additives can have surfactant-like effects on film percolation and can be used for the deposition of thinner conductive continuous Ag films, they also have associated side effects that contribute to a higher film resistivity (at least when used continuously during deposition). Specific strategies of gas deployment at the beginning of the growth as already reported [111,138] could be a way of circumventing them, as we have already started to explore using "flash" introduction of N_2 or O_2. In any case, using O_2 as a surfactant gas additive should be limited to very low O_2 flow values (the "low O_2 regime") lest oxide formation overcomes the "float out" behaviour one should expect from an actual surfactant substance. N_2, on the contrary, does not incorporate into the film even at high flow, according to XPS.

The final chapter tackled the interplay between the use of gas additives (N_2 and O_2) and the use of an epitaxial template for Ag, namely an AZO underlayer. Due to the Ag(111)/ZnO(0001) epitaxial relationship intrinsically leading to more flattened particles, a lower percolation threshold thickness and a stronger (111) texture compared to SiO_x, our results showed that the film growth mechanism was mostly insensitive to gas additives at low gas flow. The strong (111) out-of-plane texture induced by the AZO underlayer decreased only slightly (if at all) with increasing gas flow, even if the film crystallinity did suffer from excessive N_2 and O_2 addition. The oxidation dynamics by plasma-activated O species also changed, with Ag films being more oxidized when deposited on AZO than on SiO_x. A more efficient Eley-Rideal oxidative mechanism was put forward in parallel to a change in Ag surface mobility. Despite these drawbacks at higher gas flows, it was possible to reach an unprecedented value of 1.3 nm for the percolation threshold thickness using a combination of an AZO underlayer and the introduction of N_2.

Regarding the perspectives for this work, other kinds of real-time measurement techniques could be used in order to obtain further insights into the growth of Ag. Real-time stress measurement,

in particular, is a versatile tool for monitoring and understanding film deposition through the build-up of stress at different stages of film growth. Previous works [43,286], among which some on our own experimental setup [12,287,288], have shown the interest of the technique, not only during growth, but also to monitor relaxation processes that could be linked to film ageing. In the context of gas additive, the use of *in situ* photoemission turned out to be decisive but sometimes limited to the extreme surface. To avoid uncertainties brought by sputter-profiling with energetic ion beams, the use of photoemission profiling with less-damaging ion cluster source, preferentially *in situ*, could be of interest to bring more insight into the dynamics of film oxidation. Hard X-ray Photoemission Spectroscopy (HAXPES) would be also of relevance to characterize oxidation profile. Plasma characterization/diagnostics could help further linking the actual nature of activated species in the plasma and their impacts on film chemistry and growth [289]. For instance, it could be used to study the role of charged species such as O_2^- and their bombardment of the growing film during deposition at high $\%O_2$. The effect of the increase in applied voltage with $\%O_2$ was not taken into account in this work. Finally, more advanced structural characterization techniques, in particular x-ray diffraction at synchrotron or TEM imaging coupled with Automatic Crystal Orientation Mapping (ACOM), could be implemented to gain a better understanding of film microstructure and perform a comprehensive study of film texture evolution. At last, TEM with *in situ* deposition capability could help understanding whether certain sites in AZO underlayers (such as grain boundaries) act as nucleation sites for Ag.

From an applicative point of view, this work brought us closer to elucidating the effects and mechanisms behind some of the reported strategies for the deposition of Ag thin films with outstanding properties. It also proved that even if the use of gas surfactants appears to be an attractive way of tailoring metallic film growth, it is not suitable for all metals: the effect on film growth will ultimately depend on the chemical interaction of the gas surfactant with the metal. Finally, the use of AZO and N_2 or O_2 gas additives led to a change in the growth mode, from a purely 3D growth towards a more 2D-like growth. In spite of the negative effects on film crystallinity and conductivity, we could see our improved understanding on the mechanism of surfactant effects being used for the production and optimization of Low-E glazing products, to produce larger in-plane grain sizes and generally favour microstructural traits leading to a higher film conductivity and higher thermal insulation performance.

References

[1] Ministère de la Transition Ecologique. https://www.statistiques.developpement-durable.gouv.fr/edition-numerique/chiffres-cles-du-climat-2022/9-panorama-francais-des-gaz-a. vii

[2] Ministère de la Transition Ecologique. https://www.notre-environnement.gouv.fr/themes/climat/les-emissions-de-gaz-a-effet-de-serre-et-l-empreinte-carbone-ressources/article/les-emissions-des-gaz-a-effet-de-serre-du-secteur-residentiel. vii

[3] E. Hagen et F. Rubens, Connections of the reflection and emission procedure of metals to their electrical conductivity, *Ann. Phys.-Berlin*, vol. 11, p. 873–901, juil. 1903. vii

[4] G. K. Dalapati, A. K. Kushwaha, M. Sharma, V. Suresh, S. Shannigrahi, S. Zhuk et S. Masudy-Panah, Transparent heat regulating (THR) materials and coatings for energy saving window applications: Impact of materials design, micro-structural, and interface quality on the THR performance, *Progress in Materials Science*, vol. 95, p. 42–131, juin 2018. vii

[5] C. G. Granqvist, Electrochromics for smart windows: Oxide-based thin films and devices, *Thin Solid Films*, vol. 564, p. 1–38, août 2014. vii

[6] A. Krasnov et L. Uzai, Optical considerations for automotive windshields with improved thermal performance, *Optical Materials*, vol. 139, p. 113807, mai 2023. vii

[7] Handbook of Chemistry and Physics. vii, 18

[8] S. R. Kasi, H. Kang, C. S. Sass et J. W. Rabalais, Inelastic processes in low-energy ion-surface collisions, *Surface Science Reports*, vol. 10, p. 1–104, jan. 1989. 4

[9] M. Ohring, *Materials Science of Thin Films: deposition and structure*. Academic Press, second edition édition , 2002. 4, 5, 12

[10] P. Sigmund et M. Szymonski, Temperature-dependent sputtering of metals and insulators, *Appl. Phys. A*, vol. 33, p. 141–152, mars 1984. 5

[11] N. Mahne, M. Čekada et M. Panjan, Total and Differential Sputtering Yields Explored by SRIM Simulations, *Coatings*, vol. 12, p. 1541, oct. 2022. 5

[12] Q. Hérault, *Vers la compréhension de la croissance des couches minces d'argent par pulvérisation à la lumière de mesures operando*. Thèse de doctorat, Sorbonne Université, 2019. 5, 11, 16, 17, 22, 32, 39, 40, 105, 108, 116, 119, 141

[13] A. Galerie, *Traitements de surfaces en phase vapeur*. Cachan, France: Hermès, Lavoisier, 2022. 6

[14] D. Depla et S. Mahieu, *Reactive Sputter Deposition*. No. 109 de Springer Series in Materials Science, Springer Berlin, Heidelberg, 2008. 6

[15] D. Depla, S. Mahieu et R. De Gryse, Depositing Aluminium Oxide: A Case Study of Reactive Magnetron Sputtering, *in Reactive Sputter Deposition* (D. Depla et S. Mahieu, éds), Springer Series in Materials Science, p. 153–197, Berlin, Heidelberg: Springer, 2008. 6, 7

[16] E. Bauer, Phänomenologische theorie der kristallabscheidung an oberflächen. i, *Zeitschrift für Kristallographie - Crystalline Materials*, vol. 110, no. 1-6, p. 372–394, 1958. 7

[17] E. Bauer et H. Poppa, Recent advances in epitaxy, *Thin Solid Films*, vol. 12, p. 167–185, sept. 1972. 7

[18] T. Michely et J. Krug, *Islands, Mounds and Atoms*, vol. 42. Springer, 01 2004. 8, 19, 25

[19] F. Bocchese, I. Brown, D. Cornil, P. Moskovkin, J. Muller, S. D. Kenny, R. Smith et S. Lucas, Low-E glass improvement by the understanding and control of the Ag growth, *Applied Surface Science*, vol. 611, p. 155600, fév. 2023. 10, 19

[20] G. Ehrlich et F. G. Hudda, Atomic view of surface self-diffusion: Tungsten on tungsten, *The Journal of Chemical Physics*, vol. 44, p. 1039–1049, mai 2004. 11

[21] R. L. Schwoebel et E. J. Shipsey, Step Motion on Crystal Surfaces, *Journal of Applied Physics*, vol. 37, p. 3682–3686, juin 2004. 11

[22] J. A. Venables, *Introduction to Surface and Thin Film Processes*. Cambridge University Press, 2000. 12, 13, 116

[23] C. Ratsch et J. A. Venables, Nucleation theory and the early stages of thin film growth, *J Vac Sci Technol A J Vac Sci Technol A*, vol. 21, p. S96–S109, sept. 2003. 13

[24] J. A. Venables et J. H. Harding, Nucleation and growth of supported metal clusters at defect sites on oxide and halide (001) surfaces, *Journal of Crystal Growth*, vol. 211, p. 27–33, avril 2000. 14

[25] R. Lazzari et J. Jupille, Growth kinetics and size-dependent wetting of Ag/Alpha-Al_2O_3(0001) nanoparticles studied via the plasmonic response, *Nanotechnology*, vol. 23, p. 135707, avril 2012. 14, 19

[26] P. Jensen, Growth of nanostructures by cluster deposition: Experiments and simple models, *Rev. Mod. Phys.*, vol. 71, p. 1695–1735, oct. 1999. 14, 15, 19

[27] J. Carrey, J.-L. Maurice, F. Petroff et A. Vaurès, Growth of au clusters on amorphous Al_2O_3: Evidence of cluster mobility above a critical size, *Phys. Rev. Lett.*, vol. 86, p. 4600–4603, mai 2001. 15

[28] L. Bardotti, P. Jensen, A. Hoareau, M. Treilleux et B. Cabaud, Experimental Observation of Fast Diffusion of Large Antimony Clusters on Graphite Surfaces, *Phys. Rev. Lett.*, vol. 74, p. 4694–4697, juin 1995. 15

[29] C. Herring, Effect of Change of Scale on Sintering Phenomena, *Journal of Applied Physics*, vol. 21, p. 301–303, avril 1950. 15

[30] V. Gervilla, G. A. Almyras, B. Lu et K. Sarakinos, Coalescence dynamics of 3D islands on weakly-interacting substrates, *Sci Rep*, vol. 10, p. 2031, fév. 2020. 15, 16, 19, 121

[31] P. Grammatikopoulos, M. Sowwan et J. Kioseoglou, Computational Modeling of Nanoparticle Coalescence, *Advanced Theory and Simulations*, vol. 2, no. 6, p. 1900013, 2019. 15

[32] M. José-Yacamán, C. Gutierrez-Wing, M. Miki, D.-Q. Yang, K. N. Piyakis et E. Sacher, Surface Diffusion and Coalescence of Mobile Metal Nanoparticles, *J. Phys. Chem. B*, vol. 109, p. 9703–9711, mai 2005. 15, 17

[33] P. Deltour, J.-L. Barrat et P. Jensen, Fast Diffusion of a Lennard-Jones Cluster on a Crystalline Surface, *Phys. Rev. Lett.*, vol. 78, p. 4597–4600, juin 1997. 15

[34] K. E. J. Lehtinen et M. R. Zachariah, Effect of coalescence energy release on the temporal shape evolution of nanoparticles, *Phys. Rev. B*, vol. 63, p. 205402, avril 2001. 15

[35] B. Buesser et S. E. Pratsinis, Morphology and Crystallinity of Coalescing Nanosilver by Molecular Dynamics, *J. Phys. Chem. C*, vol. 119, p. 10116–10122, mai 2015. 15

[36] S. Grachev, M. De Grazia, E. Barthel, E. Søndergård et R. Lazzari, Real time monitoring of nanoparticle film growth at high deposition rate with optical spectroscopy of plasmon resonances, *J. Phys. D: Appl. Phys.*, vol. 46, p. 375305–375315, 2013. 17

[37] I. M. Rycroft et B. L. Evans, The in situ characterization of metal film resistance during deposition, *Thin Solid Films*, vol. 290-291, p. 283–288, déc. 1996. 17, 43

[38] A. I. Maaroof et B. L. Evans, Onset of electrical conduction in Pt and Ni films, *Journal of Applied Physics*, vol. 76, p. 1047–1054, juil. 1994. 17

[39] G. Zhao, W. Shen, E. Jeong, S.-G. Lee, S. M. Yu, T.-S. Bae, G.-H. Lee, S. Z. Han, J. Tang, E.-A. Choi et J. Yun, Ultrathin Silver Film Electrodes with Ultralow Optical and Electrical Losses for Flexible Organic Photovoltaics, *ACS Appl. Mater. Interfaces*, vol. 10, p. 27510–27520, août 2018. 17, 32

[40] L. Wang, J. Liu, L. Zhao, X. Fan et Q. Wang, Improvement of the conductivity and transmittance of AZO/Ag/AZO composite film via lattice oxygen ratio regulation, *Optical Materials*, vol. 122, p. 111672, déc. 2021. 17, 32

[41] G. Zhao, W. Shen, E. Jeong, S. G. Lee, H. S. Chung, T. S. Bae, J. S. Bae, G. H. Lee, J. Tang et J. Yun, Nitrogen-Mediated Growth of Silver Nanocrystals to Form UltraThin, High-Purity Silver-Film Electrodes with Broad band Transparency for Solar Cells, *ACS Appl Mater Interfaces*, vol. 10, p. 40901–40910, nov. 2018. 17, 28, 60, 63, 67

[42] A. Saedi et M. J. Rost, Thermodynamics of deposition flux-dependent intrinsic film stress, *Nat Commun*, vol. 7, p. 10733, fév. 2016. 18, 33

[43] E. Chason, M. Karlson, J. J. Colin, D. Magnfält, K. Sarakinos et G. Abadias, A kinetic model for stress generation in thin films grown from energetic vapor fluxes, *Journal of Applied Physics*, vol. 119, p. 145307, avril 2016. 18, 141

[44] H. L. Skriver et N. M. Rosengaard, Surface energy and work function of elemental metals, *Phys. Rev. B*, vol. 46, p. 7157–7168, sept. 1992. 18, 32

[45] A. Stankic, R. Cortes-Huerto, N. Crivat, D. Demaille, J. Goniakowski et J. Jupille, Equilibrium shapes of supported silver clusters, *Nanoscale*, vol. 5, p. 2448–2453, 2013. 18, 72

[46] K. S. Gadre et T. L. Alford, Contact angle measurements for adhesion energy evaluation of silver and copper films on parylene-n and SiO_2 substrates, *Journal of Applied Physics*, vol. 93, p. 919–923, déc. 2002. 18

[47] S. H. Park, K. S. Lee et A. S. Reddy, Low emissivity Ag/Si/glass thin films deposited by sputtering, *Solid State Sciences*, vol. 13, p. 1984–1988, nov. 2011. 18

[48] J. A. Meyer, J. Vrijmoeth, H. A. van der Vegt, E. Vlieg et R. J. Behm, Importance of the additional step-edge barrier in determining film morphology during epitaxial growth, *Phys. Rev. B*, vol. 51, p. 14790–14793, mai 1995. 19, 26

[49] B. S. Swartzentruber, Direct measurement of surface diffusion using atom-tracking scanning tunneling microscopy, *Phys Rev Lett*, vol. 76, p. 459–462, jan. 1996. 19

[50] C. Revenant, G. Renaud, R. Lazzari et J. Jupille, Defect-pinned nucleation, growth, and dynamic coalescence of Ag islands on MgO(001): Anin situgrazing-incidence small-angle x-ray scattering study, *Physical Review B*, vol. 79, no. 23, 2009. 19

[51] I. M. Goldby, L. Kuipers, B. von Issendorff et R. E. Palmer, Diffusion and aggregation of sizeselected silver clusters on a graphite surface, *Applied Physics Letters*, vol. 69, p. 2819–2821, nov. 1996. 19

[52] C. Kittel, *Introduction to Solid State Physics*. California: John Wiley & Sons, Inc., 8th edition édition , 2005. 20

[53] F. Corbella, *Impact of texture on resistivity of silver-based model low-emissive coatings*. These de doctorat, Sorbonne université, mai 2022. 20, 32, 118, 119, 121, 135

[54] K. Fuchs, The conductivity of thin metallic films according to the electron theory of metals, *Math. Proc. Cambridge Philos. Soc.*, vol. 34, p. 100–108, 1938. 20

[55] E. H. Sondheimer, The mean free path of electrons in metals, *Adv. Phys.*, vol. 1, p. 1–42, 1952. 20

[56] A. F. Mayadas et M. Shatzkes, Electrical-resistivity model for polycrystalline films: the case of arbitrary reflection at external surface, *Phys. Rev. B*, vol. 1, p. 1382, 1970. 20, 97

[57] J. Mashaiekhy, Z. Shafieizadeh et H. Nahidi, Effect of substrate temperature and film thickness on the characteristics of silver thin films deposited by DC magnetron sputtering, *Eur Phys J-Appl Phys*, vol. 60, nov. 2012. 22

[58] W. Kim, D. Ku, K. Lee et B. Cheong, Effect of oxygen content and deposition temperature on the characteristics of thin silver films deposited by magnetron sputtering, *Applied Surface Science*, vol. 257, no. 4, p. 1331–1336, 2010. 22, 30, 89, 94, 96

[59] A. A. Baski et H. Fuchs, Epitaxial growth of silver on mica as studied by AFM and STM, *Surface Science*, vol. 313, p. 275–288, juil. 1994. 22

[60] M. B. Cinali et z. D. Coşkun, Optimization of physical properties of sputtered silver films by change of deposition power for low emissivity applications, *Journal of Alloys and Compounds*, vol. 853, p. 157073, fév. 2021. 23

[61] V. Kapaklis, P. Poulopoulos, V. Karoutsos, T. Manouras et C. Politis, Growth of thin Ag films produced by radio frequency magnetron sputtering, *Thin Solid Films*, vol. 510, no. 1-2, p. 138–142, 2006. 23

[62] Y. S. Jung, Study on texture evolution and properties of silver thin films prepared by sputtering deposition, *Applied Surface Science*, vol. 221, no. 1-4, p. 281–287, 2004. 23

[63] I. Petrov, P. B. Barna, L. Hultman et J. E. Greene, Microstructural evolution during film growth, *Journal of Vacuum Science & Technology A: Vacuum, Surfaces, and Films*, vol. 21, no. 5, p. S117–S128, 2003. 23, 24

[64] M. Vergöhl, N. Malkomes, B. Szyszka, F. Neumann, T. Matthée et G. Bräuer, Optimization of the reflectivity of magnetron sputter deposited silver films, *Journal of Vacuum Science & Technology A*, vol. 18, p. 1632–1637, juil. 2000. 23, 24

[65] H. Windischmann, Intrinsic stress in sputter-deposited thin films, *Critical Reviews in Solid State and Materials Sciences*, vol. 17, p. 547–596, jan. 1992. 23

[66] C. A. Davis, A simple model for the formation of compressive stress in thin films by ion bombardment, *Thin Solid Films*, vol. 226, p. 30–34, avril 1993. 23

[67] J. A. Thornton, High Rate Thick Film Growth, *Annual Review of Materials Science*, vol. 7, no. 1, p. 239–260, 1977. 23, 24

[68] J. A. Thornton, The microstructure of sputterdeposited coatings, *Journal of Vacuum Science & Technology A*, vol. 4, p. 3059–3065, nov. 1986. 23

[69] C. R. M. Grovenor, H. T. G. Hentzell et D. A. Smith, The development of grain structure during growth of metallic films, *Acta Metallurgica*, vol. 32, p. 773–781, mai 1984. 23

[70] B. A. Movchan et A. V. Demchishin, Structure and properties of thick condensates of nickel, titanium, tungsten, aluminum oxides, and zirconium dioxide in vacuum., *Fiz. Metal. Metalloved*, jan. 1969. 23

[71] S. Mahieu, P. Ghekiere, D. Depla et R. De Gryse, Biaxial alignment in sputter deposited thin films, *Thin Solid Films*, vol. 515, p. 1229–1249, déc. 2006. 23

[72] P. Brault, A.-L. Thomann et M. Cavarroc, Theory and molecular simulations of plasma sputtering, transport and deposition processes, *Eur. Phys. J. D*, vol. 77, p. 19, fév. 2023. 23

[73] G.-S. Jang, D.-Y. Kim et N.-M. Hwang, The Effect of Charged Ag Nanoparticles on Thin Film Growth during DC Magnetron Sputtering, *Coatings*, vol. 10, no. 8, p. 736, 2020. 23

[74] Y. Mikami, K. Yamada, A. Ohnari, T. Degawa, T. Migita, T. Tanaka, K. Kawabata et H. Kajioka, Effect of dc bias voltage on the deposition rate for ni thin films by rf-dc coupled unbalanced-magnetron sputtering, *Surface and coatings technology*, vol. 133, p. 295–300, Nov 2000. 23

[75] S. Burinskas et J. Dudonis, Synthesis of cu/cr multilayer thin films deposited by unbalanced magnetron sputtering, *Materials Science-Medziagotyra*, vol. 15, no. 3, p. 220–223, 2009. 23

[76] R. Said, W. Ahmed et J. Gracio, Closed field unbalanced magnetron sputtering ion plating of ni/al thin films: Influence of the magnetron power, *Journal of Nanoscience and Nanotechnology*, vol. 10, p. 2558–2563, Apr 2010. 2nd International Conference on Advanced Nano Materials, Univ Aveiro, Aveiro, Portugal. 23

[77] T. Wang, Q. Zhang, S. Yu et G. Zhang, Development of latent fingermarks by unbalanced magnetron sputtering deposited ultra-thin metal film, *Vacuum*, vol. 194, Dec 2021. 23

[78] T. Tran, Y. Kim, N. Baule, M. Shrestha, B. Zheng, K. Wang, T. Schuelke et Q. H. Fan, Single-beam ion source enhanced growth of transparent conductive thin films, *J. Phys. D: Appl. Phys.*, vol. 55, p. 395202, juil. 2022. 23

[79] T. Tran, X. Wang, M. Shrestha, K. Wang et Q. H. Fan, Ultra-thin silver films grown by sputtering with a soft ion beam-treated intermediate layer, *J. Phys. D: Appl. Phys.*, vol. 56, p. 365501, juin 2023. 23

[80] A. Anders, A structure zone diagram including plasma-based deposition and ion etching, *Thin Solid Films*, vol. 518, p. 4087–4090, mai 2010. 24, 25

[81] D. W. Hoffman, J. Park et T. S. Morley, Inert gases in sputtered tungsten: A test of predictive capability, *Journal of Vacuum Science & Technology A*, vol. 12, p. 1451–1456, juil. 1994. 24

[82] K. Kamoshida, Argon entrapment in magnetron-sputtered Al alloy films, *Thin Solid Films*, vol. 283, p. 57–60, sept. 1996. 24

[83] M. Kawamura, R. Sagara, Y. Abe, T. Kiba et K. H. Kim, Large-grained Ag thin films with low electrical resistivity produced by sputtering in Kr gas, *Jpn J Appl Phys Jpn J Appl Phys*, vol. 59, avril 2020. 24

[84] R. Sagara, M. Kawamura, T. Kiba, Y. Abe et K. H. Kim, Characteristics of Ag thin films sputter deposited using Ar or Kr gas under different pressure, *Surface and Coatings Technology*, vol. 388, p. 125616, avril 2020. 24, 25

[85] T. Hamano, E. Kudo, M. Kawamura, T. Kiba, Y. Abe, K. H. Kim et H. Murotani, Characteristics and environmental durability of Ag films with and without Al surface layer sputtered in Ar or Kr gas, *Thin Solid Films*, vol. 704, p. 138020, juin 2020. 24

[86] K. Mizukoshi, T. Yamamura, Y. Tomioka et M. Kawamura, Effects of sputtering with Kr gas and insertion of lowermost layer on electrical resistivity of Ag-multilayer, *Jpn. J. Appl. Phys.*, vol. 61, p. 095503, août 2022. 24

[87] G. Q. Zhao, E. Jeong, E. A. Choi, S. M. Yu, J. S. Bae, S. G. Lee, S. Z. Han, G. H. Lee et J. Yun, Strategy for improving Ag wetting on oxides: Coalescence dynamics versus nucleation density, *Appl Surf Sci*, vol. 510, avril 2020. 25

[88] M. Copel, M. C. Reuter, E. Kaxiras et R. M. Tromp, Surfactants in epitaxial growth, *Phys. Rev. Lett.*, vol. 63, p. 632–635, août 1989. 26

[89] J. Vrijmoeth, H. A. van der Vegt, J. A. Meyer, E. Vlieg et R. J. Behm, Surfactant-Induced Layer-by-Layer Growth of Ag on Ag(111): Origins and Side Effects, *Phys. Rev. Lett.*, vol. 72, p. 3843–3846, juin 1994. 26

[90] J. J. De Miguel, Epitaxial growth and the role of surfactants, *Surf. Rev. Lett.*, vol. 04, p. 353–359, avril 1997. 26

[91] J. Ferrón, L. Gómez, J. M. Gallego, J. Camarero, J. E. Prieto, V. Cros, A. L. Vázquez de Parga, J. J. de Miguel et R. Miranda, Influence of surfactants on atomic diffusion, *Surface Science*, vol. 459, p. 135–148, juil. 2000. 26

[92] H. L. Meyerheim, D. Sander, R. Popescu, W. Pan, I. Popa et J. Kirschner, Surfactant-Mediated Growth Revisited, *Phys. Rev. Lett.*, vol. 99, p. 116101, sept. 2007. 26

[93] H. A. van der Vegt, W. J. Huisman, P. B. Howes, T. S. Turner et E. Vlieg, Surfactants used in Ag(111) homoepitaxy: Sb, In, Pt and O_2, *Surface Science*, vol. 365, p. 205–211, sept. 1996. 26

[94] Z. Zhang et M. G. Lagally, Atomic-scale mechanisms for surfactant-mediated layer-by-layer growth in homoepitaxy, *Phys. Rev. Lett.*, vol. 72, p. 693–696, jan. 1994. 26

[95] A. Picone, Metal Thin Film Growth on Metals: Surfactant Effects, *in Encyclopedia of Interfacial Chemistry* (K. Wandelt, éd.), p. 221–231, Oxford: Elsevier, jan. 2018. 26

[96] S. Oppo, V. Fiorentini et M. Scheffler, Theory of adsorption and surfactant effect of Sb on Ag(111), *Phys. Rev. Lett.*, vol. 71, p. 2437–2440, oct. 1993. 26

[97] W. Li-Li et W. Feng-Min, Simulation of surfactant effects on the growth of metal homo-expitaxial Sb–Ag/Ag(111), *Chinese Phys. B*, vol. 19, p. 066801, juin 2010. 26

[98] X. Liu, Y. Han, J. W. Evans, A. K. Engstfeld, R. J. Behm, M. C. Tringides, M. Hupalo, H.-Q. Lin, L. Huang, K.-M. Ho, D. Appy, P. A. Thiel et C.-Z. Wang, Growth morphology and properties of metals on graphene, *Progress in Surface Science*, vol. 90, p. 397–443, déc. 2015. 26

[99] K. Sarakinos, A review on morphological evolution of thin metal films on weakly-interacting substrates, *Thin Solid Films*, vol. 688, p. 137312, oct. 2019. 26

[100] A. Romanyuk, R. Steiner, D. Mathys, V. Thommen et P. Oelhafen, Use of tin as a surfactant material for the growth of thin silver films on silicon oxide, *Surface Science*, vol. 602, p. L49–L52, mai 2008. 26, 31

[101] K. Fukuda, S. H. N. Lim et A. Anders, Coalescence of magnetron-sputtered silver islands affected by transition metal seeding (Ni, Cr, Nb, Zr, Mo, W, Ta) and other parameters, *Thin Solid Films*, vol. 516, no. 14, p. 4546–4552, 2008. 26, 31

[102] G. Jeffers, M. A. Dubson et P. M. Duxbury, Island to percolation transition during growth of metal films, *J. Appl. Phys.*, vol. 75, p. 5016–5020, 1994. 27, 30, 116

[103] B. Lu, L. Souqui, V. Elofsson et K. Sarakinos, Scaling of elongation transition thickness during thin-film growth on weakly interacting substrates, *Appl Phys Lett Appl Phys Lett*, vol. 111, août 2017. 27

[104] A. Jamnig, D. G. Sangiovanni, G. Abadias et K. Sarakinos, Atomic-scale diffusion rates during growth of thin metal films on weakly-interacting substrates, *Sci Rep*, vol. 9, p. 6640, avril 2019. 27

[105] A. Jamnig, N. Pliatsikas, G. Abadias et K. Sarakinos, On the effect of copper as wetting agent during growth of thin silver films on silicon dioxide substrates, *Applied Surface Science*, vol. 538, p. 148056, fév. 2021. 27

[106] A. Jamnig, N. Pliatsikas, G. Abadias et K. Sarakinos, Manipulation of thin metal film morphology on weakly interacting substrates via selective deployment of alloying species, *Journal of Vacuum Science & Technology A*, vol. 40, p. 033407, avril 2022. 27

[107] J. F. Pierson, D. Wiederkehr et A. Billard, Reactive magnetron sputtering of copper, silver, and gold, *Thin Solid Films Thin Solid Films*, vol. 478, p. 196–205, mai 2005. 28, 30, 71, 72, 89, 94, 100

[108] J. Bulir, M. Novotny, J. Lancok, L. Fekete, J. Drahokoupil et J. Musil, Nucleation of ultrathin silver layer by magnetron sputtering in Ar/N_2 plasma, *Surf Coat Tech*, vol. 228, p. S86–S90, août 2013. 28

[109] G. Zhao, S. M. Kim, S. G. Lee, T.-S. Bae, C. Mun, S. Lee, H. Yu, G. H. Lee, H.-S. Lee, M. Song et J. Yun, Bendable solar cells from stable, flexible, and transparent conducting electrodes fabricated using a nitrogen-doped ultrathin copper film, *Advanced Functional Materials*, vol. 26, p. 4180–4191, 2016. 28

[110] R. H. H. Ko, A. Khalatpour, J. K. D. Clark et N. P. Kherani, Ultrasmooth ultrathin Ag films by AlN seeding and Ar/N_2 sputtering for transparent conductive and heating applications, *APL Materials*, vol. 6, p. 121112, 2018. 28, 56

[111] A. Jamnig, N. Pliatsikas, M. Konpan, J. Lu, T. Kehagias, A. N. Kotanidis, N. Kalfagiannis, D. V. Bellas, E. Lidorikis, J. Kovac, G. Abadias, I. Petrov, J. E. Greene et K. Sarakinos, 3D-to-2D Morphology Manipulation of Sputter-Deposited Nanoscale Silver Films on Weakly Interacting Substrates via Selective Nitrogen Deployment for Multifunctional Metal Contacts, *Acs Appl Nano Mater*, vol. 3, p. 4728–4738, mai 2020. 28, 29, 30, 56, 60, 63, 70, 71, 96, 100, 140

[112] J. Yun, H. S. Chung, S. G. Lee, J. S. Bae, T. E. Hong, K. Takahashi, S. M. Yu, J. Park, Q. Guo, G.-H. Lee, S. Z. Han, Y. Ikoma et E.-A. Choi, An unexpected surfactant role of immiscible nitrogen in the structural development of silver nanoparticles: an experimental and numerical investigation, *Nanoscale*, vol. 12, p. 1749–1758, 2020. 28

[113] C. Geng, J. Li, T. Weiske et H. Schwarz, Complete cleavage of the N-N triple bond by Ta_2N^+ via degenerate ligand exchange at ambient temperature: A perfect catalytic cycle, *Proceedings of the National Academy of Sciences*, vol. 116, p. 21416–21420, oct. 2019. 28, 30

[114] E. S. Shanley et J. L. Ennis, The chemistry and free energy of formation of silver nitride, *Ind. Eng. Chem. Res.*, vol. 30, p. 2503–2506, nov. 1991. 28

[115] M. Kawamura, Y. Abe et K. Sasaki, Orientation of metal films deposited by sputtering using Ar/N_2 gas mixtures, *Thin Solid Films*, vol. 469-470, p. 491–494, déc. 2004. 28

[116] M. Kawamura, Y. Abe et K. Sasaki, Sputter-deposition of Ag films in a nitrogen discharge, *Thin Solid Films*, vol. 515, p. 540–542, oct. 2006. 28, 29, 71, 73, 119

[117] S. Agarwal, B. Hoex, M. C. M. van de Sanden, D. Maroudas et E. S. Aydil, Absolute densities of N and excited N_2 in a N_2 plasma, *Applied Physics Letters*, vol. 83, p. 4918–4920, déc. 2003. 28

[118] A. Bousquet, L. Spinelle, J. Cellier et E. Tomasella, Optical Emission Spectroscopy Analysis of Ar/N_2 Plasma in Reactive Magnetron Sputtering, *Plasma Process. Polym.*, vol. 6, p. 605–609, 2009. 28

[119] N. Kang, S.-g. Oh, F. Gaboriau et A. Ricard, Determination of Absolute Nitrogen Atom Density in Ar-N_2 ICP Discharge, *Journal of the Korean Physical Society*, vol. 59, p. 3031–3036, nov. 2011. 28

[120] Y.-S. Liang, C. Xue, Y.-R. Zhang et Y.-N. Wang, Investigation of active species in low-pressure capacitively coupled N_2/Ar plasmas, *Physics of Plasmas*, vol. 28, p. 013510, jan. 2021. 28

[121] J. M. Ricart, J. Torras, J. Rubio et F. Illas, Ab initio cluster model study of geometry and bonding character of atomic nitrogen chemisorbed on the Cu(100) and Ag(100) surfaces, *Surface Science*, vol. 374, p. 31–43, mars 1997. 28, 63, 71

[122] G.-C. Wang, L. Jiang, X.-Y. Pang et J. Nakamura, Cluster and Periodic DFT Calculations: The Adsorption of Atomic Nitrogen on M(111) (M = Cu, Ag, Au) Surfaces, *J. Phys. Chem. B*, vol. 109, p. 17943–17950, sept. 2005. 28, 63, 71

[123] D. B. Kokh, R. J. Buenker et J. L. Whitten, Trends in adsorption of open-shell atoms and small molecular fragments on the Ag(111) surface, *Surface Science*, vol. 600, p. 5104–5113, déc. 2006. 28, 63, 71

[124] H. Ueta, M. A. Gleeson et A. W. Kleyn, The interaction of hyperthermal nitrogen with N-covered Ag(111), *J. Chem. Phys.*, vol. 135, p. 074702, août 2011. 28, 65, 71

[125] L. Martin-Gondre, G. A. Bocan, M. Alducin, J. I. Juaristi et R. Díez Muiño, Energy dissipation channels in the adsorption of N on Ag(111), *Computational and Theoretical Chemistry*, vol. 990, p. 126–131, juin 2012. 28

[126] L. Martin-Gondre, G. A. Bocan, M. Blanco-Rey, M. Alducin, J. I. Juaristi et R. Diez Muino, Scattering of Nitrogen Atoms off Ag(111) Surfaces: A Theoretical Study, *J. Phys. Chem. C*, vol. 117, p. 9779–9790, mai 2013. 28

[127] M. A. Gleeson et A. W. Kleyn, Nitrogen interactions at metal surfaces, *Nucl. Instrum. Methods Phys. Res. Sect. B-Beam Interact. Mater. Atoms*, vol. 317, p. 109–114, déc. 2013. 28

[128] B. W. J. Chen, D. Kirvassilis, Y. Bai et M. Mavrikakis, Atomic and Molecular Adsorption on Ag(111), *J. Phys. Chem. C*, vol. 123, p. 7551–7566, avril 2019. 28, 81

[129] J. I. Juaristi, E. Diaz, G. A. Bocan, R. D. Muino, M. Alducin et M. Blanco-Rey, Angular distributions and rovibrational excitation of N_2 molecules recombined on N-covered Ag(111) by the Eley-Rideal mechanism, *Catal. Today*, vol. 244, p. 115–121, avril 2015. 28

[130] J. Yun, H. S. Chung, S. G. Lee, J. S. Bae, T. E. Hong, K. Takahashi, S. M. Yu, J. Park, Q. X. Guo, G. H. Lee, S. Z. Han, Y. Ikoma et E. A. Choi, An unexpected surfactant role of immiscible nitrogen in the structural development of silver nanoparticles: an experimental and numerical investigation, *Nanoscale*, vol. 12, p. 1749–1758, jan. 2020. 28, 29, 32, 56, 60, 63, 67, 69, 71, 72, 121

[131] R. N. Carter, M. J. Murphy et A. Hodgson, On the recombinative desorption of N_2 from Ag(111), *Surface Science*, vol. 387, p. 102–111, oct. 1997. 28, 63, 71

[132] M. Blanco-Rey, E. Diaz, G. A. Bocan, R. Diez Muino, M. Alducin et J. Inaki Juaristi, Efficient N_2 Formation on Ag(111) by Eley-Rideal Recombination of Hyperthermal Atoms, *J. Phys. Chem. Lett.*, vol. 4, p. 3704–3709, nov. 2013. 28, 65, 71

[133] G. Zhao, W. Shen, E. Jeong, S.-G. Lee, S. M. Yu, T.-S. Bae, G.-H. Lee, S. Z. Han, J. Tang, E.-A. Choi et J. Yun, Ultrathin Silver Film Electrodes with Ultralow Optical and Electrical Losses for Flexible Organic Photovoltaics, *ACS Appl. Mater. Interfaces*, vol. 10, p. 27510–27520, août 2018. 29, 30

[134] J. M. Riveiro, P. S. Normile, J. P. Andrés, J. A. Gonzalez, J. A. De Toro, T. Muñoz et P. Muñiz, Oxygen-assisted control of surface morphology in nonepitaxial sputter growth of Ag, *Appl. Phys. Lett.*, vol. 89, p. 201902, 2006. 29, 30, 94

[135] W. Wang, M. Song, T.-S. Bae, Y. H. Park, Y.-C. Kang, S.-G. Lee, S.-Y. Kim, D. H. Kim, S. Lee, G. Min, G.-H. Lee, J.-W. Kang et J. Yun, Transparent Ultrathin Oxygen-Doped Silver Electrodes for Flexible Organic Solar Cells, *Advanced Functional Materials*, vol. 24, no. 11, p. 1551–1561, 2014. 29, 30, 89, 94, 97

[136] J. Yun, W. Wang, T. S. Bae, Y. H. Park, Y. C. Kang, D. H. Kim, S. Lee, G. H. Lee, M. Song et J. W. Kang, Preparation of flexible organic solar cells with highly conductive and transparent metal-oxide multilayer electrodes based on silver oxide, *ACS Applied Materials & Interfaces*, vol. 5, p. 9933–9941, 2013. 29, 30, 89, 94

[137] G. Zhao, W. Wang, T.-S. Bae, S.-G. Lee, C. Mun, S. Lee, H. Yu, G.-H. Lee, M. Song et J. Yun, Stable ultrathin partially oxidized copper film electrode for highly efficient flexible solar cells, *Nat. Commun.*, vol. 6, p. 8830, Nov 2015. 29, 30

[138] N. Pliatsikas, A. Jamnig, M. Konpan, A. Delimitis, G. Abadias et K. Sarakinos, Manipulation of thin silver film growth on weakly interacting silicon dioxide substrates using oxygen as a surfactant, *J Vac Sci Technol A*, vol. 38, p. 0734–2101, 2020. 29, 30, 89, 100, 140

[139] Y. Abe, T. Hasegawa, M. Kawamura et K. Sasaki, Characterization of Ag oxide thin films prepared by reactive RF sputtering, *Vacuum*, vol. 76, p. 1–6, oct. 2004. 30, 89, 94, 100

[140] R. Snyders, M. Wautelet, R. Gouttebaron, J. Dauchot et M. Hecq, Experimental and theoretical studies of the DC reactive magnetron sputtering deposition of silver oxide thin films, *Surface and Coatings Technology*, vol. 174-175, p. 1282–1286, sept. 2003. 30, 81, 89, 96, 99, 100

[141] R. Snyders, R. Gouttebaron, J. P. Dauchot et M. Hecq, Increasing the deposition rate of oxide films by increasing the plasma reactivity, *Surface and Coatings Technology*, vol. 200, p. 448–452, oct. 2005. 30, 89

[142] D. Chatain, F. Chabert, V. Ghetta et J. Fouletier, New experimental setup for wettability characterization under monitored oxygen activity : II Wettability of sapphire by silver-oxygen melts, *J. Am. Ceram. Soc.*, vol. 77, no. 1, p. 197–201, 1994. 30, 98

[143] M. Muolo, F. Valenza, A. Passerone et D. Passerone, Oxygen influence on ceramics wettability by liquid metals: Ag/alpha-Al_2O_3: experiments and modelling, *Mat. Sci. Eng. A*, vol. 495, p. 153–158, 2008. 30, 98

[144] G. Q. Zhao, E. Jeong, E. A. Choi, S. M. Yu, J. S. Bae, S. G. Lee, S. Z. Han, G. H. Lee et J. Yun, Strategy for improving Ag wetting on oxides: Coalescence dynamics versus nucleation density, *Appl Surf Sci Appl Surf Sci*, vol. 510, p. 0169–4332, 2020. 30, 89, 97, 116

[145] S. Grachev, M. De Grazia, E. Barthel, E. Søndergård et R. Lazzari, Real time monitoring of nanoparticle film growth at high deposition rate with optical spectroscopy of plasmon resonances, *J. Phys. D: Appl. Phys.*, vol. 46, p. 375305–375315, 2013. 30, 46

[146] J. M. Warrender et M. J. Aziz, Effect of deposition rate on morphology evolution of metal-on-insulator films grown by pulsed laser deposition, *Phys Rev B*, vol. 76, juil. 2007. 30

[147] N. Combe, P. Jensen et A. Pimpinelli, Changing shapes in the nanoworld, *Phys. Rev. Lett.*, vol. 85, p. 110–113, 2000. 30

[148] G. Zhao, E. Jeong, S.-G. Lee, S. M. Yu, J.-S. Bae, J. Rha, G.-H. Lee, Y. Ikoma et J. Yun, Insights into effects of O-incorporated Ag nanoparticles as wetting seeds toward improving Ag wetting on oxides, *Applied Surface Science*, vol. 562, p. 150135, oct. 2021. 30, 100

[149] P. Li, H. Li, J. Ma, Y. Zhou, W. Zhang, L. Cong, H. Xu et Y. Liu, Structural optimization of oxide/metal/oxide transparent conductors for high-performance low-emissivity heaters, *Adv. Mater. Interfaces*, vol. 5, p. 1801287, 2018. 30

[150] E. Jeong, S.-G. Lee, J.-S. Bae, S. M. Yu, S. Z. Han, G.-H. Lee, E.-A. Choi et J. Yun, Effects of substantial atomic-oxygen migration across silver oxide interfaces during silver growth, *Applied Surface Science*, vol. 568, p. 150927, déc. 2021. 30, 94, 98, 106

[151] E. Jeong, S.-G. Lee, S. M. Yu, S. Z. Han, G.-H. Lee, Y. Ikoma, E.-A. Choi et J. Yun, Spontaneous post-growth oxygen dissipation and electrical improvement of silver electrodes in substoichiometric oxidation states, *Appl. Surf. Sci.*, vol. 623, p. 156998, juin 2023. WOS:000957211100001. 30, 50, 128

[152] J. F. Weaver et G. B. Hoflund, Surface characterization study of the thermal decomposition of AgO, *The Journal of Physical Chemistry*, vol. 98, p. 8519–8524, 1994. 30, 80, 82, 84

[153] J. F. Weaver et G. B. Hoflund, Surface characterization study of the thermal decomposition of Ag_2O, *Chemistry of Materials*, vol. 6, p. 1693–1699, 1994. 30, 80, 84

[154] W. S. Epling, G. B. Hoflund et G. N. Salaita, Surface characterization study of the thermal decomposition of Ag_2CO_3, *The Journal of Physical Chemistry B*, vol. 102, p. 2263–2268, 1998. 30, 80, 82, 84

[155] J. F. Pierson et C. Rousselot, Stability of reactively sputtered silver oxide films, *Surf. Coat. Technol.*, vol. 200, p. 276–279, 2005. 30, 80, 89

[156] G. Schön, ESCA studies of Ag, Ag_2O and AgO, *Acta Chemica Scandinavia*, vol. 27, p. 2623–2633, 1973. 30, 80, 84

[157] J. S. Hammond, S. W. Gaarenstroom et N. Winograd, X-ray photoelectron spectroscopic studies of cadmium- and silver-oxygen surfaces, *Anal. Chem.*, vol. 47, p. 2193–2199, 1975. 30, 80, 82, 84

[158] V. K. Kaushik, XPS core level spectra and Auger parameters for some silver compounds, *J Electron Spectrosc*, vol. 56, p. 273–277, 1991. 30, 80, 82, 84

[159] X. Bao, M. Muhler, T. Schedel-Niedrig et R. Schlögl, Interaction of oxygen with silver at high temperature and atmospheric pressure: a spectroscopic and structural analysis of a strongly bound surface species, *Phys. Rev. B*, vol. 54, no. 3, p. 2249–2262, 1996. 30, 80, 81, 84

[160] L. H. Tjeng, M. B. J. Meinders, J. van Elp, J. Ghijsen, G. A. Sawatzky et R. L. Johnson, Electronic structure of ag_2o, *Phys. Rev. B*, vol. 41, p. 3190–3199, 1990. 30, 80, 81, 84

[161] G. B. Hoflund, Z. F. Hazos et G. N. Salaita, Surface characterization study of Ag, AgO, and Ag_2O using x-ray photoelectron spectroscopy and electron energy-loss spectroscopy, *Phys. Rev. B*, vol. 62, p. 11126–11133, oct. 2000. 30, 80, 82, 84

[162] G. I. N. Waterhouse, G. A. Bowmaker et J. B. Metson, Oxidation of a polycrystalline silver foil by reaction with ozone, *Appl Surf Sci*, vol. 183, p. 191–204, 2001. 30, 80, 81, 84

[163] M. Bielmann, P. Schwaller, P. Ruffieux, O. Gröning, L. Schlapbach et P. Gröning, AgO investigated by photoelectron spectroscopy: Evidence for mixed valence, *Phys. Rev. B*, vol. 65, p. 235431, 2002. 30, 80, 84

[164] T. C. Kaspar, T. Droubay, S. A. Chambers et P. S. Bagus, Spectroscopic evidence for Ag(III) in highly oxidized silver films by x-ray photoelectron spectroscopy, *The Journal of Physical Chemistry C*, vol. 114, p. 21562–21571, 2010. 30, 80, 84

[165] A. M. Ferraria, A. P. Carapeto et A. M. Botelho do Rego, X-ray photoelectron spectroscopy: Silver salts revisited, *Vacuum*, vol. 86, p. 1988–1991, juil. 2012. 30, 80, 84

[166] T. C. R. Rocha, A. Oestereich, D. V. Demidov, M. Hävecker, S. Zafeiratos, G. Weinberg, V. I. Bukhtiyarov, A. Knop-Gericke et R. Schlögl, The silver–oxygen system in catalysis: new insights by near ambient pressure x-ray photoelectron spectroscopy, *Phys. Chem. Chem. Phys.*, vol. 14, p. 4554–4564, 2012. 30, 80, 81, 86, 97, 99

[167] Logeeswaran VJ, N. P. Kobayashi, M. S. Islam, W. Wu, P. Chaturvedi, N. X. Fang, S. Y. Wang et R. S. Williams, Ultrasmooth Silver Thin Films Deposited with a Germanium Nucleation Layer, *Nano Lett.*, vol. 9, p. 178–182, jan. 2009. 31

[168] H. Aouani, J. Wenger, D. Gérard, H. Rigneault, E. Devaux, T. W. Ebbesen, F. Mahdavi, T. Xu et S. Blair, Crucial Role of the Adhesion Layer on the Plasmonic Fluorescence Enhancement, *ACS Nano*, vol. 3, p. 2043–2048, juil. 2009. 31

[169] P. Melpignano, C. Cioarec, R. Clergereaux, N. Gherardi, C. Villeneuve et L. Datas, E-beam deposited ultra-smooth silver thin film on glass with different nucleation layers: An optimization study for OLED micro-cavity application, *Organic Electronics*, vol. 11, no. 6, p. 1111–1119, 2010. 31

[170] W. Q. Chen, M. D. Thoreson, S. Ishii, A. V. Kildishev et V. M. Shalaev, Ultra-thin ultra-smooth and low-loss silver films on a germanium wetting layer, *Opt Express*, vol. 18, p. 5124–5134, mars 2010. 31

[171] J. Zhang, D. M. Fryauf, M. Garrett, V. Logeeswaran, A. Sawabe, M. S. Islam et N. P. Kobayashi, Phenomenological Model of the Growth of Ultrasmooth Silver Thin Films

Deposited with a Germanium Nucleation Layer, *Langmuir*, vol. 31, p. 7852–7859, juil. 2015. 31

[172] P. Dutheil, A. L. Thomann, T. Lecas, P. Brault et M. Vayer, Sputtered Ag thin films with modified morphologies: Influence on wetting property, *Applied Surface Science*, vol. 347, p. 101–108, août 2015. 31

[173] F. X. Bock, T. M. Christensen, S. B. Rivers, L. D. Doucette et R. J. Lad, Growth and structure of silver and silver oxide thin films on sapphire, *Thin Solid Films*, vol. 468, p. 57–64, déc. 2004. 31

[174] M. Todeschini, A. Bastos da Silva Fanta, F. Jensen, J. B. Wagner et A. Han, Influence of Ti and Cr Adhesion Layers on Ultrathin Au Films, *ACS Appl. Mater. Interfaces*, vol. 9, p. 37374–37385, oct. 2017. 31

[175] K. Mizukoshi, T. Yamamura, Y. Tomioka et M. Kawamura, Effect of TiO_2 lowermost layer on crystal orientation and electrical resistivity of glass/TiO_2/ZnO/Ag structure in Low-E glass, *Jpn. J. Appl. Phys.*, vol. 60, p. 025501, fév. 2021. 31

[176] N. Formica, D. S. Ghosh, A. Carrilero, T. L. Chen, R. E. Simpson et V. Pruneri, Ultrastable and Atomically Smooth Ultrathin Silver Films Grown on a Copper Seed Layer, *ACS Appl. Mater. Interfaces*, vol. 5, p. 3048–3053, avril 2013. 31

[177] V. Coleman et C. Jagadish, Chapter 1 - basic properties and applications of zno, *in Zinc Oxide Bulk, Thin Films and Nanostructures* (C. Jagadish et S. Pearton, éds), p. 1–20, Oxford: Elsevier Science Ltd, 2006. 31

[178] C. Agashe, O. Kluth, J. Hüpkes, U. Zastrow, B. Rech et M. Wuttig, Efforts to improve carrier mobility in radio frequency sputtered aluminum doped zinc oxide films, *Journal of Applied Physics*, vol. 95, p. 1911–1917, jan. 2004. 31

[179] K.-K. Kim, S. Niki, J.-Y. Oh, J.-O. Song, T.-Y. Seong, S.-J. Park, S. Fujita et S.-W. Kim, High electron concentration and mobility in Al-doped n-ZnO epilayer achieved via dopant activation using rapid-thermal annealing, *Journal of Applied Physics*, vol. 97, p. 066103, mars 2005. 31

[180] Z. Lin et P. D. Bristowe, A first principles study of the properties of Al:ZnO and its adhesion to Ag in an optical coating, *Journal of Applied Physics*, vol. 106, p. 013520, juil. 2009. 31

[181] C. Ekaterina, *Zinc oxide growth and its interfaces with metals observed by photoemission.* Thèse de doctorat, Sorbonne Université, 2017. 31, 32, 113

[182] C. Tang, M. J. S. Spencer et A. S. Barnard, Activity of ZnO polar surfaces: an insight from surface energies, *Phys. Chem. Chem. Phys.*, vol. 16, p. 22139–22144, sept. 2014. 31

[183] H. Rotella, Y. Mazel, S. Brochen, A. Valla, A. Pautrat, C. Licitra, N. Rochat, C. Sabbione, G. Rodriguez et E. Nolot, Role of vacancy defects in Al doped ZnO thin films for optoelectronic devices, *J. Phys. D: Appl. Phys.*, vol. 50, p. 485106, nov. 2017. 32, 105

[184] Y. Adachi, N. Ohashi, T. Ohnishi, T. Ohgaki, I. Sakaguchi, H. Haneda et M. Lippmaa, Change in polarity of zinc oxide films grown on sapphire substrates without insertion of any buffer layer, *Journal of Materials Research*, vol. 23, p. 3269–3272, déc. 2008. 32

[185] Y. Adachi, N. Ohashi, T. Ohgaki, T. Ohnishi, I. Sakaguchi, S. Ueda, H. Yoshikawa, K. Kobayashi, J. R. Williams, T. Ogino et H. Haneda, Polarity of heavily doped ZnO films grown on sapphire and SiO_2 glass substrates by pulsed laser deposition, *Thin Solid Films*, vol. 519, p. 5875–5881, juil. 2011. 32

[186] N. Jedrecy, G. Renaud, R. Lazzari et J. Jupille, Flat-top silver nanocrystals on the two polar faces of ZnO: An all angle x-ray scattering investigation, *Phys. Rev. B*, vol. 72, p. 045430, juil. 2005. 32, 118

[187] N. Jedrecy, G. Renaud, R. Lazzari et J. Jupille, Unstrained islands with interface coincidence sites versus strained islands: X-ray measurements on Ag/ZnO, *Phys. Rev. B.*, vol. 72, p. 195404, 2005. 32, 118

[188] S. Benedetti, I. Valenti, S. Valeri, S. Castilla, E. Touzé, Y. Bronstein, A. Toumar, F. Finocchi et R. Lazzari, Polar-step driven metal nucleation and growth: the Ag/ZnO($10\bar{1}0$) case, *J. Phys. Chem. C*, vol. 124, p. 6130–6140, 2020. 32

[189] S.-Q. Yang, J. Du et Y.-J. Zhao, First-principles study of ZnO/Mg heterogeneous nucleation interfaces, *Mater. Res. Express*, vol. 5, p. 036519, mars 2018. 32

[190] Y. Tsuda, H. Omoto, K. Tanaka et H. Ohsaki, The underlayer effects on the electrical resistivity of Ag thin film, *Thin Solid Films*, vol. 502, p. 223–227, avril 2006. 32, 106, 108, 118, 119

[191] R. Alvarez, J. C. González, J. P. Espinós, A. R. González-Elipe, A. Cueva et F. Villuendas, Growth of silver on ZnO and SnO_2 thin films intended for low emissivity applications, *Applied Surface Science*, vol. 268, p. 507–515, mars 2013. 32

[192] A. Bingel, O. Stenzel, P. Naujok, R. Müller, S. Shestaeva, M. Steglich, U. Schulz, N. Kaiser et A. Tünnermann, AZO/Ag/AZO transparent conductive films: correlation between the structural, electrical, and optical properties and development of an optical model, *Opt. Mater. Express, OME*, vol. 6, p. 3217–3232, oct. 2016. 32, 119

[193] S. Ernst-Roland, *Understanding and optimizing the electrical transport in silver thin films for the use as heat insulation glass coatings*. Thèse de doctorat, RWTH Aachen University, 2021. 32

[194] W. Wang, M. Song, T.-S. Bae, Y. H. Park, Y.-C. Kang, S.-G. Lee, S.-Y. Kim, D. H. Kim, S. Lee, G. Min, G.-H. Lee, J.-W. Kang et J. Yun, Transparent Ultrathin Oxygen-Doped Silver Electrodes for Flexible Organic Solar Cells, *Advanced Functional Materials*, vol. 24, no. 11, p. 1551–1561, 2014. 32

[195] E. Jeong, S.-G. Lee, J.-S. Bae, S. M. Yu, S. Z. Han, G.-H. Lee, E.-A. Choi et J. Yun, Effects of substantial atomic-oxygen migration across silveroxide interfaces during silver growth, *Applied Surface Science*, vol. 568, p. 150927, déc. 2021. 32

[196] P. Li, H. Li, J. Ma, Y. Zhou, W. Zhang, L. Cong, H. Xu et Y. Liu, Structural Optimization of Oxide/Metal/Oxide Transparent Conductors for High-Performance Low-Emissivity Heaters, *Advanced Materials Interfaces*, vol. 5, no. 24, p. 1801287, 2018. 32

[197] R. Lazzari et J. Jupille, Silver layers on oxide surfaces: morphology and optical properties, *Surf Sci Surf Sci*, vol. 482, p. 823–828, juin 2001. 33

[198] T. Siegfried, Y. Ekinci, O. J. Martin et H. Sigg, Engineering Metal Adhesion Layers That Do Not Deteriorate Plasmon Resonances, *ACS Nano*, vol. 7, p. 2751–2757, mars 2013. 33

[199] R. Lazzari, J. Jupille, R. Cavallotti et I. Simonsen, Model-Free Unraveling of Supported Nanoparticles Plasmon Resonance Modes, *The Journal of Physical Chemistry C*, vol. 118, no. 13, p. 7032–7048, 2014. 33, 43, 44, 46, 65

[200] R. Lazzari, J. Jupille, R. Cavallotti, E. Chernysheva, S. Castilla, M. Messaykeh, Q. Hérault, I. Gozhyk et E. Meriggio, Plasmonics of Supported Nanoparticles Reveals Adhesion at the Nanoscale: Implications for Metals on Dielectrics, *ACS Appl. Nano Mater.*, vol. 3, p. 12157–12168, déc. 2020. 33, 44, 45, 46, 48, 58, 67, 72, 79, 97, 98

[201] V. A. Tolmachev, E. V. Gushchina, I. A. Nyapshaev et Y. A. Zharova, Spectroscopic ellipsometry study of dielectric functions of Ag films and chemically deposited layers of Ag nanoparticles on silicon, *Thin Solid Films*, vol. 756, p. 139352, août 2022. 33

[202] D. Magnfält, *Fundamental processes in thin film growth: The origin of compressive stress and the dynamics of the early growth stages.* Thèse de doctorat, Linköping University, 2014. 33

[203] H. Z. Yu et C. V. Thompson, Correlation of shape changes of grain surfaces and reversible stress evolution during interruptions of polycrystalline film growth, *Appl. Phys. Lett.*, vol. 104, p. 141913, avril 2014. 33

[204] H. Z. Yu et C. V. Thompson, Response to "Comment on 'Correlation of shape changes of grain surfaces and reversible stress evolution during interruptions of polycrystalline film growth'" [Appl. Phys. Lett. 105, 246101 (2014)], *Appl. Phys. Lett.*, vol. 105, p. 246102, déc. 2014. 33

[205] D. Flötotto, Z. M. Wang, L. P. H. Jeurgens et E. J. Mittemeijer, Kinetics and magnitude of the reversible stress evolution during polycrystalline film growth interruptions, *Journal of Applied Physics*, vol. 118, p. 055305, août 2015. 33

[206] A. Engwall, Z. Rao et E. Chason, Origins of residual stress in thin films: Interaction between microstructure and growth kinetics, *Materials & Design*, vol. 110, p. 616–623, nov. 2016. 33

[207] C. Polop, E. Vasco, A. P. Perrino et R. Garcia, Mapping stress in polycrystals with sub-10 nm spatial resolution, *Nanoscale*, vol. 9, p. 13938–13946, sept. 2017. 33

[208] E. Vasco, E. G. Michel et C. Polop, Disclosing the origin of the postcoalescence compressive stress in polycrystalline films by nanoscale stress mapping, *Phys. Rev. B*, vol. 98, p. 195428, nov. 2018. 33

[209] S. O. Mbam, S. E. Nwonu, O. A. Orelaja, U. S. Nwigwe et X.-F. Gou, Thin-film coating; historical evolution, conventional deposition technologies, stress-state micro/nano-level measurement/models and prospects projection: a critical review, *Materials Research Express*, vol. 6, p. 122001, nov. 2019. 33

[210] C. Furgeaud, *Effets cinétique et chimique lors des premiers stades de croissance de films minces métalliques : compréhension multi-échelle par une approche expérimentale et modélisation numérique.* Thèse de doctorat, Université de Poitiers, 2019. 33

[211] E. Chason et P. R. Guduru, Tutorial: Understanding residual stress in polycrystalline thin films through real-time measurements and physical models, *Journal of Applied Physics*, vol. 119, p. 191101, mai 2016. 33

[212] D. G. Stearns et E. M. Gullikson, Nonspecular scattering from extreme ultraviolet multilayer coatings, *Physica B*, vol. 283, p. 84–91, juin 2000. 33

[213] G. Renaud, R. Lazzari, C. Revenant, A. Barbier, M. Noblet, O. Ulrich, F. , J. Jupille, Y. Borensztein, C. R. Henry, J. P. Deville, F. Scheurer, J. Mane-Mane et O. Fruchart, Real-time monitoring of growing nanoparticles, *Science Science*, vol. 300, p. 1416–1419, mai 2003. 33

[214] G. Renaud, M. Ducruet, O. Ulrich et R. Lazzari, Apparatus for real time in situ quantitative studies of growing nanoparticles by grazing incidence small angle X-ray scattering and surface differential reflectance spectroscopy, *Nuclear Instruments and Methods in Physics Research Section B: Beam Interactions with Materials and Atoms*, vol. 222, no. 3-4, p. 667–680, 2004. 33

[215] C. Revenant, F. Leroy, R. Lazzari, G. Renaud et C. Henry, Quantitative analysis of grazing incidence small-angle x-ray scattering:Pd/MgO(001) growth, *Physical Review B*, vol. 69, no. 3, 2004. 33

[216] R. Lazzari, G. Renaud, C. Revenant, J. Jupille et Y. Borensztein, Adhesion of growing nanoparticles at a glance: Surface differential reflectivity spectroscopy and grazing incidence small angle x-ray scattering, *Physical Review B*, vol. 79, no. 12, 2009. 33

[217] I. Miccoli, F. Edler, H. Pfnür et C. Tegenkamp, The 100th anniversary of the four-point probe technique: the role of probe geometries in isotropic and anisotropic systems, *J. Phys.: Condens. Matter*, vol. 27, p. 223201, mai 2015. 39, 40, 42, 53

[218] I. Gozhyk, L. Dai, Q. Hérault, R. Lazzari et S. Grachev, Plasma emission correction in reflectivity spectroscopy during sputtering deposition, *J. Phys. D: Appl. Phys.*, vol. 52, p. 095202, 2018. 43

[219] R. Lazzari, I. Simonsen et J. Jupille, Interfacial susceptibilities in nanoplasmonics via inversion of Fresnel coefficients, *Plasmonics*, vol. 9, p. 261–272, 2014. 44, 46

[220] `GranFilm` can be downloaded with a user guide from: http://www.insp.jussieu.fr/-Logiciels-.html. 45

[221] R. Lazzari et I. Simonsen, GranFilm: a software for calculating thin-layer dielectric properties and Fresnel coefficients, *Thin Solid Films*, vol. 419, no. 1, p. 124–136, 2002. 45

[222] D. Bedeaux et J. Vlieger, *Optical Properties of Surfaces*. London: Imperial College Press, 2001. 45

[223] I. Simonsen, R. Lazzari, J. Jupille et S. Roux, Numerical modelling of the optical response of supported metallic particles, *Phys. Rev. B*, vol. 61, no. 11, p. 7722–7733, 2000. 45, 46

[224] R. Lazzari, I. Simonsen, D. Bedeaux, J. Vlieger et J. Jupille, Polarizability of truncated spheroidal island supported by a substrate : models and applications, *Eur. Phys. J. B*, vol. 24, p. 267–284, 2001. 45, 46

[225] R. Lazzari, S. Roux, I. Simonsen, J. Jupille, D. Bedeaux et J. Vlieger, Multipolar plasmon resonances in supported silver particles:The case of $Ag/Al_2O_3(0001)$, *Physical Review B*, vol. 65, no. 23, 2002. 46

[226] E. D. Palik, *Handbook of Optical Constants of Solids*, vol. 1-3. Academic Press, 1985. 46

[227] S. Indrehus, *Plasmonics properties of supported nanoparticles.* Thèse de doctorat, Sorbonne Universit2, 2020. 46, 60

[228] R. Lazzari, G. Renaud, C. Revenant, J. Jupille et Y. Borensztein, Adhesion of growing nanoparticles at a glance: Surface differential reflectivity spectroscopy and grazing incidence small angle X-ray scattering, *Phys. Rev. B*, vol. 79, p. 125428, 2009. 46

[229] R. Lazzari et J. Jupille, Quantitative analysis of nanoparticle growth through plasmonics, *Nanotechnology*, vol. 22, p. 445703, 2011. 46, 61

[230] R. Lazzari et J. Jupille, Growth kinetics and size-dependent wetting of Ag/α-$Al_2O_3(0001)$ nanoparticles studied via the plasmonic response, *Nanotechnology*, vol. 23, p. 135707, 2012. 46, 61

[231] X.-Y. Gao, H.-L. Feng, J.-M. Ma, Z.-Y. Zhang, J.-X. Lu, Y.-S. Chen, S.-E. Yang et J.-H. Gu, Analysis of the dielectric constants of the Ag_2O film by spectroscopic ellipsometry and single-oscillator model, *Physica B: Condensed Matter*, vol. 405, p. 1922–1926, Apr 2010. 46

[232] I. Simonsen, R. Lazzari, J. Jupille et S. Roux, Numerical modelling of the optical response of supported metallic particles, *Phys. Rev. B*, vol. 61, no. 11, p. 7722–7733, 2000. 46

[233] R. Lazzari. `Igor Pro Paris Photoemission Package` can be downloaded with a user guide from: http://www.insp.upmc.fr/I4P-Igor-Pro-Paris-Photoemission.html?lang=en. 49

[234] S. Tougaard, Universality classes of inelastic electron scattering cross-sections, *Surf. Interface Anal.*, vol. 25, no. 3, p. 137–154, 1997. 49

[235] C. Klauber, Refinement of magnesium and aluminium Kα x-ray source functions, *Surf. Interface Anal.*, vol. 20, no. 8, p. 703–715, 1993. 49

[236] NIST X-ray photoelectron spectroscopy database. https://srdata.nist.gov/xps/Default.aspx. 49

[237] J. Yeh et I. Lindau, Atomic subshell photoionization cross sections and assymetry parameters: $1 \leq z \leq 300$, *At. Data Nucl. Data Tables*, vol. 32, p. 1–155, 1985. 50

[238] S. Guilet, L. Bataillou, O. Kerivel et R. Lazzari, Determination of the intensity/energy response function of an hemispherical photoelectron analyser based on Tougaard background, *Journal of Electron Spectroscopy and Related Phenomena*, vol. 258, p. 147225, 2022. 50

[239] S. Tanuma, C. J. Powell et D. R. Penn, Calculation of electron inelastic mean free paths (IMFPs) VII. Reliability of the TPP-2M IMFP predictive equation, *Surf. Interface Anal.*, vol. 35, no. 3, p. 268–275, 2003. 50, 113

[240] S. Tougaard, QUASES-IMFP-TPP2M Software. http://www.quases.com/products/quases-imfp-tpp2m/. 50, 63

[241] P. Zaumseil, High-resolution characterization of the forbidden Si(200) and Si(222) reflections, *Journal of Applied Crystallography*, vol. 48, p. 528–532, 2015. 52

[242] G. Zhao, W. Shen, E. Jeong, S. G. Lee, H. S. Chung, T. S. Bae, J. S. Bae, G. H. Lee, J. Tang et J. Yun, Nitrogen-Mediated Growth of Silver Nanocrystals to Form UltraThin, High-Purity Silver-Film Electrodes with Broad band Transparency for Solar Cells, *ACS Appl Mater Interfaces*, vol. 10, p. 40901–40910, nov. 2018. 56, 71, 72

[243] J. F. Moulder, W. F. Stickle, P. E. Sobol et K. D. Bomben, *Handbook of X-ray photoelectron spectroscopy*. Eden Prairie, Minnesota, USA: Physical Electronics, Perkin Elmer., 1995. 60, 63, 84

[244] E. S. Shanley et J. L. Ennis, The chemistry and free energy of formation of silver nitride, *Ind. Eng. Chem. Res.*, vol. 30, p. 2503–2506, 1991. 63, 69, 71

[245] B. W. J. Chen, D. Kirvassilis, Y. Bai et M. Mavrikakis, Atomic and Molecular Adsorption on Ag(111), *J. Phys. Chem. C*, vol. 123, p. 7551–7566, avril 2019. 63, 71

[246] Y. V. Butenko, L. Alves, A. C. Brieva, J. Yang, S. Krishnamurthy et S. L., X-ray induced decomposition of gold nitride, *Chem. Phys. Lett.*, vol. 430, p. 89–92, 2006. 65

[247] Visualization for electronic and structural analysis (vesta). https://jp-minerals.org/vesta/en/. 70, 95

[248] R. Kaischew, Sur la thermodynamique des germes cristallins., *Bull. Acad., Sci. Bulg., Ser. Phys.*, vol. 2, p. 191, 1951. 72

[249] C. T. Campbell, Ultrathin metal films and particles on oxide surfaces: structural, electronic and chemisorptive properties, *Surf. Sci. Rep.*, vol. 27, no. 1-3, p. 1–111, 1997. 72, 98

[250] F. Leroy, G. Renaud, A. Letoublon, R. Lazzari, C. Mottet et J. Goniakowski, Self-organized growth of nanoparticles on a surface patterned by a buried dislocation network, *Phys. Rev. Lett.*, vol. 95, p. 185501, 2005. 73

[251] A. Michaelides, K. Reuter et M. Scheffler, When seeing is not believing: Oxygen on Ag(111), a simple adsorption system?, *Journal of Vacuum Science & Technology A*, vol. 23, p. 1487–1497, oct. 2005. 79

[252] R. O. Suzuki, T. Ogawa et K. Ono, Use of ozone to prepare silver oxides, *J. Am. Ceram. Soc.*, vol. 82, no. 8, p. 2033–2038, 1999. 80

[253] G. I. N. Waterhouse, J. B. Metson et G. A. Bowmaker, Synthesis, vibrational spectra and thermal stability of Ag_3O_4 and related Ag_7O_8x salts (X=NO_3^-,ClO_4^-,HSO_4^-), *Polyhedron*, vol. 26, p. 3310–3322, 2007. 80

[254] C. Rehren, M. Muhler, X. Bao, R. Schlögl et C. Ertl, The interaction of silver with oxygen, *Zeitschrift für Physikalische Chemie*, vol. 174, p. 11 – 52, 1991. 80, 81

[255] S. Grönbeck, H.and Klacar, N. M. Martin, A. Hellman, E. Lundgren et J. N. Andersen, Mechanism for reversed photoemission core-level shifts of oxidized Ag, *Phys. Rev. B*, vol. 85, p. 115445, 2012. 80

[256] C. T. Campbell, Atomic and molecular oxygen adsorption on Ag(111), *Surface Science*, vol. 157, p. 43–60, 1985. 81

[257] B. Pettinger, X. Bao, I. C. Wilcock, M. Muhler et G. Ertl, Surface-enhanced raman scattering from surface and subsurface oxygen species at microscopically well-defined ag surfaces, *Phys. Rev. Lett.*, vol. 72, p. 1561–1564, 1994. 81

[258] M. Rocca, L. Savio, L. Vattuone, U. Burghaus, V. Palomba, N. Novelli, F. Buatier de Mongeot, U. Valbusa, R. Gunnella, G. Comelli, A. Baraldi, S. Lizzit et G. Paolucci, Phase transition of dissociatively adsorbed oxygen on Ag(001), *Phys. Rev. B*, vol. 61, p. 213–227, 2000. 81

[259] V. I. Bukhtiyarov, M. Hävecker, V. V. Kaichev, A. Knop-Gericke, R. W. Mayer et R. Schlögl, Atomic oxygen species on silver: Photoelectron spectroscopy and x-ray absorption studies, *Phys. Rev. B*, vol. 67, p. 235422, 2003. 81

[260] T. E. Jones, T. C. R. Rocha, A. Knop-Gericke, C. Stampfl, R. Schlögl et S. Piccinin, Thermodynamic and spectroscopic properties of oxygen on silver under an oxygen atmosphere, *Phys. Chem. Chem. Phys.*, vol. 17, p. 9288–9312, 2015. 81, 84

[261] D. Y. Zemlyanov, A. Hornung, G. Weinberg, U. Wild et R. Schlögl, Interaction of Silver with a NO/O_2 Mixture: A Combined X-ray Photoelectron Spectroscopy and Scanning Electron Microscopy Study, *Langmuir*, vol. 14, p. 3242–3248, juin 1998. 81

[262] D. Y. Zemlyanov, A. Nagy et R. Schlögl, The reaction of silver with NO/O_2, *Applied Surface Science*, vol. 133, p. 171–183, juil. 1998. 81

[263] N. M. Martin, S. Klacar, H. Grönbeck, J. Knudsen, J. Schnadt, S. Blomberg, J. Gustafson et E. Lundgren, High-coverage oxygen-induced surface structures on Ag(111), *The Journal of Physical Chemistry C*, vol. 118, p. 15324–15331, 2014. 81

[264] J. Schnadt, J. Knudsen, X. L. Hu, A. Michaelides, R. T. Vang, K. Reuter, Z. Li, E. Lægsgaard, M. Scheffler et F. Besenbacher, Experimental and theoretical study of oxygen adsorption structures on Ag(111), *Phys. Rev. B*, vol. 80, p. 075424, août 2009. 81

[265] W.-X. Li, C. Stampfl et M. Scheffler, Oxygen adsorption on Ag(111): A density-functional theory investigation, *Phys. Rev. B*, vol. 65, p. 075407, jan. 2002. 81

[266] W.-X. Li, C. Stampfl et M. Scheffler, Why is a Noble Metal Catalytically Active? The Role of the O-Ag Interaction in the Function of Silver as an Oxidation Catalyst, *Phys. Rev. Lett.*, vol. 90, p. 256102, juin 2003. 81

[267] X. Bao, J. V. Barth, G. Lehmpfuhl, R. Schuster, Y. Uchida, R. Schlögl et G. Ertl, Oxygen-induced restructuring of Ag(111), *Surface Science*, vol. 284, p. 14–22, mars 1993. 81

[268] C. T. Campbell, An XPS study of molecularly chemisorbed oxygen on Ag(111), *Surface Science Letters*, vol. 173, p. L641–L646, août 1986. 81

[269] G. N. Salaita, Z. F. Hazos et G. B. Hoflund, Surface characterization study of the thermal decomposition of Ag_2CO_3 using x-ray photoelectron spectroscopy and electron energy loss spectroscopy, *Journal of Electron Spectroscopy and Related Phenomena*, vol. 107, p. 73–81, 2000. 82, 84

[270] E. McCafferty et J. P. Wightman, Determination of the concentration of surface hydroxyl groups on metal oxide films by a quantitative XPS method, *Surf Interface Anal*, vol. 26, p. 549–564, 1998. 82

[271] Y. C. Her, Y. C. L. Chang, W. C. Hsu et S. Y. Tsai, The characteristics of reactively sputtered AgO_x films prepared at different oxygen flow ratios and its effect on super-resolution near-field properties, *Jpn J Appl Phys*, vol. 43, p. 267–272, 2004. 89, 94

[272] U. K. Barik, S. Srinivasan, C. L. Nagendra et A. Subrahmanyam, Electrical and optical properties of reactive DC magnetron sputtered silver oxide thin films: role of oxygen, *Thin Solid Films*, vol. 429, p. 129–134, 2003. 94

[273] R. C. Munoz et C. Arenas, Size effects and charge transport in metals: Quantum theory of the resistivity of nanometric metallic structures arising from electron scattering by grain boundaries and by rough surfaces, *Applied Physics Reviews*, vol. 4, p. 011102, 2017. 97

[274] W.-X. Li, C. Stampfl et M. Scheffler, Insights into the function of silver as an oxidation catalyst by *ab initio* atomistic thermodynamics, *Phys. Rev. B*, vol. 68, p. 165412, 2003. 98, 99

[275] M. Gajdoš, A. Eichler et J. Hafner, Ab initio density functional study of O on the Ag(001) surface, *Surf Sci*, vol. 531, p. 272–286, 2003. 98

[276] G. Zhao, E. Jeong, E. A. Choi, S. M. Yu, J.-S. Bae, A.-G. Lee, S. Z. Han, G. H. Lee et J. Yun, Strategy for improving ag wetting on oxides: Coalescence dynamics versus nucleation density, *Appl. Surf. Sci.*, vol. 510, p. 145515, 2020. 98

[277] L. Zhu, H. Xu, Y. Nan, J. Zhu et D. Cheng, Facet-dependent diffusion of atomic oxygen on Ag surfaces, *Comp Mater Sci*, vol. 155, p. 17–27, 2018. 98

[278] S. B. Rivers, G. Bernhardt, M. W. Wright, D. J. Frankel, M. M. Steeves et R. J. Lad, Structure, conductivity, and optical absorption of $Ag_{2x}O$ films, *Thin Solid Films*, vol. 515, p. 8684–8688, oct. 2007. 100

[279] A. Akdağ, H. F. Budak, M. Yılmaz, A. Efe, M. Büyükaydın, M. Can, G. Turgut et E. Sönmez, Structural and Morphological Properties of Al doped ZnO Nanoparticles, *J. Phys.: Conf. Ser.*, vol. 707, p. 012020, avril 2016. 105

[280] F. Wang, M. Z. Wu, Y. Y. Wang, Y. M. Yu, X. M. Wu et L. J. Zhuge, Influence of thickness and annealing temperature on the electrical, optical and structural properties of AZO thin films, *Vacuum*, vol. 89, p. 127–131, mars 2013. 105

[281] J. Voronkoff, *Interactions dans les empilements de couches NiCr/ZnO déposées par pulvérisation : impact couplé des paramètres de dépôt et de recuit.* Thèse de doctorat, Sorbonne université, 2019. 105, 106

[282] H.-L. Thi Le, R. Lazzari, J. Goniakowski, R. Cavallotti, S. Chenot, C. Noguera, J. Jupille, A. Koltsov et J.-M. Mataigne, Tuning adhesion at metal/oxide interfaces by surface hydroxylation, *J. Phys. Chem. C*, vol. 121, p. 11464–11471, 2017. 113

[283] B.-G. Jung, M. Cheon, S. J. Kim, A. Gliserin, S. H. Chew, C. R. Cho, S.-G. Kim, Y. H. Lee, S. Kim et S.-Y. Jeong, Wafer-scale high-quality Ag thin film using a ZnO buffer layer for plasmonic applications, *Applied Surface Science*, vol. 512, p. 145705, mai 2020. 119

[284] E. Jeong, S.-G. Lee, J.-S. Bae, S. M. Yu, C. Mun, S. Z. Han, G.-H. Lee, E.-A. Choi et J. Yun, Establishing Substoichiometric Ag Oxidation and Its Physicochemical, Optoelectrical, and Structural Consequences for Ag Electrodes, *ACS Appl. Electron. Mater.*, vol. 4, p. 4683–4693, sept. 2022. 128

[285] E. Jeong, T. Lee, S.-G. Lee, S. M. Yu, J.-S. Bae, G.-H. Lee, D. Choi et J. Yun, Thermal stability enhancement of ultrathin Ag film electrodes by incorporating atomic oxygen, *Applied Surface Science*, vol. 546, p. 149149, avril 2021. 128

[286] G. Abadias et P. Guerin, In situ stress evolution during magnetron sputtering of transition metal nitride thin films, *Appl. Phys. Lett.*, vol. 93, no. 11, p. 111908, 2008. 141

[287] S. Grachev, Q. Hérault, J. Wang, M. Balestrieri, H. Montigaud, R. Lazzari et I. Gozhyk, A new method for high resolution curvature measurement applied to stress monitoring in thin films, *Nanotechnology*, vol. 33, p. 185701, fév. 2022. 141

[288] Q. Hérault, I. Gozhyk, M. Balestrieri, H. Montigaud, S. Grachev et R. Lazzari, Kinetics and mechanisms of stress relaxation in sputtered silver thin films, *Acta Materialia*, vol. 221, p. 117385, déc. 2021. 141

[289] L. Xie, P. Brault, J.-M. Bauchire, A.-L. Thomann et L. Bedra, Molecular dynamics simulations of clusters and thin film growth in the context of plasma sputtering deposition, *J. Phys. D: Appl. Phys.*, vol. 47, p. 224004, mai 2014. 141

Etude par mesures *in situ* et en temps réel de l'effet d'additifs gazeux sur la croissance de couches minces d'argent par pulvérisation cathodique magnétron

Dans le cadre de la production de vitrages « bas-émissifs » (« Low-E ») avec des propriétés d'isolation thermique renforcées, des empilements diélectriques complexes contenant des couches minces d'argent d'une épaisseur d'environ 12 nm sont déposés sur des surfaces de verre. Pour le dépôt de ces couches, la pulvérisation cathodique magnétron est une technique largement utilisée par l'industrie verrière. Les recherches actuelles visent à mieux comprendre la croissance des couches minces d'Ag pendant le dépôt et à trouver des stratégies pour contrôler leur croissance et leurs microstructures. L'objectif étant d'améliorer l'efficacité d'isolation thermique de ces vitrages, tout en gardant une faible épaisseur de la couche métallique et une bonne transmission dans le visible.
Parmi les différentes techniques qui ont été développées pour contrôler la croissance des couches minces d'Ag, l'utilisation d'additifs gazeux dits « surfactants » pendant le dépôt magnétron a suscité beaucoup d'intérêt ces dernières années auprès de la communauté scientifique et l'industrie verrière. Ces gaz agissent sur les films d'argent pour contrebalancer leur tendance naturelle à une croissance type 3D ou Volmer-Weber, forçant à la place une croissance plus 2D. Idéalement, ils devraient permettre le dépôt de films conducteurs avec une plus faible épaisseur, sans pour autant s'incorporer dans le film et sans effet délétère sur sa conductivité. Au-delà de cette image idéale, cependant, le rôle de ces additifs ainsi que les mécanismes impliqués ne sont pas encore bien compris.
Les effets de l'ajout de deux gaz « surfactants », N_2 et O_2, pendant le dépôt par pulvérisation magnétron des couches minces d'Ag ont été étudiés à l'aide de caractérisations en temps réel et *in situ*. Les mesures de résistance électrique en temps réel permettent de détecter le seuil de formation d'une couche conductrice (percolation) et la résistivité du film, tandis que les mesures de réflectivité différentielle fournissent des informations sur le mouillage des nanoparticules d'Ag dans les étapes initiales de croissance (nucléation, croissance, coalescence). En parallèle, la composition chimique du film a été caractérisée par spectroscopie photoélectronique *in situ*. Des mesures ex situ de microscopie électronique de transmission et diffraction de rayons-x ont été faites en complément. Une étude systématique de l'effet de l'ajout de N_2 et O_2 a été réalisée en fonction de leur fraction dans le flux total de gaz introduit dans l'enceinte de dépôt. L'ajout de chacun des deux gaz favorise la formation d'une couche conductrice à une épaisseur plus faible que lors d'un dépôt sous Ar pur, car les gaz agissent sur les premières étapes de croissance de la couche d'Ag et sur la texture et cristallinité du film. Une oxydation complexe de l'Ag a été également observée dans le cas du O_2, mais aucune formation de nitrure ni de composé azoté n'a été détectée avec N_2. La modification de l'énergie de surface du métal augmente le mouillage des nanoparticules d'Ag et génère une compétition entre différentes orientations cristallines. Ces effets, ainsi que l'oxydation du film dans le cas du O_2, entraînent une coalescence retardée entre les nanoparticules et une perte de conductivité du film.
Finalement, pour étudier l'impact du substrat sur l'effet des gaz surfactants, des dépôts d'Ag sur une sous-couche de SiO_2 et sur une sous-couche d'oxyde de zinc dopé aluminium (AZO) ont été comparés. La plus faible énergie de l'interface métal-substrat ainsi que la plus forte texturation du film de Ag déposé sur AZO ont eu comme conséquence l'augmentation du mouillage des nanoparticules d'Ag, et la formation de couches plus conductrices et à des épaisseurs plus faibles. Des études de gradient de composition en profondeur ont montré que l'oxydation du film d'Ag sous O_2 dépend également du sub-

strat, avec une fraction d'Ag oxydé proche de l'interface substrat-métal plus importante dans le cas d'un film de Ag déposé sur AZO.

Mots-clés :
Couches minces métalliques, Croissance de couches minces, Pulvérisation cathodique magnétron, Couches minces, Argent, Caractérisation in situ.

Study of the effect of gaseous additives on the growth of Ag films during magnetron sputtering deposition, using *in situ* and real-time measurements

Complex dielectric thin-film stacks containing Ag layers (with a thickness of roughly 12 nm) are deposited on glass surfaces to produce "Low-E" glazing products, for enhanced thermal insulation applications. Magnetron sputtering deposition is the industrially relevant technique used for their production. Current research efforts in the area aim at finding ways of controlling the out-of-equilibrium growth of the metal film and its resulting microstructural properties, with the purpose of improving the insulation efficiency of the glazing whilst maintaining a low metal thickness and high optical transmission in the visible region. In this context, the use of so-called "surfactant" gas additives during sputtering deposition has garnered much attention over the last years. These gases act upon the growing Ag film to counterbalance the 3D Volmer-Weber growth mode and force a more 2D-like growth. Ideally, they should allow for the deposition of thinner, conductive films without compromising their conductivity and without incorporating into the film. However, beyond the ideal picture, the exact role of these additives and the mechanisms involved remain unclear.
The effect of two "surfactant gases", namely N_2 and O_2, on the growth of Ag films during magnetron sputtering deposition was studied using a combination of real-time and *in situ* measurements. Real-time electrical film resistance was used to probe the percolation threshold thickness and film resistivity, while Surface Differential Reflectance Spectroscopy provided information on the wetting behaviour of the Ag nanoparticles in the initial growth stages. Film chemistry was characterized using *in situ* X-Ray Photoelectron Spectroscopy. These analyses were further supplemented by ex situ Transmission Electron Microscopy and X-Ray Diffraction measurements. A systematic study was performed as a function of the fraction of O_2 or N_2 in the gas flow going into the deposition chamber. Both gases were shown to promote the formation of a conductive and continuous film at a lower deposited thickness than for deposition under pure Ar, mostly by acting upon the initial steps of film growth (nucleation, growth and coalescence) and by affecting the texture and crystallinity of the Ag film. A complex Ag oxidation chemistry was observed in the case of O_2, but no nitride formation could be evidenced for N_2 addition. By modifying the Ag metal surface energy, the addition of surfactant gases leads to increased nanoparticle wetting in the initial growth stages, but also leads to competition between different crystallographic orientations. This effect, alongside film oxidation in the case of O_2, results in a delayed coalescence between nanoparticles, and a decrease in film conductivity.
Finally, to see how the impact of these gases differs depending on the substrate, Ag deposition on SiO_2 and on aluminium-doped zinc oxide (AZO) underlayers was compared. The lower energy of the metal-substrate interface as well as the improved (111) textura-

tion of the Ag films on AZO led to improved nanoparticle wetting and the formation of continuous, more conductive films at a lower thickness. The film oxidation dynamics were also shown to depend on the substrate, with composition profiles for the Ag films showing a higher oxide fraction near the metal-substrate interface for AZO underlayers.

Keywords:
Metallic Thin films, Thin film growth, Magnetron sputtering deposition, Metallic films, Silver, In situ characterization.